Spectroscopy of A-type-stars

Der Naturwissenschaftlichen Fakultät
der Friedrich-Alexander-Universität
Erlangen-Nürnberg
zur

Erlangung des Doktorgrades Dr. rer. nat.

vorgelegt von

Christian Heuser

aus Erlangen

FRIEDRICH-ALEXANDER
UNIVERSITÄT
ERLANGEN-NÜRNBERG

NATURWISSENSCHAFTLICHE
FAKULTÄT

ERLANGEN CENTRE
FOR ASTROPARTICLE
PHYSICS

Als Dissertation genehmigt
von der Naturwissenschaftlichen Fakultät
der Friedrich-Alexander-Universität Erlangen-Nürnberg

Tag der mündlichen Prüfung:	01.03.2018
Vorsitzender des Promotionsorgans:	Prof. Dr. Georg Kreimer
Gutachter:	Prof. Dr. Ulrich Heber
Gutachter:	Prof. Dr. Norbert Przybilla

Zusammenfassung

Die Suche nach extrasolaren Planeten war bisher auf sonnenähnliche Sterne fokussiert und wurde vor kurzem sehr erfolgreich auf Sterne niedrigerer Massen, wie beispielsweise Proxima Centauri, ausgeweitet. Sterne mit größerer Masse als unsere Sonne haben bisher weniger Aufmerksamkeit erlangt, weil die spektroskopischen Detektionsmethoden, die für spätere Spektraltypen angewandt werden, für frühe Sterne weniger geeignet bzw. auf Planeten großer Masse in engen Umlaufbahnen beschränkt sind. Das Auffinden von Planeten um Sterne mittlerer Masse ist jedoch entscheidend für das Verständnis von der Entstehung von Planeten und der Entwicklung von Planetensystemen. Numerische Modelle sagen voraus, dass sich mit größerer Sternmasse auch die Masse der protoplanetaren Scheibe vergrößert und sich deren Lebenszeit verkürzt. Deshalb ist die Untersuchung solcher Sterne mittlerer Masse und ihrer möglichen substellaren Begleitern (Planeten und braune Zwerge) perfekt geeignet, um die Theorien der Entstehung von Planeten kurzperiodischer Umlaufbahnen zu untersuchen.
Ein durch die DFG finanziertes Projekt zur Untersuchung von B-, A- und F-Sternen, deren CoRoT-Lichtkurven Hinweise auf Transits substellarer Begleiter aufweisen, wurde gestartet. Am Anfang dieses Projektes war nur ein Hauptreihenstern der Spektralklasse A bekannt (WASP33), mittlerweile sind nur drei weitere hinzu gekommen. Die EXODAT Datenbank diente als erste Quelle für die Spektralklassifikation der Kandidaten. Danach wurde eine automatisierte Klassifikation von Spektren vom Anglo-Australischen Teleskop mittels Template-Spektren durchgeführt. Es wurden nur Objekte ausgewählt, die eine Orbital-Periode von weniger als sechs Tagen und eine maximale Transittiefe von 1.5% des Gesamtflusses aufwiesen. Die daraus resultierende Liste von Kandidaten umfasst 100 Objekte. Eine genauere Lichtkurvenanalyse führte zu einer Reduzierung dieser Liste auf 20 Systeme, für die nachfolgend Zeitserien von hochaufgelösten Spektren von bodengebundenen Teleskopen aufgenommen wurden um einerseits Radialgeschwindigkeitsmessungen und andererseits Material für quantitative Spektralanalysen zu erhalten. Das Ziel der Studie ist es, die Eigenschaften der Muttersterne, und damit auch die Natur der Begleiter, so genau wie möglich zu bestimmen.
Unsere Spektralanalyse basiert auf dem Vergleich von Modellspektren mit beobachteten Daten. Die Modellierung der Sternspektren erfolgt über Hybridverfahren, in dem die rechenaufwändigen Abweichungen vom thermodynamischen Gleichgewichtszustand (LTE) nur für die Spektrumssynthese, d.h. der Modellierung der Linienprofile durchgeführt wird. Für die Modellierung der Atmosphärenstruktur wird vereinfachend LTE angenommen, denn es konnte bereits für heiße Riesensterne sowie Hauptreihen B-Sterne gezeigt werden, dass diese Näherung gerechtfertigt ist. Eine weitere Vereinfachung bestand darin, die Modellspektren nicht für alle chemischen Elemente gleichzeitig zu berechnen. Dabei wurde je ein Spektrum mit Wasserstoff, Helium und einem einzelnen chemischen Element berechnet und dieses durch ein pures H+He Spektrum geteilt. Die daraus resultierenden Spektren wurden am Ende alle miteinander gefaltet. Diese Methode ist korrekt für Spektren mit genügendem Abstand zwischen den Absorptionslinien, führt aber zu Abweichungen bei sogenannten "Lineblends", d.h. wenn sich zwei Spektrallinien bei fast gleicher Wellenlänge überlagen, denn dies würde zu systematisch zu starken Spektrallinien führen. Wellenlängenbereiche mit ausgeprägten Linienblends werden aus dem Spektrum ausgeschnitten, um glaubwürdige Ergebnisse zu erhalten. Diese Methode wur-

de bisher nur für B-Sterne erfolgreich eingesetzt. Dies erwies sich bei den teilweise sehr eng aneinander liegenden Linien in Spektren von A-Sternen als sehr zeitaufwendig, weshalb ein extensiver Test an zehn, bereits in der Literatur sehr gut studierten, Sternen zur Quantifizierung der Effekte durchgeführt wurde. Die erhaltenen Korrekturfaktoren sind hilfreich um eine schnelle Analyse der Sterne durchführen zu können.
Das Auffinden des besten Modells zu einem beobachteten Spektrum erfolgte mithilfe verschiedener Algorithmen, wobei als Maß für die Übereinstimmung das χ^2-Kriterium verwendet wurde. Um Zeit zu sparen wurden die Modellspektren nicht während des Fitprozesses berechnet, sondern ein im Vorfeld berechnetes Modellgitter verwendet. Beim Fitprozess wurde zwischen den Gitterpunkten linear interpoliert.
Zusätzlich zu dem angesprochenen Korrekturfaktoren, die im Rahmen der Spektrumssynthese notwendig wurden, führten wir ausgiebige Tests der NLTE-Effekte aller chemischen Elemente durch, für die entsprechende Atommodelle vorhanden waren. Die Ergebnisse zeigen die Abhängigkeiten der Effekte auf die wichtigsten physikalischen Parameter der Sternatmosphäre, nämlich der Effektivtemperatur, der Schwerebeschleunigung an der Oberfläche und der Gesamtmetallizität.
Des Weiteren wurde die Liste der Absorptionslinien in optischen Spektren von B-Sternen um die von A-Sternen erweitert. Aufgrund der kühleren Atmosphäre wurden einige niedrigere Ionisationsstufen von Elementen, die auch in B-Sternen auftauchen, wichtig und aufgrund der häufig auftretenden chemischen Auffälligkeiten wurden einige zusätzliche Elemente eingeführt, z.B. seltene Erden wie Zr, La und Ce.
Die beschriebene Analysemethode wurde als erstes auf den bereits bekannten, ersten Haupreihen-A-Stern mit planetarem Begleiter WASP33 angewandt. Unsere Analyse revidiert die publizierten Ergebnisse einer photometrischen Studie und ergibt eine 500 K höhere Effektivtemperatur, eine um 0.3 dex geringerer Schwerebeschleunigung und eine 0.2 dex höherer Metallizität. Dadurch ergibt sich ein entwickelterer Stern größerer Masse ($M = 1.85 \pm 0.15\,\mathrm{M}_\odot$, $R = 2.12 \pm 0.32\,\mathrm{R}_\odot$). Für den Begleiter ergibt sich eine obere Massengrenze von $m < 4.48 \pm 0.24\,\mathrm{M}_\mathrm{Jup}$, da sich aus der Radialgeschwindigkeitskurve nur eine obere Grenze für die maximale Dopplerreflexbewegung des Hauptsterns ableiten lässt.
Eine weitere Analyse wurde für SWASP J0247-25 durch geführt, ein Doppelstern, bestehend aus einem A-Stern mit einem pulsierenden und entwickelten B-Stern-Begleiter geringer Masse. Unsere Analyseergebnisse beider Sterne decken sich sehr gut mit bereits von anderen Gruppen publizierten Werten und die des B-Sterns perfekt zu Resultaten der Asteroseismologie. Unsere Untersuchung gibt zum ersten mal einen detaillierten Einblick in die Elementhäufigkeiten in den Atmosphären beider Sterne. Die von uns gefundene Heliumhäufigkeit in der Atmosphäre des B-Sterns ist geringer als Modelle, die zur Erklärung der beobachteten Pulsation herangenommen werden, voraussagen, was wiederum auf diffusive Sedimentation des Heliums in tiefere Schichten des Sterns schließen lässt. Die beobachteten Eigenschaften des Sterns passen auch zu Evolutionsmodellen, die Diffusion mit berücksichtigen. Die vorhergesagte Anreicherung von α-Elementen konnte wir allerdings nicht bestätigen.
Insgesamt zeigt der B-Stern von den in beiden Spektren sichtbaren Elementen die geringeren Häufigkeiten als der A-Stern, was ebenfalls auf die Sedimentation auch dieser Elemente im B-Stern schließen lässt.

Der dritte analysierte Stern, WISE J0725-2351, motivierte uns zur Erweiterung unseres Gitters zu tieferen Temperaturen. Auf den ersten Blick schien es sich um einem A-Stern handeln, der sich jedoch als metallarmer (hundertfach metallärmer als die Sonne) und alter (12 Milliarden Jahre) F-Stern herausstellte. Wir führten einen Vergleich des flusskalibrierten Spektrums zu ATLAS9 Modellen durch. Die Erweiterung des Modell-Gitters zu tieferen Temperaturen (6500 K) erlaubte uns quantitative Spektralanalysen des CoRoT-Kandidaten #0307 sowie dem Doppelstern #0108 auszuführen.
Das Hauptziel dieser Arbeit lag in der quantitativen Analyse der CoRoT-Sterne. Anhand Spektren hoher Qualität wurden die atmosphärischen Parameter der Sterne revidiert und mithilfe von Evolutionsmodellen Masse und Radius bestimmt. Radialgeschwindikeitsmessungen erlaubten es uns auch die Masse der Begleiter neu zu vermessen.
Bei zwei Kandidaten (#2657 und #2721) stellten wir Hinweise auf einen massearmen stellaren Begleiter fest. Der chemisch auffällige Ap Stern #1475 ist der wahrscheinlichste Kandidat eines Hauptreihen-Sterns mittlerer Masse mit substellarem Begleiter. Unsere Analyse ergibt für die Masse des Begleiters $m \approx 82\,M_{\mathrm{Jup}}$, was an der Grenze zwischen einem massearmen Stern und einem braunen Zwerg liegt. Der kleine Radius von $r \approx 1.6\,R_{\mathrm{Jup}}$ deutet damit eher auf einen braunen Zwerg hin. Den bereits als Stern identifizierten Begleiter von #0108 konnten wir bestätigen. Unsere Analyse ergab eine Masse von $\sim 177\,M_{\mathrm{Jup}}$ und einen Radius von $r = 2.1 \pm 0.3\,\mathrm{R_{Jup}}$.
Ein weiterer spannender Kandidat für einen planetaren Begleiter ist #1712. Die Radialgeschwindigkeitsmessung aus zwei HARPS Spektren ergeben eine geringe maximale Semi-Amplitude der Radialgeschwindigkeitskurve. Diese Datenlage ist natürlich nicht ausreichend um eine definitive Aussage zu treffen, sollte sich aber der geringe Werte bestätigen, so hätte der Begleiter maximal eine Masse von einer halben Jupitermasse. Damit wäre dieser A-Stern der einzige aus unserer Untersuchung mit einem planetaren Begleiter.
Ein weiteres Highlight dieser Studie ist der erstmalige Nachweis eines substellaren Begleiters um einen Hauptreihen-B-Stern. Unsere Analyse von #4150 lässt auf einen Begleiter um die 60 Jupitermassen schließen, also einen braunen Zwerg.
Während unter den A-Sternen im CoRoT-Sample nur ein Planetenkandidat verblieben ist, erweist sich der Begleiter des F-Sterns #0307 als Planet. Damit handelt es sich um den 36. Planeten, der im CoRoT-Projekt gefunden wurde, und somit die Kennung CoRoT 36b erhalten hat. Mit unserer Analyse konnten wir die Parameter des Sterns und dessen Begleiter bestimmten. Der Begleiter hat eine Masse von $m = 2.1\,M_{\mathrm{Jup}}$, einen Radius von $r = 1.3 \pm 0.2\,R_{\mathrm{Jup}}$ und umkreist sein Muttergestirn in einem Abstand von nur 0.9 ± 0.2 AU. Damit handelt es sich um einen heißen Jupiter.
Das Gesamtergebnis unserer Studie erhärtet die Erkenntnis, dass es weniger Planeten in Jupitergröße bei Sternen mittlerer Masse zu geben scheint als bei sonnenähnlichen Sternen. Dies stützt die These, dass in diesen massereicheren Systemen die in-situ Planetenbildung von engen Begleitern, bzw. die Migrationsmechanismen zu kleineren Umlaufbahnen, weniger effektiv sind, als in protostellaren Scheiben um sonnenähnliche Sterne. Fassen wir die von CoRoT entdeckten Planeten mit denen unserer Untersuchung zusammen, kommen wir auf eine Frequenz enger planetarer Begleiter von $0.11 \pm 0.04\%$ um Sterne mittlerer Masse (1.3 – 2.1 $\mathrm{M_\odot}$), deutlich weniger als um Sterne sonnenähnlicher Masse ($0.79 \pm 0.23\%$), obwohl die Planetenhäufigkeit auf weiten Umlaufbahnen mit der stellaren Masse bei sonnenähnlichen Sternen von 0.8% auf 11% bei Sternen mittlerer Masse zunimmt.

Abstract

The hunt for extrasolar planets focussed on solar-type host stars and was recently extended very successfully to low mass main-sequence stars such as Proxima Centauri. Stars more massive than the sun have attracted less attention because the spectroscopic detection methods for late-type fail for early type stars, limiting the possible detections to massive planets and brown dwarfs in tight orbits around their hosts. However, finding planets around intermediate mass stars is crucial to understand the formation of planets in general and the evolution of such systems. Numerical models predict that the mass of the protoplanetary disk increases with the mass of the host star but its life time decreases. Thus more massive, intermediate-mass stars are perfect objects to test theories about the formation of close-in planets.
Therefore a collaborative project between the Thüringer Landessternwarte (TLS) led by Dr. Eike Günther and the Bamberg team funded by the DFG was initiated, to start a convenient program to investigate candidates for transiting substellar companions to B-, A-, and early F-type stars found by the CoRoT mission. At the start of the mission, only one single planet around a main-sequence A-type star (WASP33 b) was known, until today only three additional ones have been found. We began with a first spectral characterization for intermediate-mass-stars, using the EXODAT database of the CoRoT mission. Our target list was derived from an automated reclassification of the targets with template spectra taken at the Australian Astronomical Telescope, carried out at TLS. The list was restricted to systems with orbital periods of less than $\sim$ six days and sufficiently shallow transit depth ($< 1.5\,\%$), which led to a final target list of about 100 systems. A detailed analysis of the light curves further restricted that list to about 20 targets, for which spectroscopic follow up observations were performed. On the one hand, to obtain radial velocity measurements to exclude stellar companions which would give large amplitude variations, and on the other hand, to excerpt high quality spectra for a detailed spectroscopic analysis, that allows us to better constrain the stellar parameters and thus also the physical properties of the companion.
The detailed spectral analysis is done by using different fitting algorithms and χ^2-minimization, to find the best match of the synthetic models in a multi-parameter space to the observational data. The modeling is done with the so called hybrid approach introduced by Przybilla et al. (2006), i.e., computing the temperature-density stratification under the assumption of local thermodynamic equilibrium (LTE), of a plane-parallel, homogeneous and line-blanketed atmosphere, with the ATLAS12 code (Kurucz, 1996). For spectrum synthesis the LTE assumption was replaced by statistical equilibrium (NLTE) and line profiles were calculated for various chemical elements with the DETAIL/SURFACE package (Giddings, 1981).
A new method for an objective, χ^2-based spectroscopic analysis of early-type stars had been developed by Irrgang et al. (2014). Up to now, this technique has been applied to B-type main-sequence stars. Whether the method can be applied to A-type stars had to be shown. We performed a comparison with self-consistent detailed model spectra. This is on the one hand done intrinsically, i.e. we tested, if the known simplifications of the modeling affect the most critical parameter, that is the surface gravity, and found a systematic offset of up to 0.2 dex. Hence we had to apply corrections for this parameter depending on the effective temperature. Correction factors were deduced from a sample of standard stars: We selected a sample of ten bright, well studied A-type stars. The spectroscopic results were also compared to an independent analysis

method by fitting the synthetic spectral energy distributions to photometric measurements in a self consistent way. For all but one of our stars the result agreed within the uncertainty limits. Where available, we also matched our results with the help of evolutionary tracks and the parallax and found in most cases also a quite good agreement for the almost independently derived surface gravity.
Since NLTE spectral synthesis has been applied previously only for few A-type stars, we embarked on a study to quantify deviations from LTE. We give a detailed overview of these effects with respect to effective temperature, surface gravity and metallicity as well as individual chemical abundances.
Available atomic and ionic line lists had previously been tailored for B-type stars. These lists had to be extended for A-type stars. We included several additional elements in our models, whenever appropriate atomic data were available. The treatment of convection in the model atmosphere were adjusted as well.
The first application of our analysis strategy was carried out for the planet host star WASP33, where high quality data were available. Our spectroscopic result of the host star is about 500 K hotter, the surface gravity 0.3 dex lower and the metal abundance 0.2 dex higher than previously published photometric results. This leads to a more massive and more evolved star ($M = 1.85 \pm 0.15\,\mathrm{M}_{\odot}$, $R = 2.12 \pm 0.32\mathrm{R}_{\odot}$) than previously adopted. The properties of the companion were revised accordingly to $m<4.48 \pm 0.24\,\mathrm{M}_{\mathrm{Jup}}$ (As the radial velocity measurements only yields an upper limit for the reflex motion of the star, also the companion mass can be restricted to the given upper mass limit only) and $r = 2.21 \pm 0.33\,\mathrm{R}_{\mathrm{Jup}}$.
The second target was SWASP J0247-25, an eclipsing short-period binary system of an A-type star and a pulsating, low luminosity, i.e., evolved low-mass star of spectral type B. We found similar parameters for both companions as published before by other groups. Our results are in perfect match to asteroseismic investigations. We performed the first abundance determination for both stars. For the B-type star we found a helium abundance at the surface lower than predicted to explain the observed pulsations, which is in agreement with evolutionary models when gravitational settling of helium is taken into account. We could also rule out an enhancement of α-elements, which was suggested by a comparison to evolutionary models. In comparison to the A-type star, all elemental abundances of SWASP J0247-25 B are lower, which also supports the assumption of ongoing gravitational settling in the atmosphere of the latter.
The third target was the metal poor, subluminous F-type star WISE J0725-2351. As it turned out to be too cool for our spectral model grid, we analyzed the flux-calibrated spectrum by fitting to ATLAS9 models and found a good match to a very old (12 Gyrs) metal-poor (one hundred times lower metallicity than the sun) turn-off star at the end of its main-sequence lifetime. This study motivated us to extend our model grid also to early F-type stars, which enabled us to analyze the F-type planet host star #0307 and the binary #0108 from the CoRoT sample.
The main goal of this thesis project was the quantitative spectral analysis of the twenty CoRoT targets. When high quality spectra were available, we could improve the accuracy of the basic stellar and companion parameters, which has led to revisions of the stellar parameters previously mostly deduced from spectral classification. For some candidates we found probable false alarms, because of hints for a previously undetected stellar companion (#2657 and #2721). The most probable candidate for a substellar companion around an A-type main-sequence star is #1475. The host star is a peculiar Ap star on the main-sequence, and its companion has a mass of

$m \approx 82\,M_{\rm Jup}$ and is at the border between a brown dwarf and a low-mass main-sequence star. Together with the small radius of $r \approx 1.6\,R_{\rm Jup}$, it is likely to be a brown dwarf. The radial velocity curve of target #0108 hints at a stellar companion. We revised the stellar parameters and derived a mass of $\sim 177\,M_{\rm Jup}$ and a radius of $r = 2.1 \pm 0.3\,{\rm R_{Jup}}$, consistent with previously published results. The companion is confirmed to be a late type star.
Another interesting target is #1712. From radial velocity measurements of two HARPS spectra we obtained a small upper limit to the semi-amplitude of the radial velocity curve. If confirmed, the mass of a possible companion would be roughly half a Jupiter mass which means it is in fact a planet orbiting an A-type main-sequence star, we hoped to find. This star would be the only A-type star in our sample that actually host a hot Jupiter planet.
One of the most interesting systems is the target #4150, which we could confirm to be a main-sequence B-type star. Its companion has a mass of $\approx 60\,M_{\rm Jup}$ typical for a brown dwarf, which is the first one found in such a massive system.
For the only confirmed planet around the F-type star #0307 we revised the stellar parameters and derived a companion with a higher mass at a smaller radius ($m = 2.1\,M_{\rm Jup}$ and $r = 1.3 \pm 0.2\,R_{\rm Jup}$), compared to previously published results.
Numerical calculations predict, that around more massive host stars also the mass of the protoplanetary disk is larger and thus more planets can form, which is in agreement to observations. Around intermediate-mass stars, the frequency of long-period planets ($\sim 11\%$) is larger than for solar-type stars ($\sim 0.8\%$).
The life-time of the protostellar disk is thus long enough to produce Jupiter-like planets. From the numerous confirmed planets detected by the CoRoT mission the frequency of close-in planets can be derived. For the CoRoT targets the frequency is $0.79 \pm 0.23\%$ for host star masses less than $1.3\,{\rm M_\odot}$, in agreement to results from radial velocity surveys. This frequency is higher than that for intermediate-mass stars of $0.11 \pm 0.04\%$, derived from the general CoRoT mission in addition to our investigation. Hence, there is a lack of close-in planets around intermediate-mass stars. Thus the main conclusions from our investigation is, that in-situ formation as well as migration mechanisms for hot Jupiters in the protostellar disc are less effective for intermediate-mass than for solar-like stars.

Contents

Chapter 1

Introduction

One of the most fundamental questions that we may ask ourself: Where are we in the Universe and are we alone? The best method to come closer to an answer to the first part of that question is astronomy and astrophysics, as it uses the natural sciences to seriously explore our surrounding universe and try to figure out, what is out there. Comparing to other fields in physics, astrophysics is by far the discipline with the largest laboratory: The Universe itself. Therefore there are lots of different fields which cover different parts of our surrounding large-scale environment[1].
Cosmology sheds light to the question, how nature evolved from the Big Bang until today. Also a quite new field emerged with the commissioning of the LIGO experiment early 2016 which is investigating ripples in the space-time, so-called gravitational waves, already mathematically introduced by Einstein.
Other fields in astrophysics try to get more insight into the formation and evolution of hundreds of billion galaxies and the structures in which these are clustering, the next smaller structures seen when comparing to cosmology.
In the field of stellar astrophysics, we care about the elements of such galaxies, especially of our own Galaxy, the Milky Way: Stars and their physical structure and evolution in terms of their physicals properties, as well for nucleo-chemical changes in the abundances of chemical elements. There are also interstellar dust and gas clouds, which are of interest when considering the birth of stars or simply, if the emitted light we observe from stars and galaxies under investigation is filtered by such material. Also the dynamics of stellar systems can help us to better understand the mysterious dark matter, which is meant to be the main driver for galaxies to form and whose nature is not understood.
The stellar systems we look at could either be single stars, or multiple systems and also could host one or more planets, which itself would be the first condition which has to be fulfilled, when trying to answer the second part of the above question "are we alone" with a determined "maybe not". Since the first confirmation of a planet around the star 51 Pegasi, thousands more has been detected up to today. Also the detection of water and other molecules which hint to the existence of life has been found in some systems.
So there are many fields of interests and many connections between the different fields. In this work we concentrate on the so called intermediate-mass stars, in particular the A-type stars on the main-sequence (MS), i.e. stars which burn hydrogen in their cores. One very powerful method and our main instrument to obtain physical

[1] of course there are also links to the smallest particles which structure the (baryonic) matter itself: the astroparticle physics.

parameter of these stars is quantitative spectroscopy, which we will explain later in this work. But as we will show also, for A-type stars this method is plaqued with several difficulties: the determination of the fundamental parameter $\log(g)$, the logarithmic gravitational acceleration at the star's surface, has quite large uncertainties, especially for cooler stars ($T_{\rm eff} \lesssim 8000$ K). Therefore we introduce a photometrical method how to constrain this fundamental parameter better.

1.1 Detection of planets

The final goal of our project is to study intermediate-mass stars with transiting low-mass companions discovered by the CoRoT space mission, to find out whether the companions are massive planets ore brown dwarfs. The number of confirmed extrasolar planets has been rising enormous since the last decades. More and more sophisticated instruments in transit surveys like the CoRoT satellite or the Kepler mission contributed a lot to the current number of these systems. And there are more to follow, like PLATO, TESS and CHEOPS and also huge ground-based radial velocity campaigns. In Figure 1.1 an overview of the detection methods of extrasolar planets is given. The figure also shows the already outdated numbers (July 2015) of confirmed planets. The most effective detection method is the transit method, followed by the first method which proved the existence of a substellar companion around a solar type star, the radial velocity method, also called Doppler spectroscopy. To finally confirm a possible planet candidate, at least two independent methods have to be taken into account. Ideal for this purpose is, if transit light curves and time-resolved spectroscopy is available. The latter allows us to determine $m_{\rm companion} \sin i$ from the mass function if the mass of the host star is known. Its radius is derived from the light curve, if the radius of the host star is known. Mass and radius of the planet furthermore yield the mean density, which hints to which material the planet consists of, i.e., wether if it is a gas or a rocky planet.

1.1.1 Doppler Spectroscopy

Already Belorizky (1938) proposed to measure the gravitational pull of an unseen companion via radial velocity (RV) variations, long before the development of suitable spectrographs. With a time series of spectra which cover at least one orbital period and at a sufficiently high sampling rate one can derive the eccentricity e, period P and $m \sin(i)$. However, in general the inclination of the orbit is not known. We can dervie a minimum mass, only, by adopting $\sin i = 1$. The amplitude of the variation is dependent on the planets mass m and the orbital distance a. As demonstrated by Mayor et al. (2014), an alien observer would measure a $12\,\mathrm{m\,s^{-1}}$ variation of our Sun's radial velocity with a period of twelve years, mainly caused by Jupiter. Earth would produce a signal of $0.1\,\mathrm{m\,s^{-1}}$ with a period of one year. According to the Doppler formula

$$\Delta\lambda = \lambda \cdot \left(1 + \frac{v}{c}\right)$$

the corresponding shift $\Delta\lambda$ of the wavelength λ of an absorption line of the host star's atmosphere in the case of an orbiting earth would be of the order of $10^{-10} \times \lambda$, which is hard to measure even with modern instruments and not yet possible.
In the case of Jupiter-sized planets, it should have been possible to measure a corresponding shift already in the 1980s (Campbell & Walker, 1985), but out of a sample of

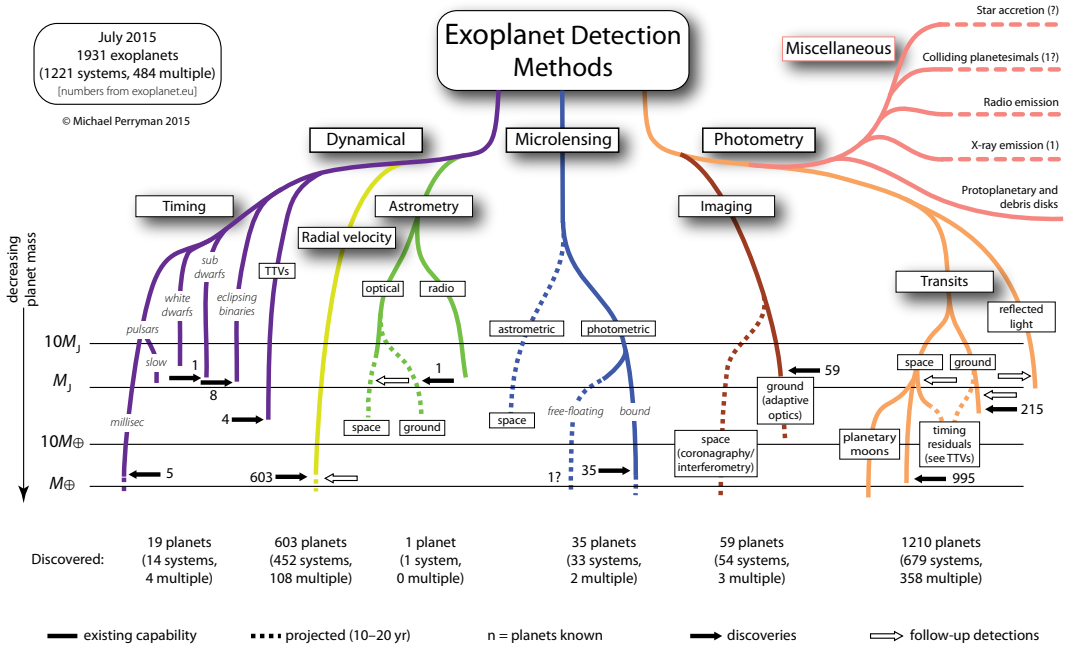

Figure 1.1: Overview of the different detection methods for extrasolar planets.

21 stars monitored for more than twelve years, no planets more massive than Jupiter could be confirmed (Walker et al., 1995).

The first confirmed exoplanet around the solar type star 51 Pegasi was detected by Mayor & Queloz (1995) in a radial velocity survey of 142 stars. The planet turned out to be one of the relatively rare kind of exoplanets, the hot Jupiters. These gaseous planets orbit very close to their host in a short period of typically some days. Their surface is illuminated by the close star, which heats up its atmosphere. Recently Brogi et al. (2013) were able to confirm 51Peg b's gaseous nature and the mass of slightly below half a Jupiter mass by directly measuring the RV variations of H_2O and CO absorption lines in its atmosphere. The formation of these kind of planets is still unclear. The formerly preferred scenario of migration in the protoplanetary disk was called into question, by the discovery of large obliquities in some of these systems (see Section 1.1.3).

With the HARPS spectrograph at ESO's 3.6m telescope and its ability to detect radial velocity variations below $1\,\mathrm{m\,s^{-1}}$ it became possible also to detect low-mass planets with Doppler spectroscopy. The detection of 41 low-mass planets around F, G and K stars (Mayor et al., 2011) reveals that for more than half of the solar type stars there is at least one planet orbiting and for these systems the multiplicity rate is above 70%. The occurrence rate of gaseous planets seems to be positively correlated with the host stars metallicity (see also Santos et al., 2004), whereas for lower mass planets no such correlation was found. Adibekyan et al. (2012) used the relative abundance of Ti with respect to Fe as a threshold for α-enhancement and found that Ti seems to play an important role for planet formation, as the occurrence of planets is rising significantly with its abundance in metal poor stars.

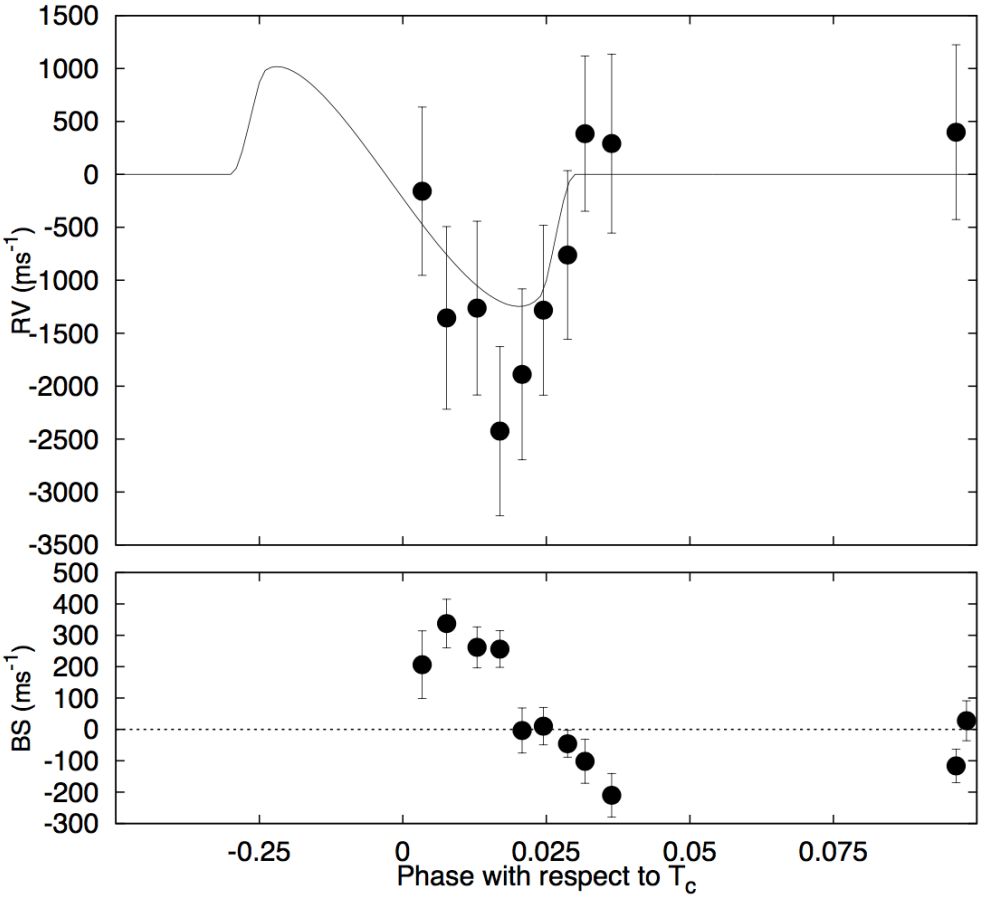

Figure 1.2: Upper panel: Example for a deviation from a sinusoidal RV due to the Rossiter McLaughlin effect, acting during the transit, adopted from Hartman et al. (2015). Lower panel: Bisector spans (BS), which is a measure of the difference of the bisector RV between the core and the wings of a line. The bisector RVs are obtained by a cross-correlation function of the lines. A positive BS indicates a blueshifted core in respect to the wings of the lines.

1.1.2 Rossiter-McLaughlin effect

For fast rotating stars, the merging of spectral lines is reducing significantly the efficiency of the radial velocity method. For this type of stars, one can look for tiny deviations from the expected radial velocity of a star, which can be caused by a transiting companion. While the companion passes the line of sight between observer and the star's surface, it blocks different parts of the rotating host star's surface. This leads to deformations in the rotationally broadened line profiles in the stellar spectrum, which has an effect for the radial velocity measurements. When spectra at different times during the transit are taken, the measured radial velocity is higher when the companion blocks a part of the star which rotates towards us and vice versa. This effect is called the Rossiter-McLaughlin (RM) effect (Rossiter, 1924), an example is given in Tab. 1.2 of the transiting exoplanet of the A-type star HAT-P 57. This effect can also be used to map the distortions of a mean line profile as a function of time to detect a planet. This method is called Doppler tomography and was successfully used for the detection of the planet to the rapidly rotating A-type star WASP33 (see Chapter 5).

1.1.3 Transit method

The most successful method in finding other worlds outside our solar system is the transit method, where tiny dips are occurring periodically in the light curves of their host stars, mostly measured by space observatories. These transits hint at the presence of gravitationally bound companions to a star. As of September 2017 75% [2] of all known planets are validated due to this detection method. Although not expected, we now know that there are planets with wide ranges of sizes, masses and a variety of orbits unlike the solar system around F, G, K and M stars. Long-term monitoring of transiting systems may allow third bodies to be detected, due to perturbations between other gravitationally active members in these systems, the transit time variations.
The most successful of these missions, again, is the Kepler survey. Its instrumentation allows a precision of 30 ppm of a 12 mag star, which is almost 100 times better than ground-based measurements, when the measured flux is binned to 6.5 h intervals. This binning has been chosen because the Earth needs that time to travel a distance of half the diameter of the Sun and consequently an earth in a solar-like system would be detectable. Radial velocity surveys detected, that more than half of the candidates are in systems with multiple transiting planets, which could be confirmed by Kepler.
An important result of the Kepler mission is that most multiple systems tend to be flat in terms of the mutual inclinations of the planets in a system, which can be taken as evidence, supporting the formation theory of planets being born in circumstellar disks, proposed already by Laplace & Young (1832). On the other hand, this finding can also be just due to a selection effect, as the transit method cannot say anything about planets which orbit at lower inclinations. If the planets are born in a circumstellar disk, one would also expect low obliquities, i.e., an alignment of the orbital plane and the rotation axis of the star (and companion). But ground-based observations showed that most of the systems, where it was possible to measure the orientation of the host stars spin axis through the Rossiter-McLaughlin effect, are misaligned, at least for the hotter stars ($\gtrsim$ 6250 K, Winn et al., 2010). Albrecht et al. (2012) found random inclinations of 14 hot Jupiters and Collier Cameron et al. (2010) found the orbit of WASP-33 b to be retrograte around an A-type star. One explanation would be that the close-in planet was forced into its orbit through a combination of a distant perturber and tidal friction (Fabrycky & Tremaine, 2007), which would also explain the high obliquity.
More gaseous as well as smaller planets are found in systems with higher metallicity, also by the Kepler survey.
Another open question is, if the planets formed in situ or have had the time to migrate inwards. The short periods of Kepler planets (<50 days) hints at a shorter formation time than the lifetime of the protoplanetary disk, thus they could be formed in situ (Chiang & Laughlin, 2013). Additionally, there is only a small fraction of pairs of planets, which have resonant periods. This is predicted to be the case, if planets migrate slowly through the disk and have low eccentricities (Peale, 1976). Arguments for migration are their natural occurrence in analytical derivations (Goldreich & Tremaine, 1980) and numerically simulations (e.g. Baruteau & Papaloizou, 2013).

[2] according to `http://exoplanet.eu/` on 09/20/2017

1.1.4 Planet formation and the role of substellar companions around intermediate stars

There are many scenarios for planet formation, but predictions are contradictory. The only way to test those predictions, and thus to find out the right ones, is to determine the properties of the planetary systems. As of September 20th in 2017, 3668 planets are confirmed [3], but most of them are around stars of masses similar to our sun. Around the most massive stars, planets are not likely to form, because of the short lifetime of protoplanetary disks of these rapidly evolving stars. The so-called intermediate mass stars (IMS) of spectral type A and F are in the center on the main-sequence of the Hertzsprung-Russell-diagram, so less massive than the hot and young O- and B- stars but more massive than the sun. For these stars, there seems to be a lack of planets from the observational site due to the following reasons: As these stars have significantly less metallic lines, the accuracy of the radial velocity technique is reduced. Secondly, IMS on the main-sequence also tend to rotate rapidly, which leads to an additional loss of lines suitable for radial velocity measurements due to the broader overlapping regions in the spectra. Hence, it is possible to detect the most massive companions on tight orbits only. In the case of transit surveys, companions around the host stars with larger surfaces lead also to shallower occultations and are therefore more difficult to detect. In addition, a large fraction of the IMS are pulsators, which makes it more difficult to excerpt the variations in the light curves caused by a planetary companion. Kennedy & Kenyon (2008a) point out that in lower mass stars planets are formed with shorter periods and thus planets around low-mass stars are best suited to be found by transit surveys. The nature of the host stars thus limit the chance of a planet discovery around IMS and thus leads to a strong bias. In this work, we concentrate on A-type stars, for which only four systems have been found so far around the main-sequence stars: WASP-33 (Collier Cameron et al., 2010), KOI-13.01 (Szabó et al., 2011), HAT-P-57 (Hartman et al., 2015) and KELT-17 (Zhou et al., 2016).
However, the detection (or non-detection) of planets around IMS is quite important, because it would put constraints on the modeling of planet genesis and evolution. As already mentioned above, the most popular scenario of a planets birthplace is the circumstellar disk. These disks were later described in models, where the density of these disks decreases with orbital radius, but with a sudden rise at the so called "snow line", the circular borderline around the star that separates water vapor from ice. The most sophisticated models use the so called "cold finger" disk, where this increase in density is increased by refreezing water, which was brought by icy material falling below the snow line. This region is believed to be the birth place of planets especially for the gas giants (e.g., Kennedy & Kenyon, 2008a).
But as already mentioned above, there are discoveries of giant planets orbiting around low mass host stars in short periods. Vigan et al. (2012) find in their direct imaging study that the number of planets declines with orbital radius around giants of A-type, which is consistent with RV-studies (e.g. Johnson et al., 2010, who found 7 planets with $M > 1\ M_J$ at > 1 AU). They suggest a peak of gas giants around A-types at distances around 3 - 10 AU. In contrast, Cumming et al. (2008) propose a flat distribution of planets around FGK stars.
Most theories predict a higher frequency for planets around IMS than solar-types (e.g. Kennedy & Kenyon, 2008b), although the lifetime of the protoplanetary disks is

[3] according to `http://exoplanet.eu/` on 09/20/2017

half as long (Mamajek, 2009) and shortens approximately with the square of the stellar mass (Muzerolle et al., 2005; Calvet et al., 2004). Because for higher mass stars the snow-line is further out, Kennedy & Kenyon (2008a) conclude that the planets reaching short orbits have a smaller range of masses, i.e., are more massive planets. Also Bowler et al. (2010) point to a higher frequency of IMS, by obtaining RV curves of 31 intermediate mass red giants and find that the frequency of Jupiter-sized planets at distances < 3 AU is 26%, which is much higher than for planets of solar like stars (5-10%). But they could not find any Jupiter-sized planet within 1AU. For the solar type stars, close-in planets could have formed in situ (Chiang & Laughlin, 2013) thus close-in planets would give some hints on how these planets have formed. There are two possible scenarios for close-in planets, born further out in the disk: Scattering or migration. Kennedy & Kenyon (2008a) found in their simulations that 10 $M_{\oplus}$ short-period planets are stable only around the lowest mass stars (0.25 $M_{\odot}$) due to scattering and these planets tend to have high eccentricities and long periods due to long circularization timescales and thus are hard to detect by RV as well as transit observations. Beaugé & Nesvorný (2012) numerically simulated the stability of planetary systems and found that systems with more planets are more stable and can thus explain hot Jupiters dynamically brought in close orbits by scattering. An interesting result of this investigations is that these systems would have produced runaway planets, i.e. planets which are ejected from the system. Most of the simulated systems have low obliquities, which is in contrast to observations (e.g. Albrecht et al., 2012; Collier Cameron et al., 2010). Winn et al. (2010) collected $\approx$ 20 planetary systems, where the angle between spin axis and orbital plane is known and found that high obliquities tend to be in systems with hotter host stars.
Another possible scenario for close-in planets is their engulfment. Villaver & Livio (2009) show that the engulfment of planets could explain the lack of close-in planets around stars M>1.5 $M_{\odot}$ and surprisingly that engulfment is more efficient for more massive planets and less massive stars. Kunitomo et al. (2011) simulated the engulfment of planets and derived the minimal orbital distance, at which a planet survives the host stars evolution as a function of the host star's and satellite's mass. They conclude that the scarcity of known close-in planets around the evolved intermediate (1.5...3$M_{\odot}$) stars, can not be fully explained by planet engulfment. The substellar companions may also play an important role in the evolution of the host star itself, e.g., a spiraling in of a massive companion onto its host star and subsequently its envelope was expelled, turning the host star into an extreme horizontal branch star (Bear & Soker, 2012). Therefore, it is of utmost importance to search for transiting planets around IMS with short orbital periods to test planet formation theories.

1.2 Outline of this thesis

As the main focus of this work is on A-type stars, Chapter 2 gives an overview of the various phenomena which an observer of such kind of stars is faced with. In Chapter 3 we explain details on the modeling of synthetic spectra of A-type stars, on the fitting procedure of these artificial spectra to observed spectra and tests of the reliability of the in this way derived atmospheric parameters. A first application of this method is executed for ten carefully selected bright stars for which spectra of outstanding quality are available in Chapter 4, and we show that the derived parameters are in quite good agreement to independent methods, such as photometry and parallax measurements. Examples for the spectral fit for the stars HD204041 and

HD189849 are shown in Appendix C and D, respectively. Another two test cases are shown for the well studied, prototypical A-type star with planet companion WASP 33 (Chapter 5) and the A-type star accompanied by the stripped core of a red giant in the system J0247 (Chapter 6). Chapter 7 presents the results of our main investigation in the search for companions of seven transiting light curve selected planet host star candidates of IMS of the COROT mission by characterizing the host star's properties in great detail. Finally, in Chapter 8 we give a summary of this thesis and future prospects.

Chapter 2

The zoo of A-type main-sequence stars

When studying A-type stars we have to be aware that they may show several spectroscopic anomalies. What is a typical A-type star? In the Harvard Spectral Sequence, an A-type star is characterized by its strong Balmer lines. They can be easily distinguished from the hotter B-type stars by the absence of He I lines on the one hand and from the cooler F-type-stars on the other hand because of their much shallower hydrogen lines and a denser forest of metal lines. But there is a whole zoo of different phenomena in A-type stars, and the different kinds often overlap. These different definitions and phenomena will be addressed in the following sections. Among the spectral classes, the A-type stars show the largest fraction of peculiar stars.

2.1 Normal composition of A-type stars and stellar rotation

On the main-sequence, they can generally be divided into two groups. Either they are rotating rapidly (up to $\lesssim 300\,\mathrm{km\,s^{-1}}$) or show various spectral peculiarities. The occurrence of meridional circulation has been invoked for fast rotators (see Section 2.2). Lemke (1993) investigated this theory, but found no significant trend of abundance anomalies with $v \sin i$ in their analysis of 20 stars with $100\,\mathrm{km\,s^{-1}} < v \sin i < 180\mathrm{km\,s^{-1}}$. In a larger investigation, Takeda et al. (2008) analyzed spectroscopically the abundances of some elements of 46 A-type stars and found that abundance anomalies, such as the overabundance of Ba and the underabundance of C, O, and Ca, decreases with increasing stellar rotation and becomes almost "normal" (which is some 0.1 dex lower than the solar value) at $v \sin i \gtrsim 100\,\mathrm{km\,s^{-1}}$.
As a rough demarcation, the range in mass, lifetime and luminosity for A-type stars on the main-sequence is between $M = 1.6-3.0\,\mathrm{M_\odot}$, $t = 0.6-2$ Gyrs and $L = 10-40\,\mathrm{L_\odot}$ respectively (Landstreet, 2004). Some of the peculiarities are related to magnetism (spotted stars), others to stellar youth (shell stars, Herbig Ae stars). Here the properties of various subclasses of peculiar A-type stars are summarized, based on the textbook by Gray & Corbally (2009), if not cited otherwise.

2.2 Am stars

In terms of the MK classification scheme, an A-type star is denoted as Am-type, if the Ca II K-line is at least five subclasses earlier than the metallic line type. A typical feature in the optical spectra of these stars is a discrepancy of luminosity determination by certain metallic lines. A blend of Fe II and Ti II at 4172 - 4179 Å hints to higher luminosity and thus to a classification as giant, whereas Fe II, Ti II and Sc II between 4395 - 4400 Å and Ti II at 4417 Å are typical for A-type dwarfs. This discrepancy in the Am stars is called the "luminosity effect".
The abundances of Ca and Sc are underabundant, while Fe, Ni and heavier elements tend to be overabundant, which only partly can explain the luminosity effects. Because of a denser line forest in the blue, line blanketing makes Am stars to appear redder than normal A-type stars.
The physical explanation, which holds for most of the observed peculiarities, is gravitational settling for elements with fewer absorption lines, e.g. helium, and radiative levitation of elements with lots of lines in the UV. The latter feel a larger photon momentum than the inward pull of gravitation, and thus are pushed outwards, leading to enhanced abundances in the photosphere. For the mostly rapidly rotating "normal" A-stars, the assumption of hydrodynamic and radiative equilibrium does not hold any more, as the simplification of a spherically symmetric plasma does not reflect the flattened geometry. This imbalance leads to circulating flows in the star. The so called "meridional circulation" mixes the interior of the star in large scales, thus no peculiarities are expected. In contrast to the "normal" A-type stars, Am stars tend to rotate more slowly ($v \sin i < 100 \mathrm{km\,s^{-1}}$). The reason of the spin down might be induced by a companion star by tidal synchronization, as most of the known Am stars are in relatively close binaries (e.g. Abt & Levy, 1985, estimated that $\approx$ 75% of the Am stars have a companion orbiting with a period < 3 years). In addition, the gravitational settling of helium surpresses the helium convection zone, which enables chemical separation out to the hydrogen convection zone. From there, chemical elements can be transported to the photosphere via overshooting.

2.3 Ap stars

Most of the Ap-type stars are hotter than the A-type stars, thus are actually of spectral type B. But the range of these peculiar stars extends to early F-types, therefore, the class is often named Cp. Related to the hot Ap stars are the helium-strong and -weak stars, as well as the mercury-manganese stars. In contrast to the Am stars, only some particular chemical elements show abnormal abundances. Different groups among the Ap stars have been classified, dependent on which element show peculiar abundances. Among them are mostly Sr II, Si II, Eu II and Cr II. Some rare earth elements may also have peculiar abundances, but are usually not explicitly named in the spectral classification type. But except in the case of roAp stars mentioned below, the Balmer-line-profiles are still a good temperature indicator.
Half of the Ap stars show spectral variability caused by spots on the surface. Thus, the abundant elements are not distributed uniformly in the atmosphere (see Fig. 2.1), but show one ore more spots of increased element abundance, which can be explained by the rather strong magnetic fields in these stars. The additional Lorentz force to charged ions can effect the peculiarities, especially at the magnetic poles. In the "oblique rotator model", where the rotation axis of the star is inclined in a fixed,

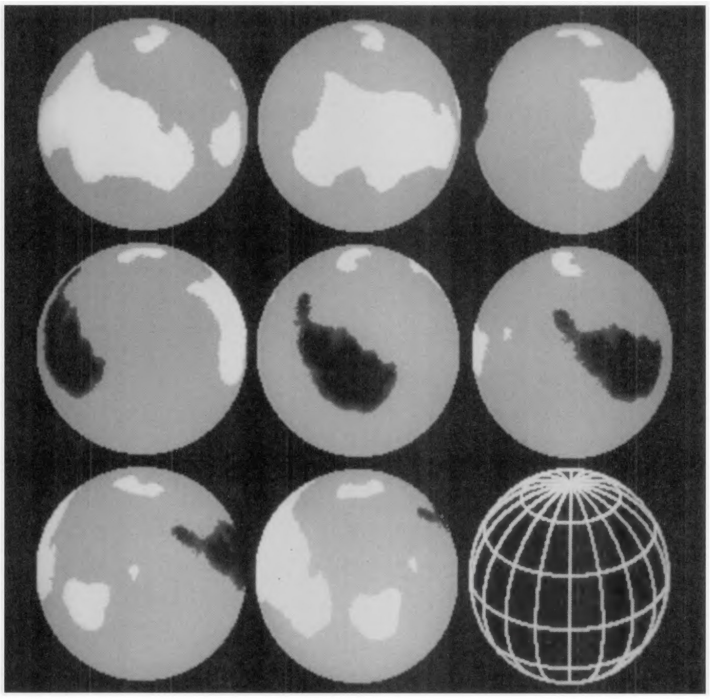

Figure 3. Doppler image of the silicon distribution on CU Vir. White represents regions of enhanced silicon (maximum $W_\lambda = 600$ mÅ) with respect to the mean value across the star ($W_\lambda = 335$ mÅ), while black represents regions that are depleted (minimum $W_\lambda = 180$ mÅ).

Figure 2.1: Silicon spots on the surface of CU Vir, taken from Hatzes (1997).

non-zero angle to the magnetic dipole, spectral variability can be explained by the star spots, which come in and out of view while the star is rotating.

2.3.1 Rapidly oscillating Ap stars (roAP stars)

An extreme case of chemically peculiar stars are the roAp stars, as they are rapidly oscillating and are distorting the atmosphere in such way that the wings of the Balmer lines matches to models of stars with 7000 - 8000 K, while the cores would fit to an effective temperature of 6000 K (Cowley et al., 2001). The most peculiar roAp star found is Przybylski's star (Przybylski, 1961), a G0 star which shows large overabundance of rare earths and even short-lived radioactive ions, such as Tc or Pm.

2.4 λ Bootis stars

A quite rare subtype ($\approx$ 2%) of A-type stars are the λ Bootis stars. Their general characteristic is a metal weak spectrum, in particular a weak Mg II line, characterized by a small ratio of Mg II λ 4481 / Fe I λ 4383. They would be classified as early type stars according to the Balmer lines, but they cover the spectral types from A0 to F3 and they appear to be on the main-sequence. Most of them show low metal abundances, except for C, N, O and S, which are close to solar values. These stars belong to the Population I and are thus mysterious, because accordingly they should be metal rich. One possible explanation could be the accretion of interstellar gas, where heavier elements are bound in dust-grains, while the lighter ones are still in

gas phase. For many stars there are signs for gas shells and if they would have been absorbed from the star's atmosphere, could explain the apparent low metallicities.

2.5 Herbig Ae/Be stars

The Herbig Ae/Be stars are in the short timescale of a collapsing protostar when it is evolving to the main-sequence. They are B- or A-type stars which show emission lines and an excess in the infrared, due to thermal emission by circumstellar material. These kind of stars are sometimes hard to investigate, as the star's chemical composition can be altered by material from a circumstellar disk or a shell around the star and by the material in the corresponding star forming region. The temperature dependent strength of the Balmer lines is largely unaffected by surrounding material and thus spectral lines as Ca I at 4426 Å and 4226 Å can be used to determine the spectral class. The Ca II K-line or He I lines, in contrast, may be partly non-photospheric and often show variations in time series of spectra. For luminosity determination one can use either the wings of the Balmer lines in early-type stars, or ionization equilibria. But the latter are suspect, especially lines forming from metastable levels.
Mora et al. (2001) identified a couple of predominantly photospheric lines, such as the Na D I lines at 5890 Å, Ca I at 6102, 6122 and 6162 Å, Fe I at 6495 Å and Li I at 6708 Å. Emission lines which may have formed in circum- or interstellar regions are again the Na D I lines, H_α, He I at 5875 and 6678 Å, some diffuse interstellar bands and some forbidden lines of O I at 6300 and 6363 Å, S II at 6716 and 6731 Å and N II at 6527, 6548 and 6583 Å arise from low density plasma.

2.6 A shell stars

A-type shell stars have Balmer line wings, which refer to dwarfs up to giants, but show some spectral characteristics of supergiants, such as Fe II and Ti II lines, the so called "shell lines", mostly with the 42 Fe II lines between 4900 – 5200 Å and at 4233 Å enhanced. Most of them are late B-type stars, but can also be of early F-type. The formation of the shells is not clear yet but it is likely that the shell stars are cool Be/B shell stars. While lots of A-type shell stars do not show spectral variability, Jaschek & Andrillat (1998) observed 14 Ae and A-type shell stars and found spectral variations in at least 8 of those and that a large fraction are found in multiple systems. Jaschek et al. (1991) showed the possibility to distinguish shell stars from normal A-stars by their O I triplet at 7773 Åbeing stronger.

2.6.1 Beta-Pictoris shell stars

Another case of shell stars are the β Pictoris shell stars. The prototype β Pic (also HD 39060, which is also one of our "standards") is an A6V star surrounded by a protoplanetary disk of gas and dust, which shows narrow absorption lines in the Ca II K and other lines, which can be variable in radial velocity and strength. The spectra itself appear "normal" except for a slightly enhanced Fe II line at 4233 Å. Other examples can be found, lots of them show the λ Bootis phenomenon.

2.7 Pulsations

According to Landstreet (2004) there are three types of pulsators amongst the A-type stars. One are the above mentioned roAp stars, the other two are the δ Scuti variables and the γ Dor stars. The rapidly evolving field of asteroseismology is capable to uncover the internal structure of the star by investigating at the pulsation frequencies and thus identifying the oscillation modes. The pulsation modes are distinguished by the restoring force, which is either gravity (g-mode) oder pressure (p-mode). The δ Scuti stars have a higher frequency and thus are p-modes, whereas γ Dor stars have lower frequency g-modes. The roAp stars show p-modes which are aligned with the magnetic axis. The first hybrid pulsator which shows both kinds of pulsations is the Am star HD8801 (Henry & Fekel, 2005). The pulsations can effect the light curve as well as the line profiles of a spectrum. Roughly one third of the main-sequence A-type stars show pulsations, which complicates the search for planetary transit signals in the light curves.

2.8 The effects of rotation

The fast rotation of the star leads to a smearing of the absorption lines. For our quantitative spectral analysis it is not a big issue, as we convolve the spectrum after calculating an "unbroadened" spectrum, and thus should be able to model the real shape. Problems occur in the normalization of the observed spectra, especially for the cooler stars, where the plethora of lines are smeared out in such way that no "true" continuum can be found. Normalization to this pseudo-continuum may introduce additional systematic errors.
The flattening of the star due to fast rotation is also neglected in our analysis. In reality, on the poles a higher temperature and surface gravity is aspected than for the equator (gravitational darkening). Thus, we only derive the "mean" parameters of a composite spectrum. As a consequence, a fast rotator would be shifted up in the HR-diagram in respect to a non-rotating star if it is seen pole-on or to the right, if seen equator on.
The most famous example for a fast rotator seen pole on is Vega (Gulliver et al., 1994). In a later study, Hill et al. (2010) derived a $v_{\mathbf{equ}} = 211 \pm 4\,\mathrm{km\,s^{-1}}$ seen from just $i = 5.8° \pm 0.1°$ and a large difference in temperature of $\Delta T_{\mathrm{eff}} = 1410\,\mathrm{K}$ and in gravity of $\Delta \log(g) = 0.26$ dex from pole to the equator.

2.8.1 Differential rotation

For the sun it is known that differential rotation occurs. In most cases this means that the rotation velocity at the equator is faster than at the poles. This differential rotation can be described relative to the latitude l with the parameter $\alpha \equiv \frac{\Omega_{\mathbf{equator}} - \Omega_{\mathbf{pole}}}{\Omega_{\mathbf{equator}}}$ (which is $\alpha = 0.2$ in the case of our sun) and the angular velocity Ω:

$$\Omega(l) = \Omega_{\mathbf{equator}} \left(1 - \alpha \sin^2 l\right)$$

Out of 110 A- to F-type stars, differential rotation was discovered only for the late A-type stars (around 7500K), although it cannot be excluded for hotter ones (Ammler-von Eiff & Reiners, 2012). Differential rotation is connected to magnetic activity of a star through the so called α-Ω-dynamo, which will not be discussed further here.

2.9 Conclusion

When attempting to investigate stars of spectral type A, we have to be aware of all the peculiarities discussed above. Slowly rotating stars would be best suited for quantitative spectral analyses, because spectral lines can fitted in isolation, while the spectra of more rapidly rotating stats are difficult to analyze. However, the frequency and degree of spectral peculiarities increase with decreasing rotation of A stars. Hence we have to be even more carefully, when analyzing the spectra of slowly rotating A-type stars.

Chapter 3

Spectral Analysis

In order to interprete observed spectra of stars, we need accurate synthetic spectra in great detail as well as an appropriate technique to derive atmospheric parameters and chemical abundances. Very important are realistic error estimates. We shall briefly describe the construction of grids of model atmospheres and synthetic spectra (Section 3.1).

3.1 Modeling stellar spectra

Most quantitative spectral analyses of A-type stars have been carried out using local thermodynamic equilibrium (LTE) model atmospheres and spectrum synthesis. It is argued that deviations from LTE (NLTE) are small. While this is likely true for the temperature-density stratification, it may not be the case for the shape of some spectral lines. Therefore we employ the so called hybrid approach discussed by Przybilla et al. (2006) and Nieva & Przybilla (2006, 2007, 2008), i.e., combining LTE temperature-density stratification of the plane-parallel, homogeneous and line-blanketed atmosphere, calculated using ATLAS12 (Kurucz, 1996), accounting for deviations in LTE by statistical equilibrium and spectrum synthesis calculations for several elements with the DETAIL/SURFACE package (Giddings, 1981; Butler & Giddings, 1985). The principles of the modeling and fitting is done as described in Irrgang et al. (2014), where the computational costly calculation of a synthetic spectrum "in the run" to be compared to a measured spectrum is avoided by using a pre calculated grid in a multi parameter-space. This space is spanned by the primary parameters effective temperature $T_{\rm eff}$, logarithmic surface gravity $\log(g)$, metallicity Z, micro-turbulence ξ and several elemental abundances of the trace elements. The pre-calculated spectra can be regarded as grid points in this space and are themselves combined spectra: In a first step an atmosphere with a scaled metallicity and background opacity is built and leads to a spectrum, which only includes lines of a single trace element in addition to the dominant hydrogen lines. In a second step, these spectra are then divided by an spectrum of a model atmosphere without any trace element to obtain a pure metal spectrum of the corresponding element. Finally, all the metal spectra plus the pure hydrogen/helium spectrum are multiplied together. This procedure saves a lot of calculation time. Imagine a grid with a single set of primary parameters, where you want to compute the combinations of only two different abundances for each of 20 trace elements. This alone would lead to over 1 million calculations. With our procedure, we only need to calculate 40 spectra (+1 with hydrogen only).

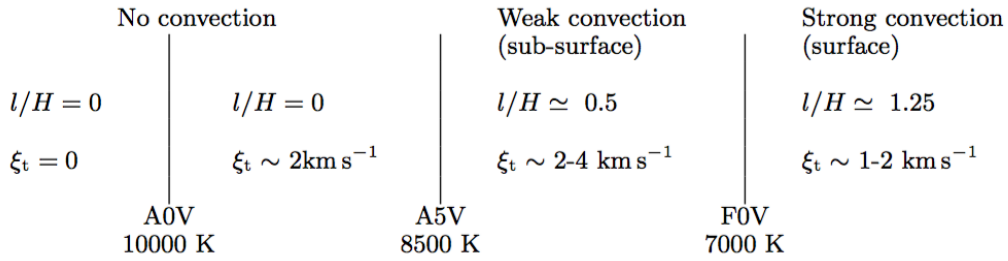

Figure 3.1: The recipe by Smalley (2004) for the treatment of convection in stellar modeling.

3.1.1 Convection

Convection in the atmosphere of stars can affect observables as the flux distribution and thus also photometric colors, as well as the atmospheric temperature stratification and thus affects the shape of the Balmer lines. Convection is usually modeled with the very simple mixing-length theory, where a single bubble rises a certain mixing-length (l) and than disperses (Böhm-Vitense, 1958). This mixing length is usually related to an arbitrary parameter $\alpha = l/H_\mathrm{p}$, where H_p is the pressure scale height. A more sophisticated model from Canuto & Mazzitelli (1991, 1992) uses bubbles of different sizes, which interact which each other and the model does not have a free parameter, as implemented by Kupka (1996). A self consistent model was proposed by Canuto et al. (1996). Another open question is, if convective overshooting, which means that bubbles can rise into radiative dominated regions, is included in those models and how it is treated. The "approximated overshooting" as used in the ATLAS code, has been found to give discrepant atmospheric parameters in photometric investigations and Smalley (2004) thus concludes to switch it off for model calculations. But still it seems to be an important issue, e.g., it affects the shape of the H_α line and can have strong effects for the end of the MS-lifetime in evolutionary models.
However, the ATLAS code we are using only allows to adjust the classical α-parameter and to decide to switch overshooting on or off. Smalley (2004) suggest a recipe (see Figure 3.1), how to set the α parameter for the mixing length and the microturbulence velocity ξ_t, based on typical values for these parameters found in the literature, and suggest to fix the values rather than treating them as fitting parameters. Smalley (2005) explain how to implement these settings in the atmospheric structure calculations by using the "ATLAS convection card". They show that for A-type stars, the right choice of α almost leads to the same Balmer line profiles as for more sophisticated models, which we adopted for our model calculations.

3.1.2 Modeling optical spectra of A-type stars

This procedure has been shown to successfully model spectra of B-type stars (Irrgang et al., 2014), because the number of metal line blends is small. Because of the larger line density, line blending becomes a major issue for (in particular late) A-type stars and breaks down for most F stars and later types. For the first time we apply the analysis technique to A-type stars, but have at first to explore its capabilities and

limitations. As the errors due to line blends[1] are not negligible especially for the cooler stars and the peculiar stars, these blends are then to be excluded for the later analysis of a measured spectrum, as this simplification in the calculations would give too strong lines compared to taking all elements into account in the atmosphere calculations (as in a simple picture the absorbed photons with the wavelength at the given blend has to be "shared" between the different elements).
Figure 3.2 gives an overview of the elements, which are relevant for the A-type stars. The NLTE-elements are marked green, the LTE-elements in blue and the other elements were added successively whenever enough atomic data was available. For some peculiar stars we still did not include some elements. So we cannot give a quantitative abundance for those elements, but this should not influence our ability for the determination of the basic parameters. The biggest step to improve our analysis would be to include Fe I in NLTE, as mentioned above.

3.1.3 The model grid

The primary atmospheric parameters in this work were adopted in such way that the grid covers the regime of the main-sequence A-type stars and can be expanded in the extreme cases, such as chemical peculiar stars. The general grid spans in temperature from 6500 to 10000 K in steps of 250 K and from 10000 to 12000 in 500 K steps, in surface gravity from $\log(g) = 3.0...4.6$ in steps of 0.2 dex. The abundance of helium is calculated for -1.36, -1.06, -0.76 dex, metallicity for -1, 0 and +1 dex with respect to the solar value and micro-turbulent velocities of either 0 or 2 km s^{-1}. The metal abundances for the trace elements are calculated around the solar values of $\pm$ 1 dex in steps of 0.2 dex and two additional values of $\pm$ 2.0 dex solar. The chemical elements which are included in this grid are C I/II, N I/II, O I/II, Mg I/II, Si I/II/III, Fe I/II/III, Al I/II, Ba II, Ca I/II, Ce II, Cr I/II, La II, Mn I/II, Na I, Ni I/II, P II, Sc I/II, Sr II, Ti I/II, V I/II, Y II and Zr II. For these elements, C,N,O, Mg, Si and Fe II/III are calculated in NLTE, where Fe I and all the others are calculated in LTE. The need for NLTE calculations we show in Section 3.5.2. Unfortunately, for some of the elements we cannot perform NLTE calculations due to the lack of relevant atomic data. Especially for the prominent Fe I lines there are quite large deviations from LTE known (e.g. Rentzsch-Holm (1996)) and unfortunately, especially for the cooler stars, Fe I lines are very dominant in respect to Fe II and even to hydrogen. In our models, NLTE Fe II/III and the LTE Fe I are in principal treated as individual elements, denoted as Fe and Fe1 respectively. To account for the NLTE effects, we link the Fe1 abundance to that of Fe with an offset of -0.1 to -0.3 dex, depending on the surface gravity, effective temperature and metallicity, which we take from Rentzsch-Holm (1996). To obtain the metallicity we also take the Fe abundance as a measure and thus link Z to the abundance of Fe. The solar abundance vector, which gives the starting parameters for the single element abundances as well as the background opacities in the calculations in ATLAS12 and DETAIL corresponds to Z=0 and is listed in Table 3.1 and 3.2.

The abundances are given in $\log_{10}$-logarithmic particle densities, relative to the total number densities. The solar helium corresponds to $\log(n_{\mathrm{He}}) = -1.06$ dex. The values were adopted from Nieva & Przybilla (2012) when available and otherwise

[1] Line broadening due to rotation and macro turbulence is here not an issue, as we fold the combined spectrum during the fitting process with an appropriate broadening profile.

Table 3.1: Logarithmic number fraction of chemical elements for the sun. When available adopted from Nieva & Przybilla (2012), otherwise from Asplund et al. (2009).

period number	element	abundance [dex]	abundance [dex] + 12
6	C	-3.71	8.29
7	N	-4.25	7.75
8	O	-3.28	8.72
9	F	-7.62	4.38
10	Ne	-3.95	8.05
11	Na	-5.77	6.23
12	Mg	-4.48	7.52
13	Al	-5.57	6.43
14	Si	-4.54	7.46
15	P	-6.61	5.39
16	S	-4.85	7.15
17	Cl	-6.81	5.19
18	Ar	-5.60	6.40
19	K	-6.96	5.04
20	Ca	-5.75	6.25
21	Sc	-8.99	3.01
22	Ti	-7.13	4.87
23	V	-8.08	3.92
24	Cr	-6.40	5.60
25	Mn	-6.56	5.44
26	Fe	-4.52	7.48
27	Co	-7.17	4.83
28	Ni	-5.84	6.16
29	Cu	-7.79	4.21
30	Zn	-7.41	4.59

Table 3.2: The rare earth elements and their solar values are listed here, but were not taken into account in the background opacities, as they are less important, even in the case of chemically peculiar stars.

period number	element	abundance [dex]	abundance [dex] + 12
38	Sr	-9.17	2.83
39	Y	-9.79	2.21
40	Zr	-9.41	2.59
56	Ba	-9.75	2.25
57	La	-10.89	1.11
58	Ce	-10.42	1.58

from Asplund et al. (2009).

3.2 Fitting procedure

The physical properties of a stellar atmosphere, can be derived by comparing an observed spectrum of the star with a synthetic one. This can be done iteratively (e.g. Nieva & Przybilla, 2010) by getting the effective temperature and the $\log(g)$ by matching the Balmer lines, which are relatively insensitive to other parameters such as the abundance of single elements or the micro turbulent velocity (and in the case for the late A-type stars also $\log(g)$). With the given temperature, one can now adjust the abundance of the trace elements for individual lines. When more than one ionization state of an element is available, this also allows us to check the consistency of $T_{\rm eff}$, as for the correct temperature the elemental abundance derived from different ionization stages should be equal. The broadening of spectral lines of different elements provides constraints on the projected rotational velocity, as well as on micro- and macro- turbulence. Because the different parameters are in complex correlations with each other, the procedure has to be refined until the set of parameters converges.

3.2.1 The fitting strategy

We don't use the iterative approach but make use of a strategy recently introduced by Irrgang et al. (2014) and a description of the modeling is given in Section 3.1. In this approach we take the chi square criterion to quantitatively estimate the quality of a fit, i.e. the whole spectrum (typically covering the wavelength range of $\sim$ 3900 – 8000 Å) is simultaneously fitted to the multi-dimensional parameter space. Therefore the synthetic spectra are linearly interpolated between the grid points.

3.2.1.1 First steps

In the first step, the radial velocity as well as the rotation velocity (RV) of the model spectrum is set by educated guessing, to speed up the fitting by choosing good starting parameters. The RV can be easily adjusted in the red part of the spectrum, as the Doppler shift is largest here. One can, e.g. use the H_α or the oxygen triplet. After this step, the $v \sin i$ (maybe together with the macroturbulence ζ) is set to an appropriate value. This can be best done by studying at an isolated, i.e. unblended line. Furthermore, the observed spectrum is cut at the chosen wavelength range between 3900 and 8000 Å and cleaned for gaps in the spectrum due to the instrument setup, spectral parts dominated by telluric absorption lines of the Earth atmosphere and for the regions with obvious artifacts, e.g. spikes from cosmic particles, improper reduction or instrumental artifacts such as reflections in the spectrograph. Surface gravity as well as the temperature can be fixed, by making use of published results, if available. Then a first fit is performed to improve the assumed starting parameters.

3.2.1.2 Omitting unreliable parts of the spectrum

After the first fit, we reduce our list of lines, which is quite large in the beginning. The lines which are actually included in our model are $\approx$ 28000 and in addition we included lines in our line list, which were identified in the observed spectra of at least one of the analyzed stars, but are not included in our synthetic spectra (> 2100). To

ignore the lines which have negligible impact to a particular blend, we exclude lines which are weaker than typically 5% of the continuum.
For some stars, we now carefully inspected the absorption lines to search for intrinsic blends. As this turned out to be the most time consuming part, we postponed this to later refined analysis by assuming that the large number of blends would statistically cancel out the effects of the error introduced by our simplification of the model calculation. We only investigated the strongest lines by stepping quickly through the spectral range and omitting intrinsic line blends, where at least two components are stronger than the previously selected threshold value. As the rotation of the star is in general non-zero, the spectrum has to be refolded to find those blends and exclude those regions around the absorption lines (now again rotationally broadened). Also obvious lines, not covered by our models but apparent in the observation, are excluded. Note that this can be reasonably done only for the slow rotators, as faster rotation smears out the lines and makes it difficult to impossible, to decide if the discrepancy between model and observation is caused by the absence of a line or just a combination of flawed atomic data for some lines or incorrect combination of abundances, temperature, gravity, turbulences and so on.

3.2.1.3 Unidentified and neglected spectral lines

In the spectra of ≈ 20 stars, which we inspected carefully for unidentified lines, we found in total almost 30000 regions in the spectrum to exclude. This is also due to the high quality of the spectra, where also small lines can be identified. Whenever a region is excluded, one can add a comment in our routine. The Table 3.3 gives an overview of the most frequent comments and can be used as a rough hint on which elements are mostly missing in our models. We only show comments which were used at least 40 times or more, to concentrate on the most common ones. Note the small number of unidentified lines in the spectrum.

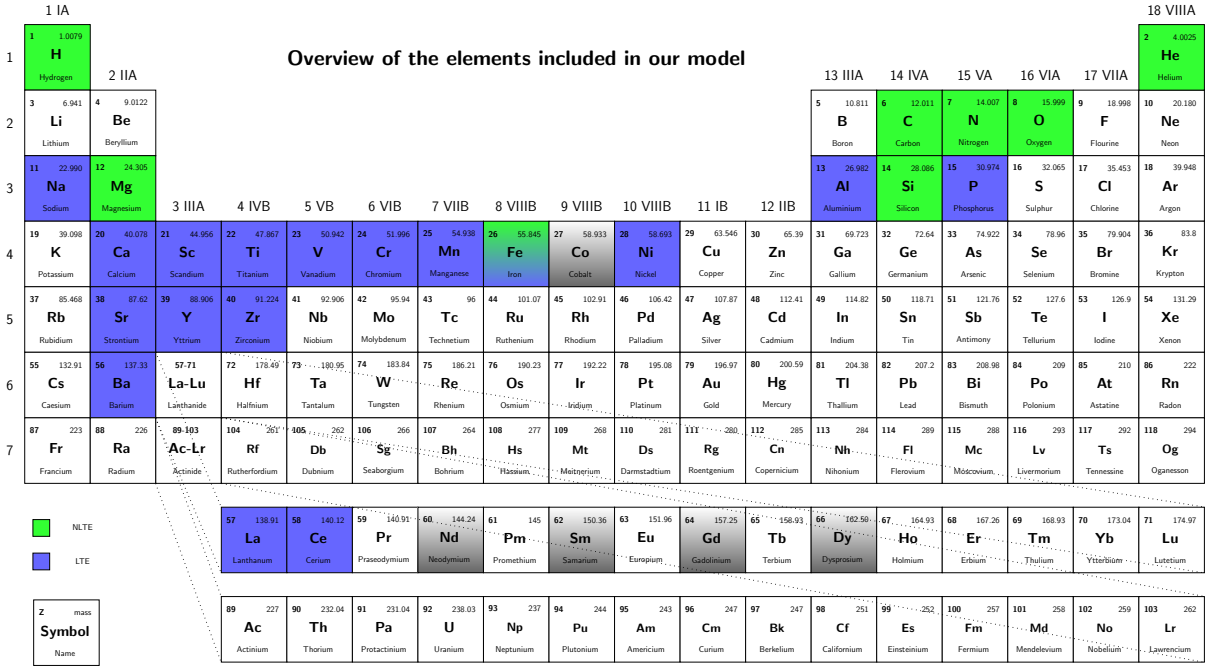

Figure 3.2: Overview of the elements in our models for A-type stars. The five elements with the largest number of lines, which have been found the most in peculiar stars, are shown with a grey shade.

3.2.1.4 Renormalization

In the next iteration step, eventually the line list is renewed if the basic parameters changes significantly ($\Delta\log(g) > 0.1$ dex, $\Delta T_{\rm eff} > 250$K) to the previous fit. If not, we assume that we did our best with the given model and what is left to be improved is the normalization done in advance by hand. We then assume that all areas which are still included in the fit and not "blended" by a line included in our model, belongs to the (pseudo-) continuum. So if such regions in the model are deviated from the observation, we adjust the model by multiplying a straight line which fits to two neighboring regions. The part of the spectrum where we can anchor those regions is defined by the adjusted line list: Every line has a certain "protected" range $\Delta\lambda_{\rm prot.}$ around it, which is derived according to the instrument resolution (R), rotational velocity ($v \sin i$) and micro(ξ)- and macro(ζ)-turbulences of the star via

$$\Delta\lambda_{\rm prot.} = \sqrt{\left(\frac{v\sin i}{c}\right)^2 + \left(\frac{\zeta}{c}\right)^2 + \left(\frac{\xi}{c}\right)^2 + \left(\frac{1}{R}\right)^2}$$

where c is the speed of light. The $\Delta\lambda_{\rm prot.}$ gives the width around the line center, which is affected by the line due to the broadening mechanisms given in the above formula. Already for moderately rotating stars (few 10 $\mathrm{km\,s^{-1}}$), there are almost no regions left, which are "true" continuum and thus the automated renormalization does not work. But for most of these stars, one can clearly see a linear offset which is most likely a consequence of improper normalization. In these cases we furthermore excluded some lines from our list, to produce non-protected pseudo-continuum regions and therefore be able to shift the model to the data and obtain a more reasonable match. Now, as the renormalization comes into play, the χ^2 landscape becomes very discontinuous, which makes the usually used fitting method not so useful anymore. The reason is that for different broadening parameters, the pixels which are averaged to get the continuum vary and thus can change the parameters and the responding χ^2 erratically. Therefore, in the last fitting steps, we alternate different numerical minimization procedures to obtain the best fit. Therefore we use the MIT tool ISIS (Interactive Spectral Interpretation System[2]), which offers several methods of different sophistication, robustness and computational speed, such as "subplex", "mpfit" or "powell".

3.2.2 Limitations of the fitting procedure

For several stars it turned out that although we thought to have a robust fitting routine which gives reproducible results, the results may differ significantly (up to 0.3 dex, i.e., $\approx 50\%$ for $\log(g)$), depending on the starting parameter, especially $T_{\rm eff}$, $\log(g)$, $\log(n_{\rm He})$ and Z. Although helium lines are absent in the cool, and are very weak in the hotter A-type stars, it would be interesting to compare the results by adopting different helium abundances in the models. However, we decided to freeze the helium abundance generally to solar to speed up the fitting procedure.
To get rid of the starting-parameter problem, we decided to prepare the spectrum as mentioned before with respect to the refinement of the line list and performed a series of fits, where we successively thawed different parameters for fitting, to imitate a fitting process by hand. This is done for a set of up to 48 different combinations of starting parameters for $T_{\rm eff}, \log(g)$ and Z (as an example see Figure 3.3). The

[2] for details see http://space.mit.edu/cxc/isis/

Table 3.3: Mostly used comments for regions, excluded from a fit. The numbers are the sum of all comments made in about 20 program stars. Left hand side is sorted for the total number, on the right hand side the same list is just in alphabetic order. Beside the element names, there are some other comments: lots of telluric lines, unidentified lines and gaps, due to the instrument setup. "DIB" stands for Diffuse Interstellar Bands, "norm" is for some regions, where we had to ignore lines to adjust the model to the pseudo-continuum and "RE" and "LE" is for the left and right end of the spectrum.

comment	total number	comment	total number
Fe2	3728	Ba2	57
Fe1	1641	C1	190
telluric	1095	Ca1	242
unidentified	888	Ca2	57
Cr2	325	Ce2	141
gap	315	Co1	191
Ti2	308	Co2	109
Cr1	275	Cr	100
Si1	256	Cr1	275
Ni1	244	Cr2	325
Ca1	242	DIB	64
Fe	210	Dy2	41
Nd2	207	Fe	210
Co1	191	Fe1	1641
C1	190	Fe2	3728
Ce2	141	gap	315
Zr2	136	Gd2	126
V2	127	La2	48
Gd2	126	LE	48
Si2	122	Mg1	50
Ti	112	Mn	50
Co2	109	Mn1	87
N1	103	Mn2	80
Cr	100	N1	103
O2	99	Nd2	207
Sm2	90	Ni	80
Mn1	87	Ni1	244
Y2	81	Ni2	77
Mn2	80	norm	60
Ni	80	O1	74
S1	79	O2	99
Ni2	77	RE	43
O1	74	S1	79
Ti1	68	S2	49
DIB	64	Si1	256
norm	60	Si2	122
Ba2	57	Sm2	90
Ca2	57	telluric	1095
Mg1	50	Ti	112
Mn	50	Ti1	68
S2	49	Ti2	308
La2	48	unidentified	888
LE	48	V2	127
Zn1	47	Y2	81
RE	43	Zn1	47
Dy2	41	Zr2	136

Table 3.4: Most common peculiar lines and their frequency of assurance in our whole star sample of A-type stars. Stars which showed at least 2 lines of one of the five elements are listed here.

	Nd II	Co I/II	Sm II	Dy II	Gd II
HD24712	120	100	54	30	67
HD189849	32	42	16	8	24
HD72660	14	28	4	0	6
SAO101686	13	19	1	4	4
HD91375	4	31	8	0	14
HD176232	4	27	9	2	4
HD159834	4	11	1	1	3
CoRoT 1475	4	9	1	1	1
HD168525	2	14	0	1	2
HD114330	2	2	0	0	0
HD204041	2	0	0	0	0
HD157087	0	12	0	0	1
HD97633	0	4	0	0	1
CoRoT 0307	0	2	0	0	1
HD119537	0	2	0	0	0
HD9672	0	2	0	0	0

different fitting steps for each set of starting parameters are:

- In the first step, all metal abundances are scaled to the starting parameter Z and are kept frozen. Free parameters are only: $T_{\rm eff}, \log(g), v \sin i, \zeta, \xi$ and $v_{\rm rad}$.
- In the second step, the magnesium abundance is thawed. This is because it is the only element calculated in NLTE, which allows its ionization equilibrium to be utilized (Mg I+II).
- In the third step, the iron abundance is thawed. This also influences the metallicity Z which is linked to Fe II/III. For most of the tests, we combined step two and three.
- In the fourth step, all the other metals are thawed.
- the last step is the above mentioned renormalization.

Between all of the steps, the fitting algorithms ("mpfit" and "subplex") are alternated and the results are saved. Also the line list is renewed between the steps, according to the parameters of the last fit. In some of the test stars, the final fundamental parameters can differ a lot. For example one of our test stars[3], HD28978, shows in the "extrema" of the best-fits in $\log(g)$ a difference of 0.3 dex. As this parameter is correlated with $T_{\rm eff}$ and Z, this corresponds to a temperature difference of 500K and 0.2 dex respectively. Looking at the χ^2 value alone can be misleading, because of the previously mentioned renormalization. Also a visual inspection of the outcomes is not helpful, as the different synthetic spectra differ in small details, only. However, if we exclude the worst fits (we take the mean χ^2 of all fits and exclude all fits, for which the χ^2 differs by more than 5 % of that mean value), the mean parameters

[3] a complete list of our test stars and the final result of our spectroscopic approach is given in Table 3.6

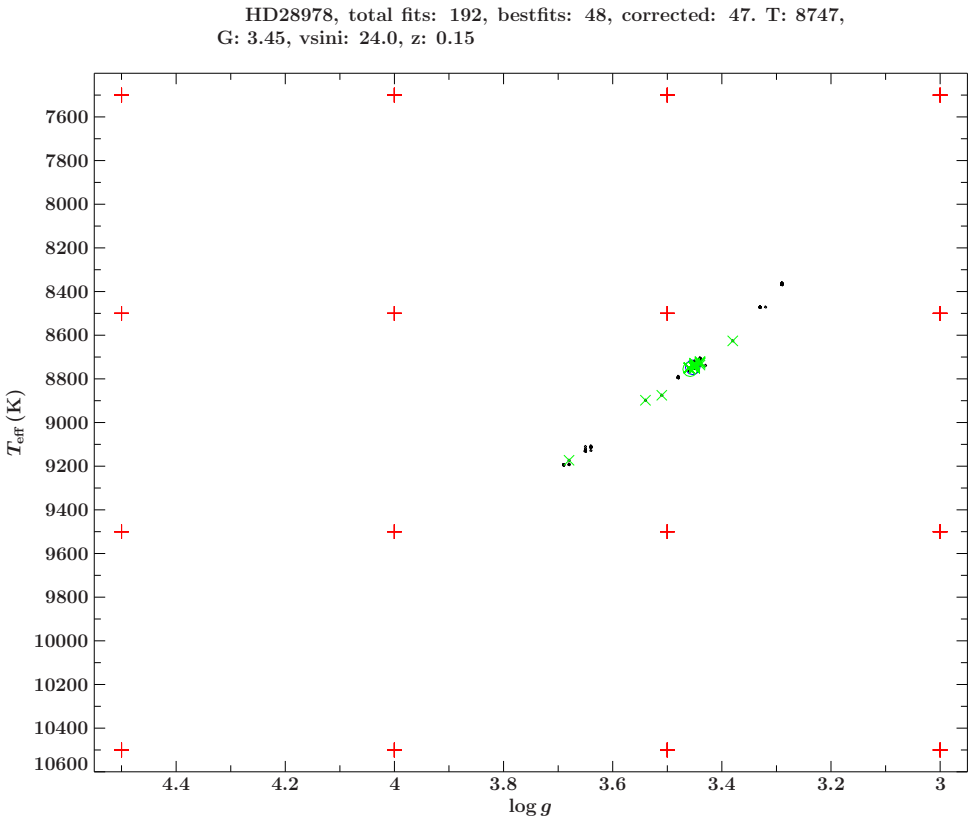

Figure 3.3: Visualization of the starting parameter (red crosses) and the fits (, black dots, green crosses mark the "best" fits for a set of starting values) for the star HD28978. For each combination of $T_{\rm eff}$ and $\log(g)$ three starting values of Z are taken. The green circle marks the mean of the best fits, the blue one the best fit with the lowest χ^2. A correlation between $T_{\rm eff}$ and $\log(g)$ is obvious. The results for the best fits range from $T_{\rm eff}/\log(g)$ = 9173/3.68 to 8626/3.38. However > 90% of the best fits lie between $\Delta T_{\rm eff}$ = 30 K and $\Delta\log(g)$ = 0.02 dex.

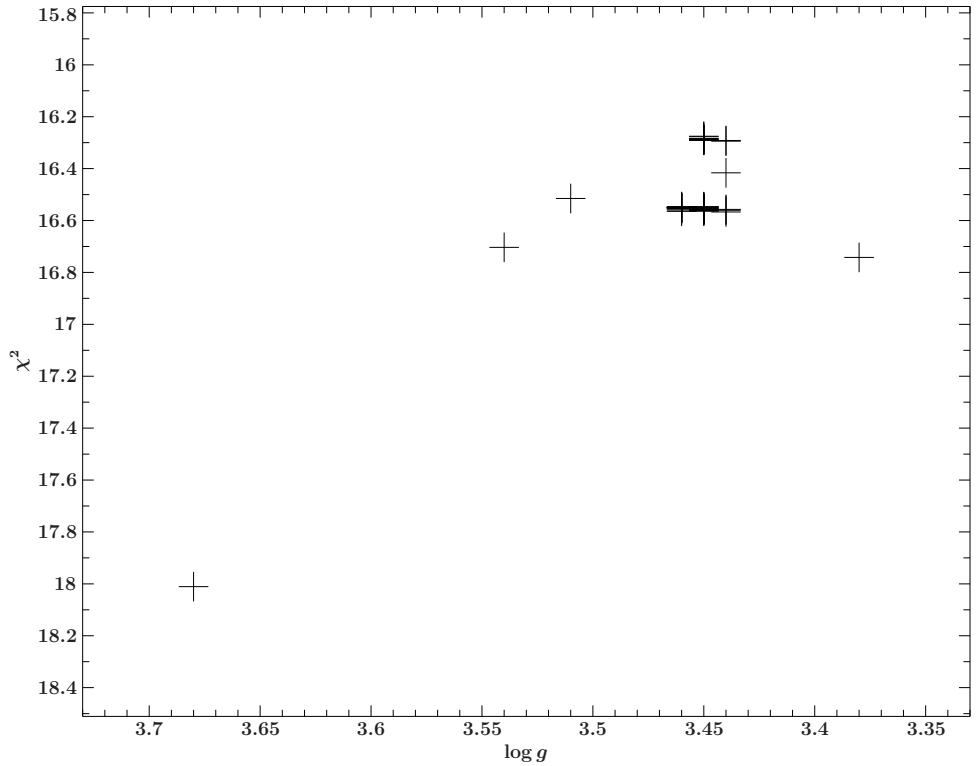

Figure 3.4: Reduced χ^2 vs. $\log(g)$ for the results of the automated fitting for HD28978. Although the best-fit results span over a relatively wide range in $\log(g)$, most of the fits end up very close together (see also caption of Table 3.3). Out of 48 different sets of starting parameters, only one is more than 5 % off the mean χ^2 (left bottom). This result is excluded. The mean χ^2 of the remaining fitting results is mostly very close to the result with the lowest χ^2 (see green and blue circles in Figure 3.3).

are always very close to the fit with the lowest χ^2 value, which is taken as the final result of the fitting (see Figure 3.3 and Figure 3.4). As the statistical errors usually can be neglected, as shown in Figure 3.3, we usually assume systematic errors to be 2% on $T_{\rm eff}$ and 0.2 dex on $\log(g)$. Another outcome is the reliability respectively a quantitative estimate of the uncertainties of the abundances. For most abundances of this star, the scatter in a quite reasonable range (± 0.1 dex around the mean) but for cerium the error is quite large (see Figure 3.5). This result is also partly reflected in our adjusted line list. For the final result, Table 3.5 gives an overview of the spectrum pixels, which are affected by which element in which ionization state. As a rule of thumb: the less pixels are affected, the larger the uncertainties should be (see Table 3.5). But there are some exceptions: silicon shows smaller errors than zirconium, although it covers almost five times less pixels in the spectrum. For stars, for which the fitting results are more stable, also the scatter in the abundances is lower.
The idea that a clear correlation between starting parameters and the fitting results exists, turned out to be false for our test stars. Either the fitting result is a complex function of several starting parameters, or its just completely random. However, in our way to start with a set of parameter combinations and excluding the extreme outliers from the mean, we can at least gain confidence taht the true (global) best values of the abundances has been found for a particular star.

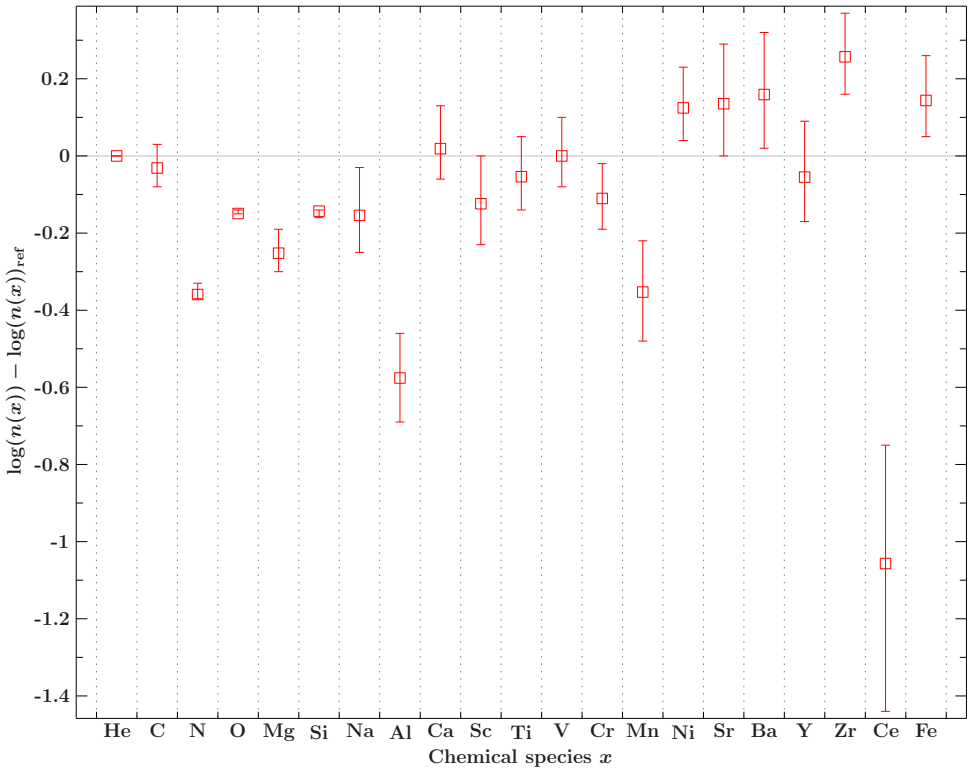

Figure 3.5: The results of the abundances of HD28978: The rectangles give the results of the fit with the lowest χ^2. The errors are derived from the extrema of the results of the automated fitting procedure.

3.3 The surface gravity problem

In the quantitative spectral analysis of A-type stars, the determination of the fundamental atmospheric parameter $\log(g)$ is rendered difficult. In B-type stars, the wings of the Balmer lines in the spectrum are well suited for the determination of that parameter. At a given temperature, the Stark effect leads to a broadening of the lines with increasing $\log(g)$, as the denser material provides more ions and electrons which electric field leads to a "smearing out" of the degenerate energy levels in the hydrogen atom. This effect is also dominant in early A-type stars.
The problem is connected to the fact that in the regime of the A-type stars the Balmer maximum can be found. The Balmer lines are transitions from the first excited state (n=2) to higher states. The number of electrons in the first excited state (and also the other excited states) rises with the temperature, as given in the Boltzmann equation

$$\frac{N_{n=2}}{N_{n=1}} = \frac{g_2}{g_1} \cdot \exp\left(\frac{E_1 - E_2}{\mathrm{k_B} T}\right)$$

with N_n as the number density of the n-th state, g_n as the statistical weight (for hydrogen $g_n = 2n^2$), E_n as the excitation energy, $\mathrm{k_B}$ as Boltzmann constant and T as temperature.
But at a temperature $\approx 9000\,\mathrm{K}$ and for electron densities typical for main-sequence stars, more and more hydrogen atoms become ionized, while the number of atoms with excited electrons still rises, and leads in total to a maximum for the strength of the Balmer lines. As the number of ionized atoms also depends indirectly proportional on the electron density, which can be deduced from the Saha equation, this

Table 3.5: sum of the affected pixels in the best fit of HD28978 for the elements in different ionization stages.

element	ion	pixels	element	ion	pixels
H	I	9087	Ti	I	230
He	I	24	Ti	II	1609
C	I	263	V	I	44
N	I	42	V	II	388
O	I	197	Cr	I	338
Mg	I	147	Cr	II	1209
Mg	II	179	Mn	I	282
Si	II	135	Mn	II	171
Fe	II	1345	Ni	I	727
Fe	III	150	Ni	II	199
Na	I	57	Sr	II	61
Al	I	31	Ba	II	70
Al	II	14	Y	II	214
Ca	I	443	Zr	II	627
Ca	II	232	Fe1	I	6611
Sc	II	312	Ce	II	14

maximum is shifted to cooler temperatures for lower surface gravity. The Saha equation for hydrogen is given by

$$\frac{N_\mathrm{p}}{N_0} = \frac{1}{U(T)}\frac{1}{N_\mathrm{e}}\frac{2\,(2\pi\, m_\mathrm{e} \mathrm{k_B} T)^{3/2}}{h^3}\exp\left(-\frac{E_I}{\mathrm{k_B} T}\right)$$

where the ionized version is a single proton, with N_0 as the number density of all neutral hydrogen excitation states, N_p as the proton number density, the partition function for neutral hydrogen $U(T) = \Sigma g_i \exp(-E_i/\mathrm{k_B} T)$, the mass of an electron m_e and the ionization energy of hydrogen E_I. This leads to the problem that in a plot of Balmer line width vs. temperature the curves overlap for the different $\log(g)$ and for stars cooler than $\approx 8000\,\mathrm{K}$ it becomes impossible to distinguish between a main-sequence and a giant star from the Balmer line wings (see Figure 3.6).

3.4 Error analysis and confidence map

We use the confidence maps as a function of effective temperature and surface gravity to calculate our statistical as well as the systematical uncertainties. In Figure 3.7 the confidence map for the test star HD204041 is shown as an example. Therefore we usually assume the uncertainties for $T_\mathrm{eff} = \pm 2\%$, $\log(g) = 0.1\,\mathrm{dex}$ for B-type and 0.2 dex for A-type stars around the best fit value. Then we step through this range of the two parameters (usually 11 steps each) and keep them fixed, while all other parameters are fitted. The corresponding $\Delta\chi^2$ can be seen color coded in the map (Figure 3.7). For most of our spectra, the errors are largely dominated by the systematics, due to shortcomings in the model or our simplifications in the deriving of our model grid. Instead of taking the quadratic mean of the systematic and the statistical errors, in most of the A-type stars we only give the systematic ones, as the calculations of the statistical errors is quite time consuming and can be neglected anyway

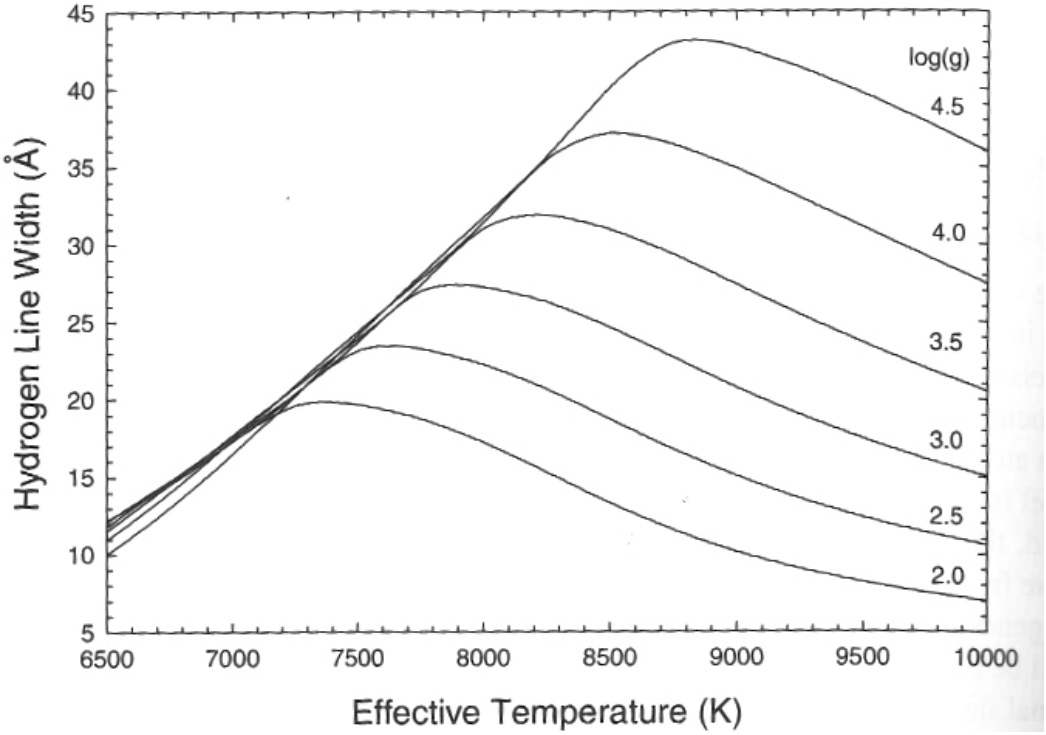

Figure 3.6: Equivalent width of the Balmer lines as function of the effective temperature for different surface gravities, adopted from Gray & Corbally (2009).

(that the statistical errors are quite low, can be deduced by the magenta line in Figure 3.7, which corresponds to a $\Delta\chi^2 = 6.63$, which reflects the 99% single-parameter confidence interval). The grey crosses mark the smallest $\Delta\chi^2$ value on each edge of the dashed-dotted rectangle, which is defined by the statistical errors. The black line marks identical $\Delta\chi^2$ values of the maxima of the four crosses. In this way, the correlation between $\log(g)$ and $T_{\rm eff}$ is reflected. We now take the minimum and maximum values of the fits within this black contour as a measure of the systematical uncertainties for the other parameters.

3.5 Feasibility test: Mock data

In order to test our modeling, we performed two tests, where we created mock data by calculating synthetic spectra, treated them like a observed ones and fitted it to our model grid. On the one hand, we want to carry out a feasibility test to quantify the effect of the intrinsic blends of lines from different metals, introduced by combining spectra calculated only with a single element beside hydrogen and helium. Therefore we calculated a bunch of spectra, considering all elements simultaneously (called MULTI spectra). On the other hand, we want to justify the more costly calculations of a handful of elements in NLTE, by fitting LTE - spectra against our NLTE grid. We performed a similar test using observed spectra rather than mock data of the planet host WASP33, which will be described in Chapter 5.

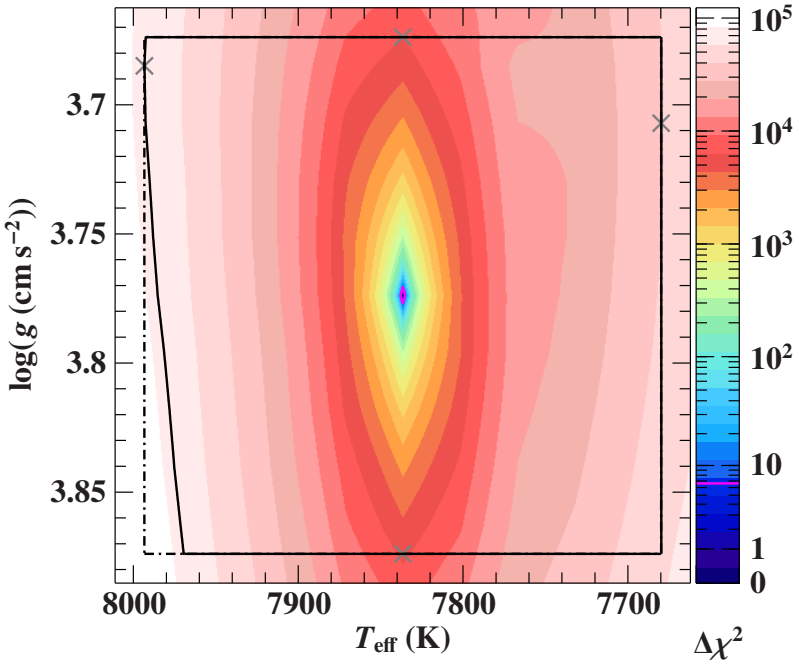

Figure 3.7: Confidence map for our test star HD204041. The dashed dotted contour is defined by the assumed systematical uncertainties around the best fit. The black line encloses the area, where we take the largest deviations for all the other parameters as uncertainties.

3.5.1 Feasibility test - effects of intrinsic line blends

In our grid, we used the simplification of combining different H+He plus one single element spectra by simply folding them together. For slow rotators, the obvious error we introduce through intrinsic blends can be directly avoided by excluding blended lines from the fits. But especially for the cooler and peculiar stars, the number of lines in the optical spectra are so dense that the accurate exclusion is on the one hand quite time consuming and on the other hand the fitted spectrum has a lot of "gaps" and we lose large parts of the observed spectra. In some particularly crowded spectra, we had to exclude more than 1000 sections for one single spectrum.
Furthermore, especially for the fast rotating stars, this procedure becomes quite messy, as we have to refold the model spectrum to its intrinsic, non-rotating version, where the lines are only broadened by intrinsic line broadening effects (such as radiative damping, thermal and collisional broadening) and the instrument and only then can identify intrinsically blended lines, which are effected by our simplification. To save time, we decided to exclude only the most obvious overlapping lines and assumed that due to the large number of blends, it would be statistically even out the error. To test if this assumption is correct, we calculated MULTI spectra (where all elements are calculated simultaneously) for our test stars with the previously fitted parameters, and fitted them against our simplified model grid. The error, introduced by our simplification is quite small in temperature ($\pm$ a few tens of K for the cooler and up to 200 K for the hotter stars and metallicity < 0.1 dex), but $\log(g)$ is systematically lower by 0.01 ... 0.18 dex, and 0.1 dex on average. The corrections for gravities are larger for the late A-type stars ($T_{\rm eff}$<8500 K) than for the earlier types. Hence we henceforth add a correction term of 0.15 dex to the results for $T_{\rm eff}$<8500 K and

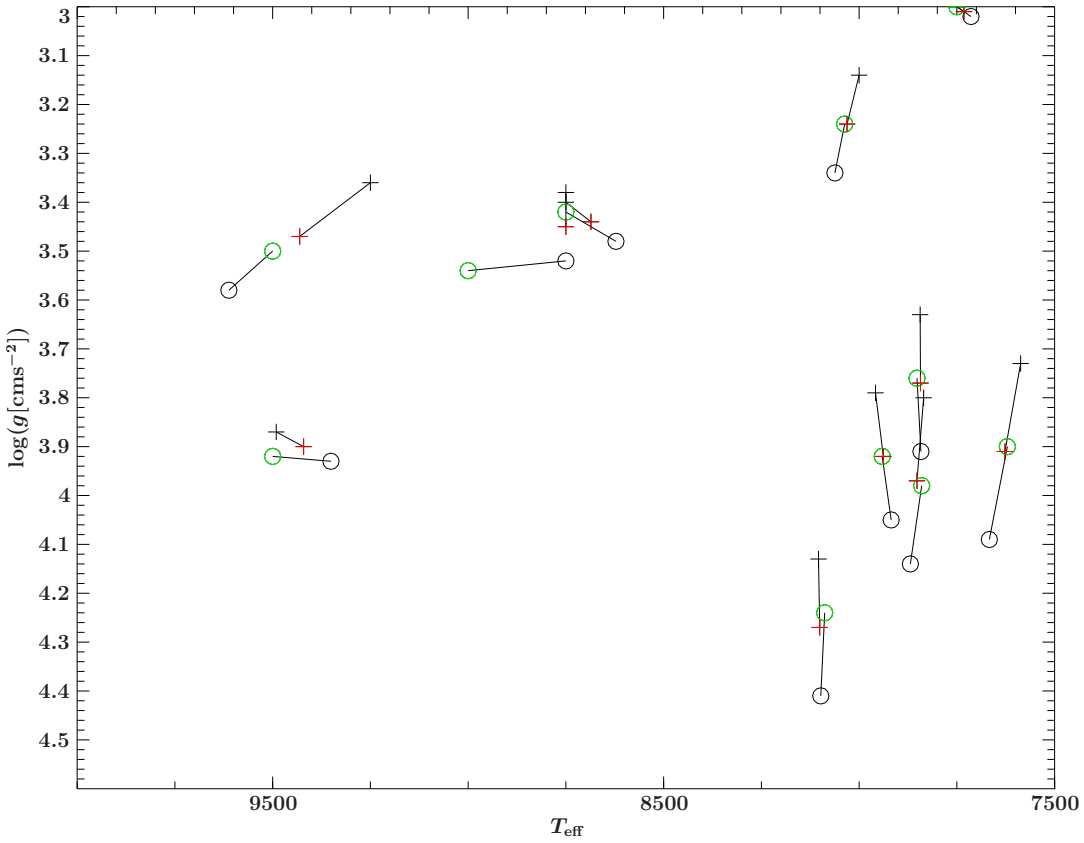

Figure 3.8: Visualization of our fitting of the MUTLI spectra against our simplified approach. The first fit of our standard stars to our simplified model grid is marked by a red cross, for which parameters we also calculated a MULTI spectrum, which treated all the elements simultaneously. Then we fittet this spectrum to our model grid, to test how good our simplified grid works. The fit can differ, especially in $\log(g)$ up to 0.2 dex (black crosses), which means we have to correct our results for the corresponding offsets. To check if a linear extrapolation works, we calculated again a MULTI spectrum, now with the values marked by a black circle. The resulting fits (green circles) as expected ends up very close to the red crosses in most cases.

0.07 dex for the hotter ones. Temperature corrections are larger (100 - 200 K) for the hotter stars, but can be positive (e.g. HD114330) and also negative (e.g. HD72660) so we do not correct for this effect in the results.
We extrapolated another "correct" spectrum and fitted it again, assuming to end up at the previous results and to find the final parameters in such way in the new spectrum. This worked quite well for most of the stars, see Table 3.6 and Figure 3.8 for details.
For our program stars, where we did not perform a detailed analysis of the errors introduced by line blends, we can take the from our test stars derived offsets and add them to our final basic parameters, to account for these systematic, non-negligible effects.

3.5.2 Non-LTE-effects

In order to quantify NLTE-effects, we fitted a LTE-model spectrum, including the elements hydrogen and helium plus one single additional metal against our NLTE-

Table 3.6: Results of the standard stars + WASP33 (HD15082): The column 'Agrid' gives the results of our fitting method. Next to it, the column 'ΔMULTI' gives the difference of the fitted "correct" (calculated with all elements together) spectrum to the previously fitted parameters, which give in principle the errors introduced by the intrinsic line blends. These offsets are used to extrapolate a parameter set, which is used to create a correct spectra (black circles in Figure 3.8) which fit would in the best case end up (green circles in Figure 3.8) at the precious fitted results (red crosses in Figure 3.8) and thus gives us the final parameters. Note the offset in $\log(g)$ can be almost 0.2 dex lower. The column 'result' gives the model parameters of the extrapolated "correct" spectra, which we take as final results for our test stars. The column "ΔMULTIre' gives the difference of the fitted extrapolated values to the final "correct" model, which would be best at zero. Only for HD28978, there are unreasonable results, as the fit tends to result at temperature grid points (8750 and 9000 K respectively). $T_{\rm eff}$ is given in Kelvin, $\log(g)$ and Z in dex, where Z=0 corresponds to solar.

star	parameter	Agrid	ΔMULTI	ΔMULTIre	result
HD28978	$T_{\rm eff}$	8750	0	250	8750
	$\log(g)$	3.45	-0.07	0.09	3.52
	Z	0.14	0.00	0.11	0.14
HD15082	$T_{\rm eff}$	7938	20	3	7918
	$\log(g)$	3.92	-0.13	0.00	4.05
	Z	0.43	0.09	-0.01	0.32
HD39060	$T_{\rm eff}$	7852	-17	-12	7869
	$\log(g)$	3.97	-0.17	0.01	4.14
	Z	0.06	0.05	-0.02	0.01
HD176232	$T_{\rm eff}$	7627	-40	-6	7667
	$\log(g)$	3.91	-0.18	-0.01	4.09
	Z	0.15	0.06	-0.01	0.09
HD145689	$T_{\rm eff}$	8101	3	-13	8098
	$\log(g)$	4.27	-0.14	-0.03	4.41
	Z	0.14	0.08	-0.02	0.06
HD91375	$T_{\rm eff}$	8686	64	64	8622
	$\log(g)$	3.44	-0.04	-0.02	3.48
	Z	-0.05	0.03	-0.02	-0.08
HD65810	$T_{\rm eff}$	8031	-31	6	8062
	$\log(g)$	3.24	-0.10	0.00	3.34
	Z	-0.13	0.03	0.00	-0.16
HD204041	$T_{\rm eff}$	7843	1	9	7842
	$\log(g)$	3.77	-0.14	-0.01	3.91
	Z	-0.79	0.04	0.01	-0.83
HD189849	$T_{\rm eff}$	7732	18	18	7714
	$\log(g)$	3.01	-0.01	-0.01	3.02
	Z	0.09	0.03	-0.04	0.06
HD114330	$T_{\rm eff}$	9431	-181	69	9612
	$\log(g)$	3.47	-0.11	0.03	3.58
	Z	0.06	-0.06	0.02	0.12
HD72660	$T_{\rm eff}$	9421	70	79	9351
	$\log(g)$	3.90	-0.03	0.02	3.93
	Z	0.40	0.02	0.01	0.38

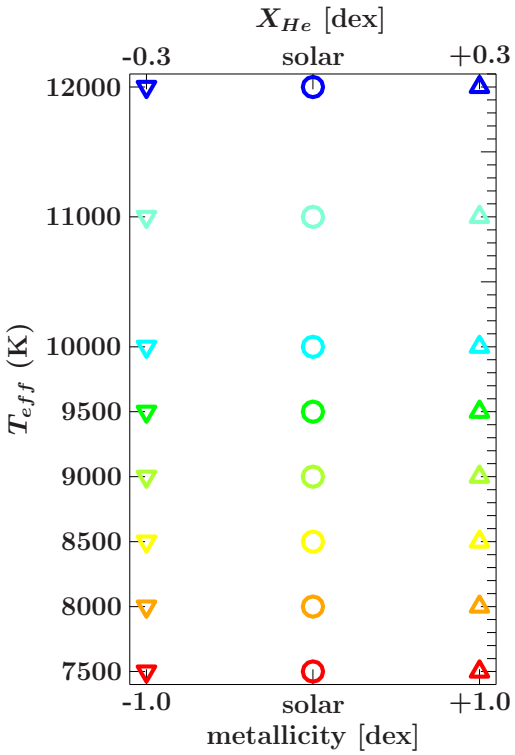

Figure 3.9: Explanation of the colors and symbols used in the tests of NLTE-effects.

model-grid. The elements under consideration were C, N, O, Mg, Si and FeII/III. Since the effects may not only depend on effective temperature and gravity, we also investigated the influence of metallicity and helium abundance. The results are given in Figure 3.10 to 3.16. Because the figures are complex, the meaning of the colors and symbols of the different plots are explained in Figure 3.9. Note that in the left column the meaning of the symbols corresponds to the helium abundance, in the right column for the scaled background metallicity Z, used in the calculation of the ATLAS atmospheric structure. Z=0 corresponds to the solar abundance vector. The value for the parameter not symbol-coded is always the solar value (in the left hand panel Z=0, in the right hand panel He=-1.06 dex) . The colors always corresponds to the temperature, blue for the hot (=12kK) and red for the cold (7500K) end. In the fitting procedure we successively kept different fitting parameters free for fitting, as we do it in our fitting procedure for real stars. The difference between NLTE-fit and the LTE-model values is defined as $\delta Y = Y_{\mathrm{NLTE}} - Y_{\mathrm{LTE}}$, the term $n(X)$ is the logarithmic particle number of a specific element X in respect to all other elements $n(X) = \log_{10}(\frac{n(X)}{n(\mathrm{all})})$.

3.5.2.1 $\delta(n(X))$ vs $\delta(\log(g))$

In Figure 3.10 and 3.11 we plot the difference for the logarithmic abundance obtained by the fit minus the original (LTE-) model versus the difference in $\log(g)$. For C, N, Si and Fe the fitted $\log(g)$ corresponds quite well to the model, except one outlier in Fe which is most probably a numeric effect. For oxygen the influence on $\log(g)$ can be up to 0.2 dex, for temperatures around 9000K and low helium and low Z, respectively. But also for solar values the difference can be 0.15 dex.

Also the derived abundances can differ at certain temperatures for all metals, by up to -1.2 dex in oxygen and +0.4 dex in iron in the most extreme cases at hot temperatures.

3.5.2.2 $\delta(n(X))$ vs $\log(g_{\mathrm{LTE}})$

Another view on the test results is the difference of the fitted minus the model abundance versus the model $\log(g)$ (Figure 3.12 and 3.13). The plots illustrates better the partly complex functions of the deviations, e.g. carbon which has deviations from -0.1 to 0.2 dex, depending on T_{eff} and $\log(g)$. Especially for nitrogen one can see that the deviation also depends slightly on the metallicity Z, rather than on the helium abundance. The effect is reversed from the cool (red), where a lower metallicity gives a stronger NLTE effect, to the hotter end (blue). Also the already mentioned strong deviations in iron and oxygen for the hot temperatures can be observed, while surprisingly magnesium is almost unaffected and even for extreme metallicities the effects are below 0.1 dex.

3.5.2.3 $\log(g_{\mathrm{NLTE}})$ vs $\log(g_{\mathrm{LTE}})$

For some elements, the free fitted $\log(g)$ slightly differs from the model, which is also reflected in Figure 3.10 and 3.11. This is shown for silicon and oxygen, for the other elements the effect is small (≤ 0.05 dex, see Figure 3.14). Note that we only show the results for a fixed helium abundance here. For a freely fittet helium abundance, the surface gravity also for magnesium und iron can differ up to 0.2 dex.

3.5.2.4 Effective temperature vs gravity

The fitted temperature corresponds mostly to the model. Only the relatively strong deviations for oxygen and silicon are shown in 3.15. For intermediate temperatures (9000 and 9500K), the fitted temperature is off the model by up to 350K.

3.5.2.5 Metallicity vs surface gravity

The fitted metallicity Z is perfectly matched for all three tested helium abundances. But it shows deviations from the models for the extreme cases of ± 1.0 dex the solar metal abundances, see Figure 3.16. For silicon and oxygen, the models around $\log(g) = 3.8$, $T_{\mathrm{eff}} = 9500\,\mathrm{K}$ and $Z = -1.0\,\mathrm{dex}$ tend to a fit with Z=0, thus a deviation of almost 1.0 dex. This discrepancy is not a problem for real fits, as Z is linked to the iron abundance, which could not be done in these tests as iron is not included in the tested models.

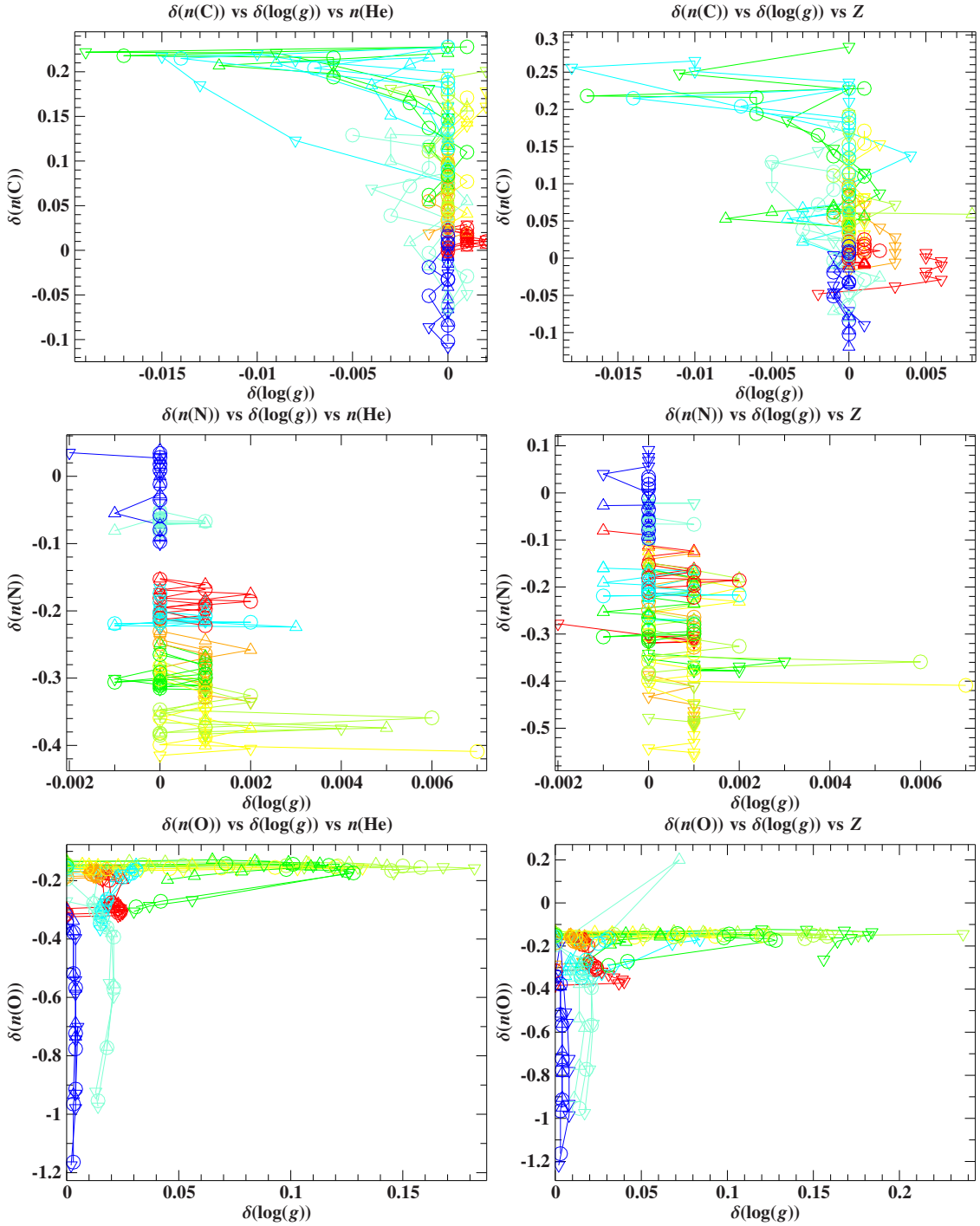

Figure 3.10: NLTE effect as difference of the model- minus fitted abundance versus the difference of the logarithmic surface gravity. The colors correspond to different effective temperatures, the symbols to the helium abundance for panels on the left hand side, to the metallicity for the panels on the right hand side. For the explanation of colorcodes and symbols see Figure 3.9.

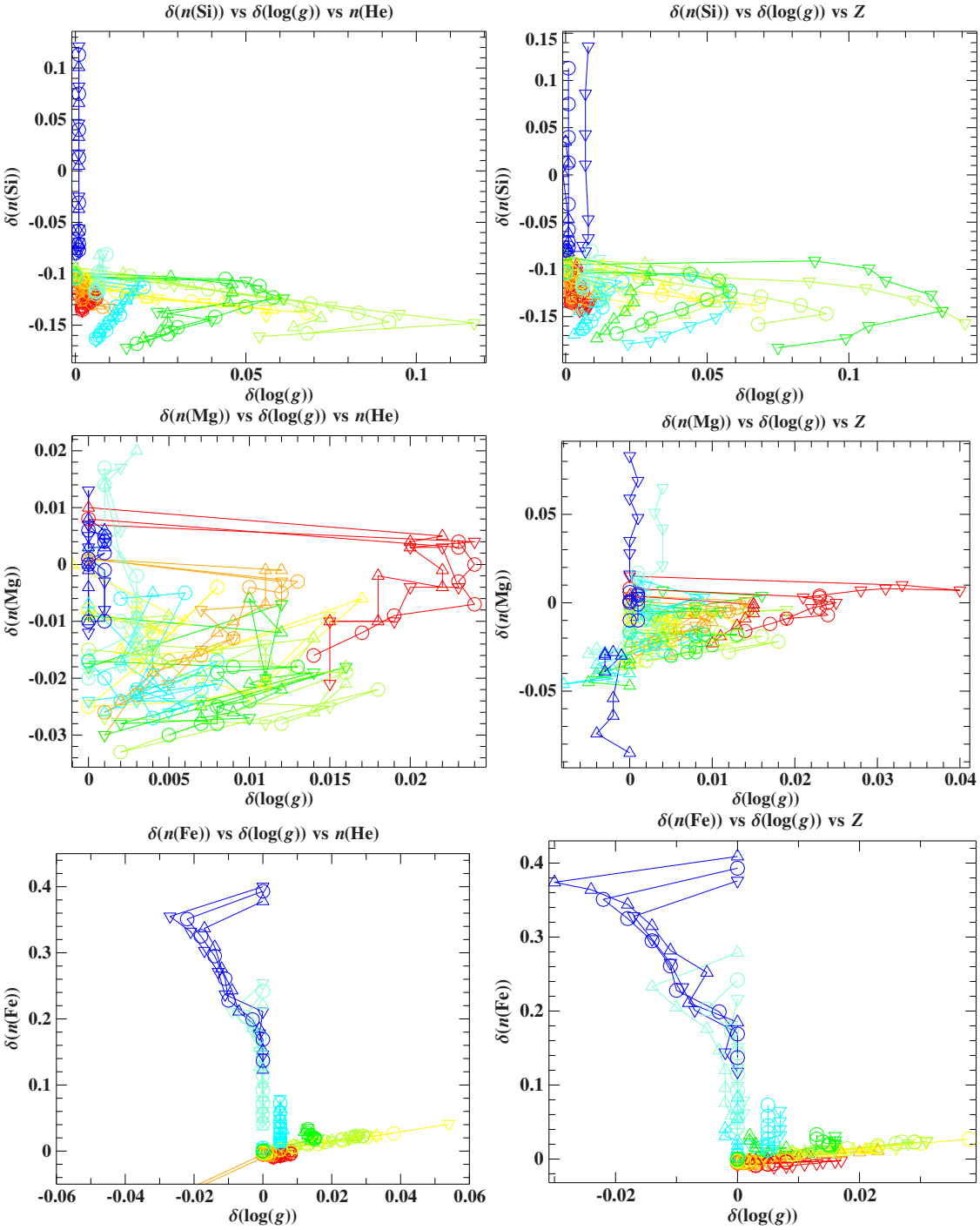

Figure 3.11: NLTE effect as difference of the model- minus fitted abundance versus the difference of the logarithmic surface gravity. The colors correspond to different effective temperatures, the symbols to the helium abundance for panels on the left hand side, to the metallicity for the panels on the right hand side. For the explanation of colorcodes and symbols see Figure 3.9.

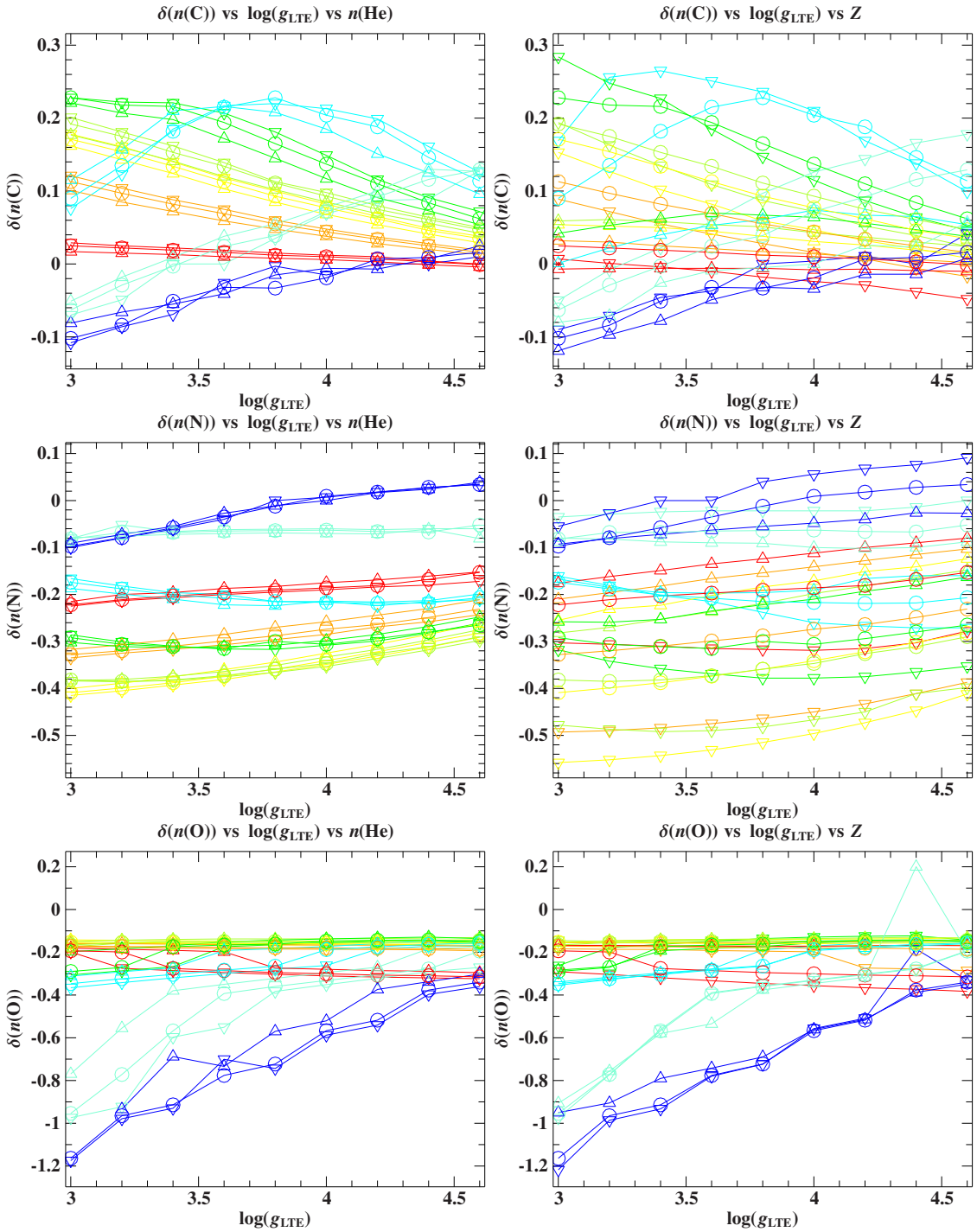

Figure 3.12: Difference of the model- minus fitted abundance versus the model $\log(g)$. For the explanation of the colorcodes and symbols, see Figure 3.9.

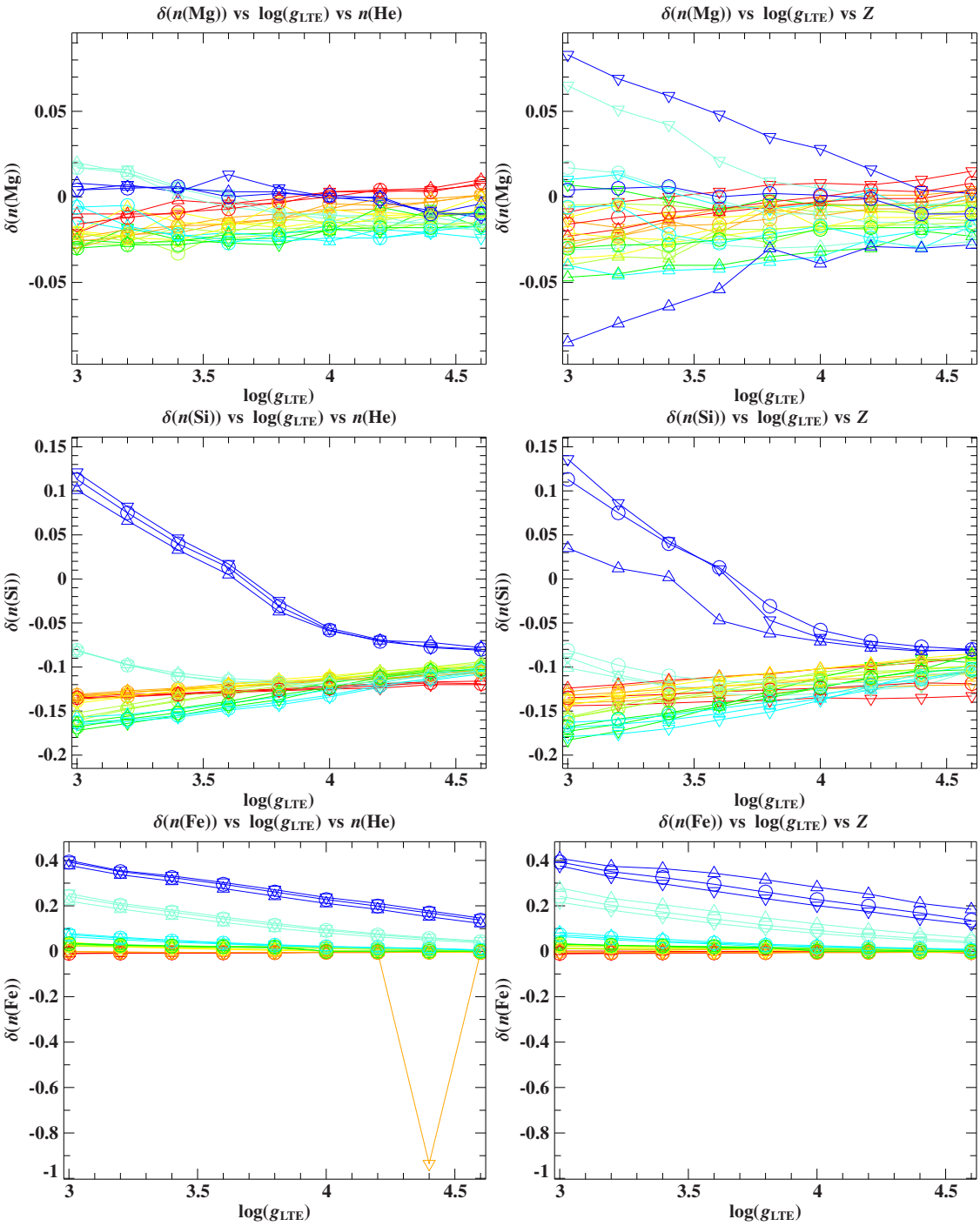

Figure 3.13: Difference of the model- minus fitted abundance versus the model $\log(g)$. For the explanation of the colorcodes and symbols, see Figure 3.9.

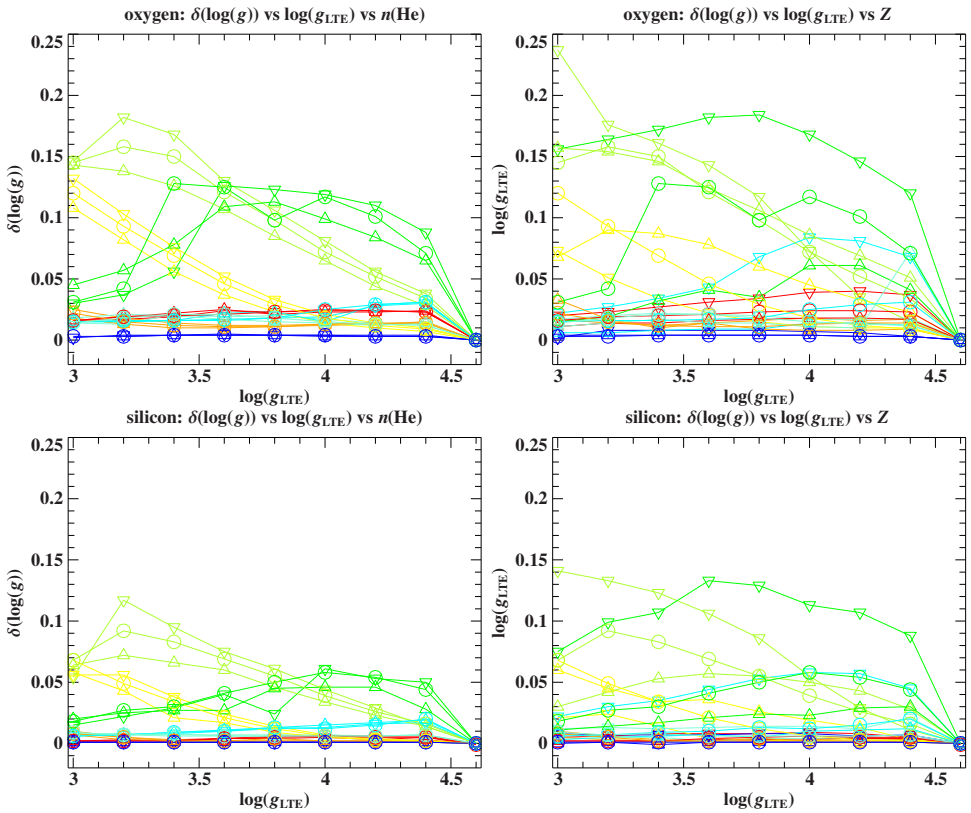

Figure 3.14: Difference of model minus fitted $\log(g)$ versus LTE model $\log(g)$. For the explanation of the colorcodes and symbols, see Figure 3.9.

3.5.2.6 Summary and conclusions

NLTE effects in general are small (< 0.15 dex), but depend crucially on a combination of the basic parameters effective temperature, surface gravity and metallicity. Only those for magnesium are negligible (< 0.05 dex). The most notable effects are found for the elements oxygen and silicon. Oxygen shows the most extreme deviations of up to -1.2 dex. The NLTE effects on the line strength can partly be compensated by a change of the surface gravity, which may increase by to 0.2 dex in the most extreme cases for oxygen and silicon. For oxygen in the hot temperature regime, the NLTE effect can be seen predominantly with respect to the abundance, while for temperatures around 9000 – 9500 K an abundance offset of up to -0.2 dex occurs in combination with up to +0.2 dex offset to the surface gravity (see Figure 3.10/3.11 or Figure 3.14). A similar behavior can be seen for silicon to a smaller account, but the abundance effect is reversed for the hotter end.
The NLTE effects on the surface gravity also partly affects the temperature in these cases, but the offsets are smaller than 100 K between $\approx$ 8000 – 10000 K, and can be neglected for all the other elements and temperatures (see Figure 3.15). Most of the deviations are complex functions of the surface gravity and temperature. Only for some cases, "simple" correlations can be seen, e.g. for oxygen, silicon and iron there is an almost linear trend for the hot end for the abundance versus density (i.e., surface gravity, see Figure 3.12 and 3.13). For carbon around 10000 K, the maximum of the abundance deviation occurs for a surface gravity of around $\log(g) = 3.8$ dex.
Only in some extreme cases, also the overall metallicity is influenced by NLTE effects. It is strongest (up to 1.0 dex) for temperatures around 9500 K, $\log(g) = 3.8$ dex

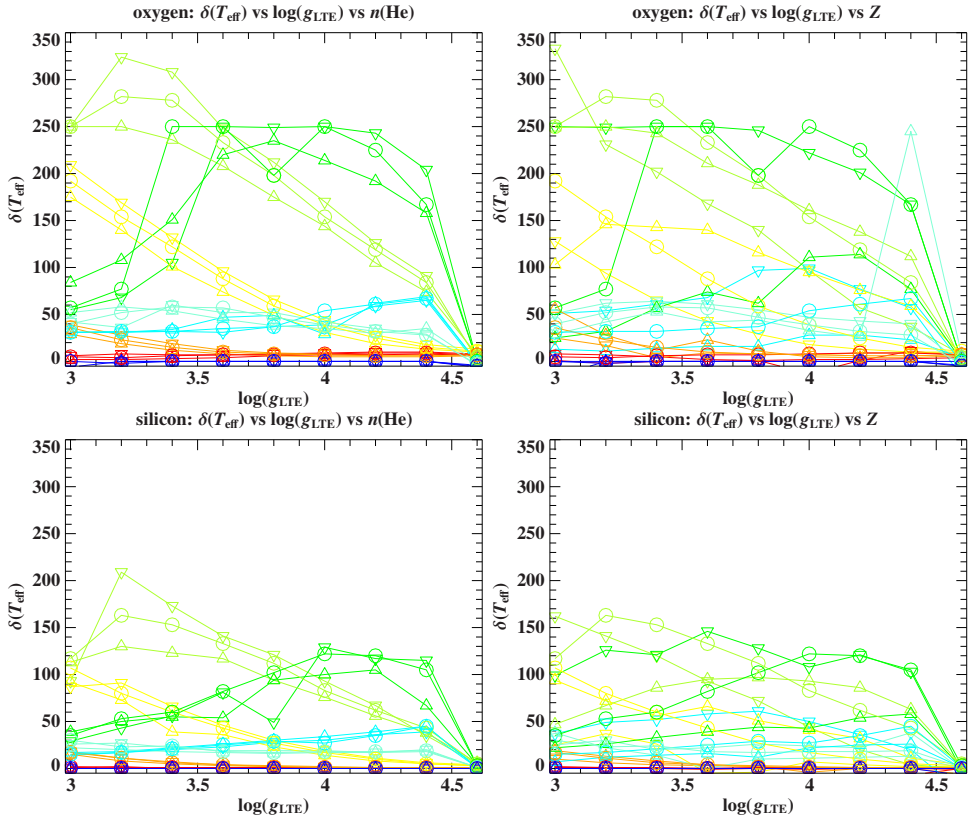

Figure 3.15: Difference of model minus fitted $T_{\rm eff}$ versus LTE model $\log(g)$. For the explanation of the colorcodes and symbols, see Figure 3.9.

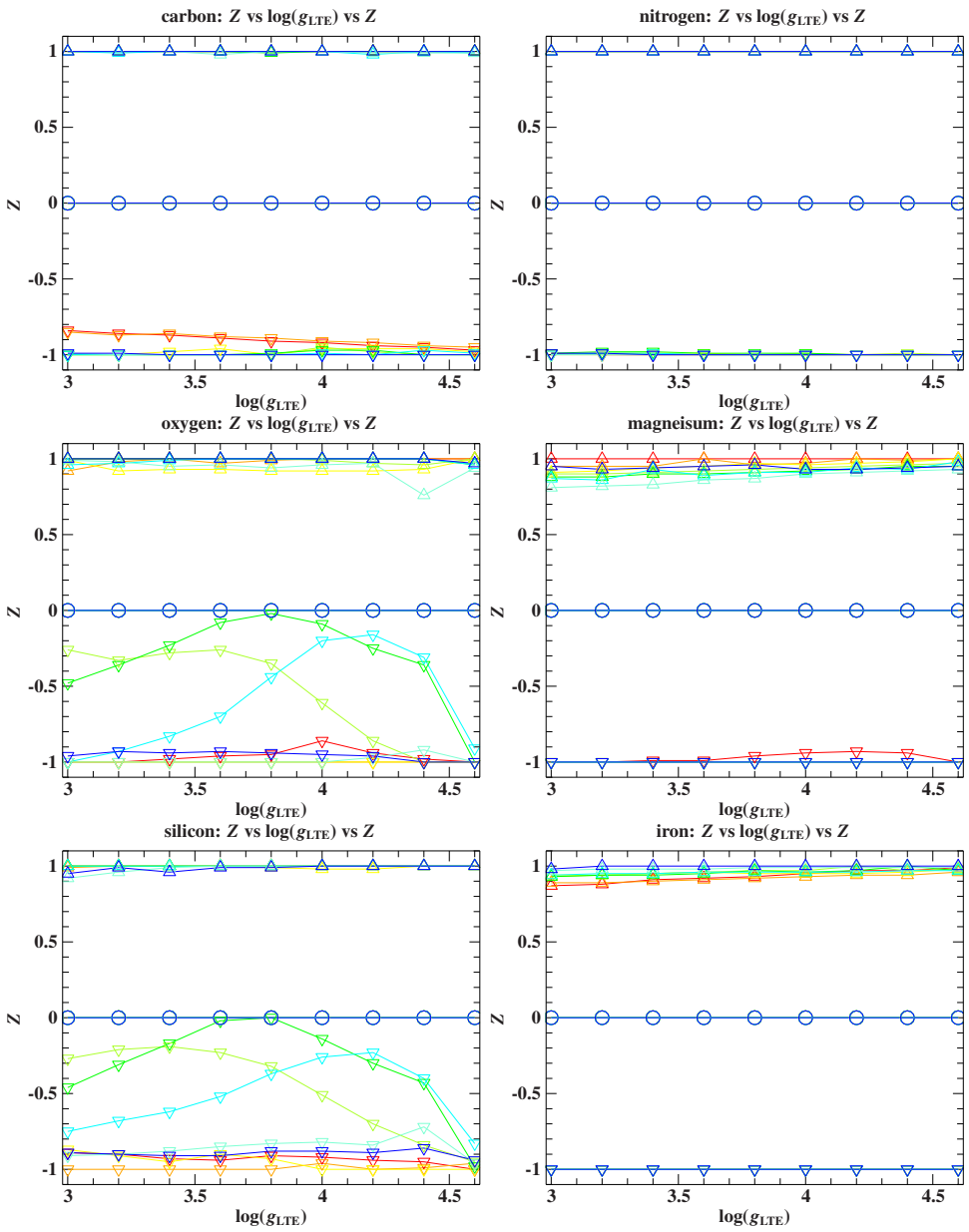

Figure 3.16: Fitted NLTE metallicity Z versus LTE model $\log(g)$. For the explanation of the colorcodes and symbols, see Figure 3.9.

Table 3.7: Chemical abundance deviations for solar metallicity and helium abundance (adoptable, e.g., from the circles in the right column of Figures 3.12 and 3.13). The categories are: late B (12 – 11000 K), early A (10 – 9000 K) and late A (8500 – 7500 K).

	late B (12 − 11 kK)		early A (10 − 9 kK)		late A (8.5 − 7.5 kK)	
	min	max	min	max	min	max
δ(n(C))	-0.10	+0.12	+0.10	+0.25	-0.02	+0.15
δ(n(N))	-0.10	+0.02	-0.40	-0.30	-0.40	-0.15
δ(n(O))	-1.20	-0.20	-0.35	-0.20	-0.30	-0.20
δ(n(Mg))	-0.03	+0.02	-0.03	+0.02	-0.03	+0.02
δ(n(Si))	-0.14	+0.11	-0.17	-0.11	-0.14	-0.11
δ(n(Fe))	+0.05	+0.40	+0.00	+0.10	+0.00	+0.05

in oxygen and silicon (see Figure 3.16).
To summarize the NLTE effects for solar metallicity and helium abundance, we extracted the basic results of the tests into Table 3.7 by dividing the temperature regime into late B, early- and late A-type stars. In general, the NLTE effects are stronger for the late B-type stars than for the A-type stars, while the early A-types show slightly stronger effects than later A-types.

Magnesium and Fe (II/III) show almost no effect in A-type stars. Si yields a small drop of -0.12 dex in its abundace. For N and O the mean NLTE-effect is about -0.3 dex, for C +0.1 dex in the late and +0.2 dex in the early A-type stars.
For late B-type stars, we have small effects for C and N, while Mg shows almost no effect, as in the A-type stars. There is a strong drop for O, depending on the surface gravity. For stars near the ZAMS the NLTE effect leads to an increase of the oxygen abundance by +0.4 dex, while it is decreased up to -1.2 dex for (sub-)giants. Fe shows an effect of +0.4 dex for the (sub-)giants.
In general, this test demonstrates the need for NLTE calculations for the elements carbon, nitrogen, oxygen, silicon and iron, but LTE modeling is sufficient for magnesium and iron (II/III) in the A-type stars. In principal the relations shown in Figure 3.9 can be used to estimate correction factors for pure LTE analyses, similar to the plots given by Rentzsch-Holm (1996), which we used for NLTE corrections for Fe I or just can be used to convince spectroscopists to spend more time in calculating more sophisticated NLTE models.

Chapter 4

The standard star sample

We selected ten slowly rotating stars from the A list for a detailed analysis. The atmospheric parameters of the stars span the range ($T_{\rm eff}$, $\log(g)$) expected for A-type stars.

4.1 Setting up the standard star sample

As first application of our analysis method on A-type stars, we extracted informations of A-type stars from different catalogues to construct a sample of possible standard stars. These catalogues were

- "Abt Mor": spectral MK classification of Abt & Morrell (1995).
- "POP": The UVES Paranal Observatory Project (UVES POP Bagnulo et al., 2003).
- "SAO": Smithsonian Astrophysical Observatory Star Catalog (Whipple, 1966).
- "Gray": Stars classified as A-types from a study of nearby stars (Gray et al., 2006).

We took these as input list for queries for high-resolution spectra in different archives, of high quality, high resolution spectra, mainly the public ESO Phase 3 archive. In the beginning, we selected preferentially slow rotators, in order to identify missing lines and to complete our grid with additional elements, where available and to complete our line list. Thereafter we extended our interest also to fast rotating stars. We also took some spectra as backup targets in different other observing runs, especially with FEROS in La Silla at the 2.2 m telescope and CAFE at the 2.2 m telescope at Calar Alto.

4.2 High resolution spectra

The following Echelle spectrographs have been used for the A star sample. As most of our analyzed spectra have been taken from UVES, we will describe the instrument in more detail.

4.2.1 FEROS

The Fibre-fed, Extended Range, Échelle Spectrograph (FEROS) is installed at the 2.2 m telescope at the La Silla Observatory in Chile. It has a complete wavelength

coverage from $\approx 3500\,\text{Å} - 9200\,\text{Å}$ at a spectral resolution of about $R = \frac{\lambda}{\Delta\lambda} = 48000$.

4.2.2 CAFE

The Calar Alto Fiber-fed Echelle spectrograph (CAFE) is mounted at the 2.2m telescope at Calar Alto in southern Spain. Its spectral coverage is $3960\,\text{Å} - 9500\,\text{Å}$ with a resolution of $R \approx 62000$.

4.2.3 UVES

The Ultraviolet and Visual Echelle Spectrograph (UVES) is an optical high resolution spectrograph, mounted at the UT2 Nasmyth platform at the Very Large Telescope (VLT) at the ESO Paranal Observatory in Chile. A schematic sketch is shown in Figure 4.1. It is principally designed to observe at high accuracy between 3000 to 11000 Å, its actual coverage is depending on the instrument settings. UVES has a dichroic beam splitter, which divides the UV from the visual-red part which can be observed individually or in parallel (dichroic mode). The blue arm is equipped with one CCD camera, the red arm is recorded with two CCDs, which leads to a small gap up to 10 Å depending on the central wavelength, which can be chosen by the observer. Beside four different observing modes, which is observing only in either the red or the blue beam, or two different dichroic (Dic#1 and Dic#2) modes, the observer can choose of two cross dispersers, each in the red (CD#3 and CD#4) and the blue (CD#1 and CD#2) beam (see also Figure 4.1). Depending on these settings, there is also a gap between the blue and the red arm. To obtain a spectrum covering the full wavelength range of our interest (3900 – 8000 Å), an object has to be observed in different modes and the resulting spectra have to be combined.

4.3 Coarse spectral analysis

An overview of the targets, where we have got high resolution ($R \gtrsim 30000$) and high SNR ($\gtrsim 200$) is shown in Table 4.1. The quality of the spectrum is flagged with "A" for the best and "C" for the lowest quality. An "X" marks spectra, which could not be fittet, either because the first fit runs to a grid border and is not at all representing the observed spectrum, or the artifacts in the spectra could not be easily removed and thus the fit becomes unreliable. The basic parameters are shown from a first fit after normalization by hand, so they can be considered as first guesses, only. For some stars, we slightly extrapolated the grid for values of $\log(g)<3.0$, but for none of these stars we found a good match to the observed spectra.

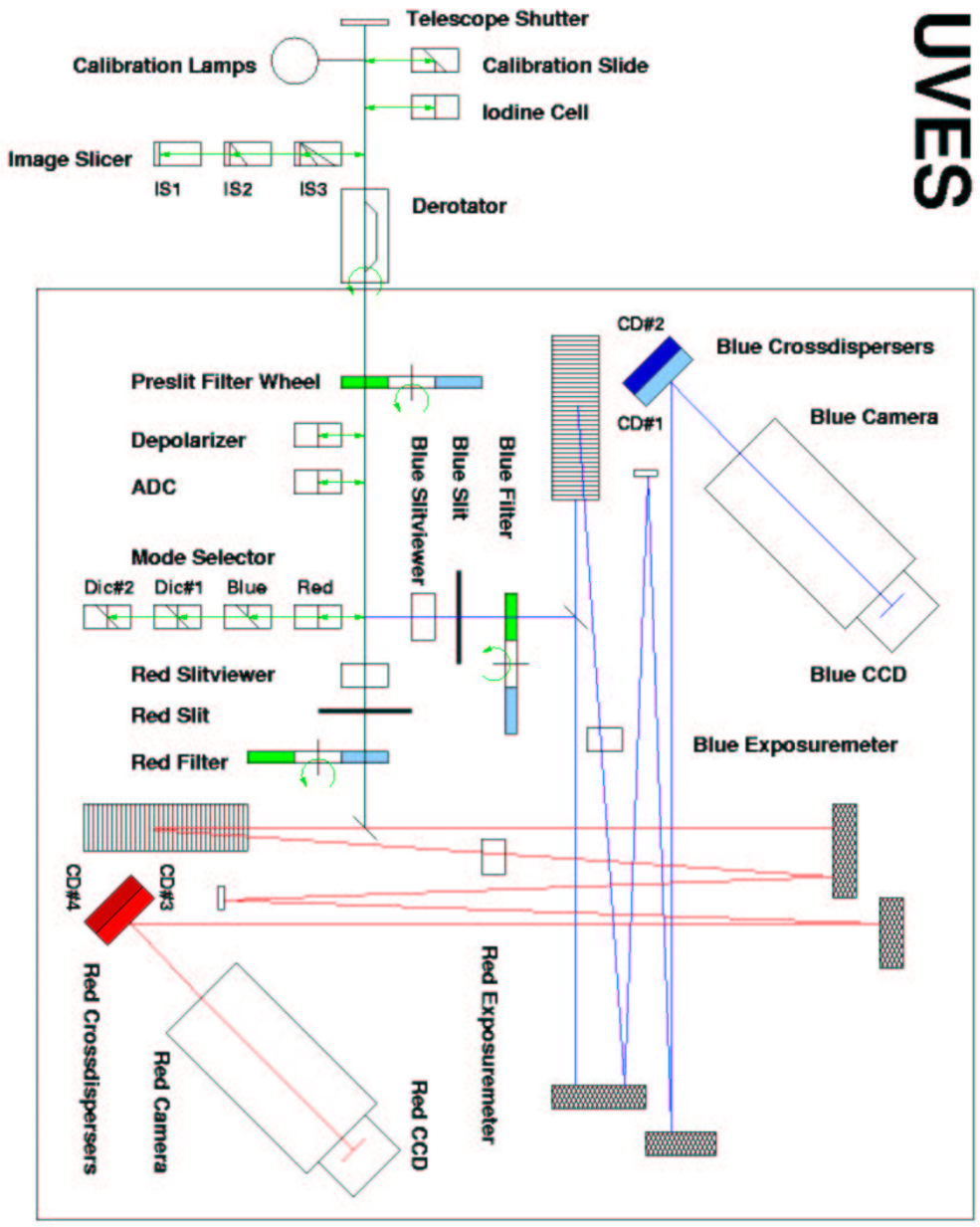

Figure 4.1: Schematic sketch of the UVES spectrograph, taken from the manual, provided by ESO.

Table 4.1: Overview of the A-type star sample. The quality of the spectrum is shown as well as an estimate for the basic parameters from a first fit, after normalization and adjusting the RV and $v \sin i$. All the selected stars have at least a SNR $\gtrsim 200$. Note that our model is limited to $\log(g) \geq 3.0$, lower values correspond to extrapolated model spectra. Our standard stars are marked with an asterisk, for the final values please see Table 4.7.

star	spec. type	catalogue	instrument	$T_{\rm eff}$	$\log(g)$	$v \sin i$	quality
HD65810*		POP	UVES	8069	3.21	230	A
HD114330*		Abt Mor	UVES	9510	3.48	0	A
HD132145	A1V		CAFE	9770	4.06	12	A
HD140232	A2m	SAO101686	UVES	7890	3.92	8	A
HD141795		Abt Mor	UVES	8106	3.68	35	A
HD145689*		POP		8093	4.26	102	A
HD157087	A3III	Am	CAFE	8820	3.43	10	A
HD159834	A7IV		CAFE	7880	3.30	16	A
HD168525	A6V		FEROS	8175	3.55	4	A
HD170296		Abt Mor	UVES	9643	3.70	178	A
HD172167	A0V		FEROS	9750	4.16	23	A
(Vega)							
HD176232*		Abt Mor	UVES	7590	3.67	0	A
HD189849*	A4III		CAFE	7700	3.03	8	A
HD204041*		Abt Mor	UVES	7845	3.75	44	A
HD216956	A3V	Gray	UVES	8620	3.99	88	A
HD28978*		Abt Mor	UVES	8875	3.52	23	A
HD319		Abt Mor	UVES	7918	3.47	61	A
HD39060*		Abt Mor	UVES	7790	3.77	78	A
HD47103		SAO 95908 A0	UVES	9760	3.60	24	A
HD72660*	A1V		FEROS	9610	3.90	0	A
HD72968		Abt Mor	UVES	8023	3.31	10	A
HD91375*	A1V		FEROS	8880	3.58	1	A
HD97633		Abt Mor	UVES	9470	3.66	21	A
HD100740		Abt Mor	UVES	7711	≤ 3.00	261	B
HD103578		Abt Mor	UVES	8572	3.53	0	B
HD108945		Abt Mor	UVES	8330	3.39	35	B
HD111133		Abt Mor	UVES	9780	3.33	0	B
HD118022		Abt Mor	UVES	7971	3.16	10	B
HD125248		Abt Mor	UVES	8616	3.21	10	B
HD13538	A1III	Gray	UVES	10290	3.46	201	B
HD141003	A2IV(A3V)	Gray	UVES	10100	3.41	197	B
HD142703		Abt Mor	UVES	9749	3.06	63	B
HD148898		Abt Mor	UVES	7888	3.56	30	B
HD16031		SAO148474	UVES	10930	≤ 3.00	0	B
HD174240		Abt Mor	UVES	9057	3.45	61	B
HD193281		Abt Mor	UVES	8030	3.49	101	B
HD195093		Abt Mor	UVES	9319	4.06	135	B
HD195094		Abt Mor	UVES	9519	4.07	148	B
HD201184	A0V	Gray	UVES	8990	3.72	204	B
HD209625		Abt Mor	UVES				B
HD47105	A0IV	runaway	FEROS	9780	3.45	26	B

HD85504	A0Vs	runaway	FEROS	9360	3.40		B
HD9672		Abt Mor	UVES	9216	3.97	160	B
HD158352		Abt Mor	UVES	8848	$\leq$ 3.00	123	C
HD163318		Abt Mor	UVES	7558	$\leq$ 3.00	124	C
HD170973		Abt Mor	UVES	9320	$\leq$ 3.00	4	C
HD170973		Abt Mor	UVES	9154	$\leq$ 3.00	0	C
HD17729		Abt Mor	UVES	9752	3.80	119	C
HD183324		Abt Mor	UVES	9519	4.27	78	C
HD187474		Abt Mor	UVES	8924	$\leq$ 3.00	9	C
HD208108		Abt Mor	UVES	9498	4.02	28	C
HD210049		Abt Mor	UVES	9530	3.89	259	C
HD216956		Abt Mor	UVES	9602	4.26	57	C
HD223640		Abt Mor	UVES	9750	$\leq$ 3.00	21	C
HD24712		Abt Mor	UVES	7500	3.04	0	C
HD30739		Abt Mor	UVES	8579	3.11	177	C
HD42303		Abt Mor	UVES				C
HD95370	A3IV	Gray	UVES				C
HD 73709		SAO98020	UVES				X
HD105262	B9	Post-AGB	CAFE	11290	$\leq$ 2.90	0	X
HD110379		SAO138917 F0V	UVES	7500	$\leq$ 3.00	24	X
HD111786		Abt Mor	UVES	12000	4.14	99	X
HD119537	A1V		CAFE	9630	$\leq$ 3.90	13	X
HD130109		Abt Mor	UVES				X
HD137569	B5III		CAFE	12300	$\leq$ 2.80		X
HD141003		Abt Mor	UVES				X
HD141851		Abt Mor	UVES				X
HD148743	A7Ib	post agb	CAFE	7500	$\leq$ 2.90	13	X
HD163506	F2Ibe		CAFE	7300	$\leq$ 2.85	19	X
HD187642		Abt Mor	UVES	7500	$\leq$ 3.00	201	X
HD189763		Abt Mor	UVES				X
HD193495		Abt Mor	UVES	7500	4.40	0	X
HD203875		Abt Mor	UVES	7612	$\leq$ 3.00	101	X
HD205811		Abt Mor	UVES				X
HD24071		Abt Mor	UVES				X
HD27397	F0IV	Gray	UVES	8520	$\leq$ 3.00	89	X
HD36112		SAO7217 A2 simbad: A5IVe	UVES	7560	4.40	64	X
HD60178		Abt Mor	UVES	9644	3.94	15	X
HD60179 (Castor)		Abt Mor	UVES	9661	3.95	19	X
HD73634	A6II	Gray	UVES	8990	$\leq$ 3.00	0	X
HD75063	A1II(III)	Gray	UVES	10240	$\leq$ 3.00	28	X
HD93702		Abt Mor	UVES				X

From this input list, we selected our "standard-sample": If the signal to noise ratio was not high enough, but several spectra were taken in a row ($\approx$ a few nights), we coadded the spectra. In addition, the spectra had to be flat in terms of the normalization, or should be at least easily renormalized. Especially quite a lot UVES spectra ($\approx$ 1/3) showed some ugly jumps, which might be caused by inproper reduction or flatfielding. As UVES can be run in different observing modes which thus

results in gaps in the wavelength coverage, we only downloaded spectra, where the full coverage between 3900 - 8000 Å could be established by combining the spectra. In this way, we received a sample as uniform as possible for our standard test stars. The spectra, where all the above criteria are fulfilled are marked with an "A" in Table 4.1. Also note that especially our standard stars (marked with an asterisk) have been analyzed later in more detail, see Table 4.7 for the final results, which differ by no more than $\Delta T_{\rm eff}$ = 200 K and $\Delta \log(g)$ = 0.2 dex, except for HD39060 and HD176232, for which $\log(g)$ differs by 0.4 dex from these preliminary ones.
Figure 4.2 gives an overview of the preliminary results of the spectral analysis in the spectroscopic Hertzsprung-Russel-diagram. Also shown is the main-sequence band (Ekström et al., 2012). Most strikingly, more than 2/3 of the A stars have surface gravities lower than any main-sequence model. This applies also to our standard stars. Not even half of our standard stars are on the main-sequence, and in principal, most of our standard stars seems to be in evolved evolutionary states, following the used evolutionary tracks by Ekström et al. (2012). The treatment of convection overshoot (see Section 3.1.1) in evolutionary models can change the placement of the MS in the $T_{\rm eff}$-$\log(g)$-diagram significantly. As shown in Napiwotzki et al. (1991), the end of the MS-lifetime of a star can shift to lower surface gravities ($\log(g) \approx 3.4$ dex at $T_{\rm eff} \approx 7000$ K) for older models from Bertelli et al. (1986). If we assume the surface gravity $\log(g)$ to be 0.2 dex lower, however, still half of our standard stars would be off the MS. The gaps on the hot and cool end are selection effects, as the corresponding temperature for main-sequence stars of A9 and A0 are roughly 7500 and 10000 K.

4.4 Photometric analysis

Photometry is the measurement of electromagnetic fluxes of different passbands by using particular filters. Often the ratio of the measured fluxes, so called colors, are used, which have the advantage to cancel out instrumental offsets. Usually the flux is given relative to a reference object, thus in magnitudes. We use a set of those passbands/colors to compare it to low resolution synthetic spectra. These flux calibrated spectra can be also used to obtain the fundamental atmospheric parameters of a star. E.g. the Balmer jump and the slope of the flux in the red part of the spectrum can be used for this purpose. In particular some colors are good to determine physical parameters of the star, e.g. c_1 and m_1 are good indicators for $\log(g)$, at least in the later type stars. Another advantage of this method is that the fitting can be done easily also for fast rotating stars, as the rotation has a negligible effect on the spectral energy distribution.
We used online available photometric data in the way described by Johannes Schaffenroth (2016) and in a not yet published paper by Irrgang et al. (in prep.). Stars that qualify for the sample have to have photometric measurements in all the following passbands and colors: Johnson U-B, B-V and V, Hipparcos Hp, Tacho B_t, V_t, 2MASS J,H,K, WISE W1 and W2, Stroemgren b-y, m1, c1, $H_{\beta AF}$ and Geneva U-B, V-B, B1-B, B2-B, V1-B, G-B. In the first place we also used flux-calibrated UV spectra from IUE binned into box filters (see MSc. thesis of Johannes Schaffenroth) to be included in our fits, but it turned out to give often unreasonable results and thus are not used at all. In Table 4.2 we show the photometric results of our fit to ATLAS12 models. As for the independent parameter determination the value of Z gives often values at the grid border or varying a lot compared to the spectroscopic results, we decided to fix it to the final results of our spectroscopic approach. But as can be seen, the basic

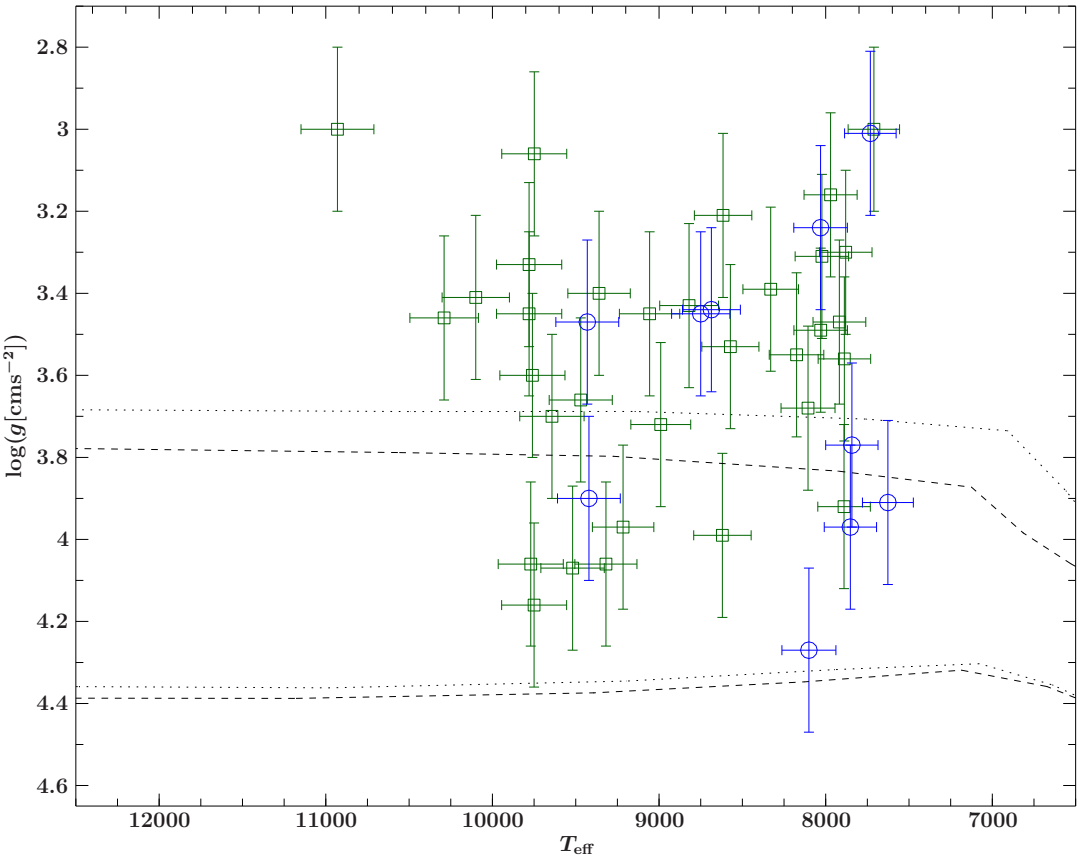

Figure 4.2: Plot of the analyzed spectra listed in Table 4.1. The blue circles corresponds to our "standard sample", where we have also performed a photometric analysis. All other stars with spectral quality "A" and "B" are represented by the green squares. The dashed and dotted lines define the main-sequence, according to models by Ekström et al. (2012), without and with high rotation respectively (rotational velocity in units of the critical rotation velocity: w = 0.3).

Table 4.2: Results of our photometric fitting: on left hand site the results are given for the metallicity z bound to the value derived with our spectroscopic approach ("z=spec"), the uncertainties corresponds to one sigma single parameter confidence levels (see Figure 4.3 as an example). On the right hand side, the metallicity was treated as a free fitting parameter ("z=free"), the errors are in the same order as on the left hand side. Remarkable is the star HD65810, which shows two photometric solutions, which also can be seen in the confidence map (see Figure 4.4).

star	Teff	logg	z=spec	E(B-V)	Teff	logg	z=free	E(B-V)
HD28978	8887^{+146}_{-153}	$3.61^{+0.05}_{-0.06}$	0.14	0.04	8809	3.69	-0.76	0.03
HD39060	7959^{+50}_{-43}	$4.17^{+0.04}_{-0.04}$	0.01	0	7946	4.15	-0.18	0
HD176232	7370^{+139}_{-63}	$3.89^{+0.13}_{-0.08}$	0.09	0.02	7358	3.89	0.14	0.01
HD145689	8189^{+144}_{-61}	$4.22^{+0.08}_{-0.06}$	0.06	0	8185	4.22	0.02	0
HD91375	9070^{+160}_{-199}	$3.62^{+0.07}_{-0.08}$	-0.08	0.03	9217	3.69	-1	0.03
HD65810	9351^{+174}_{-238}	$3.72^{+0.10}_{-0.10}$	-0.16	0	9482	3.57	-1	0.01
HD65810*					8310^{+99}_{-104}	$3.72^{+0.07}_{-0.07}$	-1	0.00
HD204041	7836^{+39}_{-38}	$3.96^{+0.04}_{-0.04}$	-0.83	0	7838	3.95	-1	0
HD189849	7631^{+107}_{-49}	$3.45^{+0.10}_{-0.06}$	0.06	0	7654	3.46	0.11	0
HD114330	9436^{+147}_{-156}	$3.53^{+0.11}_{-0.11}$	0.12	0.01	9466	3.49	0.57	0.02
HD72660	9644^{+81}_{-83}	$3.88^{+0.05}_{-0.05}$	0.38	0.02	9661	3.85	0.76	0.03

parameters are very similar and the results are in most cases very well in agreement with our spectroscopic values. The reddening was left as a free parameter, and was in the order of $E(B-V) \leq 0.04$) in all our test stars. The results are summarized in Table 4.2 and as an example the fit for HD28978 is shown in Figure 4.6, the corresponding confidence map in Figure 4.3. Remarkable is the star HD65810, which shows two photometric solutions, which also can be seen in the confidence map (see Figure 4.5). The solution for the lower temperature is obtained for a free metallicity, while the temperature was restricted to the lower temperatures. The corresponding confidence map can be seen in Figure 4.5.

Unfortunately, we could not find an individual source in the literature, where all of our standard stars were analyzed uniformly, which would have been another very good benchmark to test our method. But as the targets are all quite bright, there were several studies which obtained fundamental parameters using photometric and spectroscopic analysis, which were either obtained by comparison to other standard stars or by fitting to models. Table 4.3 gives an overview of the parameters $T_{\rm eff}$, $\log(g)$ and Z from our standards and summarize the methods employed.

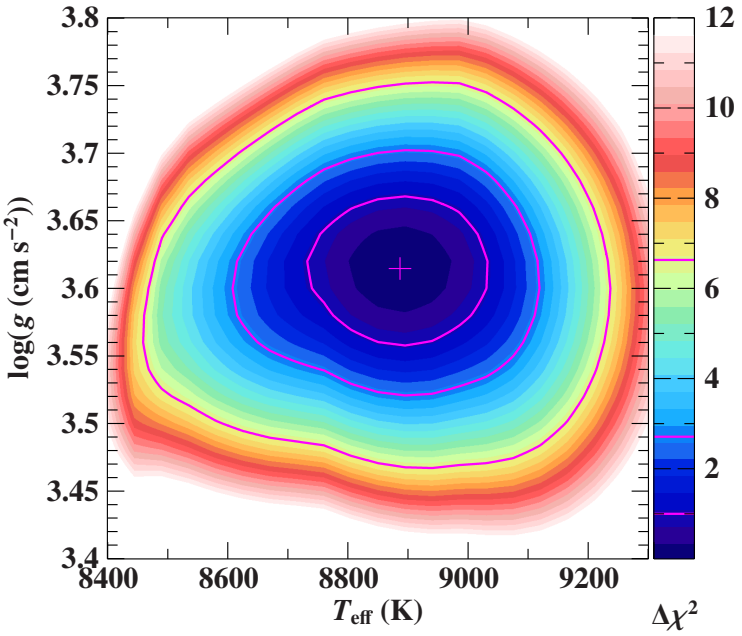

Figure 4.3: Confidence map for HD28978. The magenta lines correspond to the 68, 90 and 99% single parameter confidence level intervals. For the errors given in Table 4.2, for all our stars the 68% confidence level, which corresponds to the one sigma level, is taken.

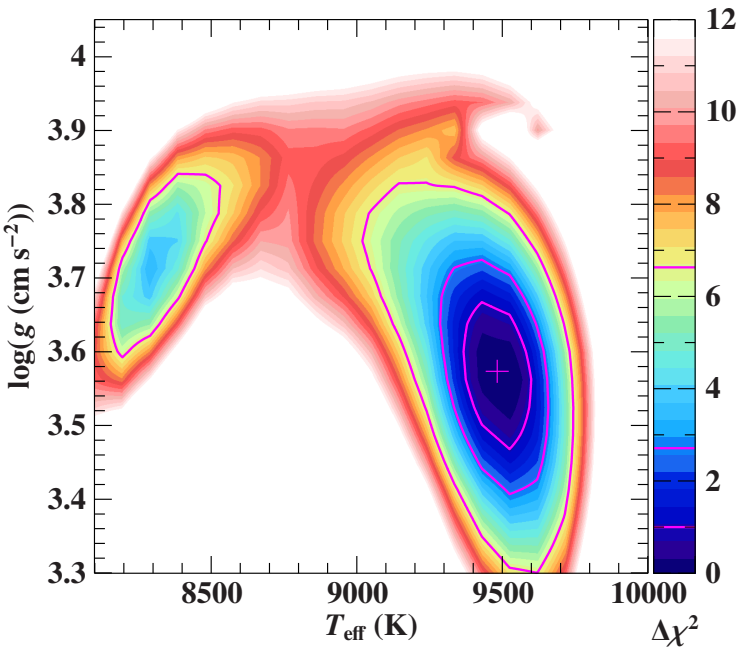

Figure 4.4: Confidence map for HD65810 and a freely fitted metallicity, which shows the twofold solution. The magenta lines correspond to the 68, 90 and 99% single confidence level intervals.

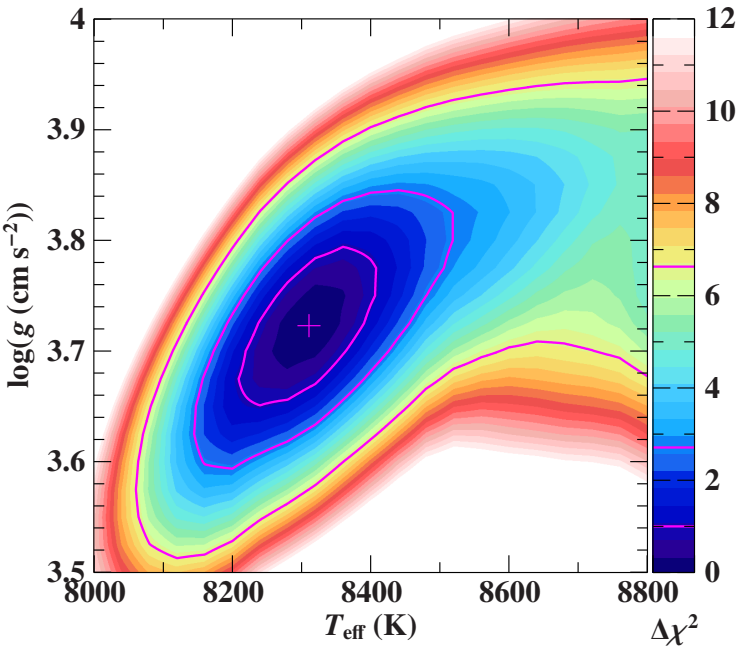

Figure 4.5: Confidence map for HD65810 and the metallicity bound to the spectroscopic result and the temperature restricted to lower values. The magenta lines correspond to the 68, 90 and 99% single confidence level intervals.

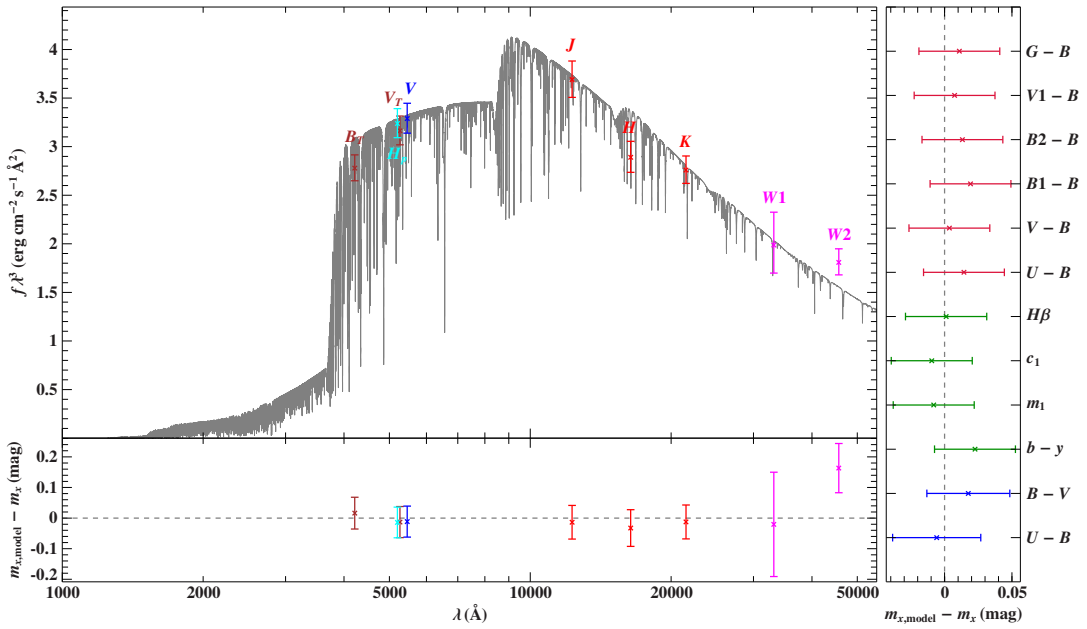

Figure 4.6: Plot of the photometric fitting for HD28978. Left hand upper panel: The fluxes from literature are shown in colors with errorbars, in grey is the best-fit ATLAS12 model spectrum. In the left lower panel, the residuals are given. On the right hand side, the residuals of the colors are shown.

Table 4.3: Summary of the atmospheric parameters, extracted from literature. The fourth column denotes, if the parameters given have been deduced either from spectrospoy (S) or photometry (P). The labels refer for the following references: 1: Paunzen et al. (2001), 2: Grenier et al. (1999), 3: Gray et al. (2006) (spectra and photometry fittet to ATLAS9 models), 4: Abt & Morrell (1995), 5: Houk & Cowley (1975), 6: Houk & Smith-Moore (1988), 7: Lemke (1989) (Strömgren photometry), 8: Prugniel et al. (2011) (comparison to observed spectra of ELODIE library), , 9: Koleva & Vazdekis (2012) (comparison to NGSL library (optical+UV spectra with HST)), 10: Houk & Swift (1999), 11: Koleva & Vazdekis (2012), 12: Lagrange et al. (2010), 13: Cenarro et al. (2007) (MILES library stars, calibrated with compilation of literature, HD176232: ELODIE) , 14: Cotten & Song (2016) (photometric fit against PHOENIX and Kurucz models), 15: Gullikson et al. (2016) (Strömgren photometry or spectra to Kurucz models), 16: Soubiran et al. (2016) (PASTEL catalogue, spectral analysis and asteroseismology), 17: Allende Prieto & Lambert (1999) (Hipparcos parallax, photometry and evolutionary models).

star	alt. name	spectral type(lit)	S/P	T(lit)	logg(lit)	[M/H]	remarks(lit)
HD28978	HR1448	A2IV[1]	P	9200[7]	3.7[7]		metal weak[1]
			S	8864[8]	3.42[8]	-0.26[8]	
			S	8622[9]	3.73[9]	-0.75[9]	
HD39060	beta pic	A6V[3]	S+P	8052[3]	4.15[3]	0.05[3]	debris disc[11],
		A3V[11]					direct imaging planet[12]
HD176232		A7Vp[4]	S	8743[8]	4.47[8]	0.53[8]	(Sr v. strong, Eu strong,
			S	8659[9]	4.47[9]	0.55[9]	Ca+Mg weak, Ca-K has
		A4p(EuCrSr)[14]	S	7701[13]	4.09[13]	0.06[13]	sharp and broad comp.)[4]
HD145689		A3V[5]	P	8317[17]	4.30[17]		high proper motion
		A4IV-V[14]	P	8150[14]			
HD91375		A1V[5]	P	9333[7]	3.65[7]	0.06[7]	
HD65810		A1V[6]	P	8872[15]	3.4[15]		
HD204041		A1Vb[1]	S	8100[16]	4.03[16]	-0.98[16]	high proper motion
HD189849		A4III[8]	S	7804[8]	3.89[8]		alpha2 Cvn type variable
HD114330		A1IVs+[8]	S	9570[8]	3.95[8]	-0.13[8]	
			S	9671[9]	3.57[9]	-0.24[9]	
HD72660		A0V[10]	S	9290[8]	3.39[8]	-0.2[8]	
			P	9692[7]	4.0[7]	0.34[7]	

Table 4.4: Comparison of different fundamental parameters of HD145689 derived in this investigation to published results. For the sources of the literature values, see Table 4.3.

HD145689	spectroscopy	photometry	literature	$\log(g)$ from GAIA-parallax	$\log(g)$ from Hipparcos-parallax
$T_{\rm eff}$	8098	8189^{+144}_{-61}	8150, 8318		
$\log(g)$	4.41	$4.22^{+0.08}_{-0.06}$	–, 4.30	$4.28^{+0.06}_{-0.05}$	$4.28^{+0.05}_{-0.04}$
Z	0.06				
$v \sin i$	102				

4.5 Astrometric Parallaxes: Hipparcos and first results from GAIA

For three of our standard stars GAIA provided new parallax measurements from the first data release, which gives a precise and almost independent test for deriving the surface gravity. We derived $\log(g)$ with

$$\log(g_{\rm parallax}) = \log\left(3.48545889 \cdot 10^{-6} M \cdot \left(\frac{\theta}{\pi}\right)^2\right) \tag{4.1}$$

where π is the parallax in mas, the angular diameter θ in rad which we derive from the photometric fitting, as the quotient of the diameter of the star $2R$ and the distance d: $\theta = 2R/d$, and the stellar mass M in solar masses ($1.70^{+0.08}_{-0.00}$, $1.97^{+0.25}_{-0.19}$ and $2.71^{+0.49}_{-0.12}$ $M_\odot$ for the GAIA parallaxes, respectively), which we obtain from evolutionary tracks from Ekström et al. (2012) with $T_{\rm eff}$ and $\log(g)$ from spectroscopy as input parameters. The results are $\log(g) = 4.28^{+0.06}_{-0.05}$ for HD145689, $\log(g) = 4.21^{+0.08}_{-0.08}$ for HD204041 and $\log(g) = 3.66^{+0.15}_{-0.13}$ for HD28978. We also took the older parallaxes from Hipparcos, which were available for nine of our standard stars for comparison. The given uncertainties in Table 4.6 are derived with the error propagation for the three input parameters M, π and θ. Therefore we took 0.2 dex on $\log(g)$ for deriving the uncertainty of the mass M, the from GAIA respectively Hipparcos given uncertainty on the parallax and the one sigma uncertainty of θ. The three standard stars, for which GAIA parallaxes are available are discussed in more detail in the following.

4.5.1 HD145689

This star is one of the fastest rotating stars in our standard sample ($v \sin i \gtrsim 100 \mathrm{km\,s^{-1}}$), the star was therefore difficult to analyze. As there is no real continuum left due to the fast rotation, the treatment of the renormalization has a strong effect on the fitting result. In the end we ran the automated fitting with a compromise of adjusting some crucial parts by visual inspection. The effective temperature $T_{\rm eff}$ from photometry and spectroscopy are similar and in the same range as previous results from literature. The surface gravity from parallax measurements $\log(g) \approx 4.3$ lies in between our results of our two methods (4.4 and 4.2 respectively) and is thus in perfect agreement within uncertainties of even 0.1 dex (see Table 4.4).

4.5.2 HD204041

This star is moderately rotating ($v \sin i \approx 70 \mathrm{km\,s^{-1}}$), and the spectroscopic fit looks quite well (see also Appendix C). The Balmer lines are perfectly matched from H_ε to H_β, while H_α is a little asymmetric due to normalization issues. The quite strong Ca II - K line is also well matched. Some single lines or blends are too week or too strong,

Table 4.5: Comparison of different fundamental parameters of HD204041 derived in this investigation to published results. For the sources of the literature values, see Table 4.3.

HD204041	spectroscopy	photometry	literature	$\log(g)$ from GAIA-parallax	$\log(g)$ from Hipparcos-parallax
$T_{\rm eff}$	7842	7836^{+39}_{-38}	8100		
$\log(g)$	3.91	$3.96^{+0.04}_{-0.04}$	4.03	$4.21^{+0.08}_{-0.08}$	$4.05^{+0.12}_{-0.15}$
Z	-0.83		-0.98		
$v \sin i$	68				

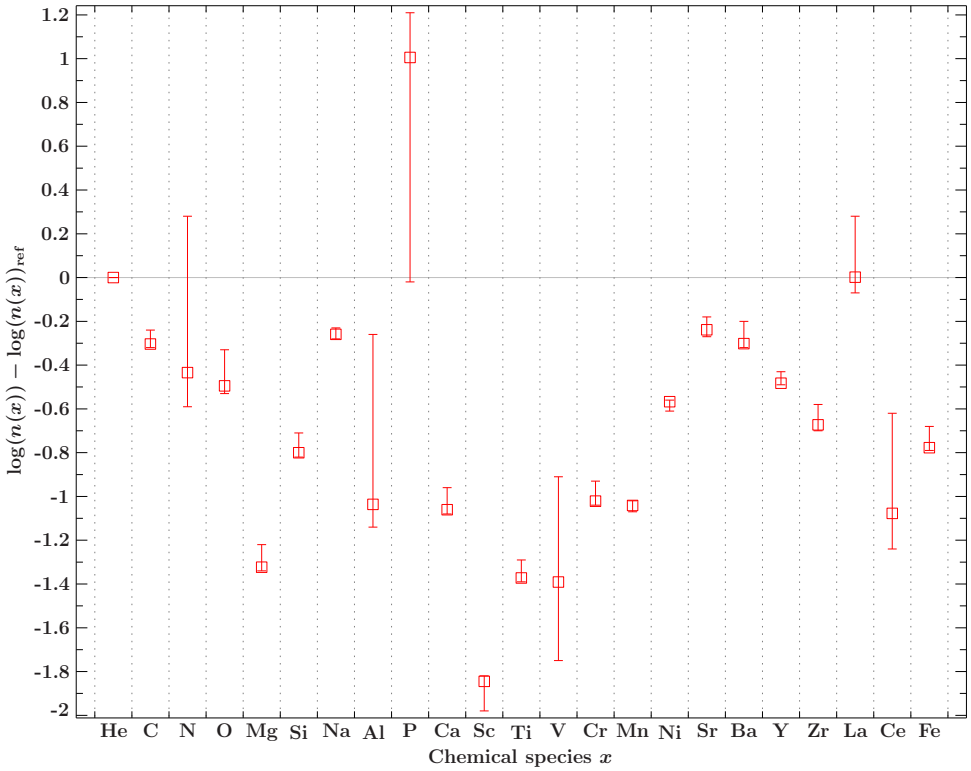

Figure 4.7: Abundance pattern for the metal poor star HD204041. The errors given represent the maximum and minimum value of the automated fitting routine, the square gives the value of the fit with the lowest χ^2.

mainly Fe I + II lines. The metallicity is the lowest in our standard star sample (Z = -0.83), which is together with $T_{\rm eff}$ and $\log(g)$ in agreement with literature values (see Table 4.5), although our results give slightly lower values. Our photometric result is in perfect agreement with spectroscopy and the result from Hipparcos, surprising is the 0.3 dex higher value from the GAIA parallax for the surface gravity. A possible explanation could be that the NLTE-effect on Fe I is much higher than assumed. In Rentzsch-Holm (1996) the effect is only shown for a metallicity of down to Z = -0.5 dex and becomes larger for lower metallicities. In Figure 4.7 the abundance pattern is given, the errors are deduced from the automated fitting routine.

4.5.3 HD28978

Unfortunately this star was the most challenging one among our standard stars for the spectroscopic analysis and we did not end up with a unique result. Some of the spectra are showing a strange behavior, which we cannot explain: sometimes the fitting parameters, especially $T_{\rm eff}$ and $\log(g)$, end up at exact grid points. This

Table 4.6: Comparison of different fundamental parameters of HD28978 derived in this investigation to published results. For the sources of the literature values, see Table 4.3.

HD28978	spectroscopy	photometry	literature	$\log(g)$ from GAIA-parallax	$\log(g)$ from Hipparcos-parallax
$T_{\rm eff}$	8750	8887^{+146}_{-153}	9200, 8864, 8622		
$\log(g)$	3.52	$3.61^{+0.05}_{-0.06}$	3.7, 3.42, 3.73	$3.66^{+0.15}_{-0.13}$	$3.73^{+0.17}_{-0.18}$
Z	0.14		–, -0.26, -0.75		
$v \sin i$	24				

behavior usually can be removed, when starting parameters or fitting algorithms are changed. This is the only object of our analyzed stars, which still ends up on grid points after the whole procedure of fitting with alternating starting parameters.
The first fit with our grid resulted in $T_{\rm eff}$ = 8750 K, $\log(g)$ = 3.45 and Z = 0.14. The fit to the artificial MULTI-spectrum (see Chapter 3.5.1) gave the same temperature and metallicity, but a slightly smaller $\log(g)$ of 0.07 dex. Thus the second calculated MULTI-spectrum (which values we use as the final result) was only changed in $\log(g)$, some minor metal abundances but the same temperature. Most of the fits (with eleven different sets of starting parameters) of this spectrum led mostly to an exactly 250 K hotter temperature. As both temperatures are neighboring grid points, this result is very unreliable. The overall fit looks quite well, but the exact value of $T_{\rm eff}$ cannot be distinguished. Our photometric results ($T_{\rm eff}$ = 8891 K and $\log(g)$ = 3.62), where we just fixed the metallicity from spectroscopy, fits quite well to $\log(g)$ = 3.65 from GAIA, to literature values and is also consistent to the Hipparcos parallax (see Table 4.6).

Table 4.7: Comparison of the results for the standard sample for the basic parameters. For the uncertainty for spectroscopic as well for the photometric $\log(g)$ we assume 0.2 dex and for $T_{\rm eff}$ = 2%. The uncertainty for the stellar mass is achieved by fitting the extrema within the $\log(g)$ and $T_{\rm eff}$ uncertainties to evolutionary tracks. For $\log(g)$ from the parallax, the uncertainty is derived with error propagation for the input parameters: stellar mass $M(\log(g), T_{\rm eff})$, θ from photometry and the parallax.

star	$T_{\rm eff}$ spec	$T_{\rm eff}$ photo	$\log(g)$ spec	$\log(g)$ photo	$\log(g)$ Gaia-parallax	$\log(g)$ Hipparcos-parallax	M stellar mass [$M_\odot$]
HD28978	8750	8887	3.52	3.62	$3.66^{+0.15}_{-0.13}$	$3.73^{+0.17}_{-0.18}$	$2.71^{+0.49}_{-0.12}$
HD145689	8098	8189	4.41	4.22	$4.28^{+0.06}_{-0.05}$	$4.28^{+0.05}_{-0.04}$	$1.70^{+0.08}_{-0.00}$
HD204041	7842	7836	3.91	3.96	$4.21^{+0.08}_{-0.08}$	$4.05^{+0.12}_{-0.15}$	$1.97^{+0.25}_{-0.19}$
HD39060	7869	7959	4.14	4.18		$4.32^{+0.06}_{-0.05}$	$1.76^{+0.16}_{-0.11}$
HD176232	7627	7370	4.09	3.98		$3.84^{+0.10}_{-0.10}$	$1.75^{+0.23}_{-0.14}$
HD91374	8622	9070	3.48	3.62			$2.74^{+0.51}_{-0.34}$
HD65810	8062	9351 (8310)	3.34	3.45		$3.74^{+0.11}_{-0.14}$	$2.62^{+0.40}_{-0.32}$
HD189849	7714	7631	3.02	3.45		$3.80^{+0.12}_{-0.14}$	$3.60^{+0.75}_{-0.59}$
HD114330	9612	9436	3.58	3.55		$3.35^{+0.17}_{-0.20}$	$3.01^{+0.49}_{-0.15}$
HD72660	9351	9644	3.93	3.89		$4.05^{+0.12}_{-0.15}$	$2.49^{+0.35}_{-0.27}$

4.6 Summary of the standard star analyses as a consistency check

We applied the new analysis technique to a set of ten bright well-studied A-type stars. We compared our spectroscopic results to those obtained by photometry and the surface gravity to values obtained by parallax measurements of Hipparcos and GAIA where available (see Table 4.7). The effective temperatures agree well to better than 2%, the surface gravity $\log(g)$ fits quite well within the uncertainties of 0.2 dex for the comparison of spectroscopy and photometry except for HD189849. In the case of HD204041, the photometric result is consistent with the one from spectroscopy, but differs by 0.3 dex, compared with the result derived from the GAIA parallax. Note that the surface gravity determined with the parallax, also is slightly dependent on the derived stellar mass. Therefore we fitted evolutionary tracks (see Figure 4.8) and allowed for uncertainties of $\Delta\log(g) \pm 0.2$ dex to estimate the uncertainty for the stellar mass. The uncertainties given for the parallax-based surface gravities in Table 4.7 are calculated with error propagation for the input parameters mass M, parallax π and angular diameter θ.

The only outlier is HD189849, which would be a giant according to our spectroscopic analysis or a main-sequence star, if the spectroscopic parallax is correct and photometric accuracy is sufficient. In addition this star is also the most chemically peculiar one from our sample, which might be a possible explanation. As in the fitting still some unrecognized line blends might be present, this will of course influence the fitting results. Because the star is quite bright ($4.7^{\rm m}$), there won't be GAIA measurements in the future, unfortunately, GAIA will be limited to ~ 6 mag.

Our method gives consistent results for the $\log(g)$ parameter for nine out of ten of our standard stars, even if we choose a tentative uncertainty on this parameter to be 0.2 dex, when compared to photometry (and parallax measurements, where available) and shows, that we can indeed improve the stellar parameters such as radius and mass, in comparison to estimates from stellar classification.

Although we choose a sample as uniform as possible, a larger sample of stars at the temperature regime typical for A-type stars, of different ages and masses (metallicity and luminosity/surface gravities) would be helpful.

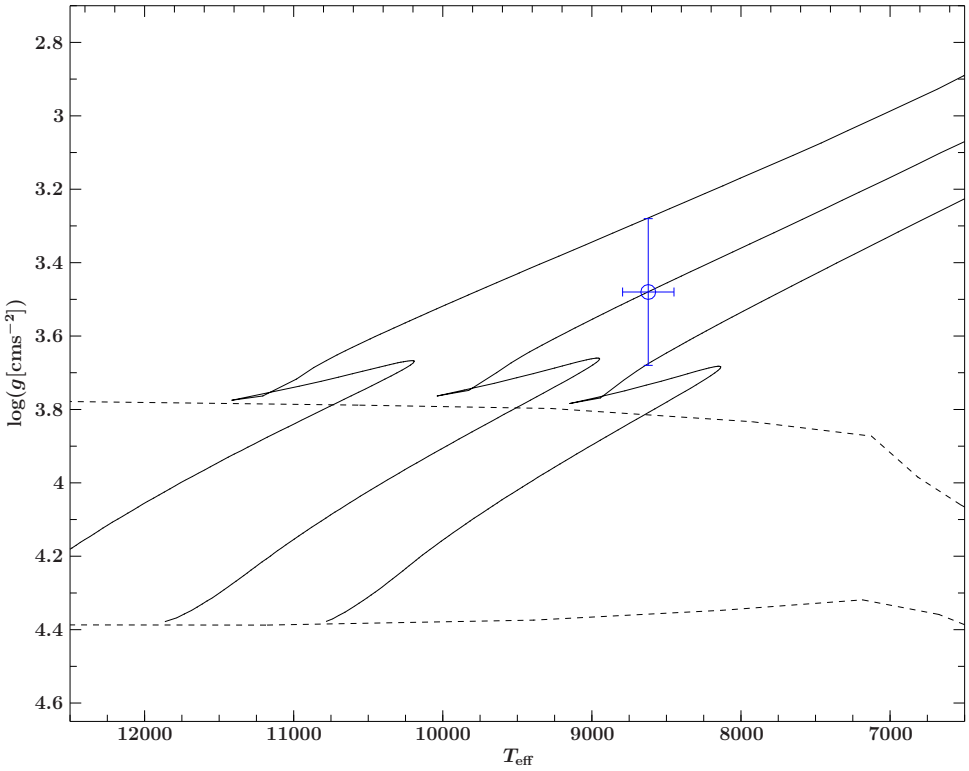

Figure 4.8: Evolutionary tracks (Ekström et al., 2012) in the (T_{eff}, $\log(g)$) plane fitted to our final spectroscopic result of HD91375. The dashed lines mark the beginning and end of the hydrogen burning phase for no rotation. To estimate the uncertainty on the stellar mass, also evolutionary tracks around the best fit of $\log(g) \pm 0.2$ dex were fitted. The tracks plotted here are starting with a rotation of $w = 0.1$ in units of critical rotational velocity.

Chapter 5

WASP 33 (HD15082) - an A-type planet host star revisited

The Wide Angle Search for Planets (WASP) is a ground based search program for planets, under the leadership of astronomical institutes in the UK. Its two robotic observation sites are located at the northern (Roque de los Muchachos Observatory on La Palma) and the southern hemisphere (South African Astronomical Observatory). Each instrumentation consists of eight wide-angle cameras, which continuously monitor the sky to search for signs of planetary transit events in the light curves. From 2006 on the survey has lead to the confirmation of over 100 extrasolar planets, mainly around FGK-type stars.
WASP 33 b was the first confirmed planet in an orbit around an A-type star (Collier Cameron et al., 2010). Due to the fast rotation and the fewer lines of A-type stars, it is not possible to achieve the accuracy for the RV measurements to derive the mass of the companion. Occultations were detected several times with a period of 1.22 days, total duration of 2.72 h and a depth of 0.015 mag in the R- and I-Band. Collier Cameron et al. (2010) used the sophisticated method of the Doppler tomography (see Section 1.1.2), to confirm the planet. Therefore a bunch of time series spectra covering the complete eclipses were taken. These observations were made at the Thüringer Landessternwarte Tautenburg (TLS) with the Coudé Échelle spectrograph of the 2-m Alfred Jensch telescope, the CS23 Échelle spectrograph on the 2.7-m Harlan J. Smith Telescope at McDonald Observatory and with FIES at the NOT in La Palma. For all the single spectra, a single "mean" profile for the spectral lines was produced using the least-squares deconvolution method (LSD). The transiting object produces a distortion in the line profiles of the star. This Rossiter-McLaughlin effect can be used to detect a transiting object and even to give constraints on the obliquity of the system (see Section 1.1.2). A time series of the LSD-profiles of the NOT time series, subtracted by the mean line profile, clearly shows the transit in Fig. 5.1. We used this well studied and quite rapidly rotating star also as a reference, to test our analysis method. From the classification from Grenier et al. (1999) as an A5mA8F4 star (this classification is deduced from comparison to template stars, see Gray et al., 2006), spectral type A5 is deduced from the Ca II - K line, A8 from the Balmer lines and F4 from the metal lines. The "m" refers to the classification as an Am star, which means the star should show an overabundances of iron-group metals like iron and nickel and underabundances of Ca and Sc. Strömgren-photometry by Hauck & Mermilliod (1997) with the calibration by Smalley (1993) yields $T_{\rm eff}$ = 7430 K, $\log(g)$ = 4.21 and $[M/H]$ = 0.21 and the Geneva photometry from the General Catalogue of Photometric

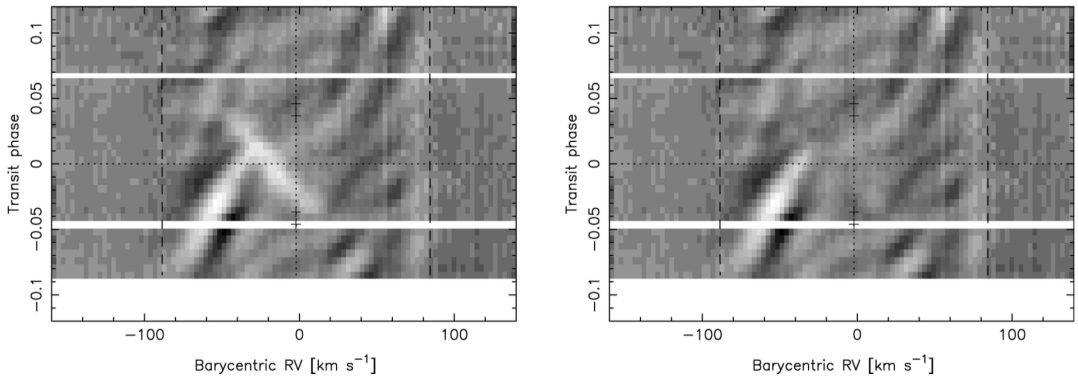

Figure 5.1: The deviations of the LSD profiles of the time series of FIES spectra from the mean line profile in greyscale. Time increases upwards. The vertical lines give the RV (dotted) and $v \sin i$ (dashed), the vertical dotted line gives the central time of the eclipse. Ingress and egress are marked in the middle vertical line with a plus symbol. The planetary signature is the white line going to the upper right in the left plot and is removed in the right, leaving only the non radial pulsations visible. The picture is taken from Collier Cameron et al. (2010).

Data with the calibration of Kunzli et al. (1997): $T_{\rm eff}$ = 7471±63 K, $\log(g)$ = 4.35±0.07 and $[M/H]$ = 0.08±0.09 and Paunzen (2015) obtained also photometrically $T_{\rm eff}$ = 7268 K and $\log(g)$ = 4.298.
For this star, we performed a automated fitting for a spectrum taken with the CAFE spectrograph, which resulted in $T_{\rm eff} = 7938 \pm 159\,K$, $\log(g) = 3.92 \pm 0.2$ dex. The corresponding metal abundance pattern relative to solar can be seen in Figure 5.2. The Am characteristic is only partly matched, iron and nickel are overabundant 0.4 respectively 0.2 dex relative to solar, but calcium and scandium both are consistent with solar values. Carbon, nitrogen and silicon are underabundant. Sodium is solar in this fit, but note that due to interstellar sodium lines, the abundance result is unreliable (see also caption of Table 5.2). All other elements are overabundant, especially the rare earth elements, which are more abundant than in the sun, up to 1.2 dex in the case of lanthanum. So the abundance pattern leads to a classification as an Ap-star, rather than Am.
As for our standard sample (see Section 3.5.1), we included this star in our feasibility test: We calculated a MULTI-spectrum and tried to reproduce the above mentioned results by fitting this artificial spectrum to our model grid. The fit is very close to the expected values and thus we take the model parameters of the MULTI-spectrum as final results. The effective temperature is slightly corrected to $T_{\rm eff}$ = 7918 K, the surface gravity is around 0.1 dex higher ($\log(g)$ = 4.05) and the metallicity is reduced of about 0.1 dex to Z = 0.32. Thus our result of the effective temperature is more than 500 K hotter and our surface gravity up to 0.3 dex lower, than in the case of the photometric results by Paunzen (2015). A reason for this discrepancy could be the difference in metallicity, as we find a more than 0.2 dex higher metal abundance compared to Kunzli et al. (1997).
Our results change the properties of the stars mass and radius, as well of those of the companion. Fits to evolutionary tracks from Ekström et al. (2012) leads to a more massive star with a larger radius. Thus the upper mass limit for the companion and its radius rose, as can be seen in Table 5.1. To quantify how the parameter correction influences the metal abundances, we compare the respective result in Table 5.2.

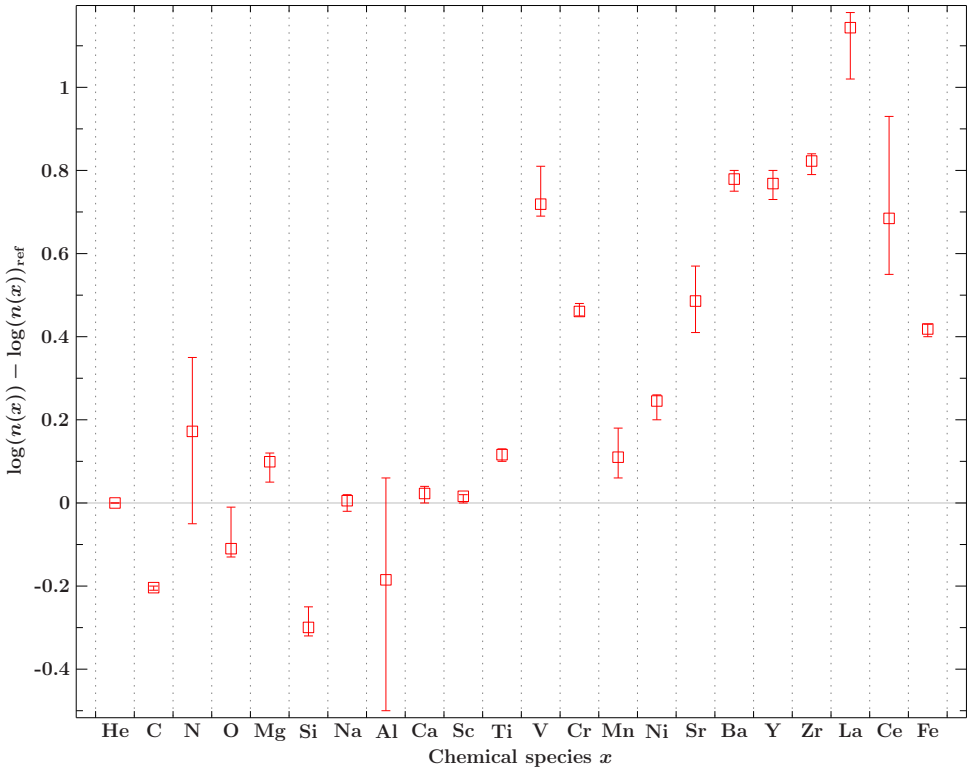

Figure 5.2: Abundance pattern of HD15082, relative to solar. The errors represent the maximum and minimum values of the automated fitting routine, the square corresponds to the best fit.

Table 5.1: Comparison of the stellar and companion mass and radius to previous results from Collier Cameron et al. (2010).

	This work	Collier Cameron et al. (2010)
M [$M_\odot$]	1.85 $\pm$0.15	1.495 $\pm$0.031
R [$R_\odot$]	2.12 $\pm$0.32	1.444 $\pm$0.034
m [$M_{\rm Jup}$]	$<$4.48 $\pm$ 0.24	$<$ 4.1
r [$R_{\rm Jup}$]	2.21 $\pm$0.33	1.497 $\pm$0.045

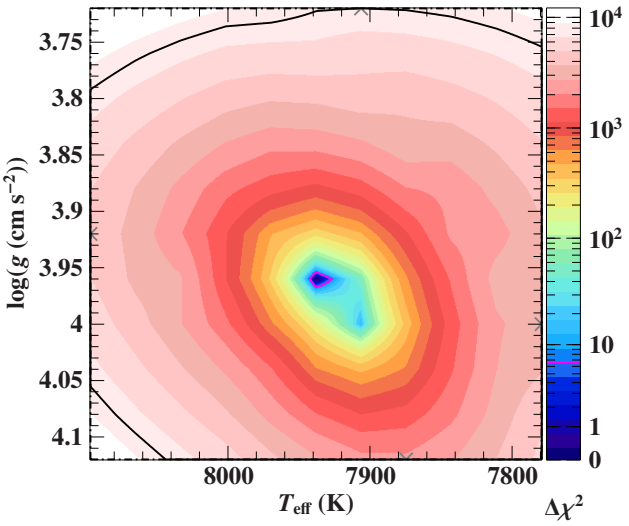

Figure 5.3: Confmap ($T_{\rm eff}$, $\log(g)$) for the CAFE spectrum of WASP33 (HD15082).

The errors for most of the elements is ≤ 0.1 dex, and are thus only slightly smaller than the typical errors, which we get from the confidence maps (see, e.g., Table 7.4), and thus should in principle be considered in the uncertainties. But as we cannot quantify the errors for all our program stars because of lack of time, we just mention this fact here for integrity. On the other hand, the abundances also are correlated to the surface gravity parameter which is affected by the incorrect treatment of the line blends, and so one could also optimistically assume that the deviations shown here are already included in the errors from the confidence map calculations.

Table 5.2: Difference of the parameters from the MULTI-Spectrum fit to our A-grid, which represents the errors introduced by line blends. All abundance deviations are smaller or at the level of the iron deviation of ≈ 0.1 dex. Only cerium deviates in the order of 0.2 dex and sodium is 0.45 dex higher than in the fit to the observed spectrum. This might be caused by interstellar sodium lines, which are not included in our model spectra but cut out and thus not fittet in the observed one. The uncertainties given are derived with help of the confidence map (Figure 5.3), calculated for the fit of the observed data to our A-grid.

parameter	result (MULTI params)	uncertainties	solar	relative to fit to A-grid
$T_{\rm eff}$	7918	± 158		-20
$\log(g)$	4.05	± 0.2		0.13
Z	0.32	$^{+0.11}_{-0.09}$		-0.11
$v \sin i$	78.9	$^{+1.8}_{-0.0}$		
ζ	21.4	$^{+0.9}_{-6.1}$		
$v_{\rm rad}$	1.91	$^{+0.18}_{-0.17}$		
ξ	2	± 0		
C	-3.93	± 0.05	-3.71	-0.02
N	-4.07	$^{+0.8}_{-0.3}$	-4.25	-0.07
O	-3.44	$^{+0.13}_{-0.07}$	-3.28	-0.05
Mg	-4.4	$^{+0.08}_{-0.09}$	-4.48	-0.01
Si	-4.87	$^{+0.09}_{-0.06}$	-4.54	-0.08
Fe	-4.2	$^{+0.11}_{-0.09}$	-4.52	-0.11
Na	-5.31	$^{+0.14}_{-0.13}$	-5.77	0.45
Al	-5.78	$^{+2.0}_{-0.4}$	-5.57	-0.1
Ca	-5.81	$^{+0.09}_{-0.11}$	-5.75	-0.08
Sc	-8.99	± 0.09	-8.99	-0.01
Ti	-7.04	$^{+0.11}_{-0.09}$	-7.13	-0.02
V	-7.39	$^{+0.08}_{-0.16}$	-8.08	-0.1
Cr	-5.99	$^{+0.10}_{-0.09}$	-6.4	-0.06
Mn	-6.49	± 0.15	-6.56	-0.1
Ni	-5.67	$^{+0.16}_{-0.13}$	-5.84	-0.07
Sr	-8.63	$^{+0.14}_{-0.13}$	-9.17	-0.02
Ba	-8.95	$^{+0.13}_{-0.10}$	-9.75	0.01
Y	-9.06	$^{+0.10}_{-0.11}$	-9.79	-0.02
Zr	-8.61	$^{+0.11}_{-0.15}$	-9.41	-0.04
La	-9.73	$^{+0.15}_{-0.09}$	-10.89	-0.01
Ce	-9.74	$^{+0.09}_{-0.11}$	-10.42	-0.2

Table 5.3: Synthetic spectral lines stronger than 5% in the best fit (of the MULTI-spectrum) for WASP33.

element	ion	pixels	element	ion	pixels
H	I	30423	Ti	I	912
C	I	317	Ti	II	1617
N	I	34	V	I	505
O	I	212	V	II	1147
Mg	I	305	Cr	I	2612
Mg	II	257	Cr	II	1908
Si	II	103	Mn	I	770
Fe	II	1134	Mn	II	342
Fe	III	140	Ni	I	2082
Na	I	250	Ni	II	414
Al	I	72	Sr	II	62
Al	II	12	Ba	II	71
Ca	I	531	Y	II	404
Ca	II	493	Zr	II	826
Sc	I	7	Fe1	I	16212
Sc	II	282	La	II	790
			Ce	II	2347

Chapter 6

The EL CVn star J0247

The eclipsing binary 1SWASP J024743.37-251549.2 (J0247) was detected in the archive of the WASP survey by Maxted et al. (2011) during the search for subdwarf stars. They found a deep eclipse in the light curves with a period of 0.6678 days accompanied with a smaller eclipse. It turned out to be an A-type star with a hotter companion due to the flat shape of the deeper eclipse and steep ingress and egress. The companion is far too small to be a main-sequence star. Maxted et al. (2014) suggested that it is a very low-mass evolved star ($0.25\,M_{\odot}$), which could be produced by a red giant star, which recently transferred mass via Roche lobe overflow to its MS (A-type) companion. Evolutionary models of the binary, including thermal and chemical diffusion of elements and gravitational settling, predict that the B-type companion now is burning hydrogen in a thick shell and will evolve to a low mass He-WD, as soon as the hydrogen fuel in its shell is depleted.
The discovery of this kind of eclipsing binary was the first of 17 similar systems and has led to the definition of a new type of binaries, named after the brightest prototype EL CVn (Maxted et al., 2014).
In addition to the variations of the flux due to eclipses, both stars are pulsating (Maxted et al., 2013). While the A-type stars is a "normal", metal-poor $\delta-$Scuti star with periods of about half an hour, the B-type companion shows periods in the order of some minutes. The derived temperature and luminosity are quite off the usual instability strip for such pulsations. However, at lower hydrogen abundances, instability-"islands" appear in pulsation models (Jeffery & Saio, 2013) and would be best matched with models at very hydrogen deficient envelopes with $X = 0.002$. As evolutionary models are contradictory to this extreme low value, the best match is found at a hydrogen poor envelope of $X = 0.25$, which is still consistent with the atmospheric parameters and pulsation frequencies found by Maxted et al. (2011, 2014).

6.1 J0247 B

Within about six weeks, 58 spectra were taken by Maxted with UVES at the VLT in the end of 2011. As the B-type companion is completely occulted by the A star, it was possible to measure the spectrum of the A star during the occultation of the companion. The spectrum of the companion was then disentangled from the composite spectra, taken outside of the eclipse by considering the respective radial velocity shifts. Maxted provided us with the disentangled spectra of both stars. A close inspection of the data showed sinosoidal variations of the continuum, which might be due to insufficient flat fielding of the Echelle orders. Since the coverage of the Echelle or-

ders is increasing with wavelength, an increase of the periodicity might be expected. In order to find an objective way to rectify the spectrum, we cut out the cores of the Balmer lines and fitted a sinosoidal function (SF) to the continuum (see Figure 6.1). We divided the spectrum in three parts with cuts at 5000 Å and 7000 Å, where we multiplied a synthetic spectrum ($T_{\rm eff}$=10500 K, $\log(g)$=4.4, $\log[X/X_\odot] = -0.9$) with the SF. We included a monotonic increase of the period of the sinosoid, a constant amplitude and an offset in phase and left these as free fitting parameters for each of the spectral regions, while the other spectral parameters were kept fixed. After the fit we applied the SF to the whole spectrum, which removed the artifacts and allowed us to start the analysis. In a later step of the fitting process the synthetic spectrum is additionally corrected for a residual linear slope.

6.1.1 Spectral analysis for a fixed surface gravity

As there is a strong correlation between effective temperature and surface gravity, we decided to take the well constrained value of $\log(g)$ from Maxted et al. (2013). They fittet light curve models to data obtained with the ULTRACAM instrument at the NTT, which take into account the eclipses and ellipsoidal deformation of the companion. The fit results for a fixed orbital period P, is the surface brightness ratio J_2, the stellar radius $r_{\rm A}$ of J0247 A in units of the system separation a, the ratio of the stellar radii ($r_{\rm B}/r_{\rm A}$), the mid-eclipse time T_0 and the impact parameter $b = \cos(i)/(r_{\rm A}+r_{\rm B})$, where i is the inclination of the orbit. The time series of UVES spectra allowed the radial velocity curves of both companions to be determined (see Figure 6.2). The results are the masses of the two stars $M_{\rm A} = 1.345 \pm 0.007\,{\rm M}_\odot$ and $M_{\rm B} = 0.186 \pm 0.002\,{\rm M}_\odot$, radii, $R_{\rm A} = 1.697 \pm 0.011\,{\rm R}_\odot$ and $R_{\rm B} = 0.368 \pm 0.005\,{\rm R}_\odot$, from which their surface gravities can be derived with high accuracy: $\log(g_{\rm A}) = 4.111 \pm 0.006$ and $\log(g_{\rm B}) = 4.567 \pm 0.011$.

For the analysis of the spectrum of the B-type companion, the best fit was found by applying the chi-square-method by alternating different fitting algorithms, such as simplex, mpfit and powell (similar to the method explained in Section 3.2.2). Therefore, we restricted $\log(g)$ to the uncertainty interval of the surface gravity $\log(g) = 4.576 \pm 0.011$. In Table 6.2 we list the strongest lines (less than 95% of the continuum flux in the core), which can be identified in our synthetic spectrum for the best fit. Lines which are not visible in the observed spectrum are listed in parenthesis. For a more realistic uncertainty estimation we have to evaluate the systematical uncertainties. Therefore we calculate a confidence map (see Figure 6.3) for $T_{\rm eff}$ and $\log(g)$, where we assume a systematical uncertainty for the effective temperature of 2% ($\approx$ 214K) and for $\log(g)$ of 0.011 dex, as given by Maxted et al. (2013). For the other parameters, we take the largest deviations from the best fit value, which were taken from the calculation of the confidence map, as systematical uncertainties. The final uncertainty is the square root of the sum of the squares of the systematical and the statistical errors, which is strongly dominated by the systematics.

The results are given in Table 6.1. Remarkable is the rather high helium abundance of $\log(X_{\rm He}) = -0.661^{+0.165}_{-0.217}$. To demonstrate the sensitivity of the helium lines with respect to the abundance, we show in Figure 6.7 a comparison of the strongest helium lines to a synthetic model at solar abundances. It is obvious that the higher abundance fits much better, except for the line at 5875 Å. At 4471 Å there might be a blend with an unidentified line.

From asteroseismology Jeffery & Saio (2013) predicted a mass fraction for helium between 0.7 and 0.8 in the zone driving the oscillations, which is even higher than our

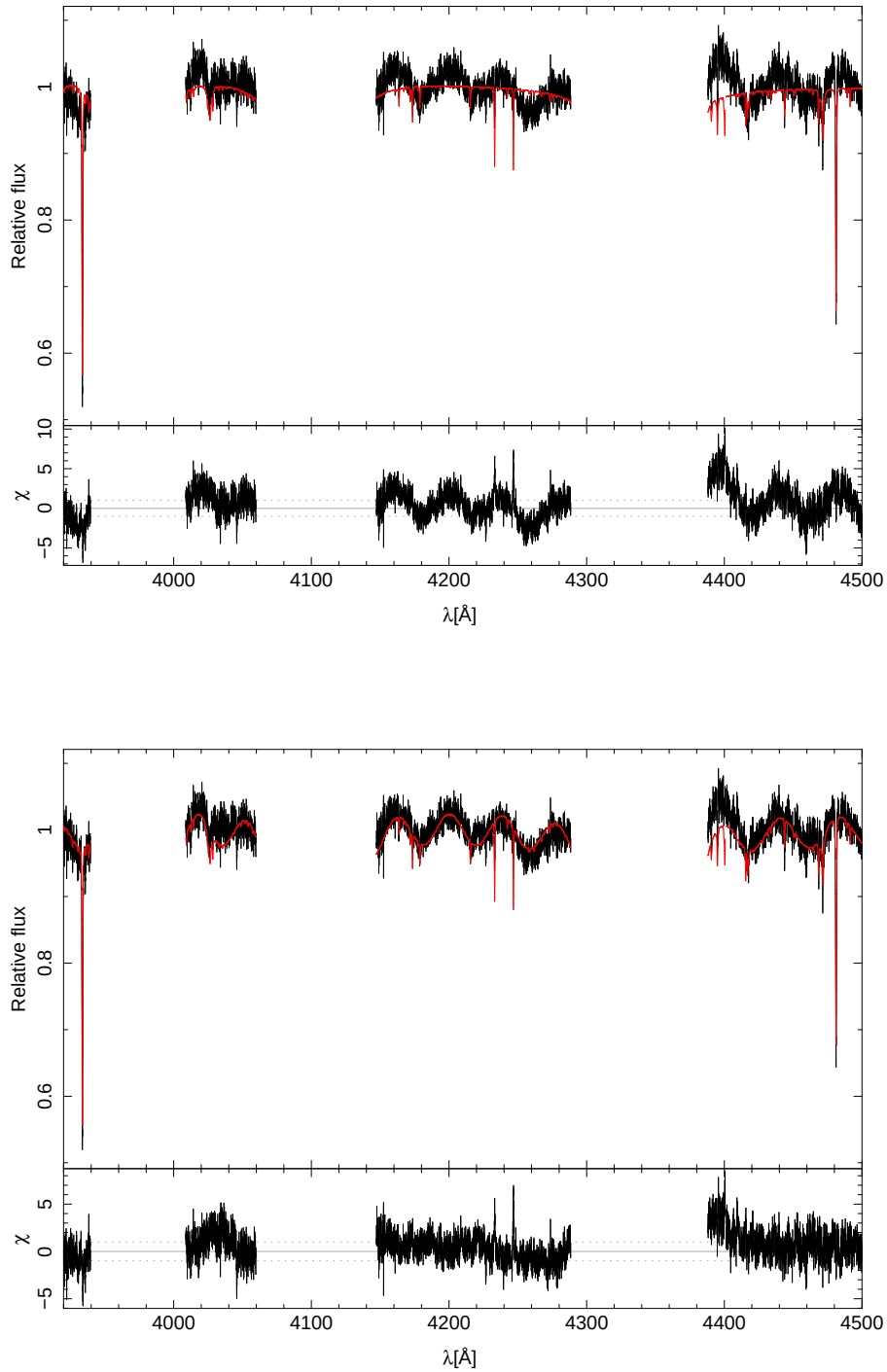

Figure 6.1: Upper panel: sinosoidal continuum variation in the residuals of a model spectrum with $T_{\rm eff}$ = 10500 K, $\log(g)$ = 4.4 and $\log[X/X_{\odot}]$ = −0.9. Lower panel: fit of the sinosoidal function to the continuum between the the Balmer lines.

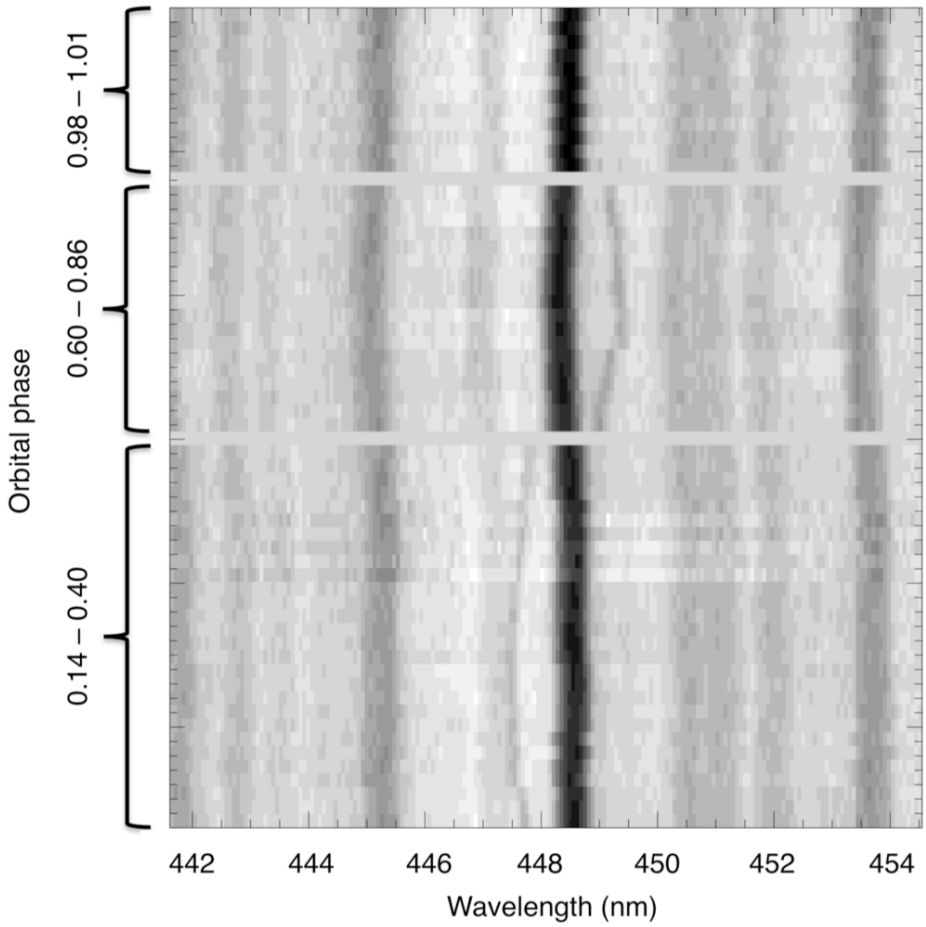

Figure 6.2: Time series of UVES spectra obtained for J0247-25 in grey-scale around the Mg II line at 4481 . The broad black line is from the faster rotating A-type star (a blend of Mg II with some Fe I lines) and the thinner Mg II line in anti phase stems from the faint B-type star companion. Spectral lines of the A star are broadened by rotation. Spectra are plotted in phase order and gaps have been inserted between different phase ranges as indicated. The upper 12 spectra were taken during the total eclipse of the B-star companion (from Maxted et al. (2013), supplementary material).

Table 6.1: Results for the gravity of J0247 B beeing fixed (left columns) and varied (right columns). The uncertainties are adopted from the confidence maps, which is shown for the fixed $\log(g)$ in Figure 6.3 and for the freely fitted $\log(g)$ in Figure 6.10.

parameter	result(fixed)	uncert.	result(free)	uncert.
$T_{\rm eff}$	10677	± 216	10870	± 230
$\log(g)$	4.582	± 0.012	4.70	$^{+0.11}_{-0.12}$
$v \sin i$	26	$^{+3.9}_{-1.7}$	27.33	$^{+2.41}_{-3.47}$
ζ	26.77	$^{+4.36}_{-4.08}$	23.3	$^{+6.0}_{-1.4}$
$v_{\rm rad}$	66.18	$^{+0.49}_{-0.52}$	66.18	$^{+0.53}_{-0.56}$
He	-0.66	$^{+0.17}_{-0.22}$	-0.87	$^{+0.19}_{-0.27}$
O	-4.44	$^{+0.05}_{-0.05}$	-4.40	$^{+0.08}_{-0.09}$
Mg	-5.34	$^{+0.07}_{-0.07}$	-5.29	± 0.09
Si	-5.34	$^{+0.11}_{-0.13}$	-5.31	$^{+0.11}_{-0.13}$
Fe	-5.48	$^{+0.04}_{-0.06}$	-5.46	$^{+0.09}_{-0.08}$
Ca	-6.6	$^{+0.09}_{-0.10}$	-6.50	± 0.13
Ti	-7.65	$^{+0.05}_{-0.05}$	-7.52	$^{+0.12}_{-0.11}$

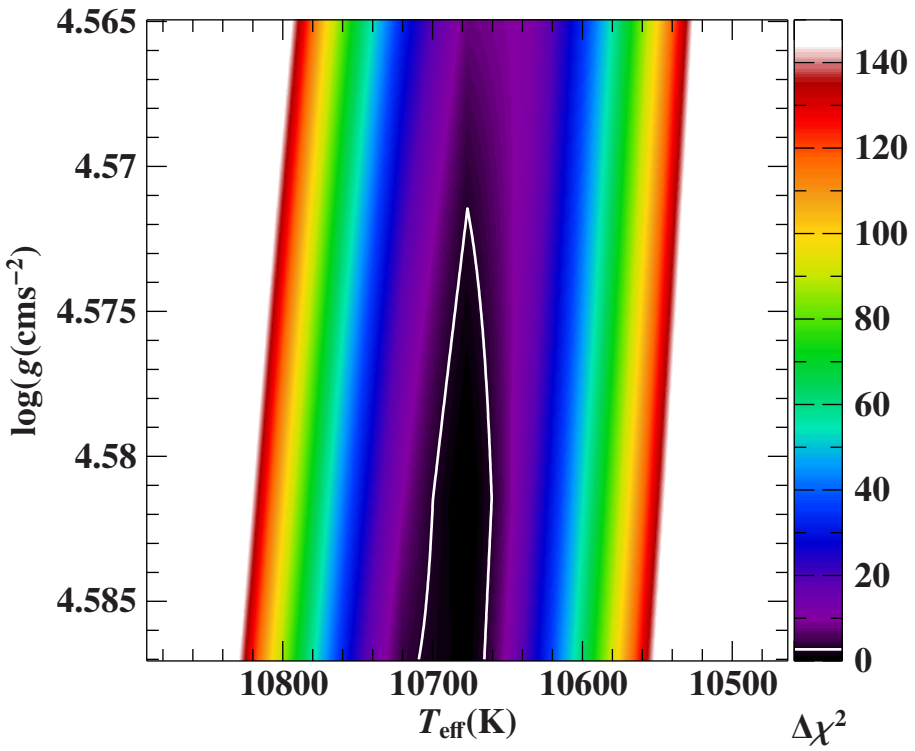

Figure 6.3: Confidence map calculated for $\log(g) = 4.576 \pm 0.011$ and the best fit for $T_{\rm eff} = 10677 \pm 2\% \approx 214$K. Within this parameter range we take the largest deviations for each fittet parameter and take these as systematic errors. The white contour marks a $\Delta\chi^2$ of 3 ($\approx$ 90% confidence level).

Table 6.2: List of lines in the synthetic spectrum, which have, in their unbroadened appearance, less than 95% flux in the core. Parenthesized lines are not visible in the observations due to gaps arising from the instrumental setup.

Ca II 3933.66	(Fe II 4555.89)	Fe III 4178.84	H I 3970.07	(N I 7468.31)	Ti I 4301.93	Ti II 4399.77
Ca II 3968.47	(Fe II 4583.84)	Fe III 4178.85	H I 4101.73	O I 7771.94	Ti II 3900.55	Ti II 4417.72
Fe II 4173.46	(Fe II 4629.34)	Fe III 4508.32	H I 4340.46	O I 7774.17	Ti II 3913.47	Ti II 4443.79
Fe II 4178.86	(Fe II 4923.93)	(Fe III 5169.01)	(H I 4861.32)	O I 7775.39	Ti II 4012.39	Ti II 4450.48
Fe II 4233.17	(Fe II 5018.44)	Fe I 4045.81	H I 6562.80	Si II 4128.07	Ti II 4028.34	Ti II 4464.45
Fe II 4303.18	(Fe II 5169.03)	Fe I 4063.59	He I 4471.48	Si II 4130.89	Ti II 4163.65	Ti II 4468.51
Fe II 4351.77	(Fe II 5197.58)	Fe I 4063.63	He I 5875.65	(Si II 5041.03)	Ti II 4171.91	Ti II 4501.27
Fe II 4385.39	(Fe II 5234.62)	Fe I 4071.74	(Mg I 5167.32)	(Si II 5055.98)	Ti II 4290.22	(Ti II 4533.97)
Fe II 4416.83	(Fe II 5276.00)	Fe I 4271.76	(Mg I 5172.68)	Si II 6347.10	Ti II 4294.10	(Ti II 4549.62)
Fe II 4491.40	(Fe II 5316.61)	Fe I 4307.90	(Mg I 5183.60)	Si II 6371.36	Ti II 4300.05	(Ti II 4563.76)
Fe II 4508.25		Fe I 4325.76	Mg II 4481.13		Ti II 4301.91	(Ti II 4571.97)
Fe II 4515.34		Fe I 4383.54	Mg II 4481.15		Ti II 4307.86	
(Fe II 4520.22)		Fe I 4404.75	Mg II 4481.32		Ti II 4312.86	
(Fe II 4522.63)			Mg II 7877.05		Ti II 4314.98	
(Fe II 4549.47)			Mg II 7896.37		Ti II 4395.03	

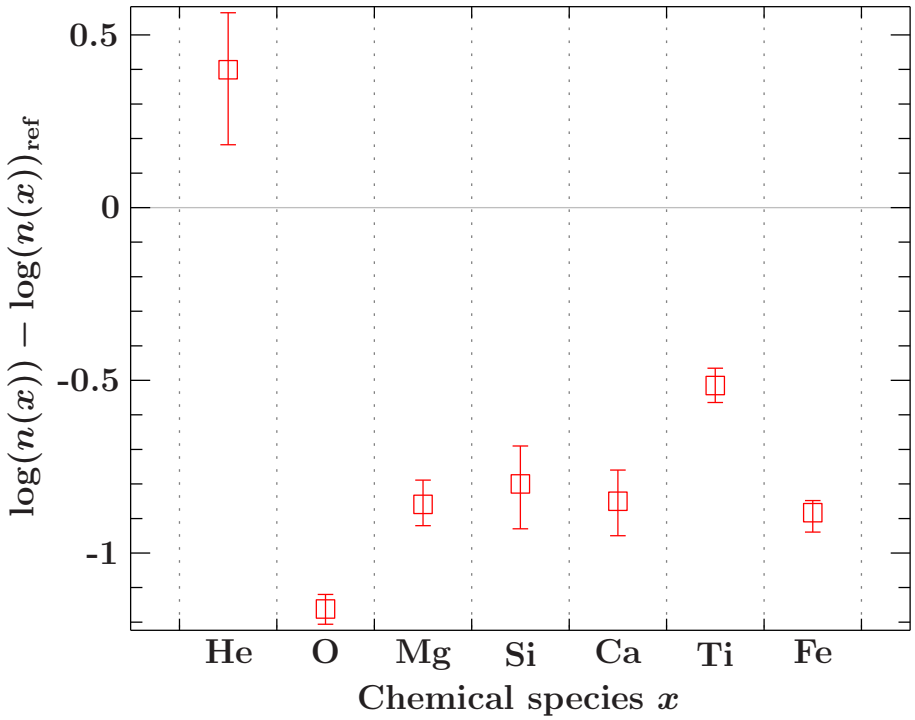

Figure 6.4: Abundances of J0247 B, relative to solar values. Calcium, magnesium and silicon scale perfectly with the iron abundance, oxygen is even less abundant. Titanium shows a small overabundance relative to the other elements.

spectroscopic result. Whereas the surface abundance is predicted by evolution models to be Y = 0.5-0.7, because gravitational settling of helium can decrease its abundance. Our result corresponds to a helium mass fraction at the surface of $Y = 0.52^{+0.14}_{-0.02}$, which is consistent with that range.
Maxted et al. (2013) supposed an enhanced alpha-element abundance, which we could not confirm (see Figure 6.4). Their atmospheric parameters for the A-star companion only allow a mass fraction for metals of Z = 0.004 – 0.019. Our spectroscopic result for J0247 B of $Z = 0.0046^{+0.0010}_{-0.0008}$ lies at the lower end of that range. The reason for that could be that Maxted et al. (2013) took helium abundances up to Y = 0.4. As we measured a higher helium abundance by 0.1 dex (corresponding to a 25% higher mass fraction), which might explain that we end up at the lower border of that range for the relative metal abundance. To demonstrate the need for NLTE calculations, we checked the difference to LTE. While departures from LTE are small for Mg, Ca, Ti and Fe lines, strong effects can be seen in some important O I and Si II lines (see Figure 6.8), neglecting these would have given spuriously higher abundances for those elements.

6.1.2 Spectral analysis for an unconstraint surface gravity

In order to obtain independent results for the star, we also fitted the spectrum without fixing $\log(g)$. The results are listed in Table 6.1. The elemental abundances are still consistent with the previous ones within the mutual errors. However, the gravity has increased to $\log(g) = 4.70^{+0.11}_{-0.23}$. Only the helium abundance is not as high as for the fixed surface gravity, while the metal abundances slightly rose. A comparison of

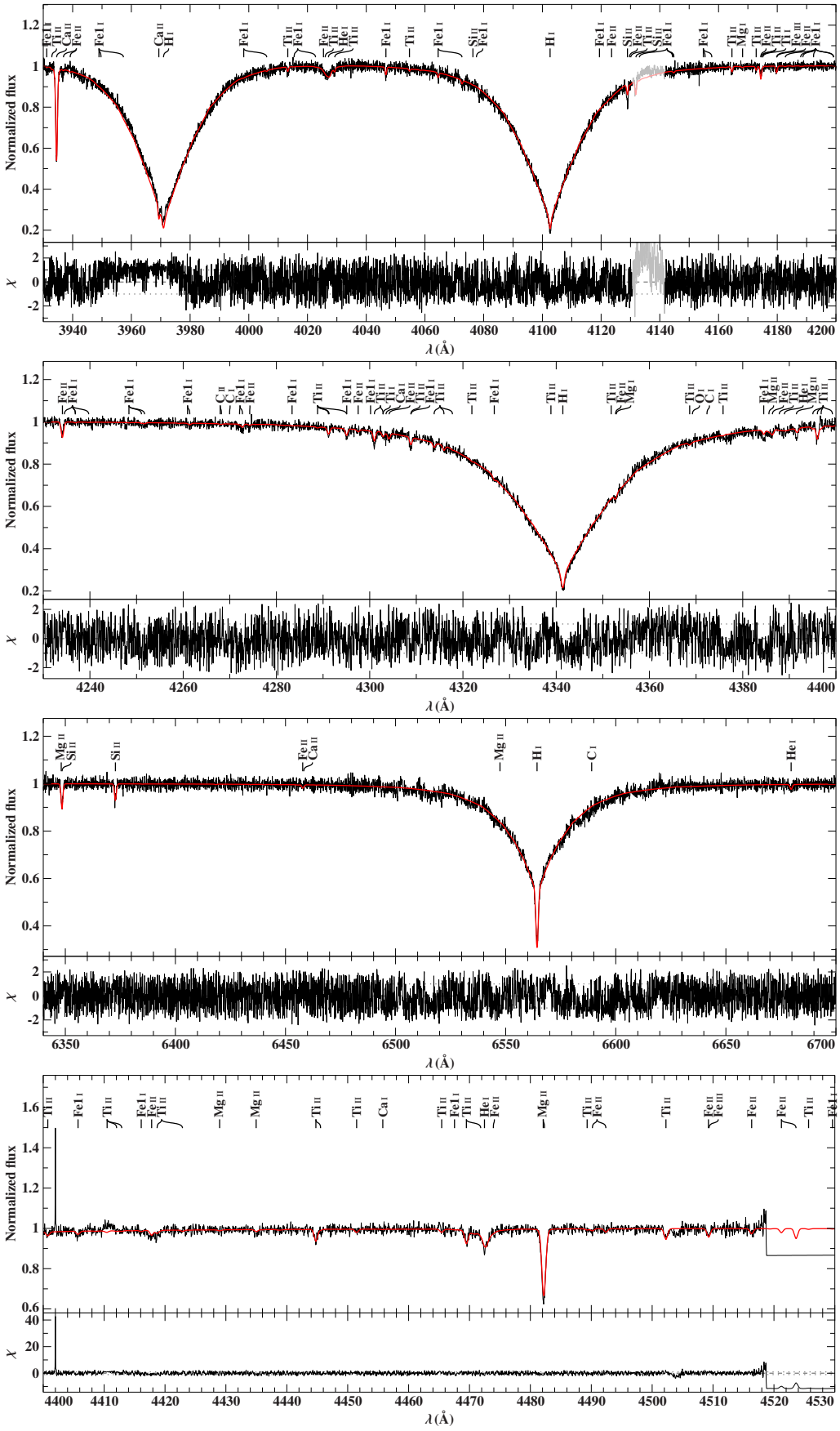

Figure 6.5: Fit to the UVES spectrum of J0247 B: $H_\varepsilon, H_\delta, H_\gamma$ and H_α, some weaker metal lines and Mg II.

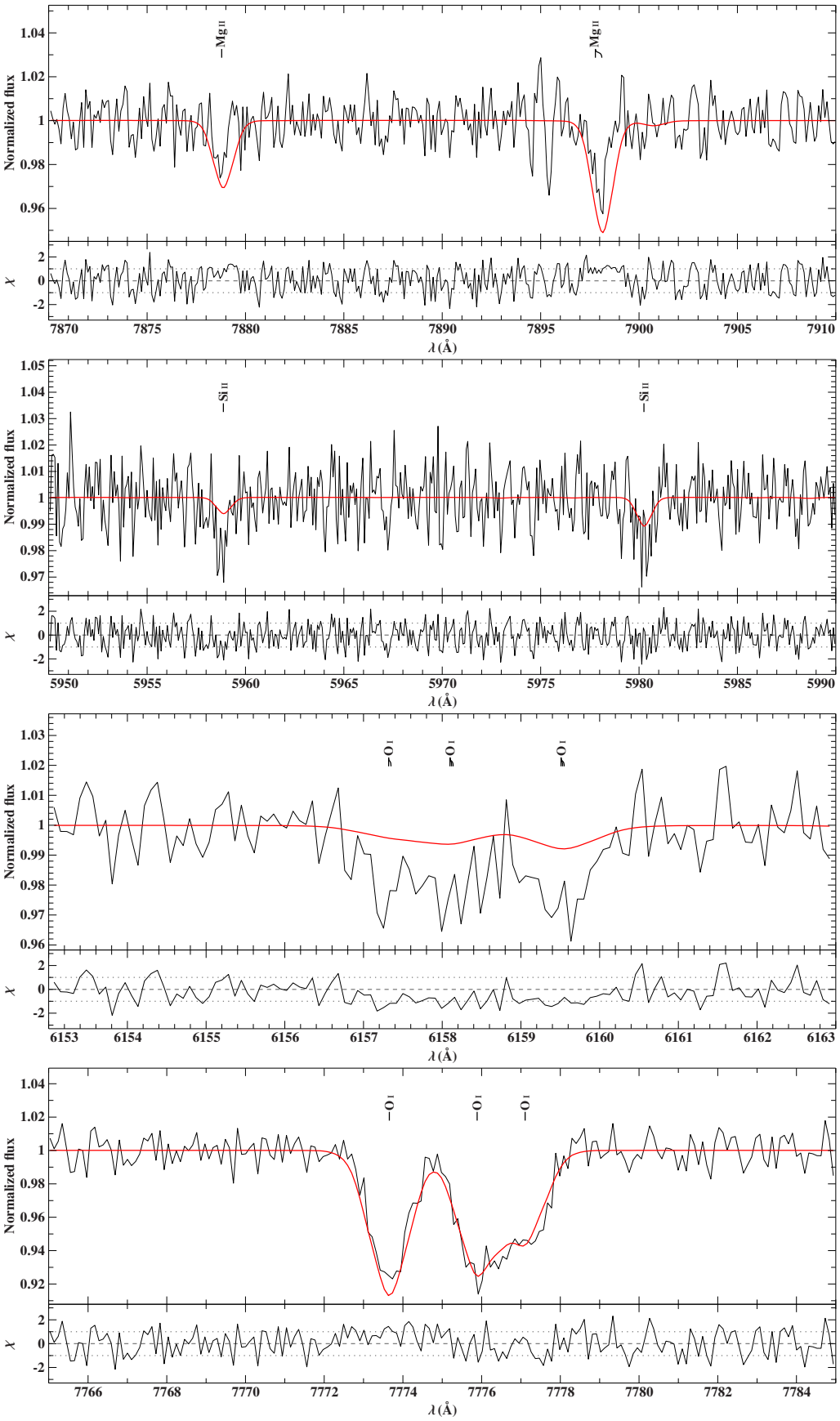

Figure 6.6: Same as Figure 6.5: Mg II doublet, Si II and the O I triplet.

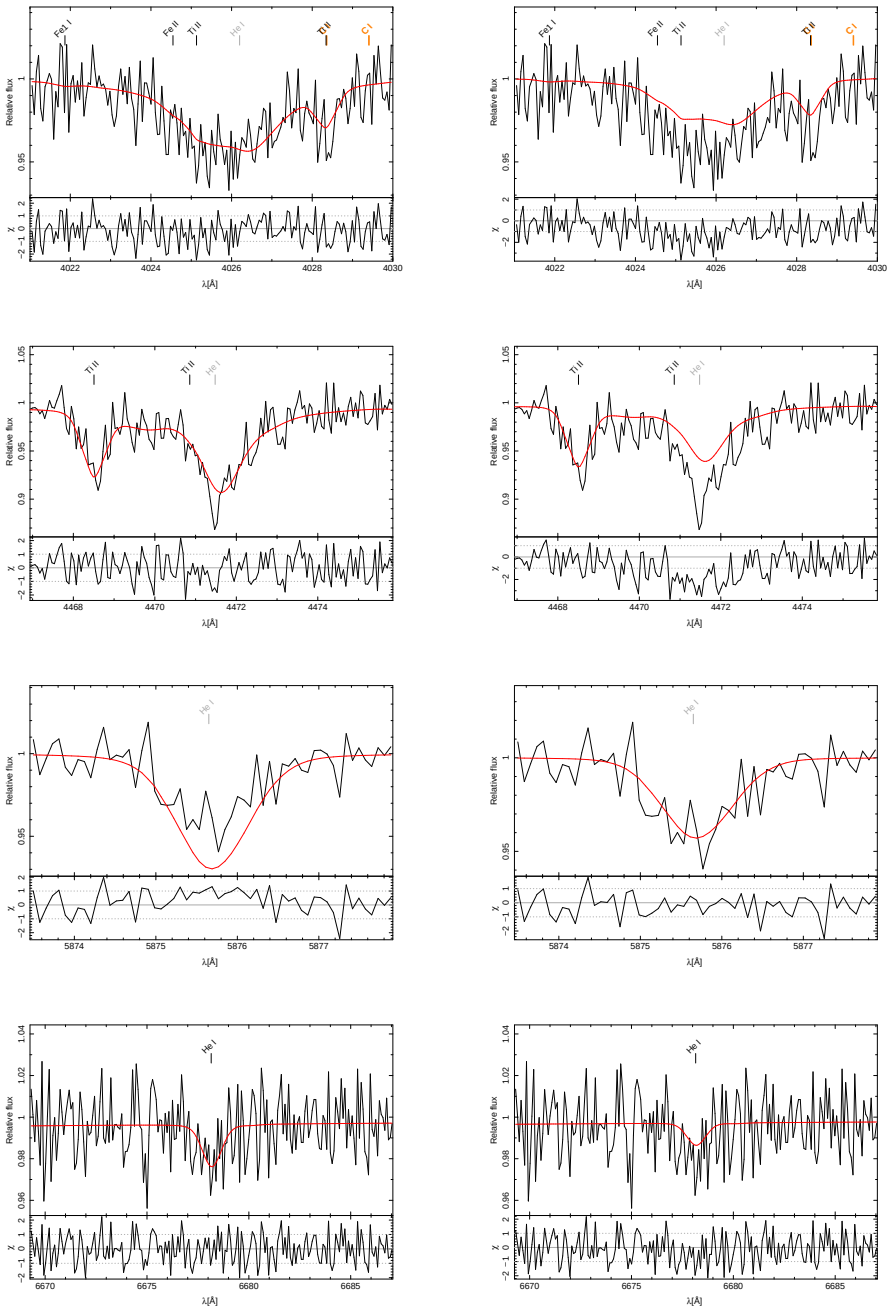

Figure 6.7: Comparison of He lines in the UVES spectrum of J0247 B of synthetic spectra for [He/H] = -0.65 dex (left) and [He/H] = -1.06 dex ("solar", right). The higher abundance (left hand side) fits better, except of 5875Å.

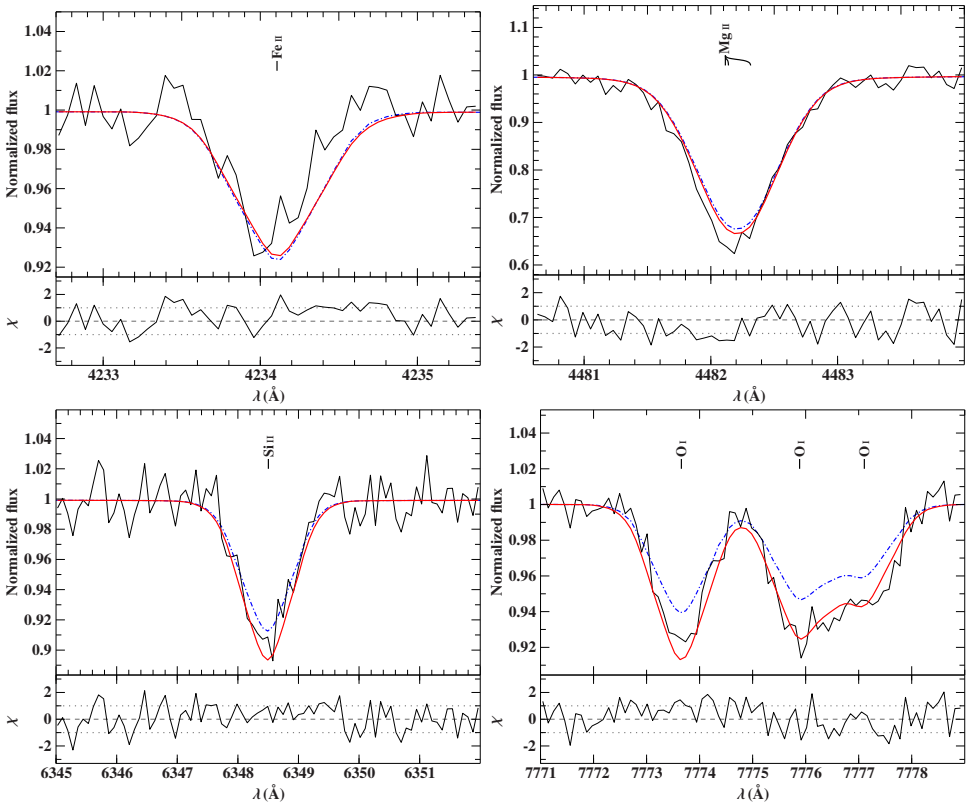

Figure 6.8: NLTE effects for J0247 B: Solid black line: observed UVES spectrum. Solid, red line: Synthetic model spectra from NLTE calculation. Blue, dashed dotted line: Synthetic spectra from LTE calculation. The abundances are in both cases: log(n(Fe)) = -5.48, log(n(Mg)) = -5.34, log(n(Si)) = -5.34, log(n(O)) = -4.44.
The residuals shown arise from comparison of the observed spectrum with the NLTE synthesis.

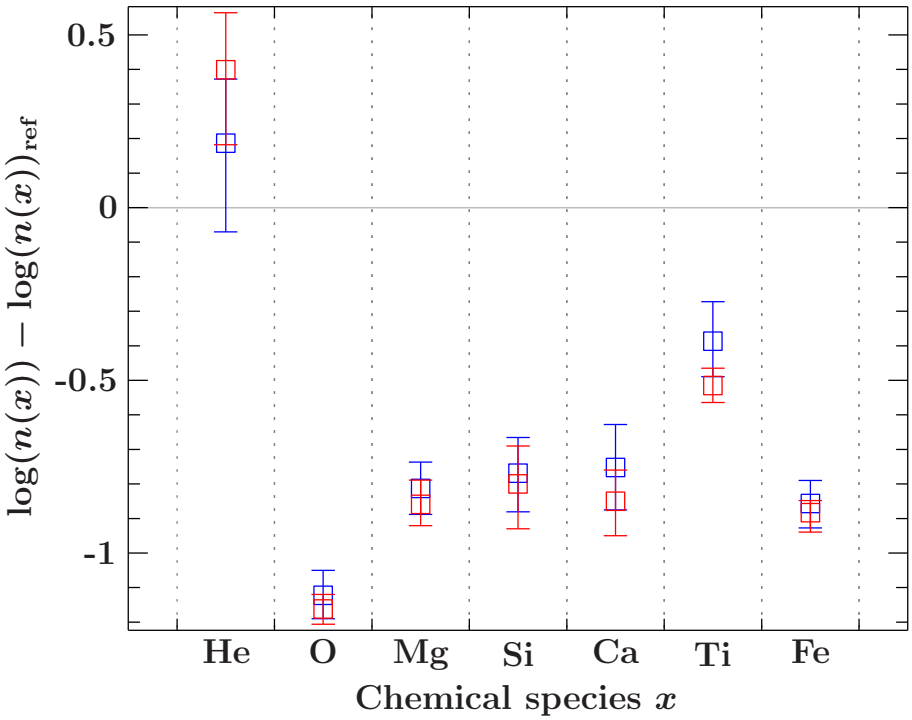

Figure 6.9: Abundances, relative to solar: In red are the results from the fixed $\log(g)$ (≈ 4.58), in blue from the fit with free $\log(g)$(≈ 4.7).

the derived metal abundances are shown in Figure 6.9. The corresponding confidence map (see Figure 6.10) has been calculated for ± 0.1 dex in $\log(g)$ and $\pm 2\%$ around the best fit, the errors are given in the same way as explained in the previous section for the fixed $\log(g)$.
This would lead to smaller radii of the two stars, also their luminosity would become smaller and thus their positions in the HR diagram would change, which would indeed fit better to the proposed evolutionary tracks shown by Maxted et al. (2013).
Our revised results are recently found to be in perfect match to asteroseismic investigations (Istrate et al., 2017).

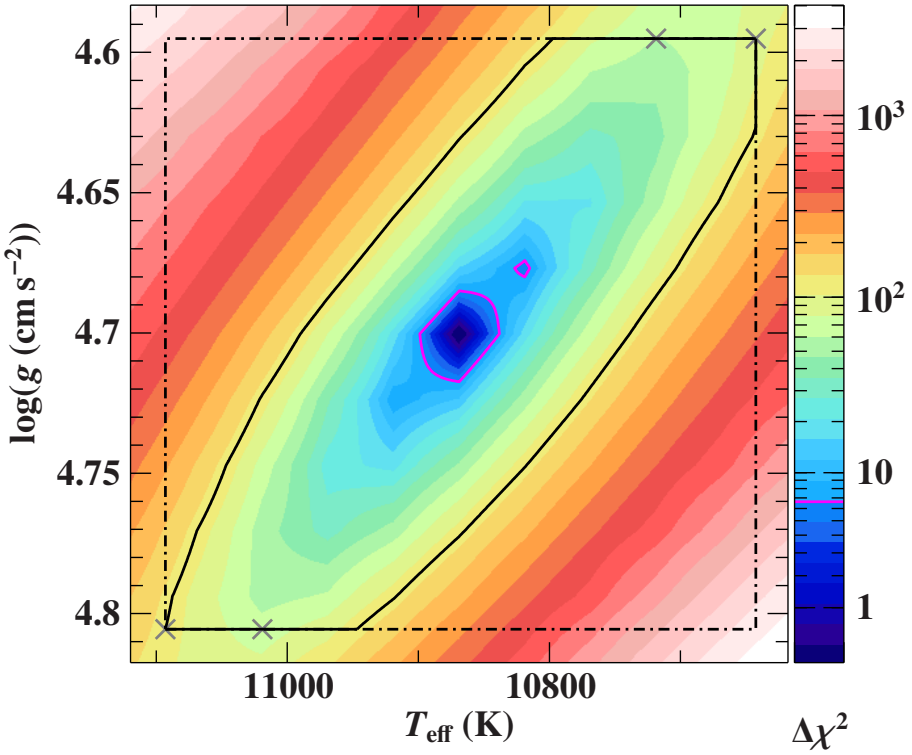

Figure 6.10: Confidence map for a freely fitted $\log(g)$ for J0247 B.

6.2 J0247 A

The evolutionary model by Maxted et al. (2013), would be consistent with an A-type MS star of a metallicity between 1/5 solar and solar and a high helium abundance of up to Y = 0.4. They also fitted the SED of the composite spectra to obtain an estimate of the basic stellar parameters, which resulted in $T_{\rm eff}$ = 7730 K, $\log(g)$ = 4.1 for the A-type star. From the light curve and RV analysis, they obtain $\log(g) = 4.111 \pm 0.006$ (see Section 6.1.1).
Our quantitative spectral analysis of the UVES spectrum of J0247 A is summarized in Table 6.3, the errors given are adopted from the confidence map (Figure 6.12). We find results for the basic parameters $T_{\rm eff}$, $\log(g)$ and metallicity, consistent with the analysis by Maxted et al. (2014). Of course we cannot derive the helium abundance, as the A-type companion is too cool to show those lines in the spectrum, so we assumed helium to be solar. The abundances, relative to solar, are given in Figure 6.11. The chemical composition is peculiar, with sodium, vanadium and lanthanum consistent with solar values, carbon, aluminum and cerium are depleted by almost -2.0 dex. These extreme values are as reliable as the abundances for Sr or Ba, as there are similar sufficient pixels affected by those lines ($\approx$ 100).
In comparison to the abundance results of the B-type star, all values are higher except for helium. This might be explained by gravitational settling going on in the B-type star. In principal the same abundance pattern is matched as Mg, Si, and Fe are at the same abundance level in respect to solare, while Ti is a bit more abundant. Only oxygen is more abundant in the A-type star, relative to the other elements under consideration.

Table 6.3: Results of the quantitative spectral analysis for J0247 A in comparison to solar values (abundance vector from Table 3.1). Uncertainties are adopted from the confidence map (Figure 6.12).

parameter	result	uncert.	solar
T_{eff}	7550	$^{+150}_{-160}$	
$\log(g)$	4.18	$^{+0.21}_{-0.20}$	
$v \sin i$	91.0	$^{+0.7}_{-0.1}$	
ζ	2.9	$^{+5.1}_{-2.9}$	
v_{rad}	64.1	$^{+0.7}_{-0.5}$	
ξ	2.0	$^{+0.1}_{-0.3}$	
He	−1.06	(fixed)	−1.06
C	−4.61	±0.11	−3.71
O	−3.51	$^{+0.10}_{-0.12}$	−3.28
Mg	−5.02	$^{+0.07}_{-0.08}$	−4.48
Si	−4.96	±0.09	−4.54
Fe	−5.06	$^{+0.08}_{-0.09}$	−4.52
Na	−5.76	$^{+0.11}_{-0.12}$	−5.77
Al	−7.37	$^{+0.09}_{-0.08}$	−5.57
Ca	−6.37	±0.05	−5.75
Sc	−9.59	$^{+0.11}_{-0.10}$	−8.99
Ti	−7.36	$^{+0.05}_{-0.03}$	−7.13
V	−8.16	±0.11	−8.08
Cr	−7.07	$^{+0.12}_{-0.06}$	−6.40
Mn	−7.37	$^{+0.11}_{-0.12}$	−6.56
Ni	−6.15	±0.11	−5.84
Sr	−9.65	$^{+0.10}_{-0.11}$	−9.17
Ba	−10.22	±0.11	−9.75
Y	−10.08	$^{+0.11}_{-0.10}$	−9.79
Zr	−9.96	$^{+0.12}_{-0.10}$	−9.41
La	−10.81	$^{+0.12}_{-0.10}$	−10.89
Ce	−12.32	$^{+0.11}_{-0.18}$	−10.42

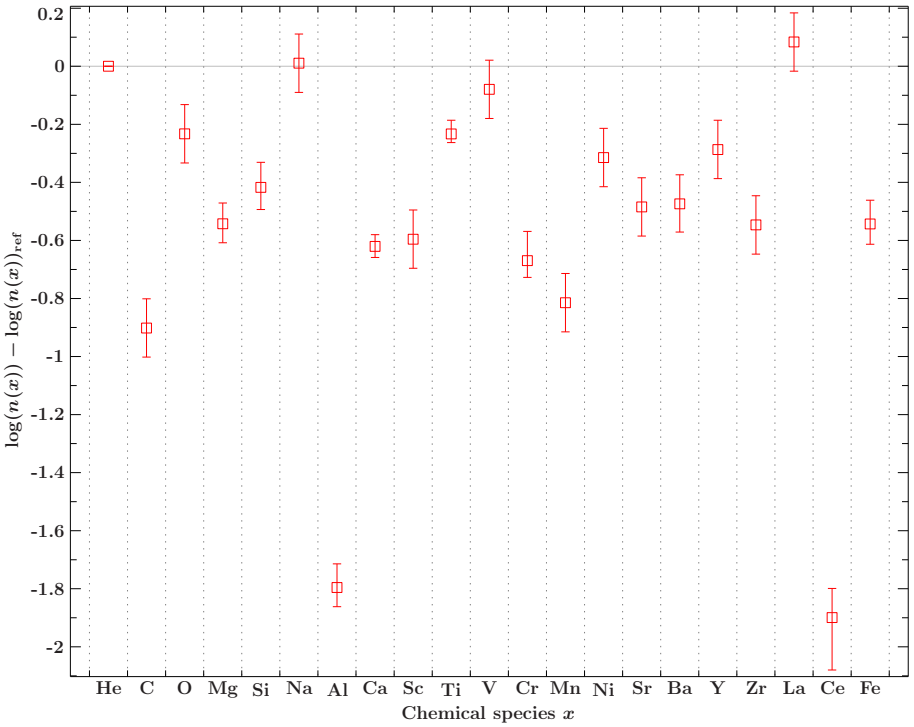

Figure 6.11: Differential abundances derived for J0247 A relative to solar.

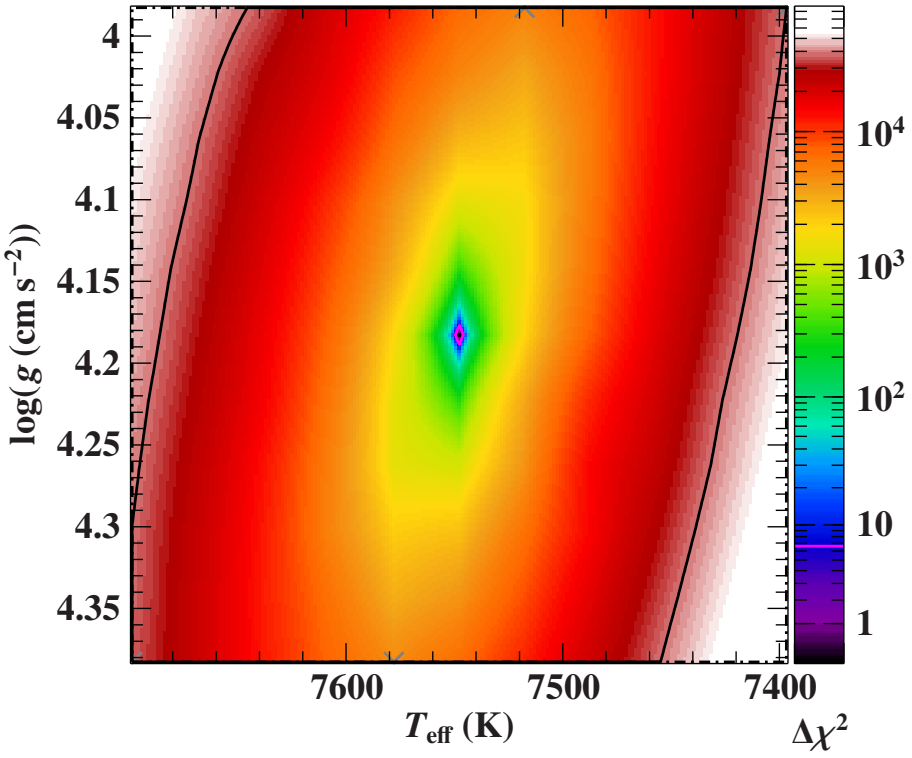

Figure 6.12: Confidence map ($T_{\rm eff}, \log(g)$) for J0247 A. The map is derived in the way described in Section 3.4.

Chapter 7

CoRoT-targets

The CoRoT ("COnvection ROtation and planetary Transits") mission was designed to continuously monitor up to 120000 stars in two fields (galactic center and anti galactic center directions) for half a year each during its two and a half year mission.
The satellite was launched on December 27 in 2006 and was in operation until October 2012 thus in fact light curves in three different bands for almost five years were collected. In total 163.664 stars have been observed with the individual runs lasting between 21 and 152 days (for a summarize of the outcome of the mission, see Moutou et al., 2013). The Soyuz rocket brought the satellites mass of 630 kg to a circumpolar orbit at an altitude of 896 km. The mission was originally designed to last 2.5 years and had two main objectives: The detection and study of oscillations of the stars brightness (asteroseismology) and the search for extrasolar (terrestrial) planets of F- and G-type stars. It was equipped with a 27 cm telescope and 4 CCD cameras with 2048 $\times$ 2048 pixels each and had a field of view of 2.8°$\times$2.8°, which was used half for each mission objective. It produced 1.5 Gbit data per day and was operated from the Mission Center in Toulouse, under the leadership of the French National Space Agency (CNES) and with large contributions by the European space agency (ESA). The photometric light curves consists of three color bands, only for the fainter stars (V > 14.5 mag) a monochromatic light curve was obtained. Due to the limited transfer rate, selections had to be done in terms of which targets the full time resolution with a sampling rate of 32 seconds was provided. The selection criteria were set by the ground team. Since one of the CCDs for the exoplanet search failed in March 2009, this means for the remaining one that typically out of 5640 only 500 have the full time resolution, while the rest was binned to a sampling rate of 8 minutes.

7.1 Search for planets around intermediate mass stars (IMS) from the CoRoT mission

The study of intermediate type stars and their possible planets is crucial to understand the formation of planetary systems. As the main focus of the mission was on cooler stars, Sebastian & Guenther (2011) designed a method, to classify IMS stars among the mission targets by matching low resolution spectra, taken with the AAOmega spectrograph to spectral atlasses. Among 14187 observed stars of the CoRoT fields IRa01, LRa01, and LRa02, Sebastian & Guenther (2011) identified 562 A-stars, which were then taken as an input list for a more detailed analysis of the

CoRoT light curves, to look for shallow, planet-like transit events. The target list was then further restricted to candidates with periods of less than six days and a transit depth of less than $\approx 1.5\%$. For illustration an original light curve from CoRoT and its detrended version can be found in Figure 7.1, which clearly shows a periodic transit event of 1% depth with a period of about 20 days. A zoom in of the transit in the phase folded light curve is shown in Figure 7.2.
The goal of the survey was to find out the frequency of close-in planets around intermediate-mass ($1.3 - 2.1\,\mathrm{M}_{\odot}$) main-sequence stars in comparison to close-in planets around solar type stars. The CoRoT mission is ideal to find at least the more massive planets, as the accuracy is well suited to find planets with radii $\geq 1 R_{\mathrm{Jup}}$ on close orbits (<0.1 AU) with a high probability. Sebastian (2016) classified 7131 CoRoT targets in the anti-center field, based on low resolution spectra. This investigation revealed a contribution of IMS to the whole sample to be almost one third. Together with the published and confirmed planets discovered by the CoRoT mission as well as the results presented in this work, Sebastian (2016) derived the the close-in planet frequency. For stars of masses smaller than $1.3\,\mathrm{M}_{\odot}$ the frequency is $0.79 \pm 0.23\,\%$ in agreement with results from RV surveys. Our investigations of IMS revealed for this value $0.11 \pm 0.04\,\%$ and is thus a significantly smaller frequency than for solar like stars. The frequency is even still lower, if all the unsolved systems with an IMS presented in this work would be a planet hosts.
The confirmation of the planetary nature of the companion cannot be done via RV-methods due to the usually fast rotation. Therefore we exclude all other possibilities explaining the periodic light curve variations, as described by Léger et al. (2009) in the case of the first rocky planet, discovered by CoRoT. A detailed light-curve analysis ist done to exclude spots, gracing eclipses by stellar companions, and oscillations. Another possible scenario to mimic a transit is an eclipsing binary in the background of the target, which cannot be resolved by the photometric mask of CoRoT, e.g. the light of the main target plus the binary is added and thus can be mistaken for a planetary transit. Therefore images taken with PISCES at the Large Binocular Telescope (LBT) with a higher resolution are studied, to exclude such false positives by searching for nearby background stars within the field of view of the photometric mask. Also the combination of a giant host star and a main-sequence (MS) star can have very similar light curves as a MS star plus planetary companion. To exclude giant primaries, a low resolution spectrum was taken in Tautenburg with the NASMYTH spectrograph at the Alfred Jensch telescope. Such a spectrum is fittet to a grid of template spectra to obtain the spectral type and luminosity class quickly. Finally, the last false-positives (FPs) can be produced by gracing eclipsing binaries, which can not be detected by the analysis of the light curve, because the effects are too small. Therefore, ground based RV-measurements are taken, because a binary would produce large variations during an orbital period. If all other possibilities are excluded as explained above, high resolution spectra are taken with different instruments, such as UVES at the ESO VLT or HARPS at the ESO 3.6m telescope in La Silla, to perform a detailed analysis of the host star to constrain the properties of the planet.

In the following section we will introduce the principles of the spectroscopic campaign and discuss the results of these investigations in more detail. We analyzed two high quality spectra of the A-type stars #1475 and #1712 each and found self-consistent spectroscopic results. Also we present the results for the A-type stars #2657, #2721 and #0108 and the most interesting target, the B-type star #4150 with a

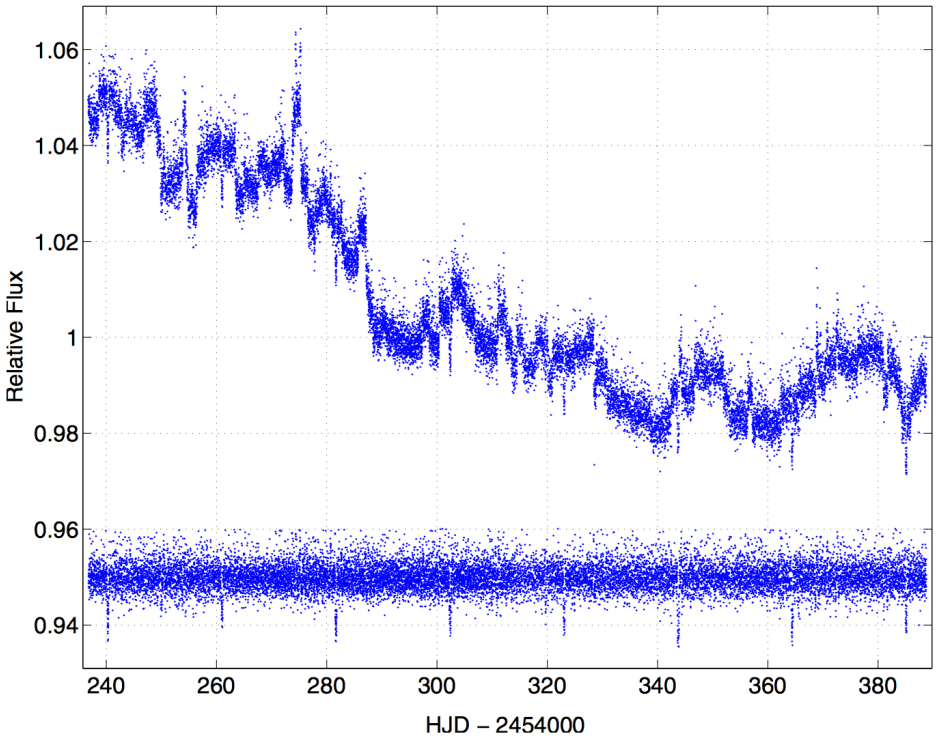

Figure 7.1: Raw CoRoT light curve of LRc01 E1 4780, a late F-type star with a M-dwarf companion, adopted from Tal-Or et al. (2013). At the bottom of the plot, the detrended light curve clearly shows a periodic transit every ≈ 21 days.

Table 7.1: Overview of the CoRoT targets with atmospheric parameters, determined from spectroscopy in a coarse analysis. The follow-up spectroscopy was done with the following instruments: U=UVES, C=CAFE, S=SANDIFORD, H=HARPS, F=FIES, CS=CAFOS, T=TWIN.

Win-ID	Daniel	CoRoT	Teff	logg	instruments	remarks
LRa02_E1_1475	A4V	A5V	7800	3,70	U,C,(ISIS)	C: binary?
LRa02_E1_0725	A5IV	B2IV			(S)	
LRc09_E2_3322	A5IV	F8IV			(H),T?	H:8*SNR=5, T:F-type
LRc08_E2_4203	A5V	F8IV	6800	2,90	U,(C?),(T?)	U:binary?
LRc10_E2_3265	A5V	F8IV			(T?)	
IRa01_E2_2721	A6V	A5IV	8000	3,00	U,(S),(C?)	binary?
IRa01_E1_4591	A7V	A5IV			(H),(C?)	H:SNR=18+12
LRc03_E2_2657	A7V	F1IV	7700	3,10	U?,(U),(C?),(T?)	Binary? U:several SNR=70
LRc07_E2_0108	A9IV	A0V	7400	4,30	CS,T,(H),(S)	H:SNR=40
LRa02_E2_4150	B5V	O9V	15900	4,40	H,F,C,(S),(U)	MgCaTI lines?, U: SNR=35
LRc05_E2_0168	F?	A5IV			(IDS),CS	F-type
LRa01_E2_0963	F0V	F6V				
LRc07_E2_0307	F3V	F8IV	6800	4.13	(H),(U)	U:many 30-80SNR,H:6*25SNR
LRa02_E2_1023	F4V	A7V			(S)	
LRa01_E2_0203	F5IV	A5V			(U)	U:many 30-90SNR
LRa01_E2_1578	F5IV	F6V			(S)	
LRc02_E1_0132	F6II	A0V			(S)	
IRa01_E2_1712	F6V	F6V	8000	3,70	H,F,(C?),(U)	U: SNR=40
LRc07_E2_0482	F7V	F8IV			(S)	
LRc07_E2_0187	F8V	G2V			(IDS)	
LRc07_E2_0146	F8V	G5IV			(IDS),(ISIS)	

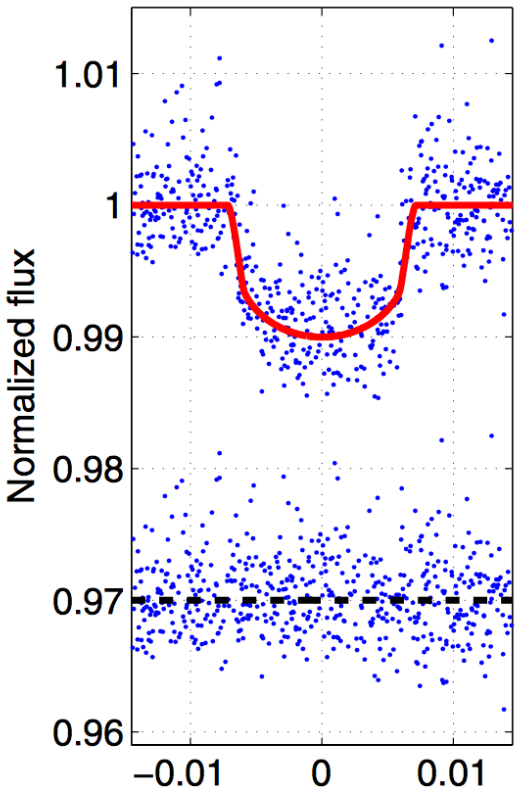

Figure 7.2: Phase folded light curve of LRc01 E1 4780 around the eclipse, adopted from Tal-Or et al. (2013).

Table 7.2: Overview of our observing runs.

date	nights	instrument	observer
May 2012	5	TWIN@3.5m(Calar Alto)	C. Heuser
October 2012	7	IDS@INT (La Palma)	C. Heuser
December 2012	5	ISIS@WHT (La Palma)	T. Kupfer
January 2013	11	SANDIFORD@OST (Mc Donald)	C. Heuser, S. Geier
March 2013	4	EFOSC2@NTT (La Silla)	C. Heuser
June 2013	4	ISIS@WHT (La Palma)	C. Heuser
May 2013	5	IDS@INT (La Palma)	C. Heuser
June 2014	5	IDS@INT (La Palma)	C. Heuser
July 2014	4	TWIN@3.5m (Calar Alto)	E. Ziegerer

possible substellar companion. Further we also reanalyzed #0307 (CoRoT 36b), which is one of three "hot Jupiters" (CoRoT-34/35/36 b, Grziwa et al. (in prep.)) around three MS F-type stars, using the technique explained above. To be able to perform a fit to a UVES spectrum of the target #0307 (and for the TWIN data of #0108), we extended the grid slightly into the early F-type stars ($T_{\rm eff}$ = 6500 K).

7.2 The spectroscopic campaign

The aim of our spectroscopic follow-up campaign is twofold:

- to constrain RV-variations to derive upper limits on the semi-amplitude K.
- to perform quantitative spectral analyses

To obtain the RV-measurements, we performed several observing runs on telescopes equipped with high- and medium resolution spectrographs, where ever we could get our hands on. During the project phase between 2012 and 2015, we were awarded several observing runs in visitor mode (see Table 7.2). I for myself, therefore carried out observing runs at the NTT with EFOSC2 at the ESO La Silla observatory, the Otto Struve Telescope at McDonald observatory (Texas) with its spectrograph SANDIFORD, with TWIN at the 3.5m Telescope at Calar Alto in Spain and several runs at the Roque de los Muchachos observatory at La Palma, mostly with the IDS spectrograph at the INT but also at the WHT with its spectrograph ISIS to obtain time series of spectra of our targets, to search for obvious radial velocity shifts to exclude binaries.

7.3 The CoRoT target #1475

The CoRoT target LRa02 E1 1475 (henceforth #1475) was already marked as of high priority by the CoRoT team and therefore follow-up observations were carried out with several telescopes and instruments. The star showed a transit event every 2.12 days in the light curves from CoRoT with a depth of 0.30%. Imaging with the Canada France Hawaii Telescope (CFHT) confirmed that the transit was on target. Spectroscopy with CRIRES at the ESO-VLT could rule out a contamination by a cool stellar companion (Guenther et al., 2013). Sarro et al. (2013) detected pulsations with a period of roughly one third of the orbital period and derived the spectral parameters using spectra taken with GIRAFFE to $T_{\rm eff}$ = 8396 (fit to models based on Kurucz and TLUSTY (KT-model)) respectively $T_{\rm eff}$ = 7909 (compared to empiric spectra from the ELODIE dataset) and $\log(g)$ = 3.8 (also from the KT-model).
Daniel Sebastian (2016) used a mean of the different parameters also including our

Table 7.3: Overview of the different atmospheric parameters for #1475. The two different temperatures from GIRAFFE results from 1: Kurucz and TLUSTY synthetic models and 2: fit to template spectra from the ELODIE dataset. *: a correction of 0.15 dex to the surface gravity is applied, as explained in Section 3.5.1.

	GIRAFFE1	GIRAFFE2	HARPS	UVES
$T_{\rm eff}$	8396	7909	7831^{+157}_{-158}	7813 ± 157
$\log(g)$(*corrected)	3.8	3.8	$3.89^{*} \pm 0.21$	$3.88^{*} \pm 0.21$

result ($T_{\rm eff}$ = 8068±163 K, $\log(g)$ = 3.8), which corresponds to a main-sequence star of spectral type A7V, and a low metallicity) and derived a mass of M = 1.98±0.05 $M_\odot$ and a radius of R = $2.93 \pm 0.03\,R_\odot$, using stellar evolution models by Georgy et al. (2013). These stellar parameters would result in a companion size of R = $1.6 \pm 0.1\,R_{\rm Jup}$. With the mean of our two spectroscopic results the mass of the host is not significantly changed, but with a less evolved star and thus a smaller radius, also the companions radius would shrink to r $\lesssim 1.5\,R_{\rm Jup}$. Taking the RV measurements from UVES, HARPS and CRIRES spectra into account, this leads to a companion mass of $81.5^{+4.8}_{-4.3}$ $M_{\rm Jup}$. Also a tidal deformation with an amplitude of 122 ± 23 ppm of the very close orbiting companion could be detected by analyzing the phase folded CoRoT light curve. Sebastian (2016) also derived an inclination of i = 71.5° from the light curve. With this amplitude and the derived stellar parameters mass, radius and orbital period and a factor describing the response of the stars surface due to the tidal effects of the companion (set to α_{ellip} = 1), the companion mass yields $6.8\,M_{\rm Jup}$. Although this value is an order of magnitude smaller that the previous result, it gives another hint to the substellar nature of the companion.

We analyzed the high resolution UVES and HARPS spectra by fitting them to our grid. The UVES spectrum showed some artifacts, possibly due to insufficient flat fielding. To improve the flat fielding, we used a spectrum from the UVES archive of the white dwarf EG131, which shows mainly the Balmer lines and almost no metal lines. This improved the normalization, e.g. the continuum now was more easy to normalize with a spline function by hand. The fitting results are given in Table 7.4, the errors were adopted from the confidence maps with assumed uncertainties on $T_{\rm eff}$ of 157 K and $\log(g)$ = 0.2 dex (Figure 7.3). The abundance pattern of both results is shown in Figure 7.4. The basic parameters agree almost perfectly for both spectra, but the abundance patterns differ slightly. The most obvious difference is in the abundances of the rare earth elements lanthanum and cerium, which are clearly overabundant in the UVES spectrum, but completely (lanthanum) and almost (cerium) absent in the HARPS spectrum. The relatively high projected rotation velocity indicates that the star lies beyond the boarder ($v \sin i \geq 150 \mathrm{km\,s^{-1}}$), where no abundance peculiarities are expected any more (see Chapter 2). To the resulting smearing out of the spectral lines, huge "mergers" of lines including several elements, could be reproduced also with different elemental abundances and the best solution cannot be distinguished "by eye". Therefore we performed several fitting runs with different starting parameters and fitting algorithms (see Section 3.2.2) and restricted both spectra to the same wavelength coverage, but the discrepancy between the spectra of the two instruments still remains. For the HARPS spectrum the cerium lines, and for both spectra the nitrogen and phosphorus lines are only few and if present very weak, which makes it unreliable to compare the results for this abundances.

A classification of the star into the MK scheme renders difficult. The Ap star phenomenon is more likely on slowly rotating stars. However, this classification fits best

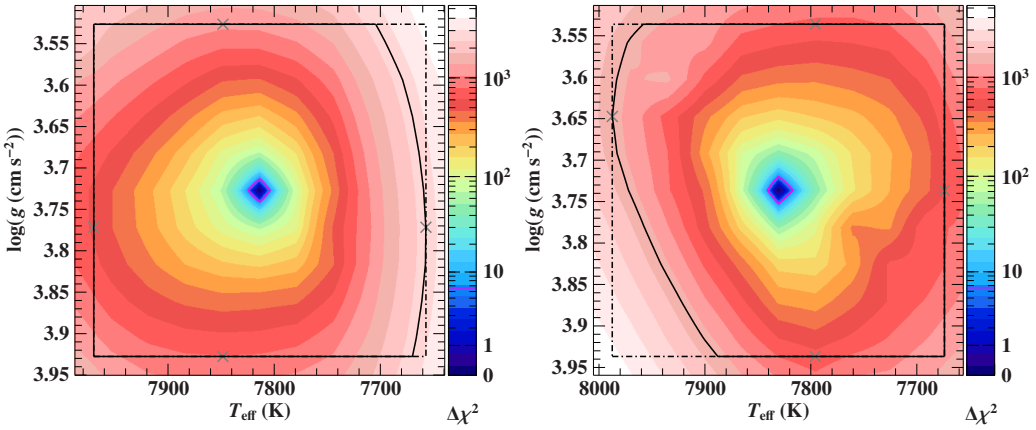

Figure 7.3: Confidence maps ($T_{\rm eff}$, $\log(g)$) of #1475 for UVES (left) and HARPS (right).

to the spectra, although the two high quality spectra have a discrepancy in which elements are peculiar. Si and Sr are overabundant according to the HARPS spectrum, while for the UVES spectrum La and Ce are peculiarly high. Hence, our classification of #1475 stays quite coarse as "ApV".

This objects is one of the most interesting candidates for a substellar companion around an A-type star and would be a good candidate for obtaining a time series of spectra during the transit, to perform Doppler tomography (see Section 1.1.1) in order to reveal the brown dwarf respectively planetary nature of the companion as well as the obliquity of the system. Also the existence of spots could be verified in this way.

Table 7.4: Results of the fitting of the HARPS and UVES spectrum of #1475, in comparison with the solar composition (see also the abundance vector in Table 3.1). *: a correction of 0.15 dex to the surface gravity is applied, as explained in Section 3.5.1.

parameter	UVES	HARPS	solar
resolution	49000	115000	
<SNR>	≈ 70	≈ 55	
$T_{\rm eff}$	7813 ± 157	7831^{+157}_{-158}	
$\log(g)^*$	$3.88^* \pm 0.21$	$3.89^* \pm 0.21$	
$v \sin i$	$145.1^{+1.5}_{-1.0}$	$138.24^{+0.51}_{-0.91}$	
ζ	$72.6^{+5.5}_{-6.8}$	$104.0^{+8.6}_{-7.1}$	
$v_{\rm rad}$	$-1.2^{+0.9}_{-1.0}$	$24.59^{+0.52}_{-0.61}$	
ξ	$2.00^{+0.00}_{-0.10}$	$1.75^{+0.16}_{-0.10}$	
C	$-3.89^{+0.14}_{-0.08}$	-3.49 ± 0.09	–3.71
O	$-4.15^{+0.47}_{-0.30}$	$-3.77^{+0.25}_{-0.29}$	–3.28
Mg	$-5.11^{+0.12}_{-0.11}$	-4.76 ± 0.13	–4.48
Si	$-4.51^{+0.11}_{-0.09}$	$-4.23^{+0.10}_{-0.08}$	–4.54
Fe	$-4.69^{+0.11}_{-0.04}$	$-4.52^{+0.10}_{-0.12}$	–4.52
Na	$-6.89^{+0.23}_{-0.25}$	$-6.24^{+0.19}_{-0.18}$	–5.77
Al	$-5.55^{+0.25}_{-0.21}$	$-5.32^{+0.34}_{-0.25}$	–5.57
Ca	$-5.73^{+0.11}_{-0.08}$	-5.83 ± 0.12	–5.75
Sc	$-9.43^{+0.19}_{-0.21}$	$-9.54^{+0.20}_{-0.22}$	–8.99
Ti	-7.59 ± 0.11	-7.44 ± 0.10	–7.13
V	$-8.04^{+0.26}_{-0.22}$	$-7.88^{+0.17}_{-0.24}$	–8.08
Cr	$-6.72^{+0.10}_{-0.08}$	$-6.77^{+0.10}_{-0.11}$	–6.40
Mn	$-6.76^{+0.22}_{-0.23}$	$-7.33^{+0.29}_{-0.30}$	–6.56
Ni	$-6.20^{+0.22}_{-0.25}$	-5.79 ± 0.21	–5.84
Sr	$-9.04^{+0.23}_{-0.20}$	$-8.85^{+0.27}_{-0.26}$	–9.17
Ba	$-10.49^{+0.32}_{-0.33}$	$-10.68^{+0.32}_{-0.18}$	–9.75
Y	$-10.23^{+0.25}_{-0.14}$	$-10.07^{+0.23}_{-0.25}$	–9.79
Zr	$-9.45^{+0.20}_{-0.17}$	$-9.61^{+0.22}_{-0.24}$	–9.41
La	$-10.04^{+0.21}_{-0.24}$	-10.89 (fixed)	–10.89
Ce	$-9.55^{+0.20}_{-0.19}$	$-11.30^{+0.63}_{-1.08}$	–10.42

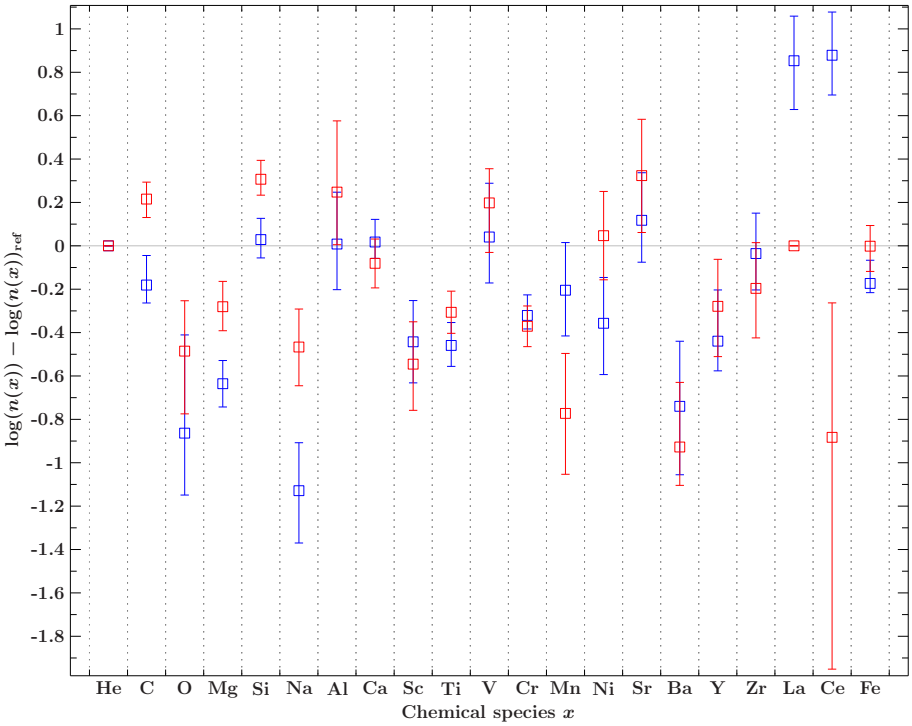

Figure 7.4: Abundances of #1475 relative to solar values. Blue are from the models fitted to the UVES spectrum, red corresponds to the HARPS spectrum. The errors were adopted from the confidence maps (Figure 7.3) with uncertainties on $T_{\rm eff}$ of 157 K and $\log(g)$ = 0.2 dex.

7.4 The CoRoT target #1712

The CoRoT target IRa01 E2 1712 (henceforth #1712), shows a transit depth of 0.24% with a period of 2.767 days. From ground based follow-up photometry an eclipsing background binary could be excluded, thus the transit occurs on target. Moutou et al. (2009) detected a variation of the RV in two HARPS spectra of 60 m/s, which is in the order of the uncertainty of these measurements. In addition they found a possible variation of the line profile, which they conclude indicates a binary. Because of a coarse parameter determination ($T_{\rm eff} = 6700 \pm 100\,K$, and $\log(g) = 3.5 - 4.0$ dex), they conclude that a triple stellar system would be the most probable solution.
Later, the star was also observed with FIES at the NOT. We analyzed both, the HARPS and the FIES spectrum, our results are listed in Table 7.5, consistent fundamental parameters are derived from the HARPS and the FIES spectra. Our solution is $\approx$ 1000 K hotter (7920 K and 8030 K, respectively) than Moutou et al. (2009). Here also we added 0.15 dex on $\log(g)$ due to the effect of blended lines (according to Section 3.5.1) and thus resulting in a main-sequence star, which is consistent to the classification as A9V by Sebastian (2016). Also most of the abundances are very similar, except some weaker lines such as from nitrogen or aluminum. We could not find a spectroscopic signature from a second star, possibly contaminating the observed spectra, which renders the triple system scenario unlikely.
The abundance pattern for both spectra are shown in Figure 7.5. Obvious is the trend, that the abundances are lower in the FIES data for all elements, except C and Al where it is reversed. This systematic deviation might be introduced by different normalization respectively data reduction. For both stars Ca and Sc are less abundant than the solar value, while the heavier metals are overabundant. This leads to

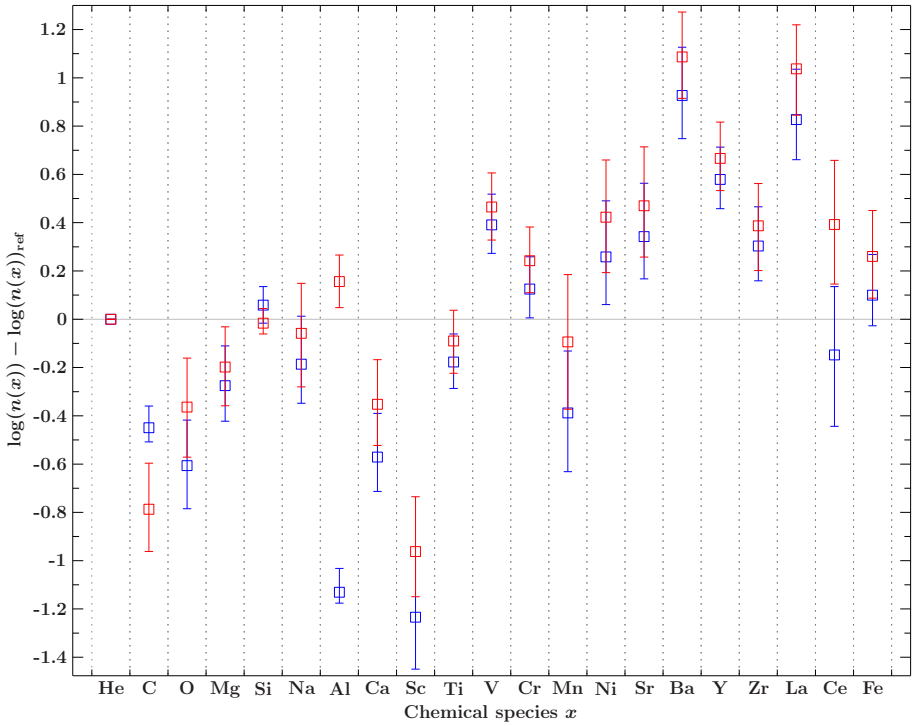

Figure 7.5: Abundances of #1712 relative to solar values. Blue are from the models fitted to the FIES spectrum, red corresponds to the HARPS spectrum. The errors were adopted from the confidence maps (Figure 7.6) with uncertainties on $T_{\rm eff}$ of 157 K and $\log(g) = 0.2$ dex.

a classification as Am9V or IV. If the detected transit is due to a companion, it would have a radius of $r \approx 1.7\,R_{\rm Jup}$. If we take the small variations of 60 m/s from the two HARPS spectra and the stellar mass from evolutionary tracks from Ekström et al. (2012) as basis, the upper mass limit for the companion would be $0.53\,M_{\rm Jup}$. Hence, further spectroscopy is needed to confirm the small RV variation to derive an upper mass limit.

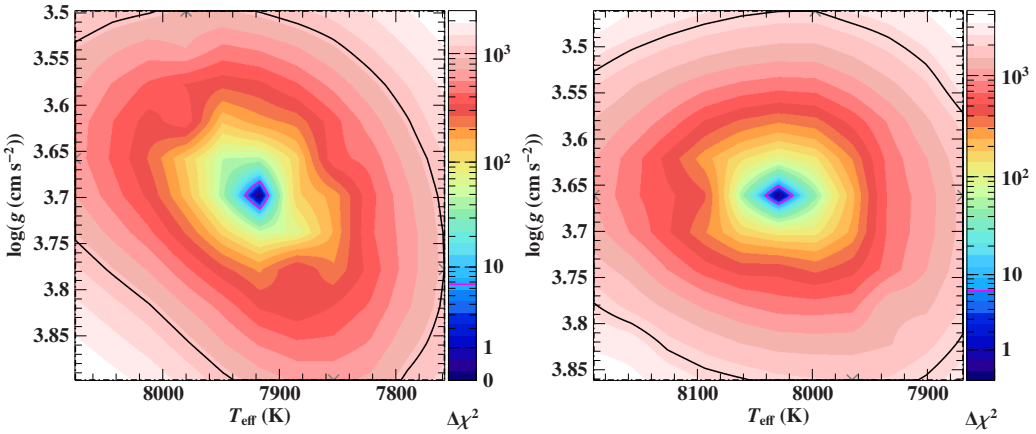

Figure 7.6: Confidence maps ($T_{\rm eff}$, $\log(g)$) of #1712 for FIES (left) and HARPS (right).

Table 7.5: Results of the quantitative spectral analysis of the FIES and HARPS data of #1712, in comparison with the solar values (abundance vector from Table 3.1). *: a correction of 0.15 dex to the surface gravity is applied, as explained in Section 3.5.1.

parameter	FIES	HARPS	solar
resolution	67000	115000	
<SNR>	44	45	
$T_{\rm eff}$	7920 ± 160	8030 ± 170	
$\log(g)^*$	$3.85^{*}\ ^{+0.20}_{-0.21}$	$3.81^{*} \pm 0.21$	
$v \sin i$	$50.93^{+0.48}_{-0.01}$	$43.33^{+0.20}_{-0.05}$	
ζ	$27.5^{+1.7}_{-2.5}$	$33.1^{+2.2}_{-2.5}$	
$v_{\rm rad}$	$2.02^{+0.07}_{-0.03}$	$-24.84^{+0.08}_{-0.06}$	
ξ	2 ± 0	2 ± 0	
C	$-4.16^{+0.09}_{-0.05}$	$-4.50^{+0.16}_{-0.13}$	–3.71
O	$-3.89^{+0.15}_{-0.13}$	$-3.64^{+0.15}_{-0.16}$	–3.28
Mg	$-4.76^{+0.14}_{-0.11}$	-4.68 ± 0.13	–4.48
Si	$-4.48^{+0.07}_{-0.06}$	$-4.56^{+0.06}_{-0.04}$	–4.54
Fe	$-4.42^{+0.16}_{-0.09}$	$-4.26^{+0.15}_{-0.13}$	–4.52
Na	$-5.96^{+0.17}_{-0.13}$	$-5.83^{+0.14}_{-0.17}$	–5.77
Al	$-6.70^{+0.11}_{-0.05}$	-5.41 ± 0.09	–5.57
Ca	$-6.32^{+0.16}_{-0.11}$	-6.10 ± 0.14	–5.75
Sc	$-10.22^{+0.21}_{-0.17}$	$-9.95^{+0.19}_{-0.15}$	–8.99
Ti	-7.31 ± 0.09	$-7.22^{+0.09}_{-0.11}$	–7.13
V	$-7.69^{+0.11}_{-0.09}$	-7.61 ± 0.11	–8.08
Cr	-6.27 ± 0.10	$-6.16^{+0.12}_{-0.10}$	–6.40
Mn	$-6.95^{+0.21}_{-0.18}$	-6.65 ± 0.21	–6.56
Ni	$-5.58^{+0.20}_{-0.16}$	$-5.42^{+0.18}_{-0.17}$	–5.84
Sr	$-8.83^{+0.19}_{-0.14}$	$-8.70^{+0.20}_{-0.17}$	–9.17
Ba	$-8.82^{+0.17}_{-0.13}$	$-8.66^{+0.15}_{-0.13}$	–9.75
Y	$-9.21^{+0.12}_{-0.09}$	$-9.12^{+0.12}_{-0.11}$	–9.79
Zr	$-9.11^{+0.13}_{-0.11}$	$-9.02^{+0.12}_{-0.15}$	–9.41
La	$-10.06^{+0.17}_{-0.13}$	$-9.85^{+0.12}_{-0.15}$	–10.89
Ce	-10.57 ± 0.21	$-10.03^{+0.21}_{-0.19}$	–10.42

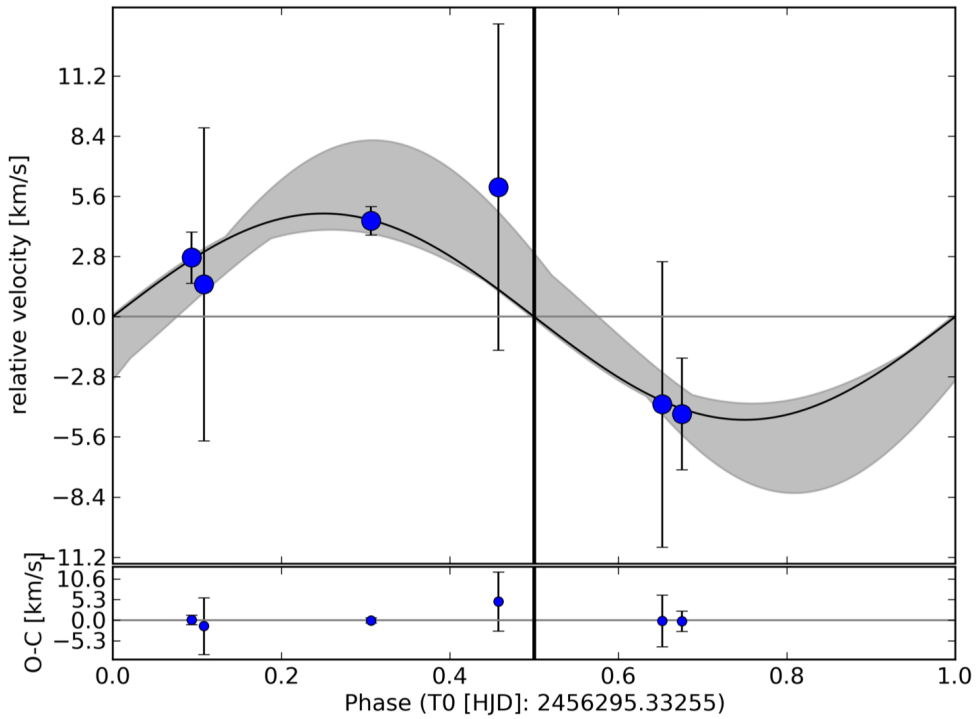

Figure 7.7: RV measurements for #2657 with the TWIN spectrograph and a sinosoidal, matching quite well to the observed transit period (adopted from Sebastian, 2016). The grey areas mark the uncertainties from the bootstrapping method.

7.5 The CoRoT target #2657 - planet or stellar companion?

The CoRot Team (2016) found a 0.2% deep transit with a period of 5.15 days in the light curves of LRc03 E2 2657 (henceforth #2657) which fits to a 0.7 R_{Jup} sized transiting object. RV measurements with TWIN fittet quite well (see Figure 7.7), assuming a stellar mass of M = 1.93 $\mathrm{M}_{\odot}$, the upper limit for the companion would be 60 M_{Jup}. Follow-up observations with HARPS and UVES could not confirm the formerly measured semi-amplitude of 4.8km s^{-1} (Sebastian, 2016) and thus excludes a massive stellar companion. Our analysis of the UVES spectra, however, could not confirm the MS nature (A7V) of the star. Most importantly, the surface gravity is too low for a main-sequence star, but points to a giant nature ($\log(g)$ = 3.25 dex, see confidence map in Figure 7.9 and the results in Table 7.6. Note that we added the correction term of 0.15 dex to the surface gravity, explained in Section 3.5.1). A fit to evolutionary tracks would lead to revised stellar parameters of $M = 2.78^{+0.4}_{-0.4}\,\mathrm{M}_{\odot}$, $R \approx 6.49\,\mathrm{R}_{\odot}$ and an age of $\approx$ 465 Myrs. This would lead to a companion mass of $\approx$ 76 M_{Jup} and a radius of $r \approx 2.9\,R_{\mathrm{Jup}}$, which fits to a brown dwarf or very low mass stellar companion.
The chemical abundances scatter around solar values, striking are the low abundances for O, Al, Mn and Ce, but these values might be unreliably, as they refer from only a few lines. There is a slight overabundance of Ca, V and Ba. But the whole pattern does not show a certain peculiarity, leading to a classification as AIII.
Furthermore we found hints for a composite spectrum. In addition to a quite fast

Table 7.6: Results of the quantitative spectral analysis of the UVES data of #2657, in comparison with the solar values (abundance vector from Table 3.1). *: a correction of 0.15 dex to the surface gravity is applied, as explained in Section 3.5.1.

parameter	UVES	solar
resolution	49000	
<SNR>	126	
$T_{\rm eff}$	7670 ± 160	
$\log(g)^*$	$3.25^{*\ +0.20}_{-0.21}$	
$v \sin i$	126^{+1}_{-1}	
ζ	46 ± 6	
$v_{\rm rad}$	$7.8^{+0.9}_{-0.5}$	
ξ	$2.0^{+0.1}_{-0.1}$	
C	-3.71 ± 0.11	–3.71
O	$-3.76^{+0.08}_{-0.12}$	–3.28
Mg	$-4.41^{+0.16}_{-0.14}$	–4.48
Si	$-4.510^{+0.04}_{-0.03}$	–4.54
Fe	$-4.50^{+0.12}_{-0.13}$	–4.52
Na	$-5.84^{+0.18}_{-0.17}$	–5.77
Al	$-7.34^{+0.21}_{-0.26}$	–5.57
Ca	-5.59 ± 0.11	–5.75
Sc	$-9.14^{+0.12}_{-0.11}$	–8.99
Ti	$-7.13^{+0.09}_{-0.11}$	–7.13
V	$-7.69^{+0.09}_{-0.11}$	–8.08
Cr	$-6.61^{+0.10}_{-0.09}$	–6.40
Mn	-7.14 ± 0.27	–6.56
Ni	$-5.99^{+0.20}_{-0.18}$	–5.84
Sr	$-9.10^{+0.22}_{-0.19}$	–9.17
Ba	$-9.50^{+0.20}_{-0.19}$	–9.75
Y	$-9.81^{+0.14}_{-0.11}$	–9.79
Zr	$-9.38^{+0.16}_{-0.14}$	–9.41
La	$-10.7^{+0.4}_{-0.5}$	–10.89
Ce	-11.0 ± 0.5	–10.42

rotating star ($v \sin i \approx 125 \mathrm{km\,s^{-1}}$), we found some sharp lines of eg. Fe I, Fe II and Mg I (see Figure 7.10). Assuming that the small variations in RV are correct, it cannot be a close binary system. If the small absorption lines come from a second star component, either in a wide orbit or just from a visual binary, the occultation can still be produced by an substellar object. But because of the contradictory classification of the host star, the companion size and mass remains unclear. Further time resolved spectroscopy is required to answer these questions. The existence of a planet, however, is quite unlikely.

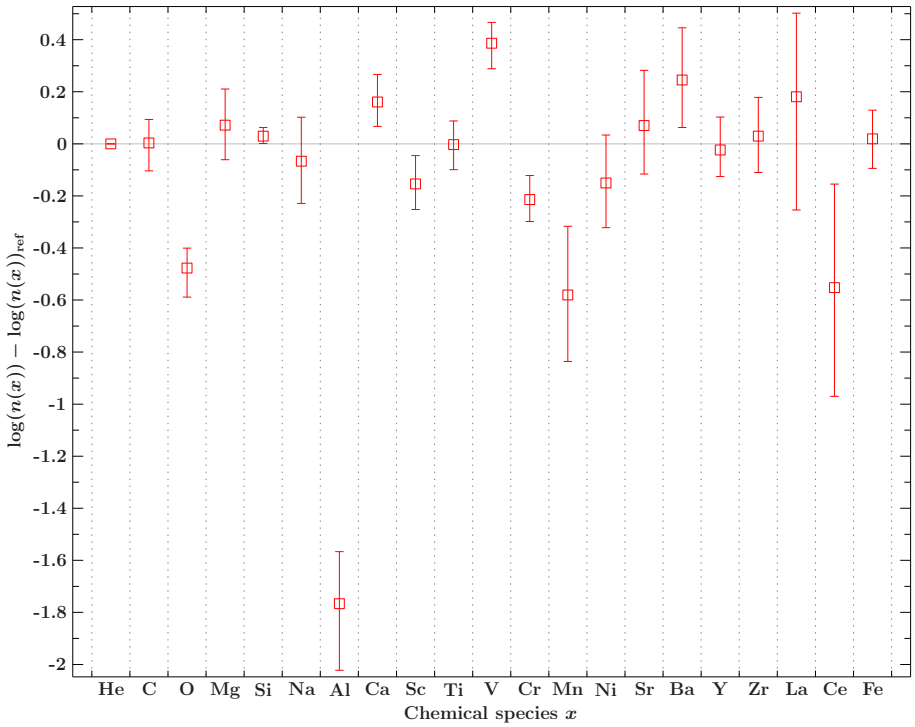

Figure 7.8: Abundances of #2657 relative to solar values from the quantitative spectral analysis of the UVES spectrum. The uncertainties were adopted from the confidence maps (Figure 7.9) with uncertainties on $T_{\rm eff}$ of 160 K and $\log(g) = 0.2$ dex.

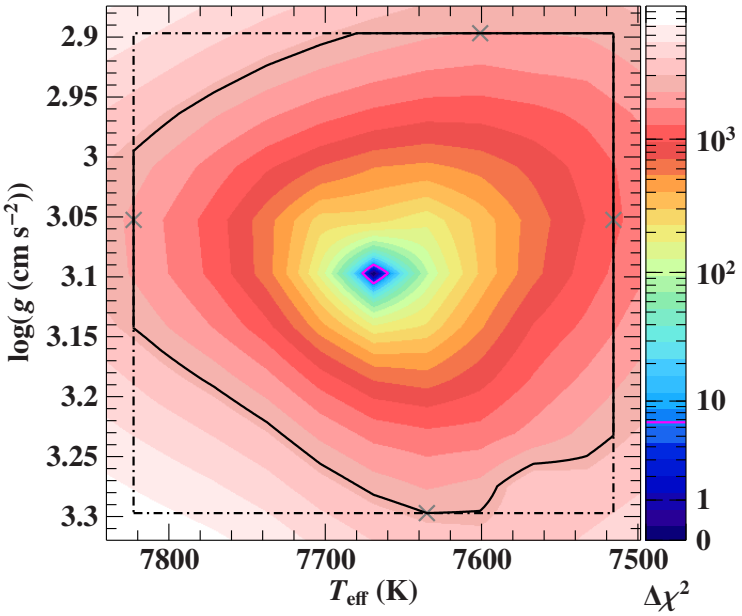

Figure 7.9: Confidence map ($T_{\rm eff}$, $\log(g)$) of #2657, which indicates atmospheric parameters appropriate for a giant, rather than a main-sequence star.

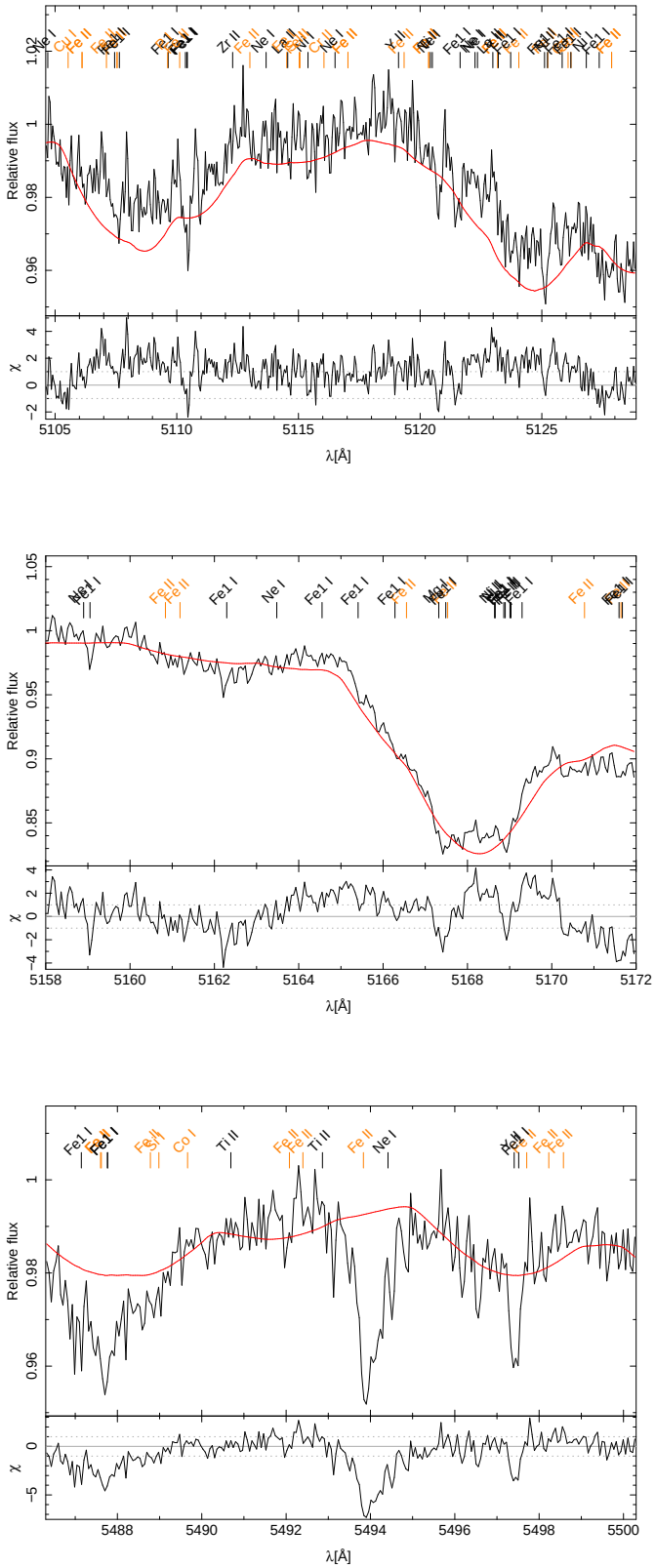

Figure 7.10: Sharp absorption lines in #2657, upper panel: weak Fe I lines (black label "Fe1 I"), middle panel: Fe I and Mg I, bottom panel: Fe I+II lines (Fe II is missing in our models, which is indicated by an orange label "Fe II").

Table 7.7: Results of the quantitative spectral analysis of the HARPS data of #4150, in comparison with the solar values (abundance vector from Table 3.1).

parameter	HARPS	solar
$v \sin i$	$33.08^{+0.58}_{-0.19}$	
ζ	$27.6^{+2.1}_{-1.7}$	
$v_{\rm rad}$	$33.04^{+0.08}_{-0.11}$	
$T_{\rm eff}$	15900 ± 400	
$\log(g)$	4.44 ± 0.11	
ξ	≤ 0.7	
He	$-2.47^{+0.07}_{-0.03}$	–1.06
C	-3.72 ± 0.08	–3.71
N	$-3.62^{+0.08}_{-0.09}$	–4.25
O	$-3.60^{+0.02}_{-0.05}$	–3.28
Ne	$-4.66^{+0.02}_{-0.01}$	–3.95
Mg	$-4.75^{+0.05}_{-0.06}$	–4.48
Al	$-6.0^{+0.0}_{-1.0}$	–5.57
Si	$-4.23^{+0.06}_{-0.07}$	–4.54
S	-5.53 ± 0.05	–4.85
Ar	$-5.60^{+0.10}_{-0.01}$	–5.60
Fe	$-3.60^{+0.07}_{-0.11}$	–4.52

7.6 The CoRoT target #4150

LRa02 E2 4150 (henceforth #4150) was classified by Sebastian (2016) to be a B4V star, which would correspond to a mass of $M \approx 5.0\,\mathrm{M}_\odot$ and a radius of $R \approx 3.0\,\mathrm{R}_\odot$. The analysis of the CoRoT light curve yields a transit depth of 0.65% at a period of 8.17 days in addition to pulsations with an amplitude of $\approx$ 1%. Two time series of spectra were taken with SANDIFORD and exclude a binary, as no large variation in the RV could be measured. In combination of data taken with FIES, HARPS and CAFE, Sebastian (2016) derived an upper mass limit of the companion to be $M \sin i = 63.46^{+1.63}_{-2.23}\,M_{\rm Jup}$. The period from the RV-fit agrees quite well to the period deduced from the CoRoT light curve.
We analyzed the HARPS spectrum, the results are listed in Table 7.7. Our values are consistent within the uncertainties to a very young ($\leq$ 5 million years) main-sequence star with a mass of $M = 4.28 \pm 0.15\,\mathrm{M}_\odot$ and a radius of $R = 2.26 \pm 0.15\,\mathrm{R}_\odot$, taking evolution tracks from Ekström et al. (2012). But note that with our best fit, the star lies below the ZAMS in the $\log(g) - T_{\rm eff}$ diagram (see Figure 7.11). However, assuming a very young main-sequence star with the above derived parameters, the companion radius would be $r \approx 1.77\,R_{\rm Jup}$ with a mass of $m \approx 57\,M_{\rm Jup}$, which fits to a brown dwarf companion in a close orbit. This would be the first substellar object detected around a B-type main-sequence star. A homogeneous time series of spectra would help to better constrain the radial velocity measurements and the physical properties of this very interesting system.

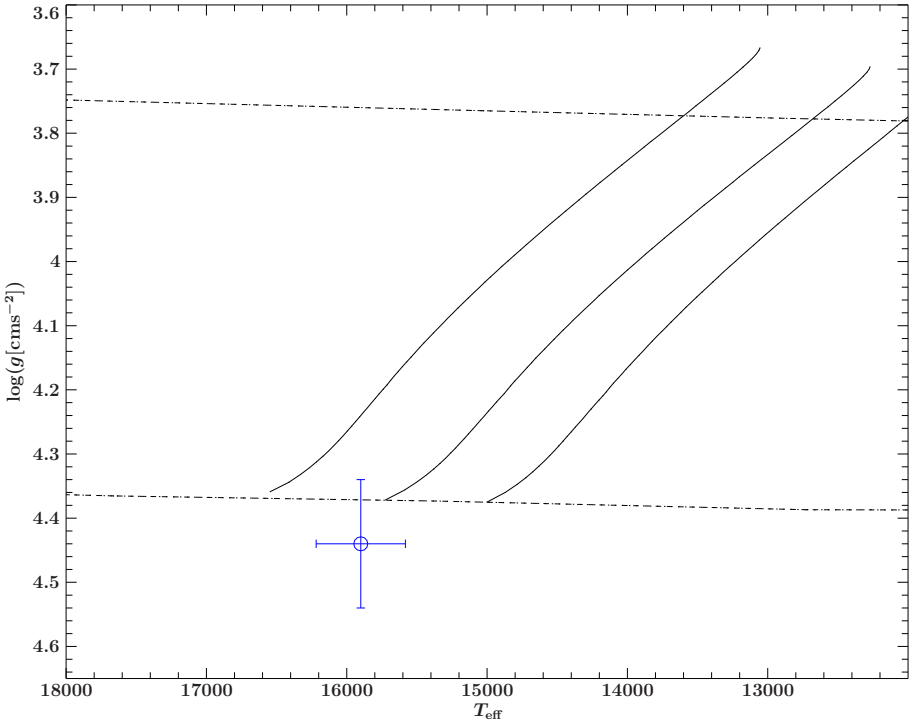

Figure 7.11: Evolutionary tracks of #4150 from Ekström et al. (2012). The dashed line marks the main-sequence, the blue circle the best fit. The evolutionary tracks are shown for zero rotation and masses of: 4.55, 4.15 and 3.85 $M_\odot$, respectively. From this plot, we read the mass of #4150 to be $4.28 \pm 0.15\,M_\odot$.

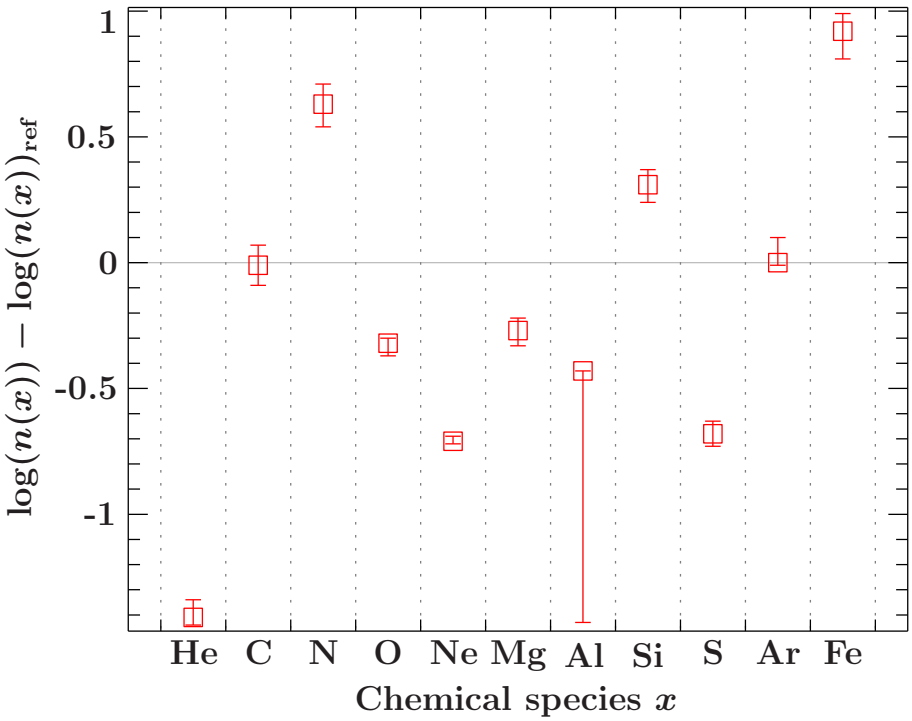

Figure 7.12: Abundances of #4150 relative to solar values from the quantitative spectral analysis of the HARPS spectrum. The uncertainties were adopted from the confidence map (Figure 7.13) with uncertainties on $T_{\rm eff}$ of 320 K and $\log(g) = 0.1$ dex.

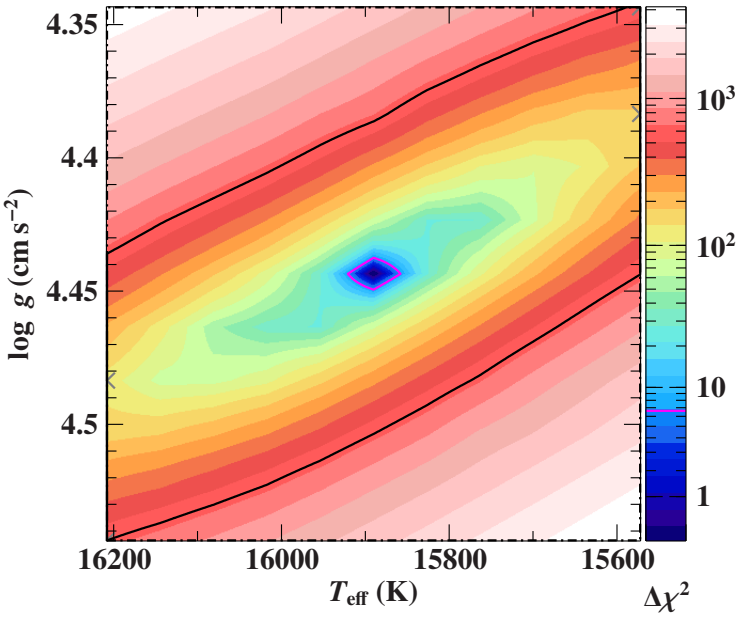

Figure 7.13: Confidence map ($T_{\rm eff}$, $\log(g)$) of #4150.

7.7 The CoRoT target #2721 - a close-in binary?

For the candidate IRa01 E2 2721 (henceforth #2721) a CFHT image revealed two other objects in and one object at the border to the mask of CoRoT. However, these objects are faint enough not to compromise spectroscopy, but could influence the transit depth in the photometric light curves. The light curves showed a 0.80% transit depth with a period of 0.61 days.
The RV measurements by Sebastian (2016) had an accuracy of a few km s^{-1} only, as the star rotates very fast ($v \sin i \gtrsim 300$km s^{-1}). Fitting a sinusoidal to SANDIFORD and CAFE data revealed a semi amplitude of almost 200 km s^{-1}. This result would lead to a maximum companion mass of 1.2 M$_\odot$, assuming an A6V main-sequence star of almost 2 M$_\odot$. This would be a very close binary, because of its short period of only 0.6 days. Sebastian (2016) concludes that the companion could be an unseen massive compact object like a white dwarf ($R \approx R_\oplus$). His fit to the RV measurements is phase shifted to the light curve of half the period. The star was further observed with higher SNR spectra taken with UVES and again with CAFE and the subsequent analysis could not confirm the previous results from the RV-measurements, but indicates a much lower semi amplitude of only $K = 17$ km s^{-1} and a mass limit of 0.12 M$_\odot$ ($\approx 125\,M_{\rm Jup}$), which now rather hints at a low-mass stellar companion but still cannot explain the phase shift. Sebastian (2016) also reported RV shift between the H$_\alpha$ and H$_\beta$ lines which we could not confirm. We downloaded the UVES Phase 3 spectra from the archive and found a consistent shift for the Balmer lines.
Our spectroscopic results cannot confirm the main-sequence nature of the star, as our fit ended up in a low surface gravity of $\log(g) = 3.00$, which corresponds to our grid border of that parameter. We therefore allowed the fitting routine to extrapolate the grid to even lower values, but the fit still remains at the above given value. The results are listed in Table 7.8 and the confidence map is shown in Figure 7.14, which clearly hints to a evolved star (giant). Assuming that the transit is on target on the star with our derived stellar radius, the companion would have a radius of $r \approx 7\,R_{\rm Jup}$,

Table 7.8: Results of the quantitative spectral analysis of the UVES data of #2721, in comparison with the solar values (abundance vector from Table 3.1). *: a correction of 0.15 dex to the surface gravity is applied, as explained in Section 3.5.1.

parameter	result	solar
resolution	60000	
<SNR>	354	
$T_{\rm eff}$	8049^{+161}_{-162}	
$\log(g)^*$	$3.15^{*\ +0.21}_{-0.21}$	
$v \sin i$	318^{+3}_{-2}	
ζ	16^{+82}_{-17}	
$v_{\rm rad}$	$-6.63^{+2.25}_{-0.99}$	
ξ	$1.98^{+0.03}_{-0.24}$	
C	$-3.34^{+0.19}_{-0.26}$	–3.71
Mg	$-4.28^{+0.20}_{-0.18}$	–4.48
Si	$-4.50^{+0.17}_{-0.09}$	–4.54
Fe	$-4.89^{+0.11}_{-0.12}$	–4.52
Na	$-6.19^{+0.25}_{-0.17}$	–5.77
Al	$-7.55^{+1.07}_{-0.09}$	–5.57
P	$-5.05^{+0.47}_{-2.66}$	–6.61
Ca	$-6.17^{+0.17}_{-0.16}$	–5.75
Sc	$-9.93^{+0.52}_{-0.72}$	–8.99
Ti	$-7.24^{+0.26}_{-0.22}$	–7.13
V	$-7.60^{+0.19}_{-0.28}$	–8.08
Cr	$-6.81^{+0.34}_{-0.29}$	–6.40
Mn	$-7.12^{+0.41}_{-0.33}$	–6.56
Ni	$-6.38^{+0.34}_{-0.38}$	–5.84
Sr	$-10.36^{+0.68}_{-0.86}$	–9.17
Ba	$-10.57^{+0.48}_{-0.30}$	–9.75
Y	$-9.99^{+0.50}_{-0.80}$	–9.79
Zr	$-9.40^{+0.29}_{-0.29}$	–9.41

but with the inconsistent mass estimate, the nature of this target remains unclear and needs further investigations, also to decide if the system consists of two or even more stellar objects. A substellar companion can be ruled out here.
The chemical abundances relative to solar values are given in Table 7.15. As the star is rotating very fast, the uncertainties on the abundances are quite large. C, Mg and V are overabundant, while most of the other elements are underabundant if not solar. So we classify this star as a metal-poor A-type giant.

7.8 The CoRoT target #0108

The flat bottom transit in the light curve of LRc07 E2 0108 (henceforth #0108) with a period of P = 14.45 days and a transit depth of 1.82% together with an assumed circular orbit fittet to the RV measurements with SANDIFORD and TWIN (see Figure 7.16) would lead to a projected mass of $m \sin i$ = 0.22 $M_\odot$ of the companion. Assuming an A9IV primary with R = 1.7 $R_\odot$ and M = 1.8 $M_\odot$, the companion radius would be R = 2.2 $R_{\rm Jup}$($\approx$ 0.22 $R_\odot$) and using the low mass star radius-mass-relation would

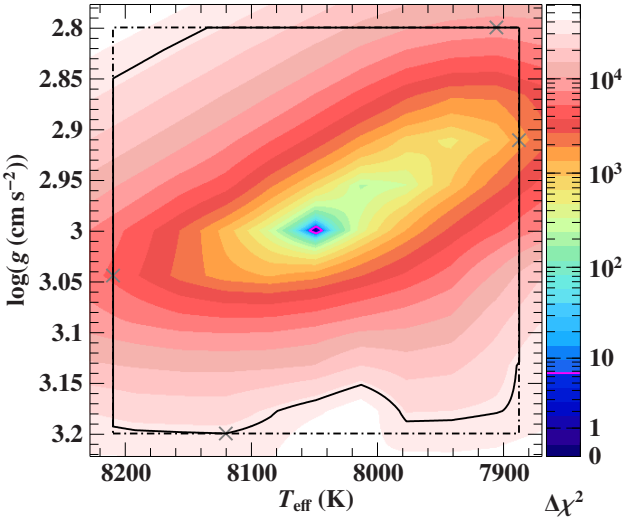

Figure 7.14: Confidence map ($T_{\rm eff}$, $\log(g)$) for #2721.

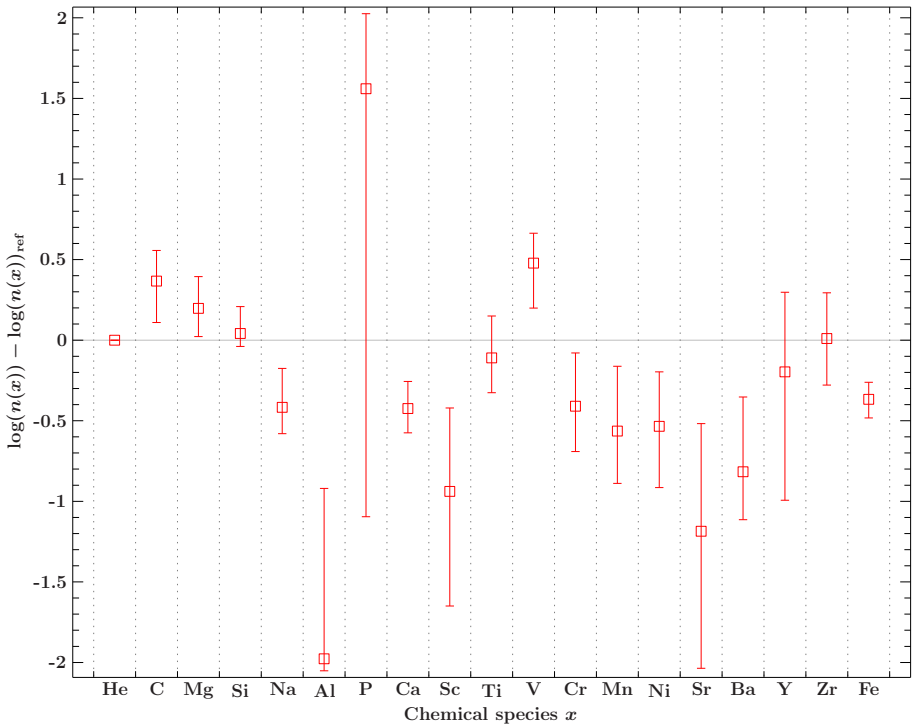

Figure 7.15: Abundances of #2721 relative to solar values from the quantitative spectral analysis of the UVES spectrum. The uncertainties were adopted from the confidence maps (Figure 7.14) with uncertainties on $T_{\rm eff}$ of 162 K and $\log(g)$ = 0.2 dex.

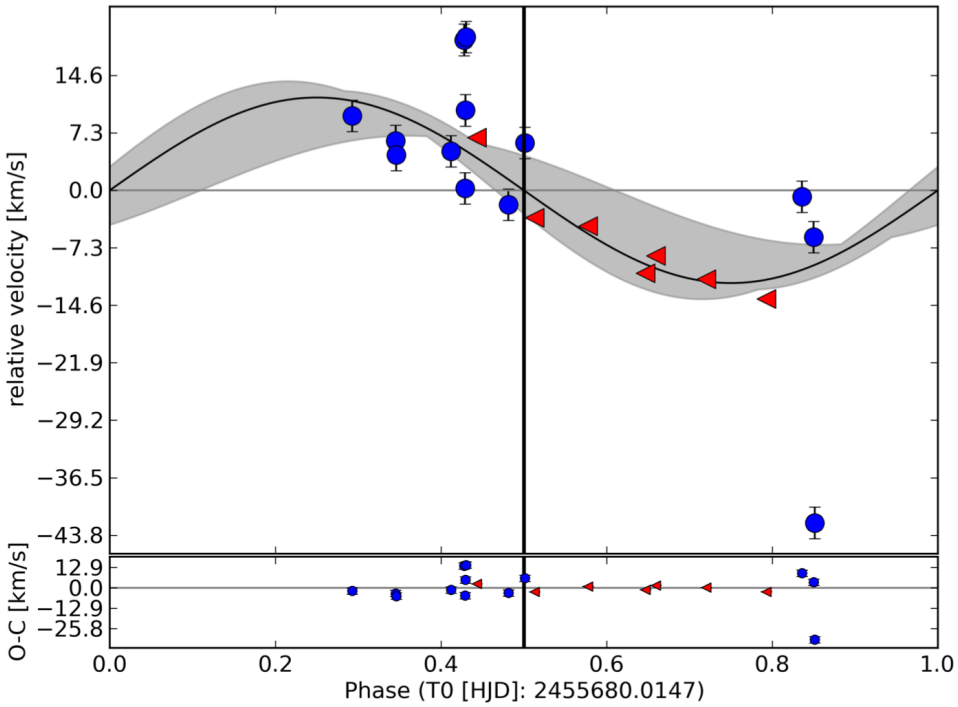

Figure 7.16: Radial velocity curve of #0108. Measurements with SANDIFORD are in red, with TWIN in blue. The Figure is adopted from Sebastian (2016), the grey area indicates the errors from the bootstrapping method.

lead to an M-dwarf with a consistent mass. Unfortunately we only have the low resolution TWIN data and are thus unable to perform a detailed spectral fitting, but a coarse fit to the data leads to $T_{\rm eff}$ = 7100 K, $\log(g)$ = 4.20 dex (after correction of 0.15 dex on that parameter, see Section 3.5.1) and a low metallicity of Z ≈ -0.7 dex which would lead to an early F-type star on the main-sequence and is thus close to the slightly evolved late type A-star, classified by Sebastian (2016). This results in a slightly smaller mass for the star ($M \approx 1.5^{+0.2}_{-0.2}$) and thus also the upper mass limit for the companion ($m \sin i$ = 0.20 $M_\odot$). The age of the system is about 1.1 Gyrs. The stellar radius would be revised to $R \approx 1.6^{+0.7}_{-0.7}\,R_\odot$) and the corresponding radius of the companion would lead to the same value as Sebastian (2016): $r \approx 2.2 R_{\rm Jup}$. A spectrum with a higher quality is required to constrain the stellar parameters and to reveal the nature of this system, but the RV curve hints to a massive companion and thus excludes a substellar companion.

7.9 The CoRoT target #0307 (CoRoT 36b)

CoRoT observed the target for almost 3 month (81 days) in 2011 with a cadence of 32 seconds. During this time, fifteen transits were observed, leading to a period of ≈ 5.62 days and a transit depth of 0.93 %. With infrared images taken with PISCES at the LBT, two nearby and formerly unknown stars have been found, but could both be excluded to be a reason for a false positive (FP), because they are too faint in the infrared images of PISCES, compared to the optical observations of CoRoT when taking the extinction of $A_v = 0.84 \pm 0.14$ mag into account. Several spectra were taken in

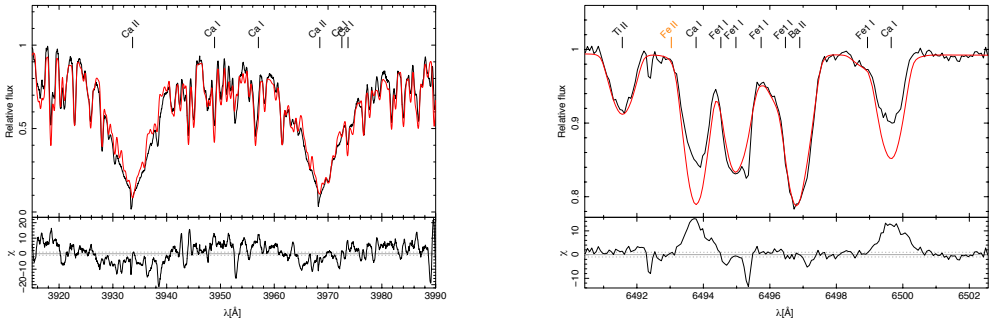

Figure 7.17: Strong Ca H+K lines and too strong Ca I lines in the spectrum of #0307.

(6) and out (10) of transit with the FIES spectrograph at the NOT and ten in transit and one out of transit with UVES at the ESO-VLT. The out of transit observations from FIES gives an upper limit for the companion mass of $<1.4\,M_{\mathbf{Jup}}$. A further hint to a transiting object results from time resolved spectroscopy. The RM-effect could be clearly detected by comparing the in and out of transit RV-measurements of FIES and UVES. The constant offset of about 0.4 km s^{-1} indicated a pole on orbit, which also is in agreement with the rather low $v \sin i$ ($\approx 25\,\mathrm{km\,s^{-1}}$). The spectral type fits best to template spectra of F3V and F5IV, respectively. The fundamental spectral parameters were derived spectroscopically with two different methods using LTE models as described in Deleuil et al. (2008), with the fitting tool Spectroscopy Made Easy (SME) (Valenti & Piskunov, 1996) and for the abundance analysis the software tool VWA as described in Bruntt et al. (2002), to be $T_{\mathrm{eff}} = 6430 \pm 70\,\mathrm{K}$ and $\log(g) = 4.0$.
We performed a quantitative spectral analysis of the UVES spectrum, the results are listed in Table 7.9 and give similar atmospheric parameters. The confidence map in Figure 7.19 demonstrates that the best fit has been achieved. The metallicity is slightly above solar, except carbon and sodium which are around solar, while aluminum, manganese and cerium are underabundant as can be seen in Figure 7.20. The overall fit looks quite well, with some exceptions. Conspicuous are the strong calcium H and K lines. In the final fit, these are quite well reproduced, but numerous smaller Ca I+II lines are mostly too strong (see Figure 7.17). The Balmer lines are matched well, except H_α and H_β, where the cores are broader in the observed spectrum. As the spectrum is quite densely populated by lines, it remains unclear wether there are some missing lines in the model spectra or there are just shortcomings in the atomic data used. For example Fe I lines are too weak in the model spectra, which is also the case in hotter stars. Also some missing lines of Co, Cr, Fe and Mn, which are quite weak in the hotter stars, could be the reason for some line-shaped signs in the residuals. There are some hints for the presence of peculiar elements, e.g. weaker lines of Eu, Nd and Er (see Figure 7.18) and an enhancement of metals relative to solar values.
The trend to underestimate $\log(g)$ (see Chapter 3.5.1), continues for the low temperatures. Thus we also added a correction of 0.15 dex on $\log(g)$. With these parameters and tracks of Ekström et al. (2012), we come to a similar upper mass limit of the companion as Grziwa et al., but we derived a slightly smaller radius of the campion, which is $r \approx 1.3 R_{\mathrm{Jup}}$, which perfectly matches with a hot Jupiter companion.

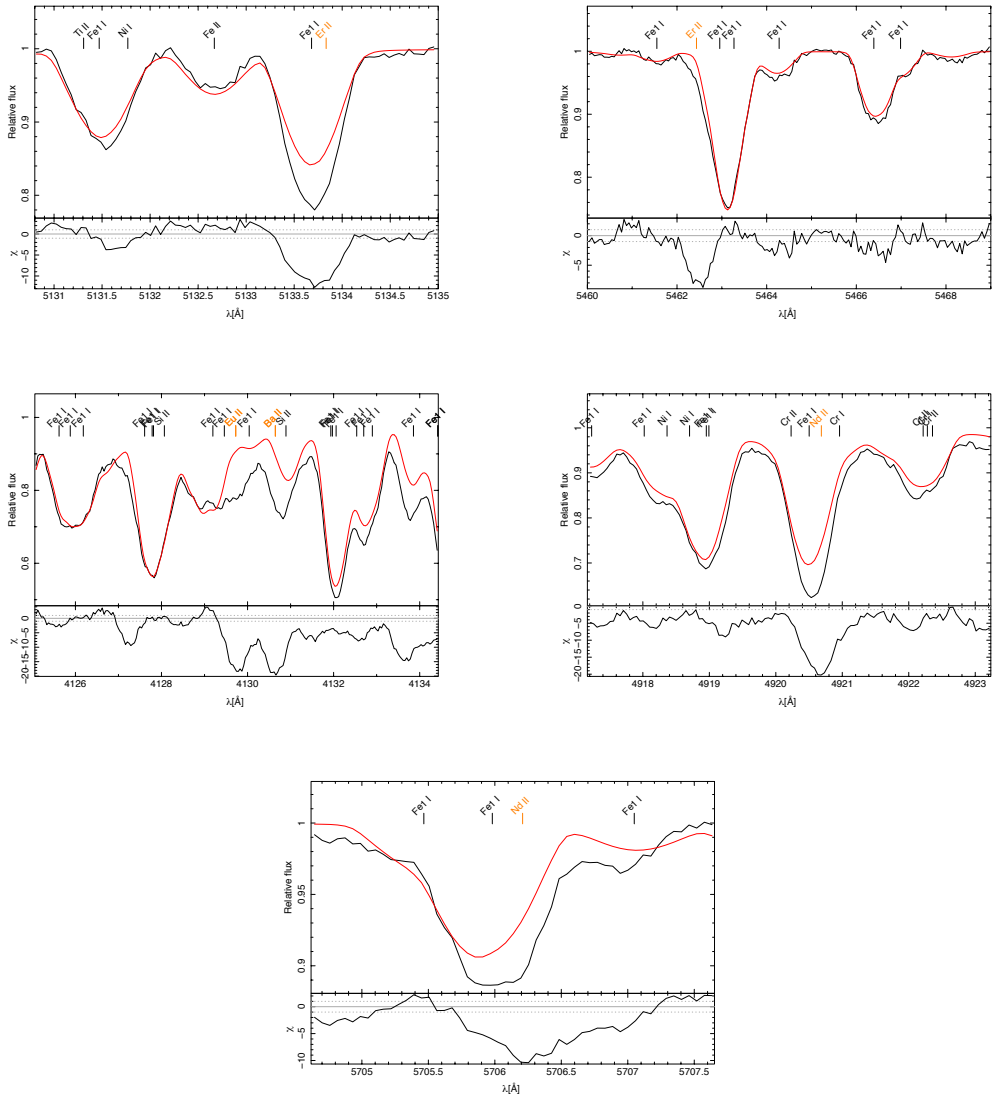

Figure 7.18: Identified peculiar lines of Er, Nd and Eu in the spectrum of #0307.

Table 7.9: Results of the quantitative spectral analysis of the UVES spectrum of #0307, in comparison with the solar values (abundance vector from Table 3.1). *: a correction of 0.15 dex to the surface gravity is applied, as explained in Section 3.5.1.

param.	result	uncert.	solar value
$T_{\rm eff}$	6806	± 137	
$\log(g)^*$	4.28^*	± 0.21	
$v \sin i$	22.25	$^{+0.27}_{-0.01}$	
ζ	16.42	$^{+0.78}_{-1.73}$	
$v_{\rm rad}$	24.21	$^{+0.06}_{-0.08}$	
ξ	1.96	$^{+0.04}_{-0.14}$	
C	-3.72	$^{+0.13}_{-0.09}$	–3.71
Mg	-4.34	$^{+0.03}_{-0.04}$	–4.48
Si	-4.47	$^{+0.21}_{-0.17}$	–4.54
Fe	-4.26	$^{+0.04}_{-0.01}$	–4.52
Na	-5.78	$^{+0.06}_{-0.05}$	–5.77
Al	-5.75	$^{+0.05}_{-0.04}$	–5.57
Ca	-5.21	± 0.02	–5.75
Sc	-8.79	$^{+0.13}_{-0.11}$	–8.99
Ti	-6.93	$^{+0.08}_{-0.06}$	–7.13
V	-7.74	$^{+0.07}_{-0.06}$	–8.08
Cr	-6.18	$^{+0.06}_{-0.05}$	–6.40
Mn	-6.73	$^{+0.09}_{-0.07}$	–6.56
Ni	-5.70	$^{+0.06}_{-0.05}$	–5.84
Sr	-8.82	$^{+0.11}_{-0.10}$	–9.17
Ba	-9.64	$^{+0.13}_{-0.09}$	–9.75
Y	-9.59	$^{+0.09}_{-0.08}$	–9.79
Zr	-9.15	$^{+0.16}_{-0.13}$	–9.41
La	-10.61	$^{+0.10}_{-0.09}$	–10.89
Ce	-10.85	$^{+0.13}_{-0.12}$	–10.42

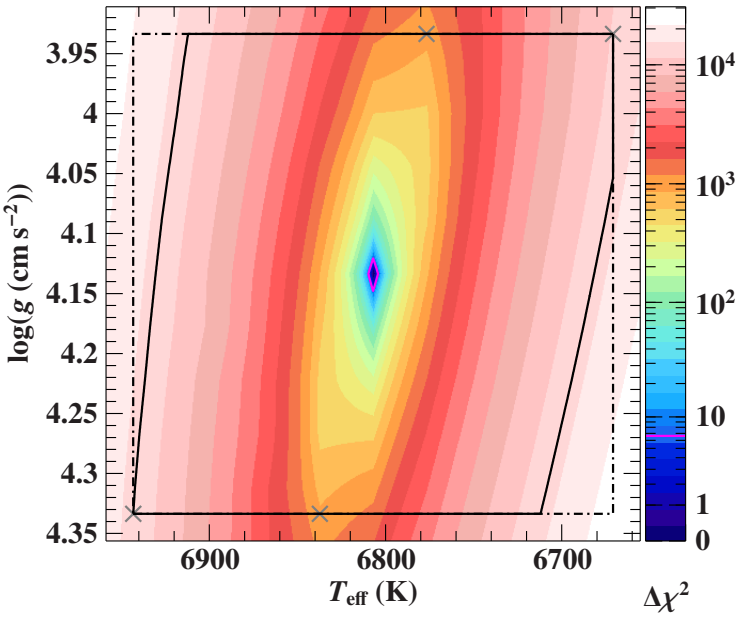

Figure 7.19: Confidence map ($T_{\rm eff}$, $\log(g)$)around the best fit of #0307.

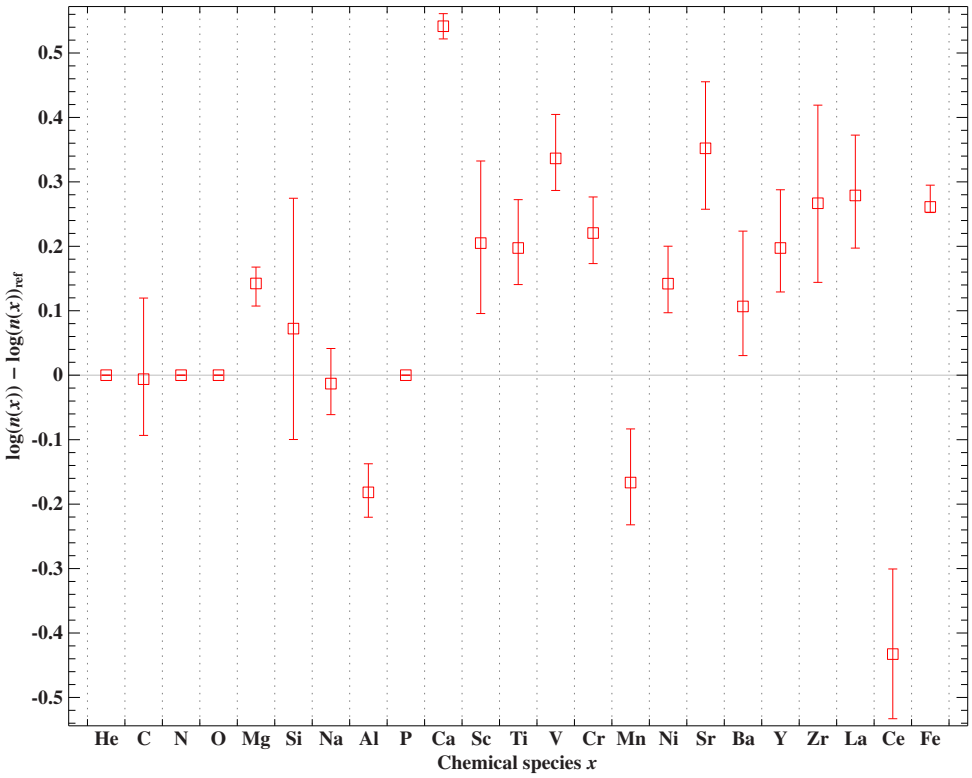

Figure 7.20: Differential abundances for #0307, relative to solar values. The errors are derived from the confidence map (Figure 7.19).

7.10 Deriving the properties of the companion

The following formulas were used to derive the results in Table 7.10. The formulas assume a circular orbit and that the companion mass can be neglected ($(M+m) \rightarrow M$). An estimate for the companion's radius, neglecting the limb darkening effect, comes simply from the relativ areas of the projected circles of the two bodies during the maximum eclipse, with the transit depth ΔF (in %) and $\mathrm{R}_{\odot} = 9.7401 \cdot \mathrm{R}_{\mathrm{Jup}}$:

$$r = 9.7401 \cdot \sqrt{\Delta F} R \tag{7.1}$$

, with r as companion's and R as star's radius. The companions mass m in units of Jupiter masses is given with the following equation:

$$m \sin i = \left(\frac{PM^2}{2\pi G} \right)^{\frac{1}{3}} = 4.6951 \cdot K (PM^2)^{\frac{1}{3}} \tag{7.2}$$

where P is the period of the eclipses in days, the masses of the companion $m[M_{\mathrm{Jup}}]$ and its host star $M[\mathrm{M}_{\odot}]$. K denotes the semi-amplitude of the RV-curve in $\mathrm{km\,s^{-1}}$. The minimum inclination i can be derived with the condition for a transit $\cos i = \frac{R+r}{a}$ through the separation of a circular two-body system a from Kepler's third law, while the mass of the companion is neglected $((M + m) \rightarrow M)$, via

$$i \geq \arccos \left(\frac{R + (r/9.7401)}{a} \right) \tag{7.3}$$

and

$$a = \left(\frac{MP^2 G}{4\pi^2} \right)^{\frac{1}{3}} = 4.2044 \cdot (MP^2)^{\frac{1}{3}} \tag{7.4}$$

, where r and R are the the radii of star and companion in units of stellar radii $\mathrm{R}_{\odot}$ and the radius of Jupiter R_{Jup}, respectively.
The resulting companion mass in Table 7.10 is derived by variing the inclination i for its minimum value and $i = 90^{\circ}$ and taking its mean value. Its uncertainty is derived by taking the extrema of the results obtained by variing all the other parameters within its uncertainties, if available. The mass and radius of the star and the semi-amplitude K, respectively its upper limit are kept fixed. An extreme case is #2721, where no minimum inclination could be derived, as for some parameter combinations (also the mean values) the separation a is smaller than the radii of star plus companion. Hence the star cannot be a giant, that is the surface gravity is underestimated.

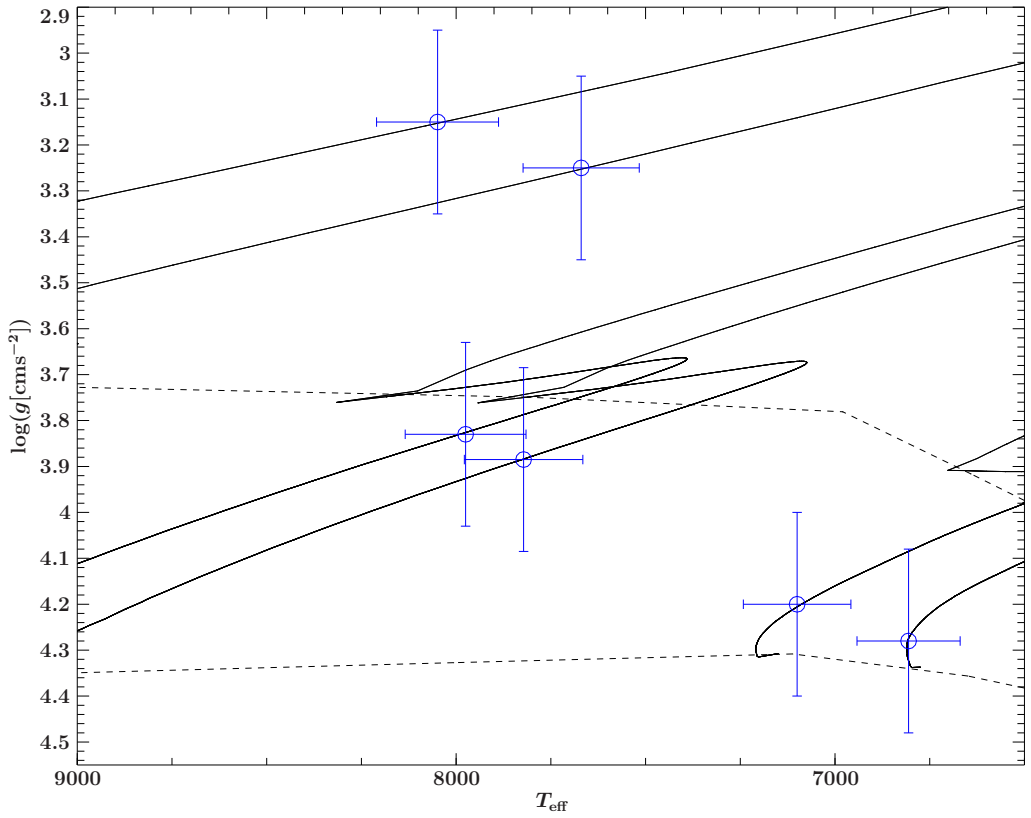

Figure 7.21: Final parameters in the $T_{\rm eff}$-$\log(g)$ diagram for the analyzed IMS CoRoT targets in this work. The black lines are evolutionary tracks from Ekström et al. (2012). The corresponding masses and radii are listed in Table 7.10. The dashed lines mark the main-sequence-phase. The rotational frequency is fixed to $w = 0.2$ [critical frequencies].

Table 7.10: Overview of the results of the reanalyzed spectra of the CoRoT targets and their best fit stellar parameters (mass, radius and age) derived from evolutionary tracks from Ekström et al. (2012), as well as the derived companion mass m and radius r. For #1475 and #1712 the mean of the spectroscopic results were taken. The period P, transit depth ΔF and semi-amplitude of the RV-curve K, respectively its upper limit and the previous results (from Sebastian (2016), if not cited otherwise) for the companion mass and radius is listed (lower part of the Table). The errors for the stellar mass and radius are estimated from the evolutionary tracks from Table 7.21 by variing $\log(g)$ within the errors.
[1]: results by Grziwa (in prep.) for #0307.
[2]: results by Moutou et al. (2009) for #1712.

star	#4150	#2721	#2657	#1712	#1475	#0108	#0307
$M[M_\odot]$	4.28 ± 0.15	3.22 ± 0.50	2.78 ± 0.60	2.13 ± 0.30	2.00 ± 0.30	1.51 ± 0.15	1.39 ± 0.15
$R[R_\odot]$	2.26 ± 0.80	7.87 ± 1.40	6.49 ± 1.40	3.48 ± 0.80	2.68 ± 0.80	1.60 ± 0.25	1.35 ± 0.25
∼age [Myrs]	4	301	465	946	953	1095	336
$<T_{\rm eff}>$	15900	8049	7670	7975	7822	7100	6806
$<\log(g)>$	4.44	3.15	3.25	3.83	3.885	4.2	4.28
$\sim v \sin i$ [km s^{-1}]	35	320	130	50	150	25	25
m [$M_{\rm Jup}$]	$54.2^{+3.3}_{-3.1}$	$< 148^{+16}_{-15}$	$< 106.5^{+22.3}_{-19.2}$	$< 0.7^{+0.1}_{-0.1}$	$75.6^{+51.3}_{-39.2}$	$177.4^{+67.4}_{-60.7}$	$< 2.1^{+0.2}_{-0.2}$
r [$R_{\rm Jup}$]	1.8 ± 0.6	6.8 ± 1.2	2.8 ± 0.6	1.7 ± 0.4	1.4 ± 0.4	2.1 ± 0.3	1.3 ± 0.2
$a[R_\odot]$	$27.69^{+0.32}_{-0.33}$	$4.47^{+0.22}_{-0.24}$	$17.63^{+1.19}_{-1.37}$	$10.67^{+0.48}_{-0.53}$	$8.74^{+0.42}_{-0.46}$	$28.62^{+0.92}_{-0.98}$	$14.83^{+0.52}_{-0.55}$
i [°]	≥ 83.5	–	≥ 60.9	≥ 65	≥ 65.1	≥ 86.1	≥ 83.5
m [$M_{\rm Jup}$]	$63.5^{+1.7}_{-2.4}$	> 125	~ 60	–	$81.5^{+4.8}_{-4.3}$	~ 220	1.4 ± 0.2[1]
r [$R_{\rm Jup}$]	2.4 ± 0.3		~ 0.7	–	1.6 ± 0.1	2.2 ± 0.2	1.9 ± 0.1[1]
K [km s^{-1}]	2.17 ± 0.07	< 17	< 6.4	< 0.060[2]	7.7 ± 3.46	11.78 ± 3.46	< 0.2[1]
P [days]	8.17	0.61	5.15	2.77[2]	2.12	14.45	5.62
ΔF [%]	0.65	0.8	0.2	0.24[2]	0.3	1.82	0.93

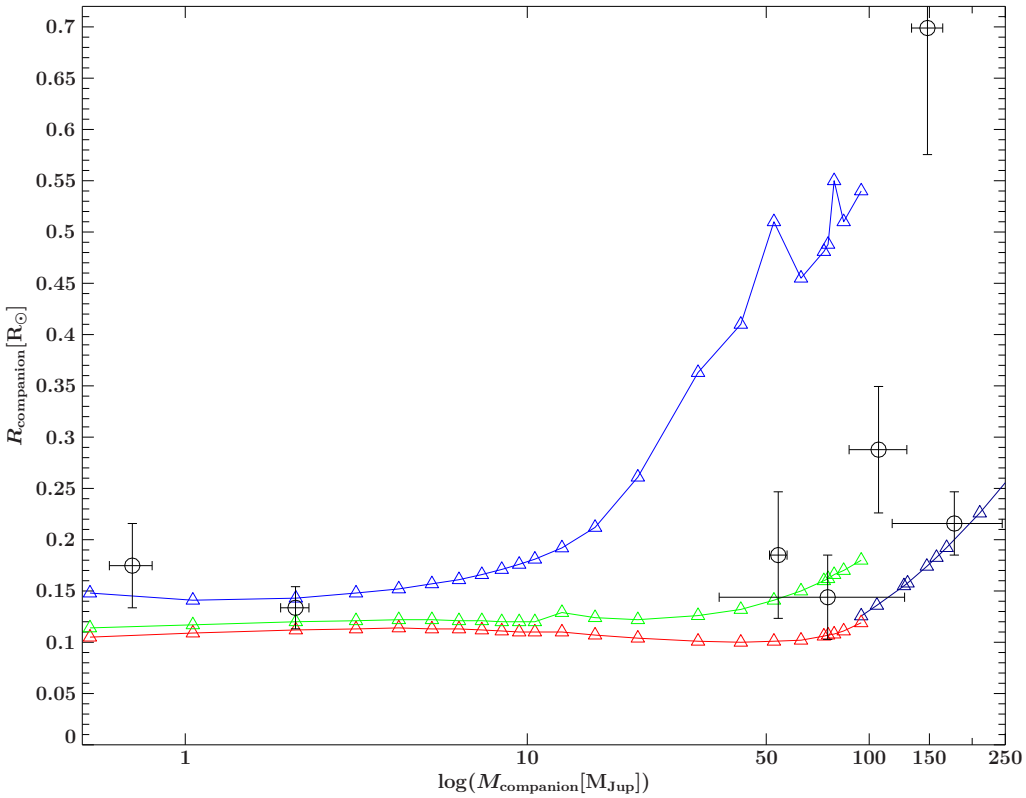

Figure 7.22: Results with error bars for the companions around the CoRoT targets analyzed in this work (in black from left to the right: #1712, #0307, #4150, #1475, #2657, #2712, #0108). On the left hand side the isochrones from Baraffe et al. (2002) are shown for 0.005, 0.1, and 0.5 Gyrs (blue, green, red triangles, respectively). On the right hand side the dark blue triangles shows the isochrone for 1Gyr for LMS from Bressan et al. (2012). Note that for four of the stars, the companion mass estimate is as the semi amplitude K just restricted to an upper limit.

7.11 Conclusions

As discussed in Section 7.1, the close-in planet frequency of IMS is lower than for solar like stars. In this work, we concentrated on the detailed analysis of stars, for which CoRoT light curves hint at the presence of the hot Jupiter type. Out of the 21 top CoRoT targets, selected by Sebastian (2016), we analyzed the 7 most interesting stars in more detail. Our investigations results in more precise stellar parameters and can thus revise the mass and radius of the companions as well as improved values for the (see Table 7.10). The most probable candidate for a substellar companion around an A-type main-sequence star is #1475. The derived atmospheric parameters of two high-quality spectra leads to classification as a peculiar Ap star on the main sequence, which confirms the results by Sebastian (2016). The mass of $m \approx 82\,M_{\rm Jup}$ is at the border of a BD or stellar companion. Together with the small radius of $r \approx 1.6 R_{\rm Jup}$, it is likely to be a brown dwarf.
The most interesting substellar companion was found around the star #4150, which would be the first one detected around a B-type star. Evolutionary tracks leads to a very young host star with a mass of $M = 4.28 \pm 0.15\,\mathrm{M}_\odot$ and a radius of $R = 2.26 \pm 0.80\,\mathrm{R}_\odot$ near the ZAMS with a companion of about $64\,M_{\rm Jup}$ and $r \approx 2.4\,R_{\rm Jup}$, that is a BD. The host star itself is a young main-sequence star with a quite high metal abundance and at the same time helium-poor.
Two of the stars, #2657 and #2721 analyzed in this work, are listed by Sebastian as unsolved cases. For both our spectroscopic analysis hints more at giant stars and thus their radius would be higher. Their derived mass is in addition outside of the mass range for IMS ($1.3\,\mathrm{M}_\odot - 2.1\,\mathrm{M}_\odot$ from Guenther et al., 2016). The UVES spectrum of #2657 together with evolutionary tracks hints at a mass of the companion, which is close to the stellar mass limit. But the radius is inconsistent with a substellar nature. In addition the spectrum shows strong hints for a stellar companion, because of shallow absorption lines and makes the substellar companion hypothesis unlikely. The overall abundances are quite normal (nearly solar) for an A-type star. #2721 has contradictory RV measurements and might be a multiple system. The spectroscopic analysis results in a metal poor giant. A substellar companion can be ruled out. Furthermore, assuming a system consisting of a giant and one companion would result in a very close orbit. For the mean value for the mass and assuming a circular orbit and that the companion mass is much smaller than that of the primary, the distance would be approximately half the primaries radius $a \approx 4.5\,\mathrm{R}_\odot$. So the system might be a quite interesting target for further investigation.
The RV curve of target #0108 hints at a binary star. We revised the atmospheric stellar parameters and derived a mass of $\sim 177\,M_{\rm Jup}$ and a radius of $r = 2.1 \pm 0.3\,\mathrm{R}_{\rm Jup}$, consistent with the results of Sebastian (2016). The companion is confirmed to be a late type star.
Also a quite interesting target is #1712. It was rejected by Moutou et al. (2009) to be a candidate, who concluded that the system might be a triple system. But we could not find signatures of a stellar companion in two high-quality spectra. If the small RV variation in the HARPS spectra measured by Moutou et al. (2009) is reliable, the mass of a possible companion would be roughly half a Jupiter mass and makes it together with the very small transit depth a very interesting candidate for a planet around an A-type main-sequence star. This star would be the only A-type star in our sample that actually hosts a hot Jupiter planet.
We derived a 50% higher mass of $m = 2.1\,M_{\rm Jup}$ as Grziwa et al. for the compan-

ion. The companion size is smaller ($r = 1.3 \pm 0.2 R_{\mathrm{Jup}}$) as by Grziwa et al. (in prep., $r = 1.9 \pm 0.2 R_{\mathrm{Jup}}$), which now fits even better to evolutionary tracks (by Baraffe et al., 2002, see also Figure 7.22).
Thus we conclude, that for IMSs the lifetime of the protostellar disc is not long enough, respectively the migration mechanism is not effective enough, to produce massive, close-in planets and that in-situ genesis of those planets is unlikely.

Chapter 8

Future work

In this work we applied a new method for an objective, χ^2-based spectroscopic analysis of early-type stars, which had been developed by Irrgang et al. (2014), for the first time on high resolution spectra of A-type stars. We studied a sample of well-observed, bright standard stars, the planet host star WASP33, and the evolved A+B binary SWASPJ0247. The main target sample was selected from CoRoT light curves and consisted of seven intermediate mass stars, mostly of spectral type A. These stars show shallow transits, indicating the presence of small, likely substellar companions.
The modeling of the stellar atmosphere is done with the so called hybrid approach introduced by Przybilla et al. (2006), i.e., computing the temperature-density stratification under the assumption of local thermodynamic equilibrium (LTE), of a plane-parallel, homogeneous and line-blanketed atmosphere. The detailed spectral analysis is done by using different fitting algorithms and χ^2-minimization, to find the best match of the synthetic models in a multi-parameter space to the observational data. We have shown, that this spectroscopic analysis method is indeed capable of deriving basic stellar parameters in the temperature range from 12000 down to 6500 K, as well as quantitative measurements of chemical abundances in their atmospheres at high precision. We applied this technique, which has been developed for B-type stars, for the first time for A-type stars. In principle this works shows, that the blends of lines from different chemical elements can not be treated correctly, which pose a more severe problem than for B-type stars, because such line blends have to be excluded from the fit. Hence, the analysis technique requires much more time for A-type than for B-type stars. Alternatively, correction factors have to be applied to the final results.
In general, A-type stars have much more lines in their optical spectra and also they show various kinds of chemical peculiarity, which makes them more complicated to analyze.
Another main complication is the determination of the surface gravity. Especially for the late A-type stars, the Balmer lines are no longer suitable to determine this parameter. Thus ionization equilibria are crucial diagnostic tools, but essentially only iron and magnesium are suited and line crowding is a severe problem as well. In addition, deviations from the simplification of local thermo-dynamical equilibrium in the modeling of the stellar atmosphere, can result in significant errors on those equilibria, which we have shown in this work.
To improve our models, detailed atomic data for the neutral iron model atom are missing to improve the NLTE calculations. As iron is quite prominent in the opti-

cal spectra of A-type stars, this will be a big step forward for the proper calculation of ionization equilibrium of iron und such help to better constrain the surface gravity of late A-type stars. For the meantime we used an NLTE correction factor from literature. Another big step in that direction would be the implementation of level dissolution in the modeling of the Balmer jump, which is a large improvement to obtain more realistic spectral energy distribution. This would not only improve the modeling of the synthetic stellar structure, but would also allow us to improve the accuracy of the photometric analysis, because the shape of the Balmer jump is a very good indicator for the surface gravity.
The Gaia satellite will provide us with unprecedented precision for the parallax measurements, which gives us a benchmark to further improve the spectroscopic determination of the surface gravity. The new parallax measurements will allow us to check, wether our outlier of our standard star sample HD189849 is due to shortcomings in our analysis technique or results from a erroneous measurement by the Hipparcos survey. Also for our CoRoT targets, for the first time precise parallax measurements will become available and allow us to test our results directly. In particular this will show us, if the mysterious star #2721 is really a giant.
Gaia also will allow us to further test the photometric determination of the surface gravity. Gaia spectrophotometry will be based on low-resolution spectroscopy and will support us with the flux measurements of 30 different wavelengths, while the best resolution is obtained around the Balmer jump, and is therefore ideal to constrain the surface gravity.
Gaia will also find planet host candidates by a time series of astrometric measurements and thus build a good starting point for further investigations in the field of exoplanet research, where our method is very well applicable.
Together with high-quality spectra, our method allows spectroscopist to look for shortcomings in the stellar modeling, such as inappropriate or insufficient atomic data. Furthermore, the abundance determination can be used to test evolutionary models, i.e. to what extend diffusion or gravitational settling is going on in the atmospheres of intermediate-mass stars.
Stellar properties, derived from evolutionary models, such as its mass and radius, can be used to constrain the properties of possible companions. As we have shown, our spectroscopic method in combination with high-precision radial velocity measurements and light-curves, is an ideal combination to investigate transiting companions around intermediate-mass stars. This analysis technique thus is a very good extension to higher masses, in the search for exoplanets and builds a perfect instrument, to better understand the formation and evolution of planets in general.

Appendix A

Bibliography

Abt H.A., Levy S.G., 1985, apjs 59, 229

Abt H.A., Morrell N.I., 1995, apjs 99, 135

Adibekyan V.Z., Delgado Mena E., Sousa S.G., et al., 2012, aap 547, A36

Albrecht S., Winn J.N., Johnson J.A., et al., 2012, apj 757, 18

Allen C., Santillan A., 1991, rmxaa 22, 255

Allende Prieto C., Lambert D.L., 1999, aap 352, 555

Ammler-von Eiff M., Reiners A., 2012, aap 542, A116

Asplund M., Grevesse N., Sauval A.J., Scott P., 2009, araa 47, 481

Bagnulo S., Jehin E., Ledoux C., et al., 2003, The Messenger 114, 10

Baraffe I., Chabrier G., Allard F., Hauschildt P.H., 2002, aap 382, 563

Baruteau C., Papaloizou J.C.B., 2013, apj 778, 7

Bear E., Soker N., 2012, apjl 749, L14

Beaugé C., Nesvorný D., 2012, apj 751, 119

Belorizky D., 1938, L'Astronomie 52, 359

Bertelli G., Bressan A., Chiosi C., Angerer K., 1986, aaps 66, 191

Böhm-Vitense E., 1958, ZA 46, 108

Bowler B.P., Johnson J.A., Marcy G.W., et al., 2010, apj 709, 396

Bressan A., Marigo P., Girardi L., et al., 2012, mnras 427, 127

Brogi M., Snellen I.A.G., de Kok R.J., et al., 2013, apj 767, 27

Bruntt H., Catala C., Garrido R., et al., 2002, aap 389, 345

Butler K., Giddings J.R., 1985, in Newsletter of Analysis of Astronomical Spectra No. 9 (Univ. London)

Calvet N., Muzerolle J., Briceño C., et al., 2004, aj 128, 1294

Campbell B., Walker G.A.H., 1985, In: Philip A.G.D., Latham D.W. (eds.) Stellar Radial Velocities, Vol. 88., p.5

Canuto V.M., Goldman I., Mazzitelli I., 1996, apj 473, 550

Canuto V.M., Mazzitelli I., 1991, apj 370, 295

Canuto V.M., Mazzitelli I., 1992, apj 389, 724

Castelli F., Kurucz R.L., 2004, ArXiv Astrophysics e-prints

Cenarro A.J., Peletier R.F., Sánchez-Blázquez P., et al., 2007, mnras 374, 664

Chiang E., Laughlin G., 2013, mnras 431, 3444

Collier Cameron A., Guenther E., Smalley B., et al., 2010, mnras 407, 507

CoRot Team 2016, The CoRoT Legacy Book: The adventure of the ultra high precision photometry from space, by the CoRot Team

Cotten T.H., Song I., 2016, apjs 225, 15

Cowley C.R., Hubrig S., Ryabchikova T.A., et al., 2001, aap 367, 939

Cumming A., Butler R.P., Marcy G.W., et al., 2008, pasp 120, 531

Deleuil M., Deeg H.J., Alonso R., et al., 2008, aap 491, 889

Ekström S., Georgy C., Eggenberger P., et al., 2012, aap 537, A146

Fabrycky D., Tremaine S., 2007, apj 669, 1298

Georgy C., Ekström S., Granada A., et al., 2013, aap 553, A24

Giddings J.R., 1981, Ph.D. thesis, , University of London, (1981)

Goldreich P., Tremaine S., 1980, apj 241, 425

Gray R.O., Corbally, J. C., 2009, Stellar Spectral Classification

Gray R.O., Corbally C.J., Garrison R.F., et al., 2006, The Astronomical Journal 132, 161

Grenier S., Baylac M.O., Rolland L., et al., 1999, aaps 137, 451

Guenther E.W., Fridlund M., Alonso R., et al., 2013, aap 556, A75

Guenther E.W., Sebastian D., Gandolfi D., et al., 2016, III.7 Planets orbiting stars more massive than the Sun, p. 149

Gullikson K., Kraus A., Dodson-Robinson S., 2016, aj 152, 40

Gulliver A.F., Hill G., Adelman S.J., 1994, apjl 429, L81

Hartman J.D., Bakos G.Á., Buchhave L.A., et al., 2015, aj 150, 197

Hatzes A.P., 1997, mnras 288, 153

Hauck B., Mermilliod M., 1997, VizieR Online Data Catalog 2215

Henry G.W., Fekel F.C., 2005, aj 129, 2026

Hill G., Gulliver A.F., Adelman S.J., 2010, apj 712, 250

Houk N., Cowley A.P., 1975, University of Michigan Catalogue of two-dimensional spectral types for the HD stars. Volume I. Declinations -90_ to -53_deg0.

Houk N., Smith-Moore M., 1988, Michigan Catalogue of Two-dimensional Spectral Types for the HD Stars. Volume 4, Declinations -26deg.0 to -12deg.0.

Houk N., Swift C., 1999, In: Michigan Spectral Survey, Ann Arbor, Dep. Astron., Univ. Michigan, Vol. 5, p. 0 (1999), Vol. 5., p. 0

Irrgang A., Przybilla N., Heber U., et al., 2014, aap 565, A63

Irrgang A., Wilcox B., Tucker E., Schiefelbein L., 2013, aap 549, A137

Istrate A.G., Fontaine G., Heuser C., 2017, apj 847, 130

Jaschek C., Andrillat Y., 1998, aaps 130, 507

Jaschek M., Jaschek C., Andrillat Y., 1991, aap 250, 127

Jeffery C.S., Saio H., 2013, mnras 435, 885

Johnson J.A., Howard A.W., Bowler B.P., et al., 2010, pasp 122, 701

Kennedy G.M., Kenyon S.J., 2008a, apj 682, 1264

Kennedy G.M., Kenyon S.J., 2008b, apj 673, 502

Koleva M., Vazdekis A., 2012, aap 538, A143

Kunitomo M., Ikoma M., Sato B., et al., 2011, apj 737, 66

Kunzli M., North P., Kurucz R.L., Nicolet B., 1997, aaps 122

Kupka F., 1996, In: Adelman S.J., Kupka F., Weiss W.W. (eds.) M.A.S.S., Model Atmospheres and Spectrum Synthesis, Vol. 108. Astronomical Society of the Pacific Conference Series, p. 73

Kurucz R.L., 1996, In: Adelman S.J., Kupka F., Weiss W.W. (eds.) M.A.S.S., Model Atmospheres and Spectrum Synthesis, Vol. 108. Astronomical Society of the Pacific Conference Series, p. 160

Lagrange A.M., Bonnefoy M., Chauvin G., et al., 2010, Science 329, 57

Landstreet J.D., 2004, In: Zverko J., Ziznovsky J., Adelman S.J., Weiss W.W. (eds.) The A-Star Puzzle, Vol. 224. IAU Symposium, p.423

Laplace P.S., Young T., 1832, Elementary illustrations of the celestial mechanics of Laplace.

Léger A., Rouan D., Schneider J., et al., 2009, aap 506, 287

Lemke M., 1989, aap 225, 125

Lemke M., 1993, In: Dworetsky M.M., Castelli F., Faraggiana R. (eds.) IAU Colloq. 138: Peculiar versus Normal Phenomena in A-type and Related Stars, Vol. 44. Astronomical Society of the Pacific Conference Series, p. 407

Luhman K.L., 2014, apj 781, 4

Mamajek E.E., 2009, In: Usuda T., Tamura M., Ishii M. (eds.) American Institute of Physics Conference Series, Vol. 1158. American Institute of Physics Conference Series, p.3

Maxted P.F.L., Anderson D.R., Burleigh M.R., et al., 2011, mnras 418, 1156

Maxted P.F.L., Bloemen S., Heber U., et al., 2014, mnras 437, 1681

Maxted P.F.L., Serenelli A.M., Miglio A., et al., 2013, nat 498, 463

Mayor M., Lovis C., Santos N.C., 2014, nat 513, 328

Mayor M., Marmier M., Lovis C., et al., 2011, ArXiv e-prints

Mayor M., Queloz D., 1995, nat 378, 355

Mora A., Merín B., Solano E., et al., 2001, aap 378, 116

Moutou C., Deleuil M., Guillot T., et al., 2013, icarus 226, 1625

Moutou C., Pont F., Bouchy F., et al., 2009, aap 506, 321

Munari U., Sordo R., Castelli F., Zwitter T., 2005, aap 442, 1127

Muzerolle J., Luhman K.L., Briceño C., et al., 2005, apj 625, 906

Napiwotzki R., Schoenberner D., Weidemann V., 1991, aap 243, L5

Napiwotzki R., Yungelson L., Nelemans G., et al., 2004, In: Hilditch R.W., Hensberge H., Pavlovski K. (eds.) Spectroscopically and Spatially Resolving the Components of the Close Binary Stars, Vol. 318. Astronomical Society of the Pacific Conference Series, p.402

Nieva M.F., Przybilla N., 2006, apjl 639, L39

Nieva M.F., Przybilla N., 2007, aap 467, 295

Nieva M.F., Przybilla N., 2008, aap 481, 199

Nieva M.F., Przybilla N., 2010, In: Monier R., Smalley B., Wahlgren G., Stee P. (eds.) EAS Publications Series, Vol. 43. EAS Publications Series, p.167

Nieva M.F., Przybilla N., 2012, aap 539, A143

Paunzen E., 2015, aap 580, A23

Paunzen E., Duffee B., Heiter U., et al., 2001, aap 373, 625

Peale S.J., 1976, Orbital Resonances in the Solar System, Technical report

Prugniel P., Vauglin I., Koleva M., 2011, aap 531, A165

Przybilla N., Butler K., Becker S.R., Kudritzki R.P., 2006, aap 445, 1099

Przybylski A., 1961, nat 189, 739

Rentzsch-Holm I., 1996, aap 312, 966

Rossiter R.A., 1924, apj 60

Santos N.C., Israelian G., Mayor M., 2004, aap 415, 1153

Sarro L.M., Debosscher J., Neiner C., et al., 2013, aap 550, A120

Scholz R.D., Heber U., Heuser C., et al., 2015, aap 574, A96

Sebastian D., Guenther E.W., 2011, In: Schuh S., Drechsel H., Heber U. (eds.) American Institute of Physics Conference Series, Vol. 1331. American Institute of Physics Conference Series, p.329

Smalley B., 1993, aap 274, 391

Smalley B., 2004, In: Zverko J., Ziznovsky J., Adelman S.J., Weiss W.W. (eds.) The A-Star Puzzle, Vol. 224. IAU Symposium, p.131

Smalley B., 2005, Memorie della Societa Astronomica Italiana Supplementi 8, 155

Soubiran C., Le Campion J.F., Brouillet N., Chemin L., 2016, aap 591, A118

Szabó G.M., Szabó R., Benkő J.M., et al., 2011, apjl 736, L4

Takeda Y., Han I., Kang D.I., et al., 2008, Journal of Korean Astronomical Society 41, 83

Tal-Or L., Mazeh T., Alonso R., et al., 2013, aap 553, A30

Valenti J.A., Piskunov N., 1996, aaps 118, 595

VandenBerg D.A., Bond H.E., Nelan E.P., et al., 2014, apj 792, 110

Vigan A., Patience J., Marois C., et al., 2012, aap 544, A9

Villaver E., Livio M., 2009, apjl 705, L81

Walker G.A.H., Walker A.R., Irwin A.W., et al., 1995, icarus 116, 359

Whipple F.L., 1966, Smithsonian Astrophysical Observatory Star Catalog

Winn J.N., Fabrycky D., Albrecht S., Johnson J.A., 2010, apj 718, L145

Zhou G., Rodriguez J.E., Collins K.A., et al., 2016, ArXiv e-prints

Appendix B

WISE J0725-2351, a metal poor, subluminous F-type star

Although we find millions of distant stars with all kinds of surveys, we still have not detected all stars in the solar vicinity (distance $d<25$ pc). Of course, this is true only for the faintest objects, such as M-type stars or white dwarfs (WDs). The Research Consortium on Nearby Stars (RECONS), which is searching for formerly unseen stars in the solar vicinity, added to their list of stars within 10 pc between the years 2000 and 2012 50 M dwarfs and two white dwarfs (which is an increase by 25% and $\approx$ 10%, respectively), based on parallax measurements. If these updated numbers are compared to the stars known within 25 pc distance, there is a lack of up to two-thirds for the larger volume. One reason for this lack could be that nearby stars often are found in surveys, concentrating on the search for high proper motion (HPM) stars, such that slowly moving nearby stars have been overlooked.
Two all-sky infrared imaging surveys were designed, i.a., to search for those nearby objects, as well as cool brown dwarfs and L-type subdwarfs. The Wide-field Infrared Survey Explorer (WISE) was a space based NASA survey, which has been operating over 7.5 years and was observing in four bands at 3.4, 4.6, 12, and 22 µm (W1,W2,W3,W4). Another infra-red survey, 2MASS, was also funded by NASA and the project was led by the University of Massachusetts. The three-channel cameras (J at 1.25µm, H at 1.65 µm, and Ks at 2.17 µm) were installed at two robotic 1.3m telescopes, which are located at the northern hemisphere at Mt. Hopkins in Arizona, and for the southern hemisphere at the Cerro Tololo Inter-american Observatory (CTIO) in Chile.
In a new study for HPM stars by Luhman (2014), which used these two above mentioned surveys, the relative blue star WISE J072543.88- 235119.7 was considered to be a nearby WD, that had been overlooked in previous surveys. Scholz et al. (2015) studied this object to reveal its properties. It was first suspected to be a close WD. But as can bee seen in Figure B.1, the object shows up in the transition region between the WDs and the sdF/G stars in the color-magnitude diagram. The nature of these two populations is quite different, as the WDs are stellar remnants without nucelar fusion burning, while the cool subdwarfs are population II main-sequence stars and still burning hydrogen in their cores and just have smaller radii, due to the lack of metals, which results in a smaller opacity in contrast to the solar metallicity population I stars. To reveal the nature of this object, we applied for spectroscopic follow up observations, which were done with EFOSC2 at the NTT and XSHOOTER at the ESO-VLT.

From the first inspection of the EFOSC2 low resolution spectrum, a WD could be excluded because of very prominent Ca H&K lines. The high resolution XSHOOTER spectra hints to a metal poor star of spectral type F. For the metallicity, a comparison with XSHOOTER archival spectra of the FGK benchmark stars best matches with the halo turn-off [1] star HD 84937, a metal-poor star with [Fe/H] = -2.0 dex and α-enhancement of [α/Fe]= +0.38 (VandenBerg et al., 2014).
We embarked on a quantitative spectral analysis of the flux calibrated spectrum from XSHOOTER, to compare it with ATLAS9 synthetic spectra (Castelli & Kurucz, 2004) to obtain a first estimate for the atmospheric parameters. We compared different models with [Fe/H] =-2.0, alpha enrichment of [α/Fe] =+0.4 and a mixing-length parameter of 1.25. The Balmer jump is sensitive to $\log(g)$ and the Paschen continuum mostly to $T_{\rm eff}$. The best match is found for $T_{\rm eff} = 6250 \pm 100\,$K and $\log(g) = 4.0 \pm 0.2\,$dex, as can be seen in Figure B.3. The result is confirmed by a fit [2] of the Balmer lines and some regions with metals lines to the Munari grid (Munari et al., 2005). To simplify the procedure the α-enhancement was fixed to [α/Fe] = 0.4 and $\log(g) = 4.0 \pm 0.2\,$dex and resulted in $T_{\rm eff} = 6250 \pm 100\,$K, which is in perfect agreement to the above mentioned results. In addition, the fit confirmed a metallicity of [Fe/H] = -2.0 $\pm$ 0.2. The surface gravity indicates that the star is evolved and close to terminating its main-sequence phase. Hence, the star has to be classified as a turn-off star, rather than an sdF star, with a similar age as the benchmark star HD 84937 of 12 Gyrs. Photometry allows the angular diameter through the scaling factor to be derived and together with an estimate for the stellar radius through stellar mass and surface gravity, the distance can be determined (d $\approx$ 400 pc). Using a Monte Carlo simulation for the kinematics of the star in a Galactic potential results in an velocity of the local standard of rest of $v_{\rm LSR} = 242\,{\rm km\,s^{-1}}$. The model used here, is an improved model for the Galactic potential based on the mass model of Allen & Santillan (1991), which consists of a spherically symmetric bulge, an asymmetric disc and a massive spherical dark matter halo (for details see Irrgang et al., 2013). This implies a retrograde orbit of a halo star in a bound orbit, currently passing close to the galactic disc.

[1] the point in the life-time of a star, where the core hydrogen burning phase ends, see Figure B.2

[2] This fit was performed with FITSSB2 Napiwotzki et al. (2004), which uses the χ^2 minimisation technique using a simplex algorithm.

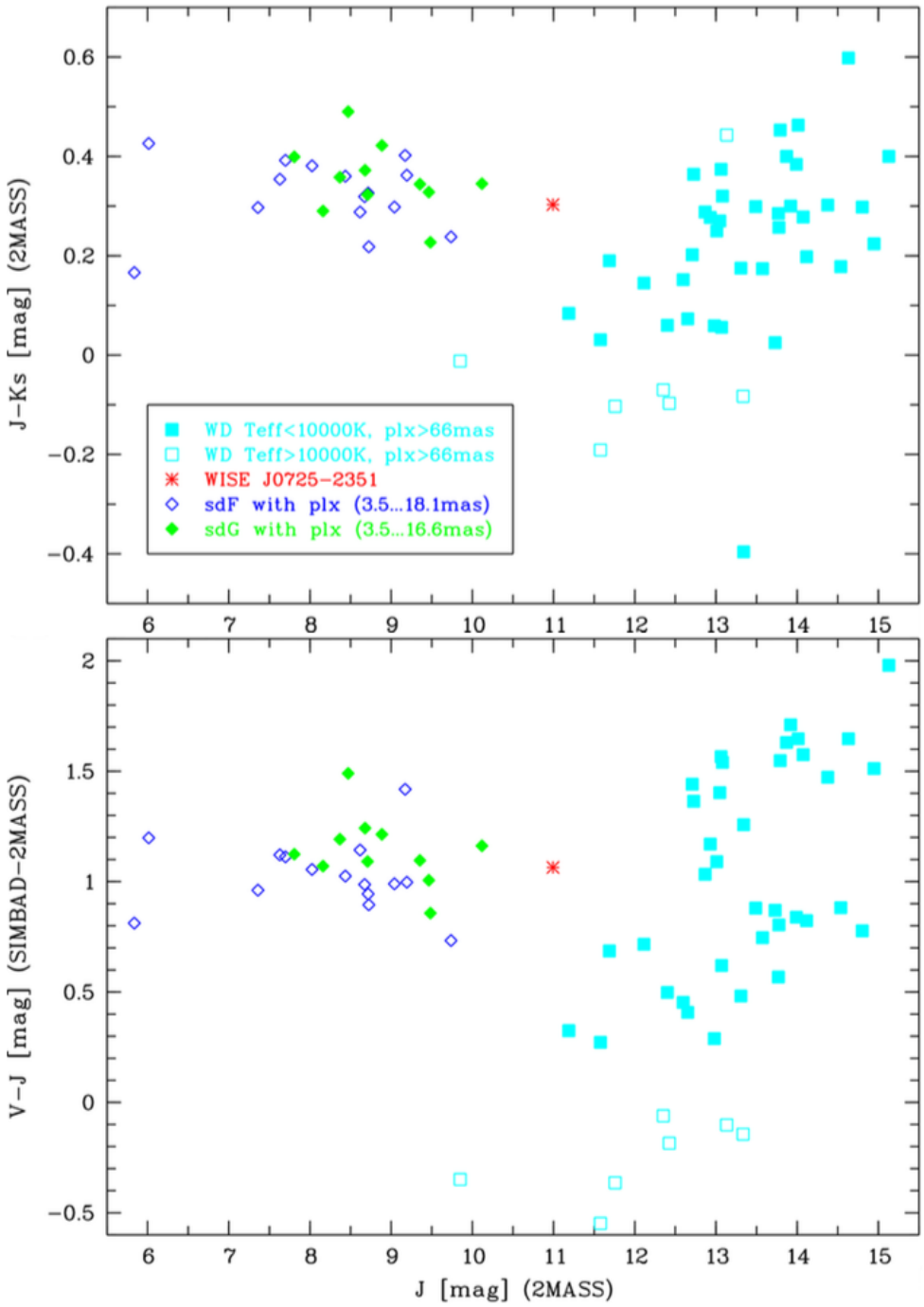

Figure B.1: WISE J0725-2351 compared to nearby WDs and sdF/sdG subdwarfs in two color-magnitude diagrams, adopted from Fig. 1 in Scholz et al. (2015).

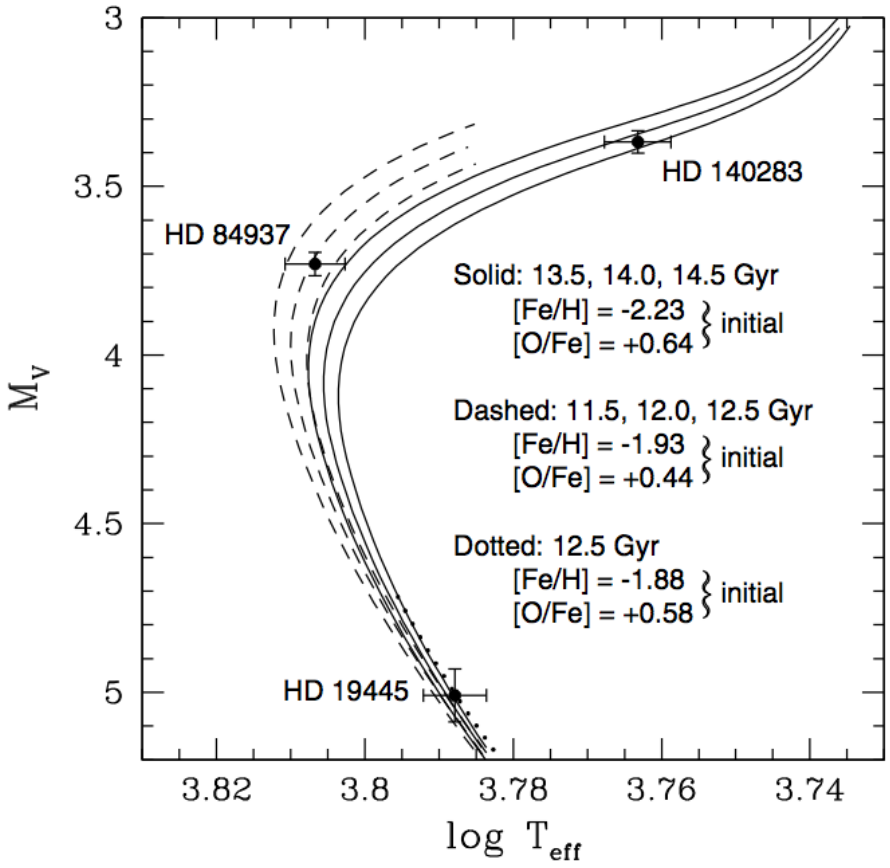

Figure B.2: Isochrones in the $T_{\rm eff}$-visual magnitude diagram for the indicated initial chemical compositions and ages, adopted from Figure 1 in VandenBerg et al. (2014). The comparison star HD 84937 lies at the turn-off point, where the end of the core hydrogen burning phase ends and the star evolves to the subgiant branch.

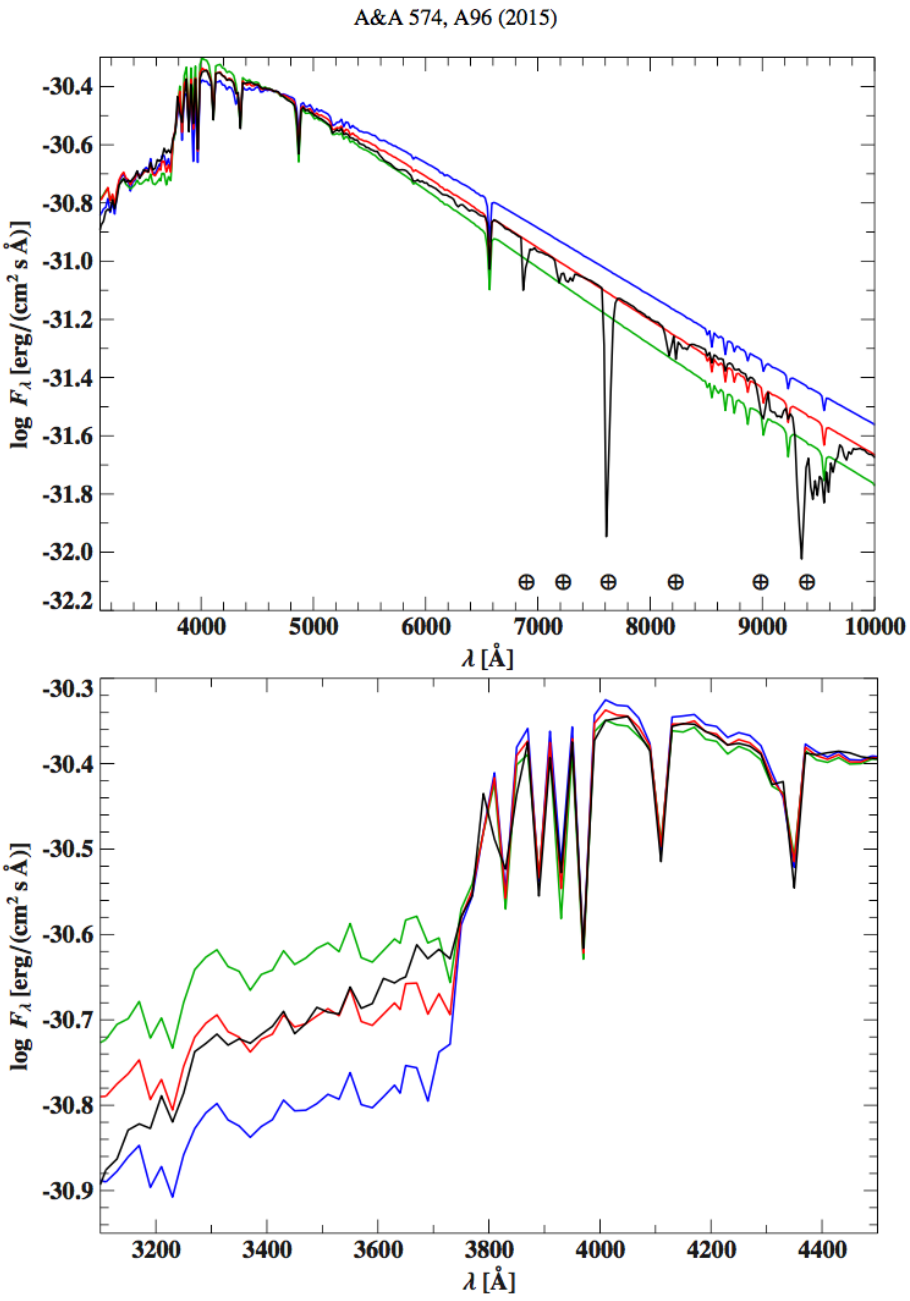

Figure B.3: X-Shooter spectrum of WISE J0725-2351 (black, telluric absorption bands are marked by a $\oplus$). Synthetic spectrum with [Fe/H] = -2.0, $T_{\rm eff}$ = 6250 K and $\log(g)$ = 4.0 (red). Top: full wavelength range and synthetic spectra with varied $T_{\rm eff}$ = 6500 K(green) and 6000 K (blue). Bottom: Balmer jump with varied $\log(g)$ = 4.5 (green) and 3.5 (blue).

Appendix C

Fit to the UVES spectrum of HD204041 + residuals

As an example, a complete fit of the UVES spectrum of the moderately rotating standard star HD204041 is shown here from $\sim$ 3900 - 8000 Å. The areas where no lines are visible or gaps in the spectrum occurred, are left out.

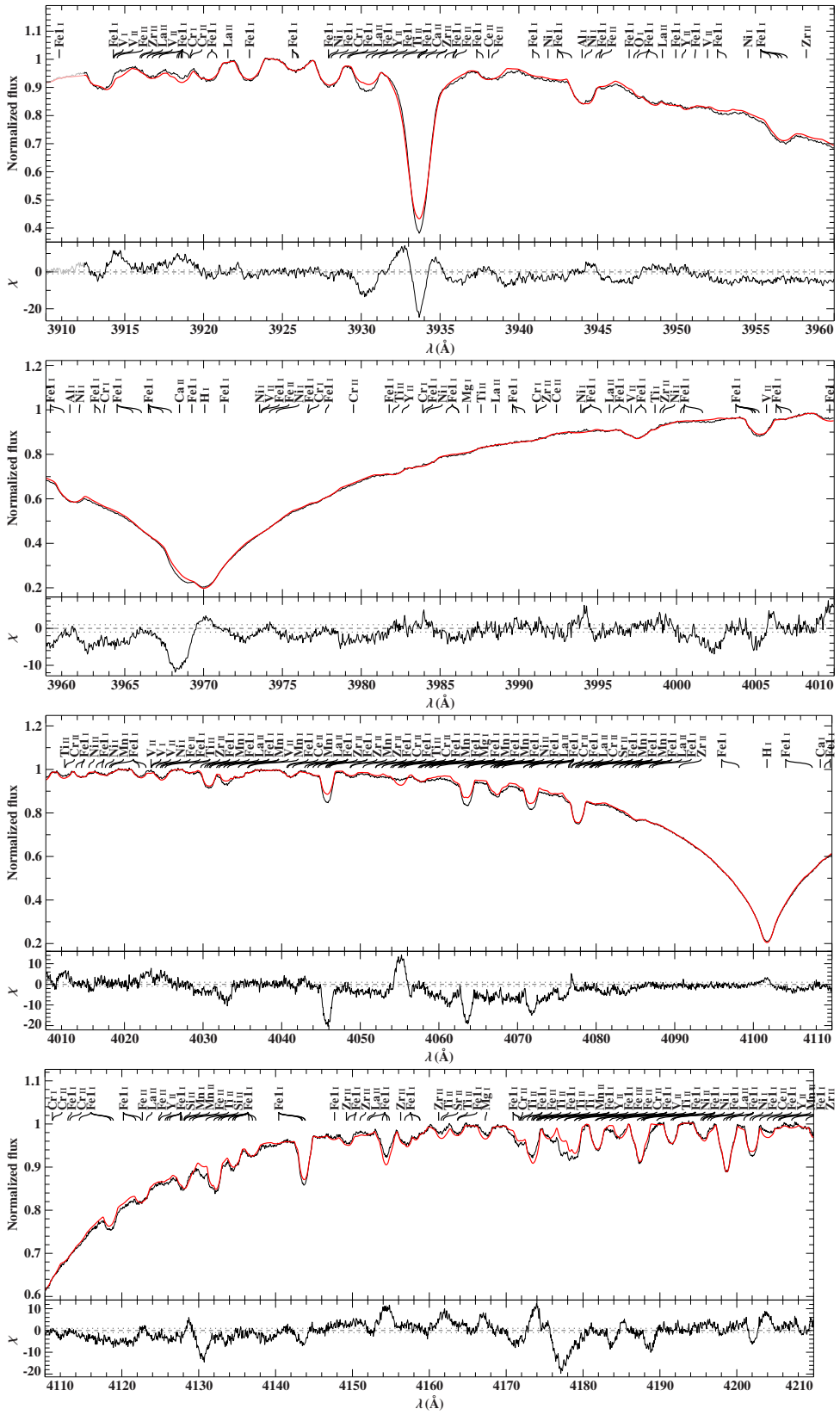

Figure C.1: Fit and residuals to the UVES spectrum of HD204041. Only lines intrinsically stronger than 5% are labeled. Black is the data, red the best fit model. Grey areas are ignored for the fit.

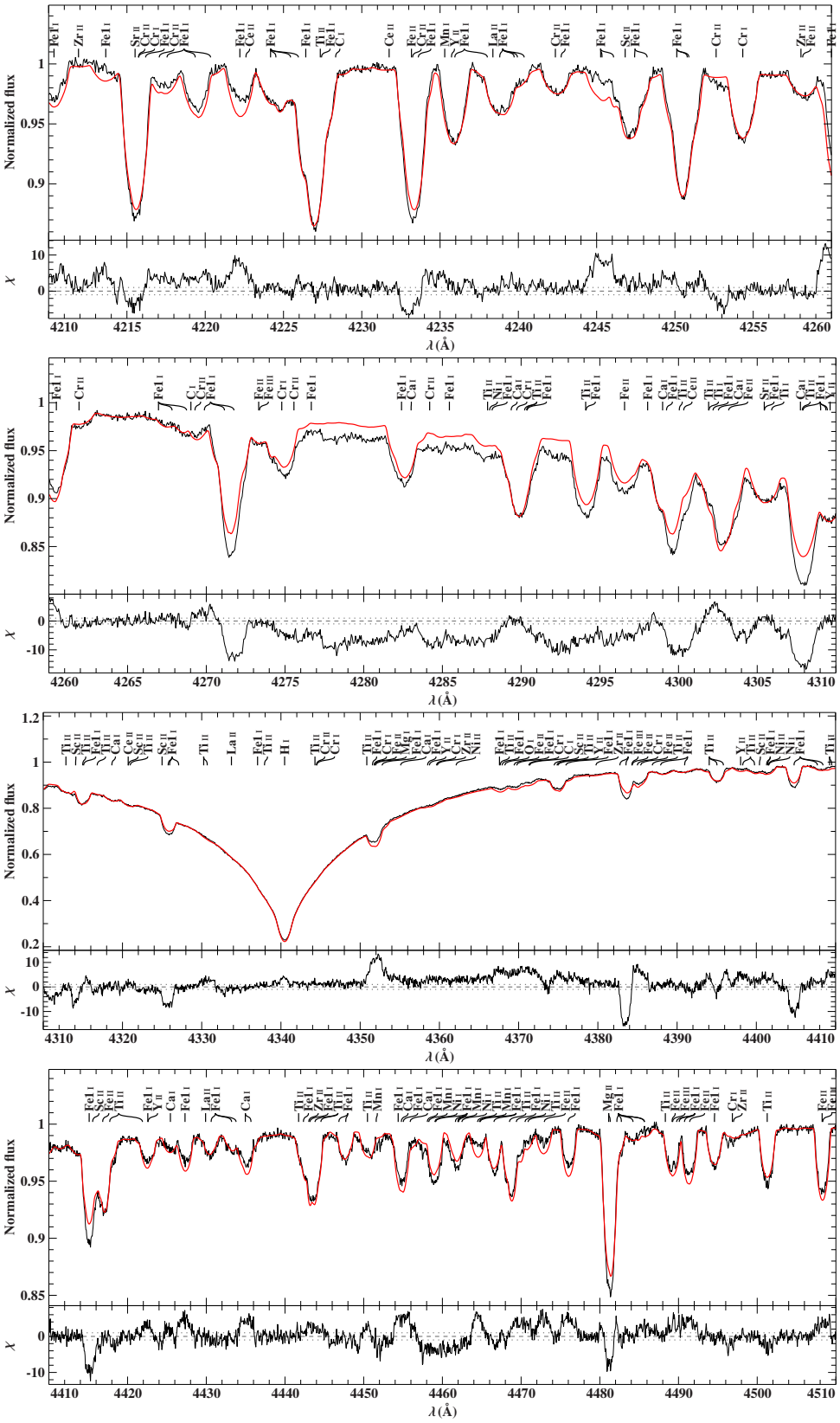

Figure C.2: Fit and residuals to the UVES spectrum of HD204041. Only lines intrinsically stronger than 5% are labeled. Black is the data, red the best fit model. Grey areas are ignored for the fit.

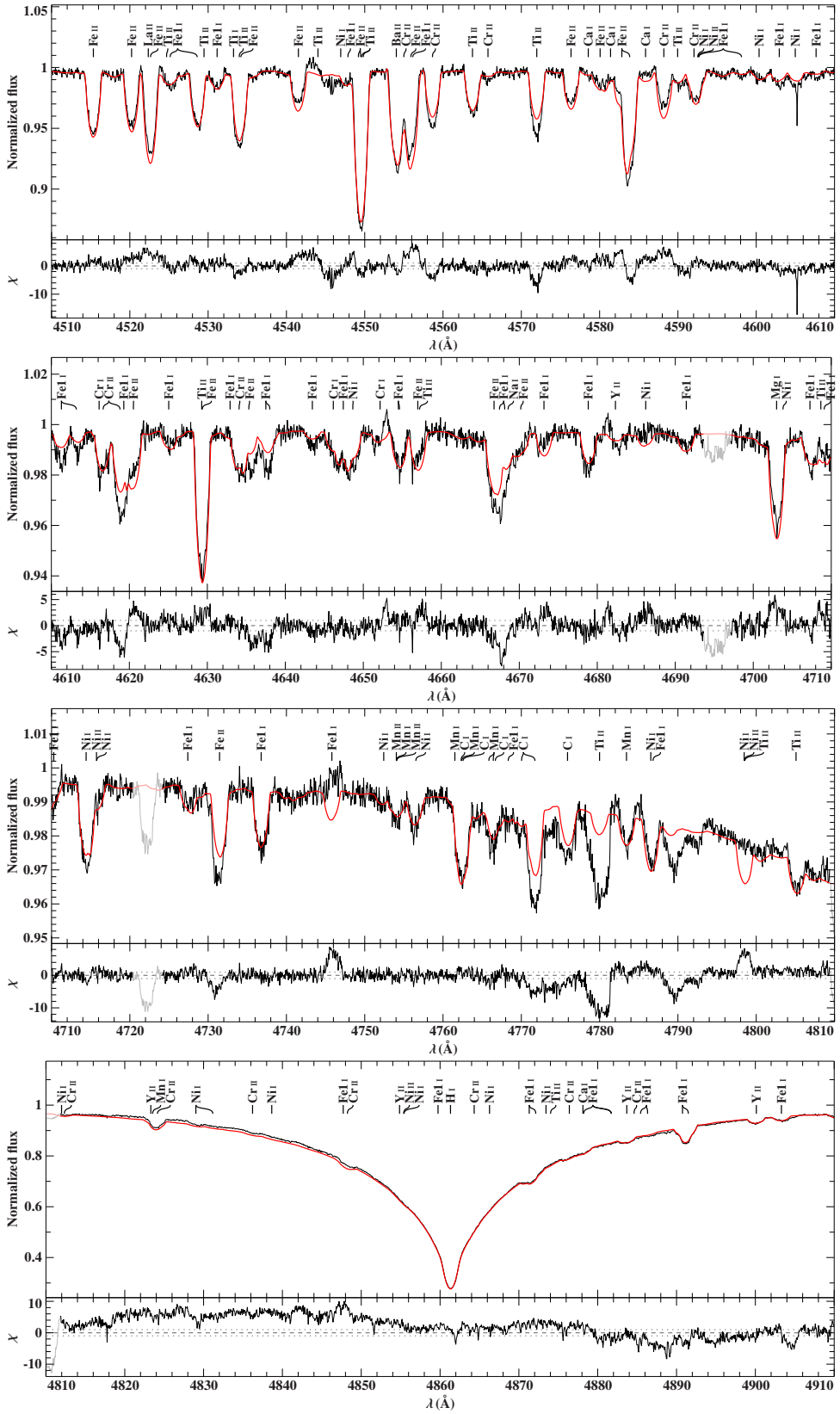

Figure C.3: Fit and residuals to the UVES spectrum of HD204041. Only lines intrinsically stronger than 5% are labeled. Black is the data, red the best fit model. Grey areas are ignored for the fit.

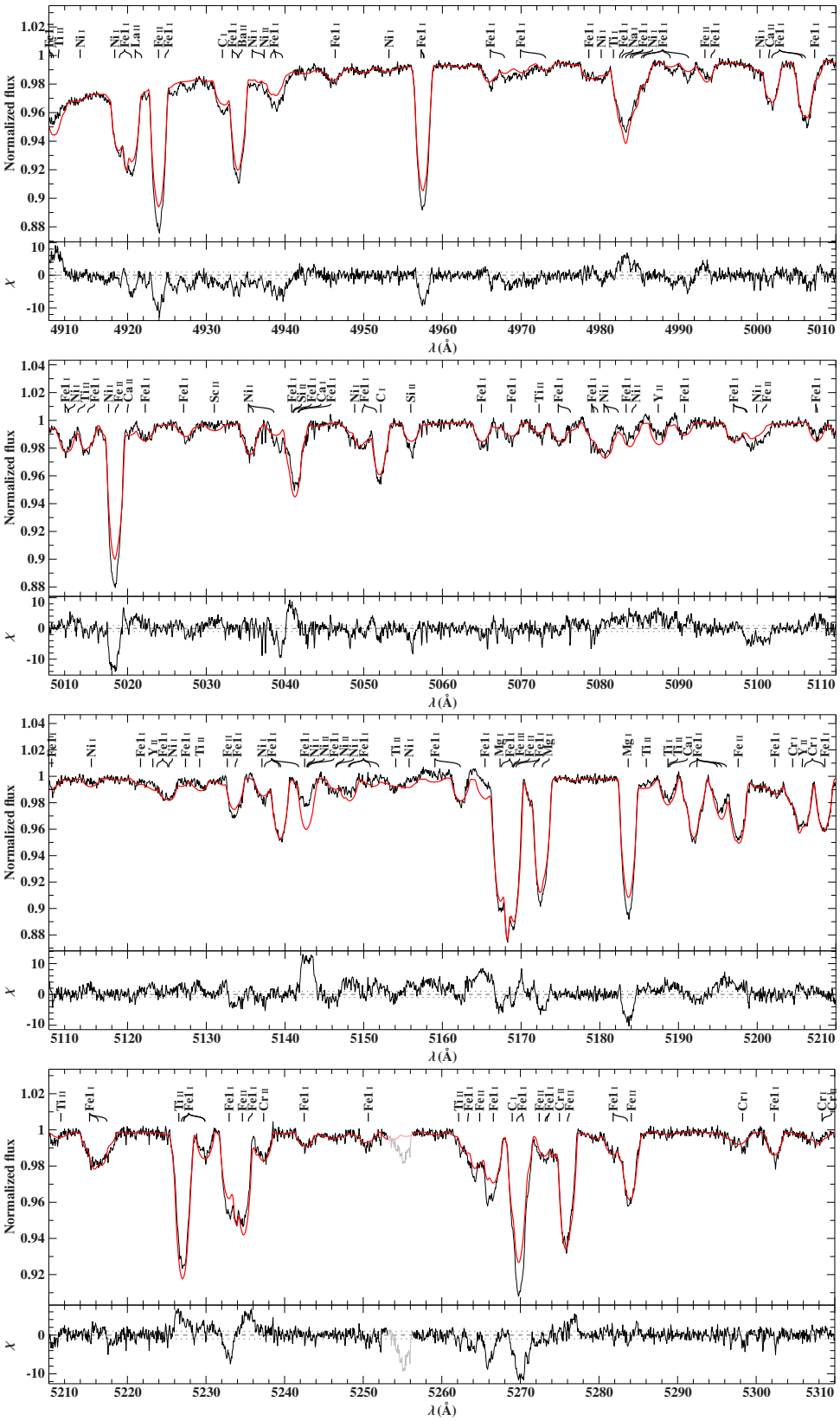

Figure C.4: Fit and residuals to the UVES spectrum of HD204041. Only lines intrinsically stronger than 5% are labeled. Black is the data, red the best fit model. Grey areas are ignored for the fit.

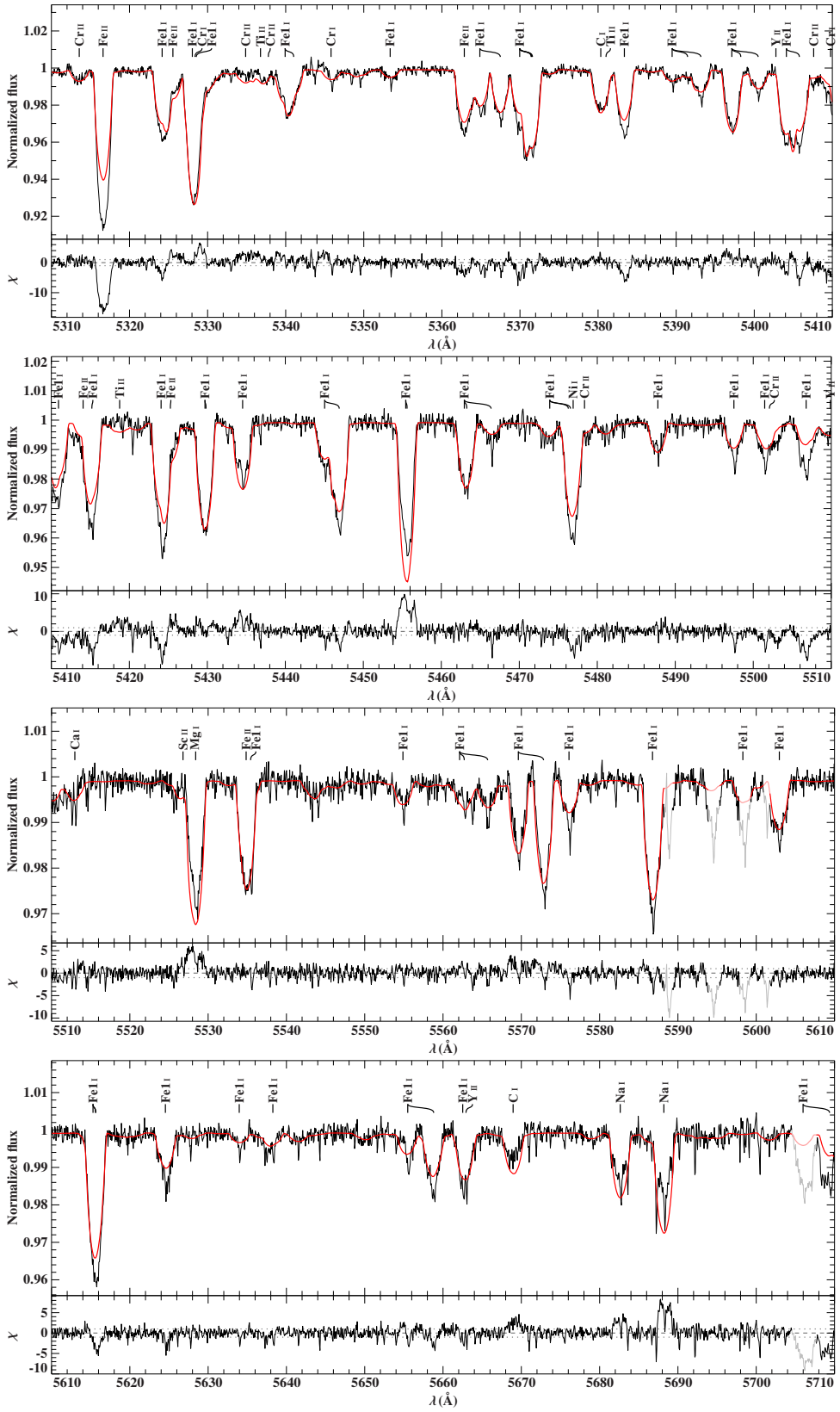

Figure C.5: Fit and residuals to the UVES spectrum of HD204041. Only lines intrinsically stronger than 5% are labeled. Black is the data, red the best fit model. Grey areas are ignored for the fit.

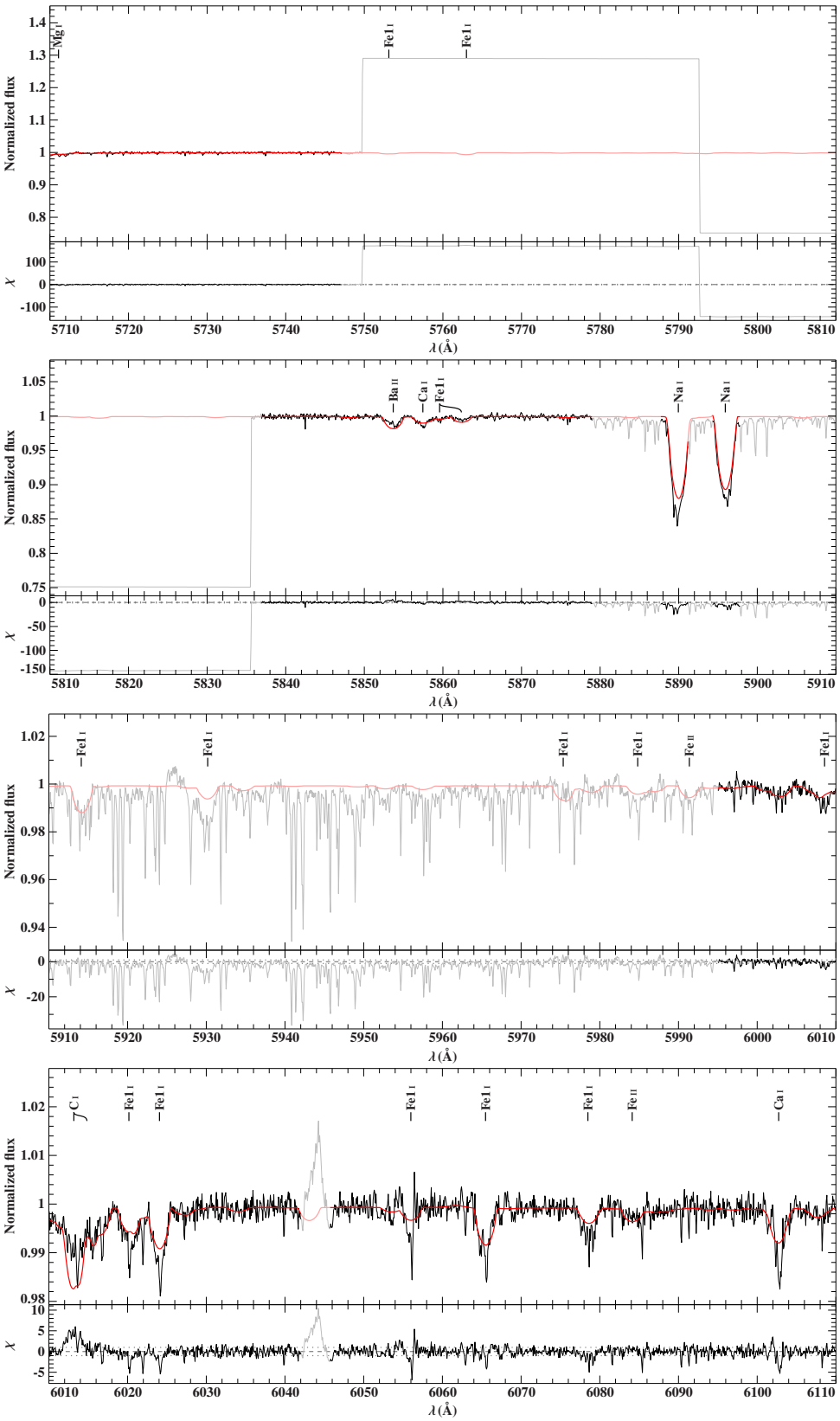

Figure C.6: Fit and residuals to the UVES spectrum of HD204041. Only lines intrinsically stronger than 5% are labeled. Black is the data, red the best fit model. Grey areas are ignored for the fit.

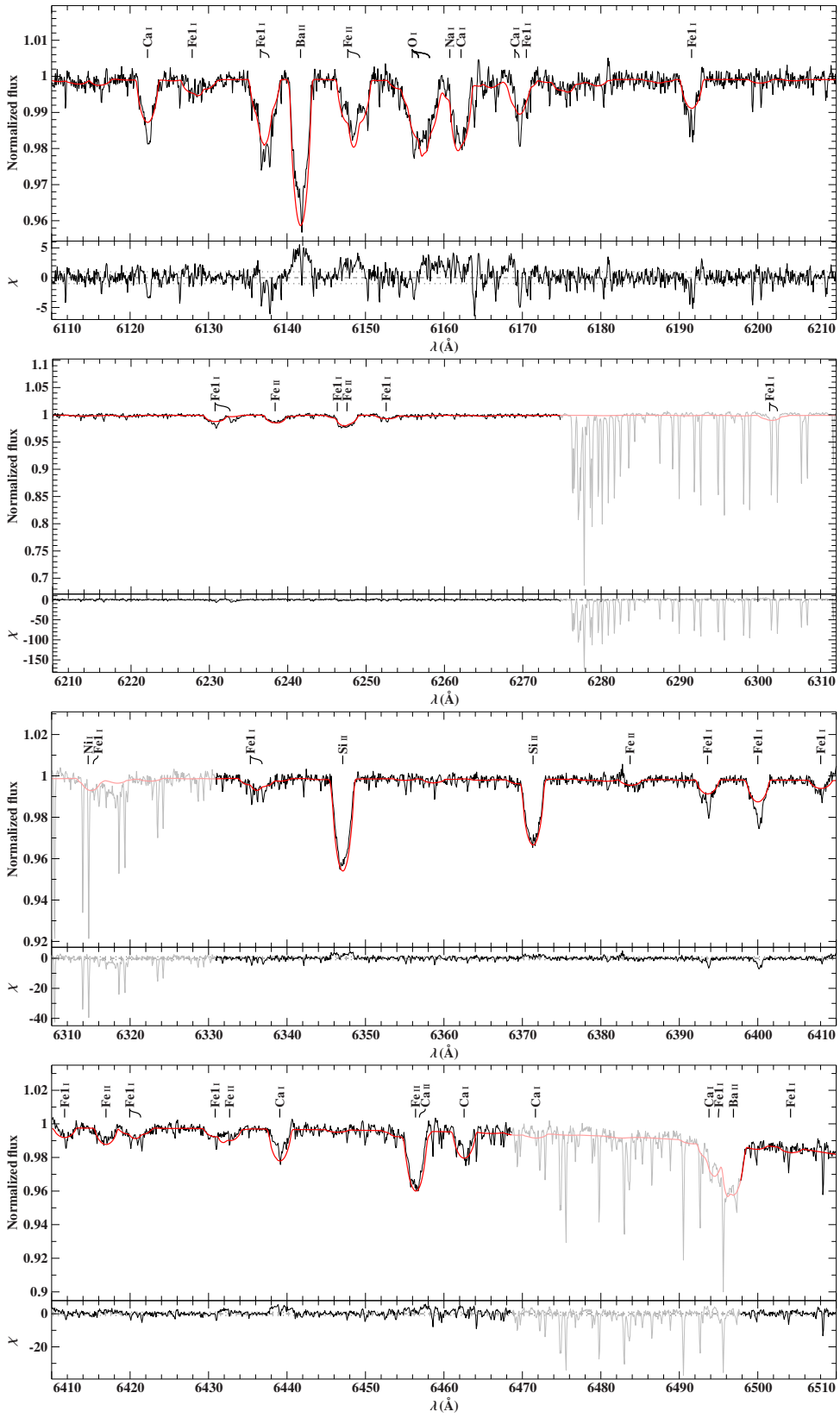

Figure C.7: Fit and residuals to the UVES spectrum of HD204041. Only lines intrinsically stronger than 5% are labeled. Black is the data, red the best fit model. Grey areas are ignored for the fit.

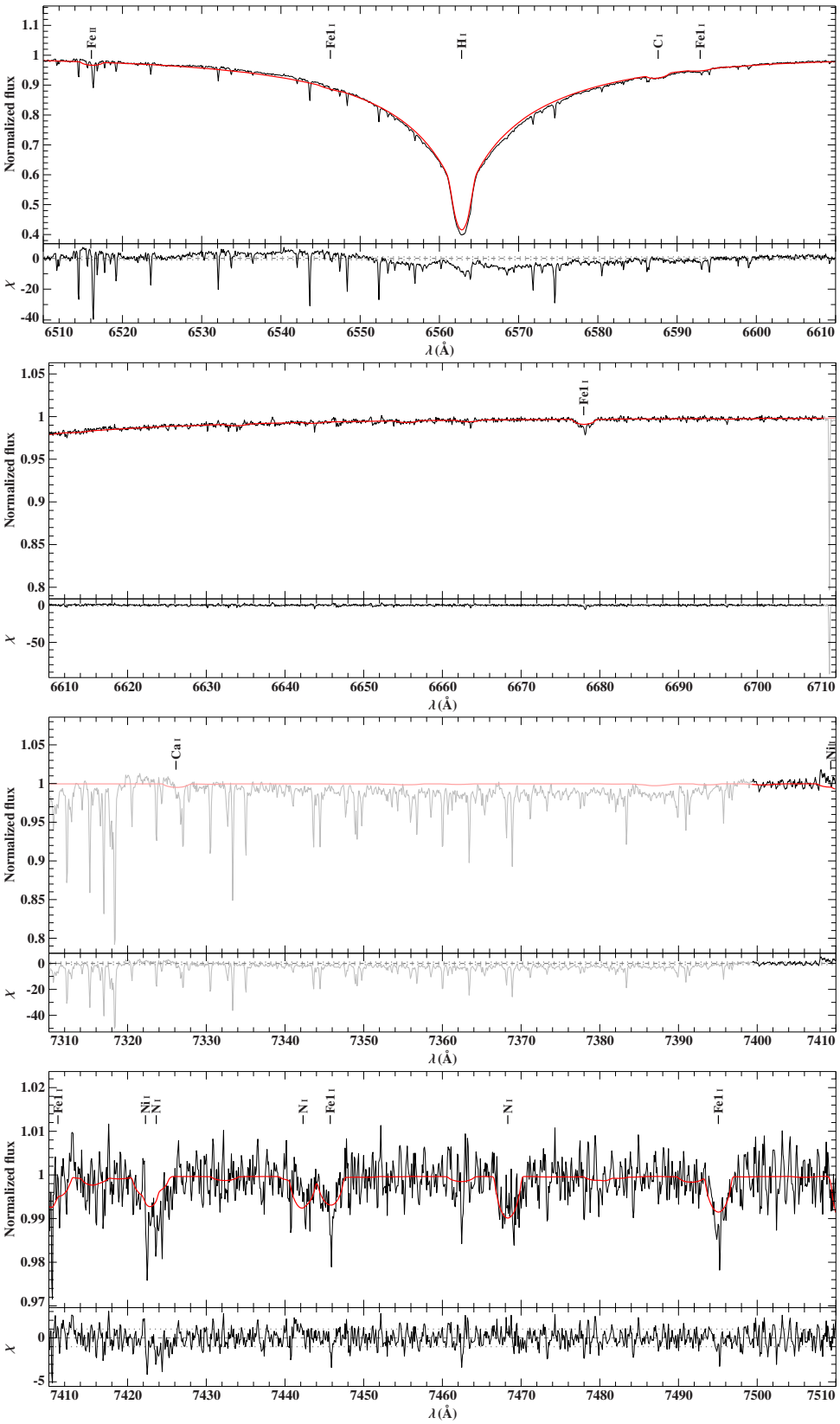

Figure C.8: Fit and residuals to the UVES spectrum of HD204041. Only lines intrinsically stronger than 5% are labeled. Black is the data, red the best fit model. Grey areas are ignored for the fit.

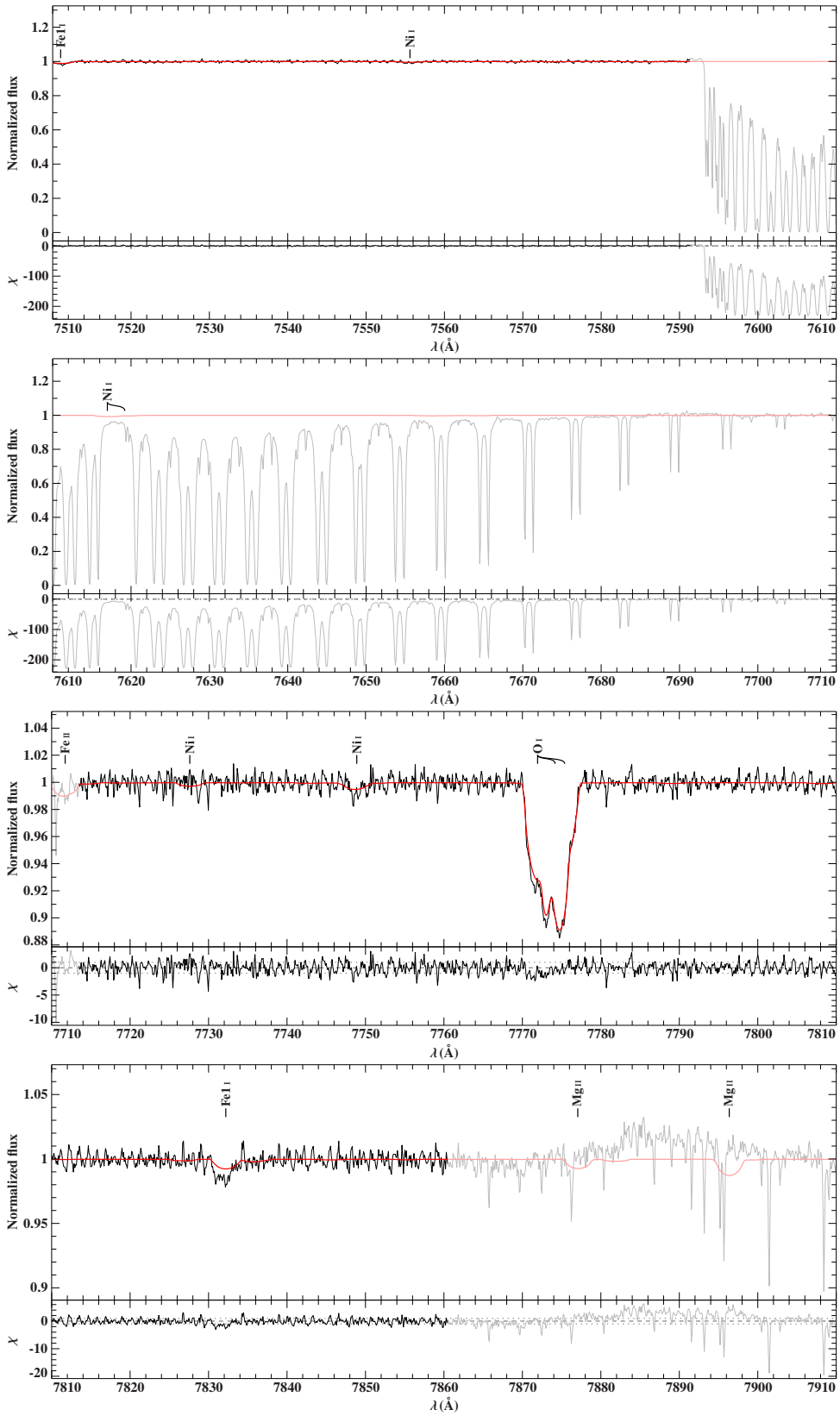

Figure C.9: Fit and residuals to the UVES spectrum of HD204041. Only lines intrinsically stronger than 5% are labeled. Black is the data, red the best fit model. Grey areas are ignored for the fit.

Appendix D

Fit to the UVES spectrum of HD189849 + residuals

As an example, the most interesting parts of the fit of the UVES spectrum of the most peculiar star of our star sample HD189849 is shown here from $\sim$ 3900 - 8000 Å. Please note, that the red markers correspond to identified lines in some of our sample stars and are not necessarily identified lines in this particular spectrum of HD189849.

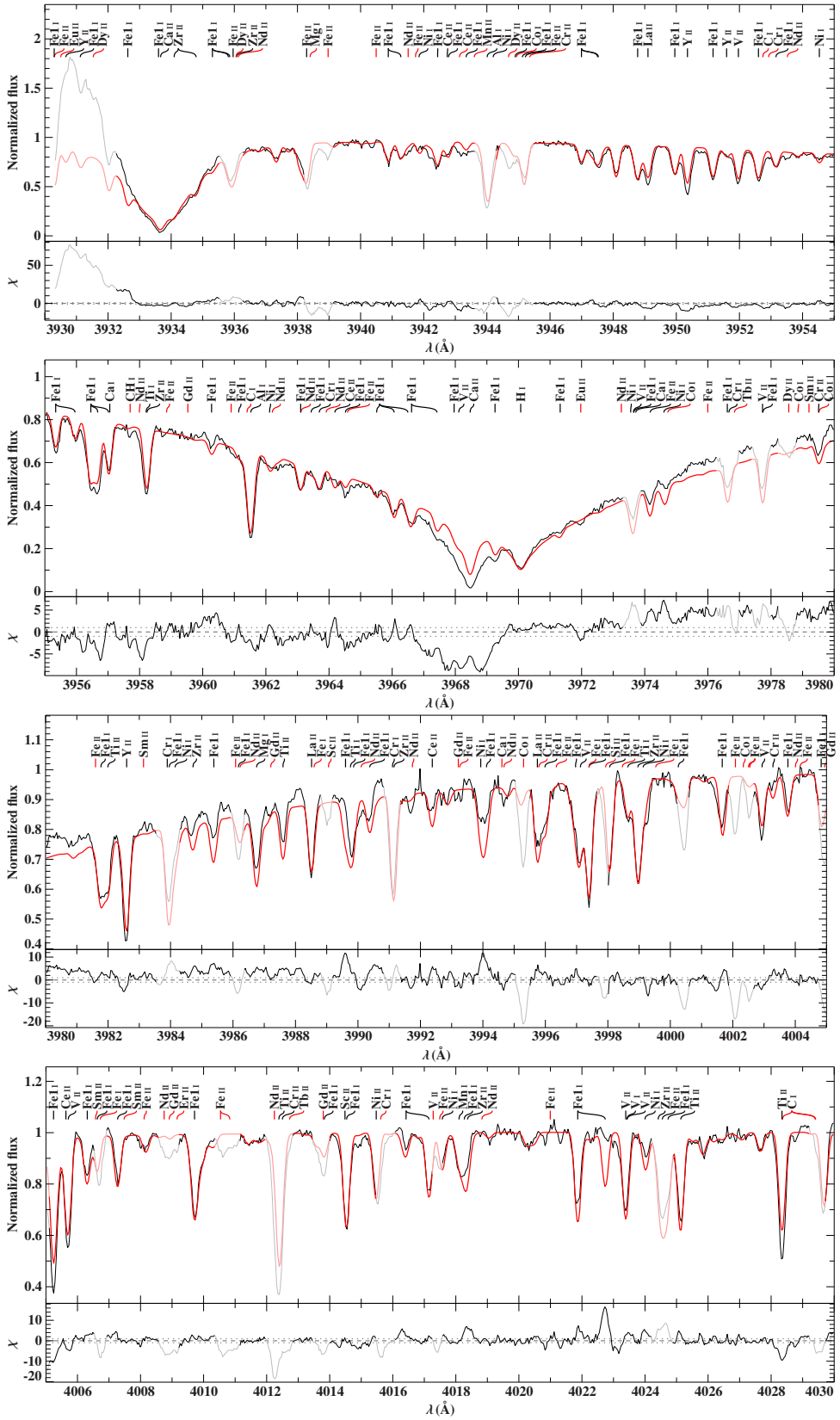

Figure D.1: Fit and residuals to the UVES spectrum of the chemically peculiar star HD189849. Only lines intrinsically stronger than 25% are labeled. The labels with red markers are observationally identified lines, which are not included in our models. Black is the data, red the best fit model. Grey areas are ignored for the fit.

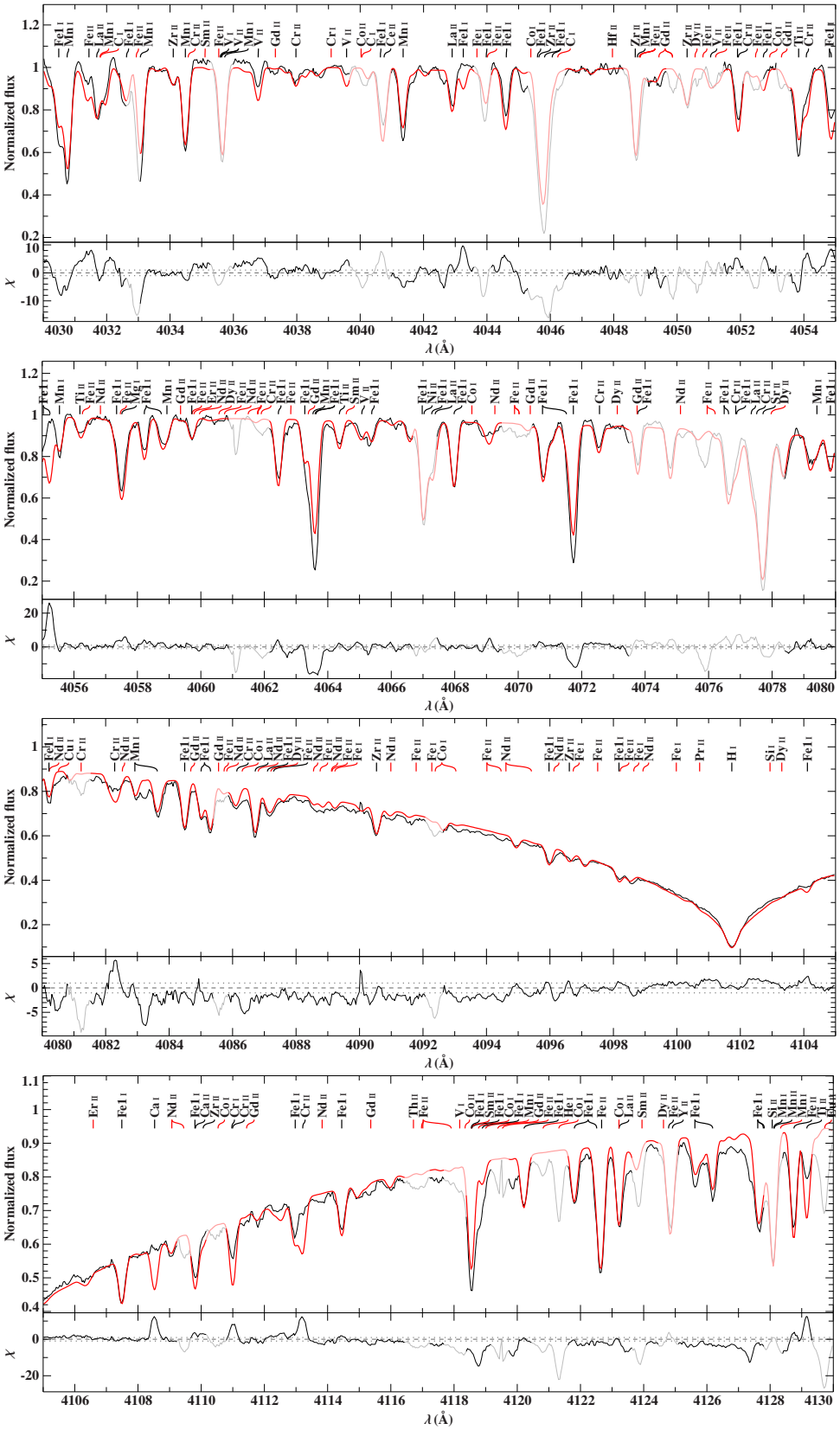

Figure D.2: Fit and residuals to the UVES spectrum of the chemically peculiar star HD189849. Only lines intrinsically stronger than 25% are labeled. The labels with red markers are observationally identified lines, which are not included in our models. Black is the data, red the best fit model. Grey areas are ignored for the fit.

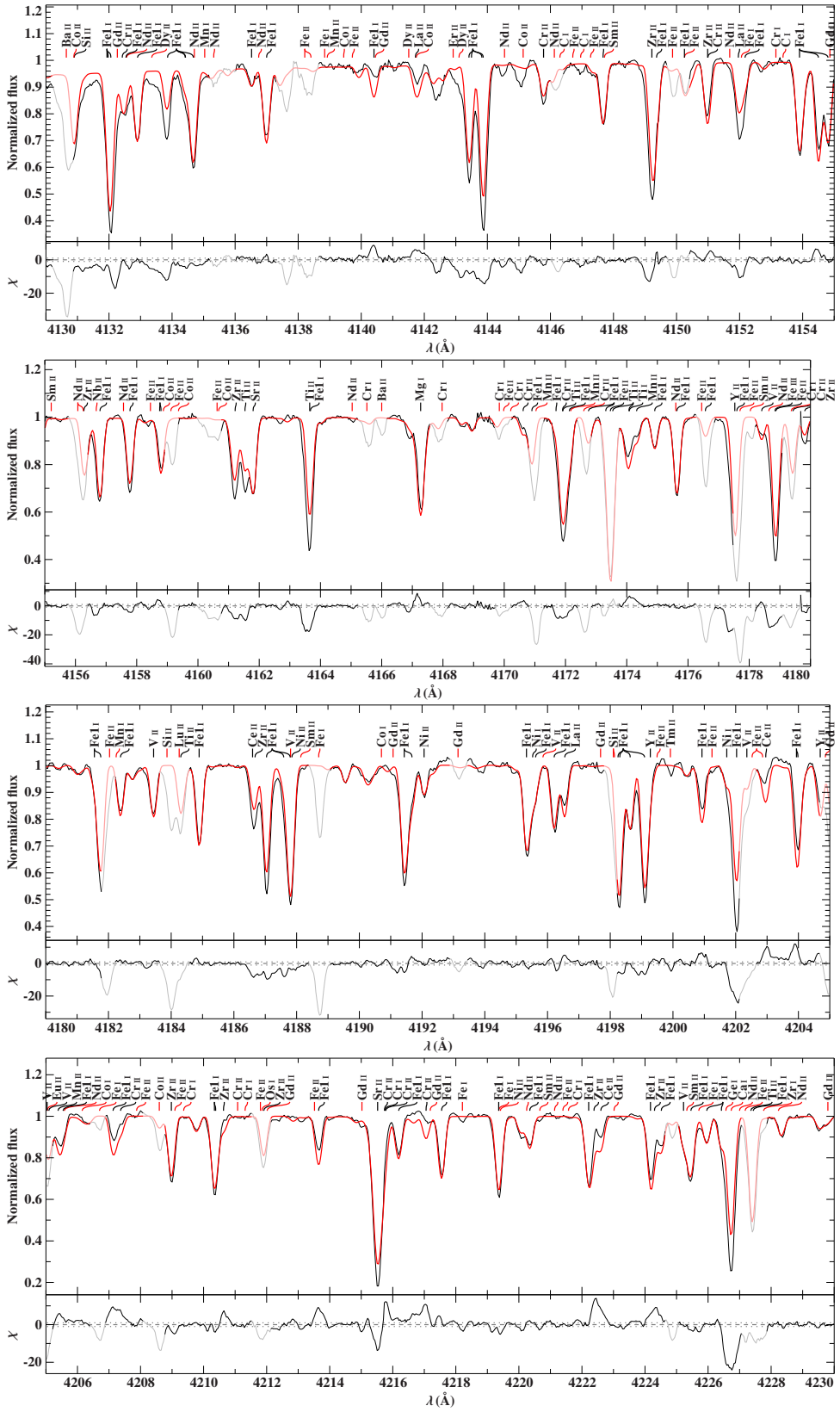

Figure D.3: Fit and residuals to the UVES spectrum of the chemically peculiar star HD189849. Only lines intrinsically stronger than 25% are labeled. The labels with red markers are observationally identified lines, which are not included in our models. Black is the data, red the best fit model. Grey areas are ignored for the fit.

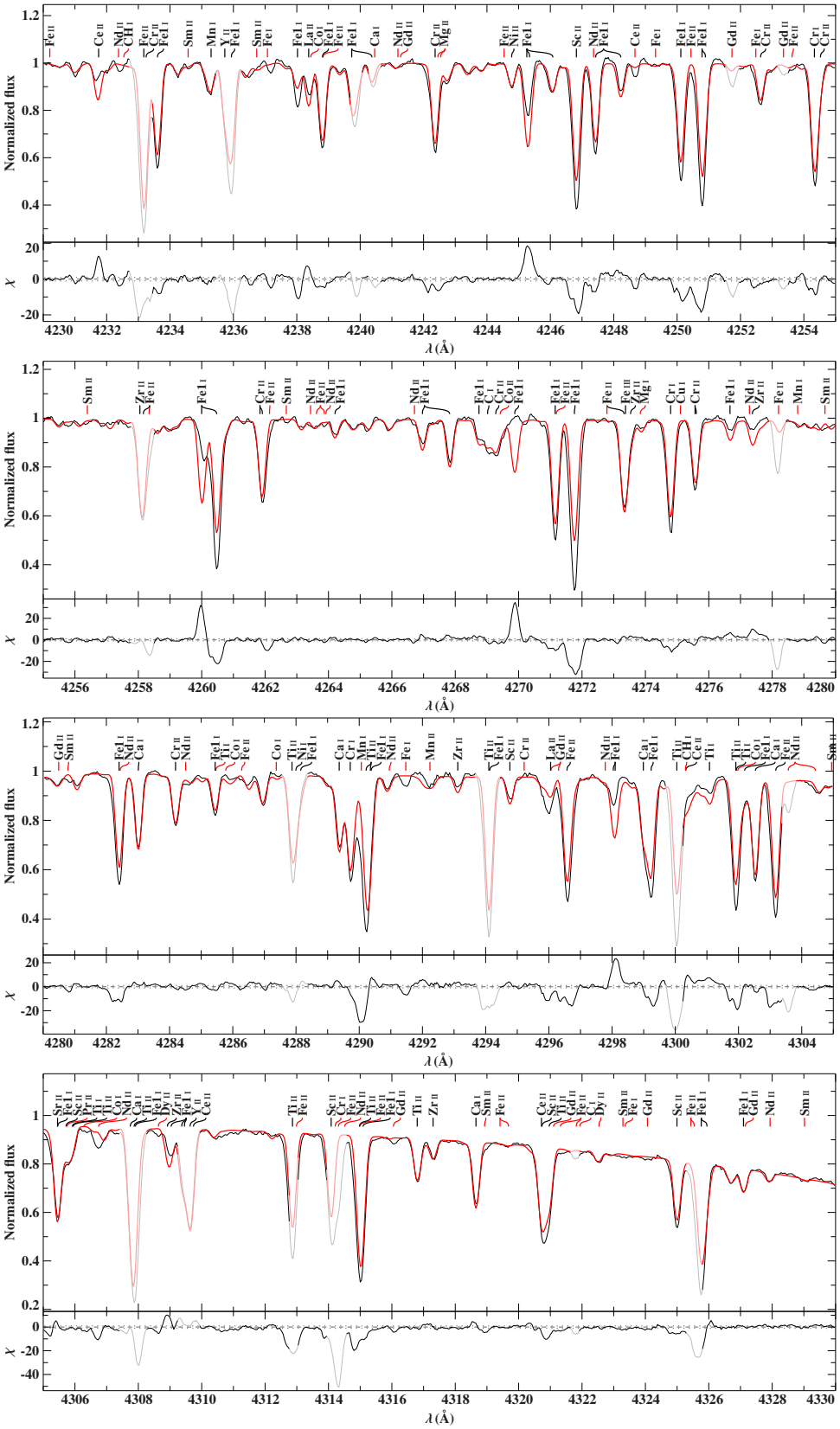

Figure D.4: Fit and residuals to the UVES spectrum of the chemically peculiar star HD189849. Only lines intrinsically stronger than 25% are labeled. The labels with red markers are observationally identified lines, which are not included in our models. Black is the data, red the best fit model. Grey areas are ignored for the fit.

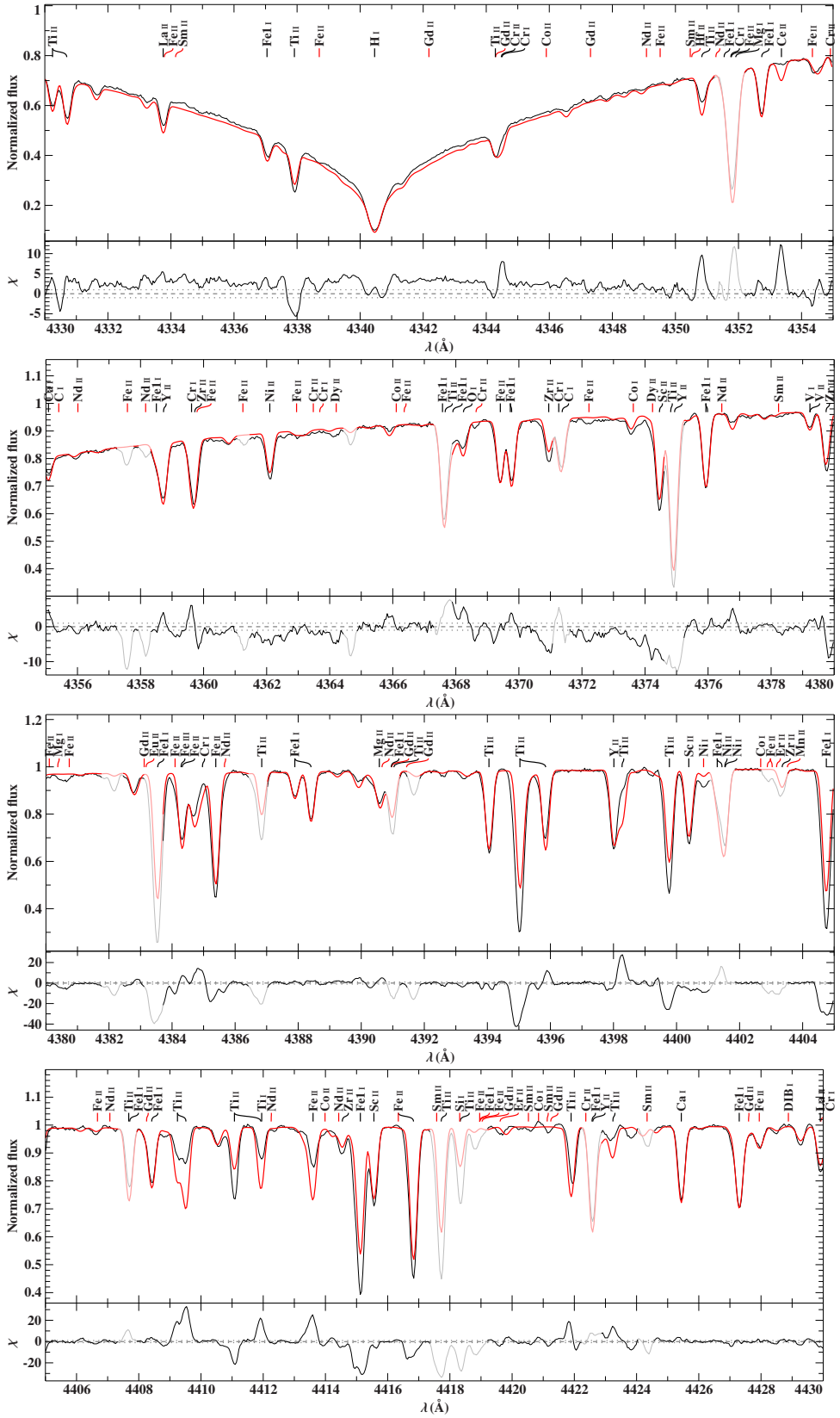

Figure D.5: Fit and residuals to the UVES spectrum of the chemically peculiar star HD189849. Only lines intrinsically stronger than 25% are labeled. The labels with red markers are observationally identified lines, which are not included in our models. Black is the data, red the best fit model. Grey areas are ignored for the fit.

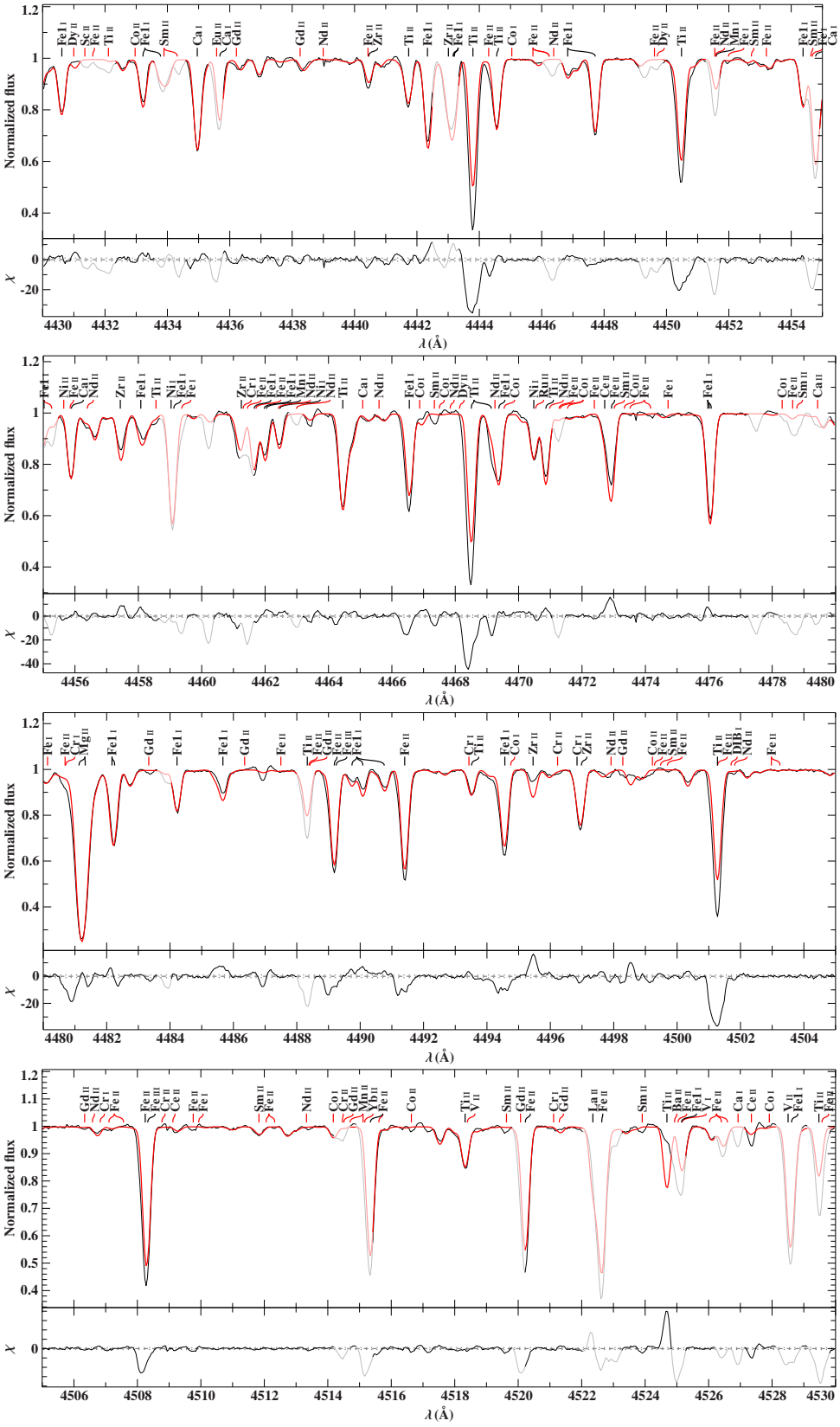

Figure D.6: Fit and residuals to the UVES spectrum of the chemically peculiar star HD189849. Only lines intrinsically stronger than 25% are labeled. The labels with red markers are observationally identified lines, which are not included in our models. Black is the data, red the best fit model. Grey areas are ignored for the fit.

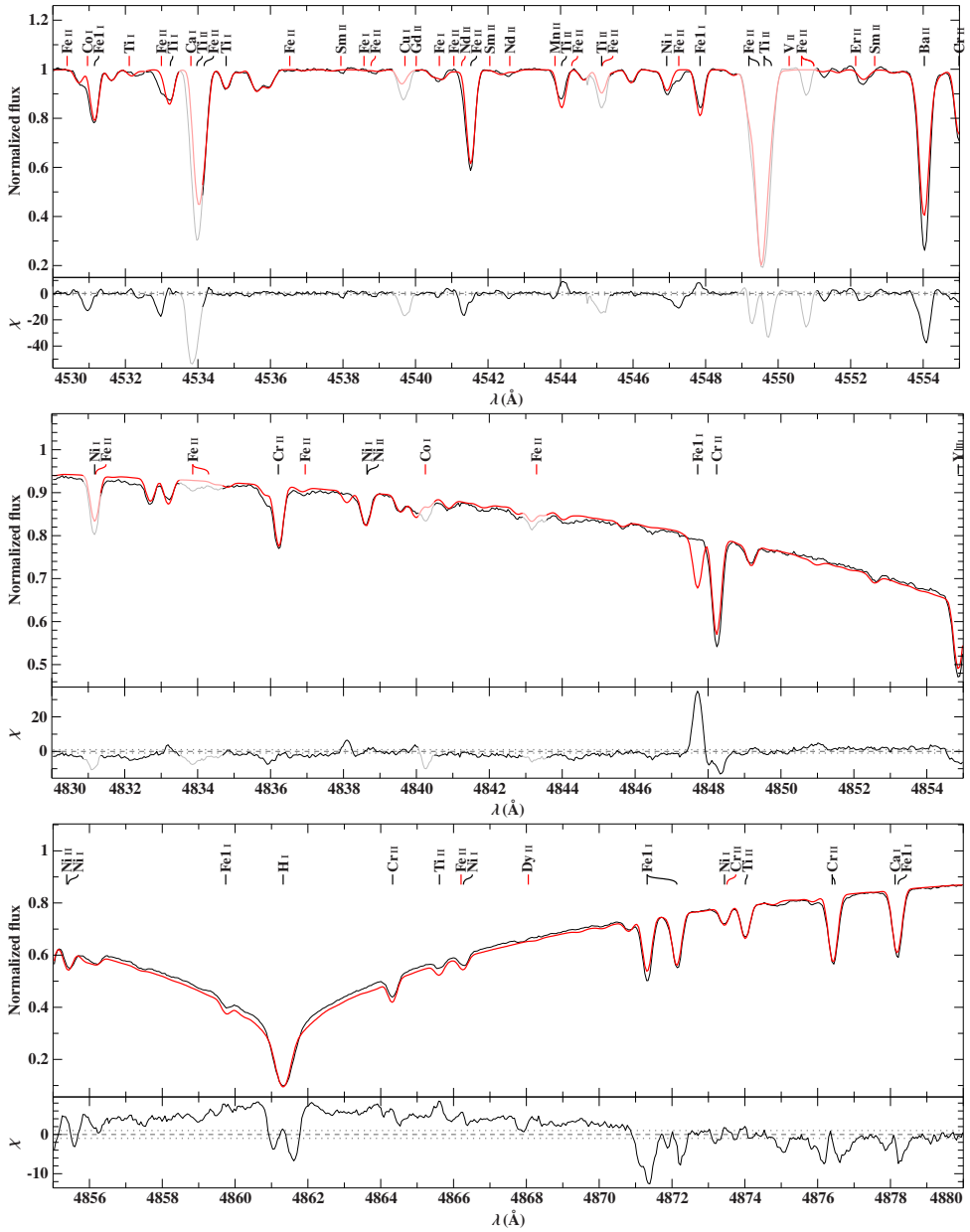

Figure D.7: Fit and residuals to the UVES spectrum of the chemically peculiar star HD189849. Only lines intrinsically stronger than 25% are labeled. The labels with red markers are observationally identified lines, which are not included in our models. Black is the data, red the best fit model. Grey areas are ignored for the fit.

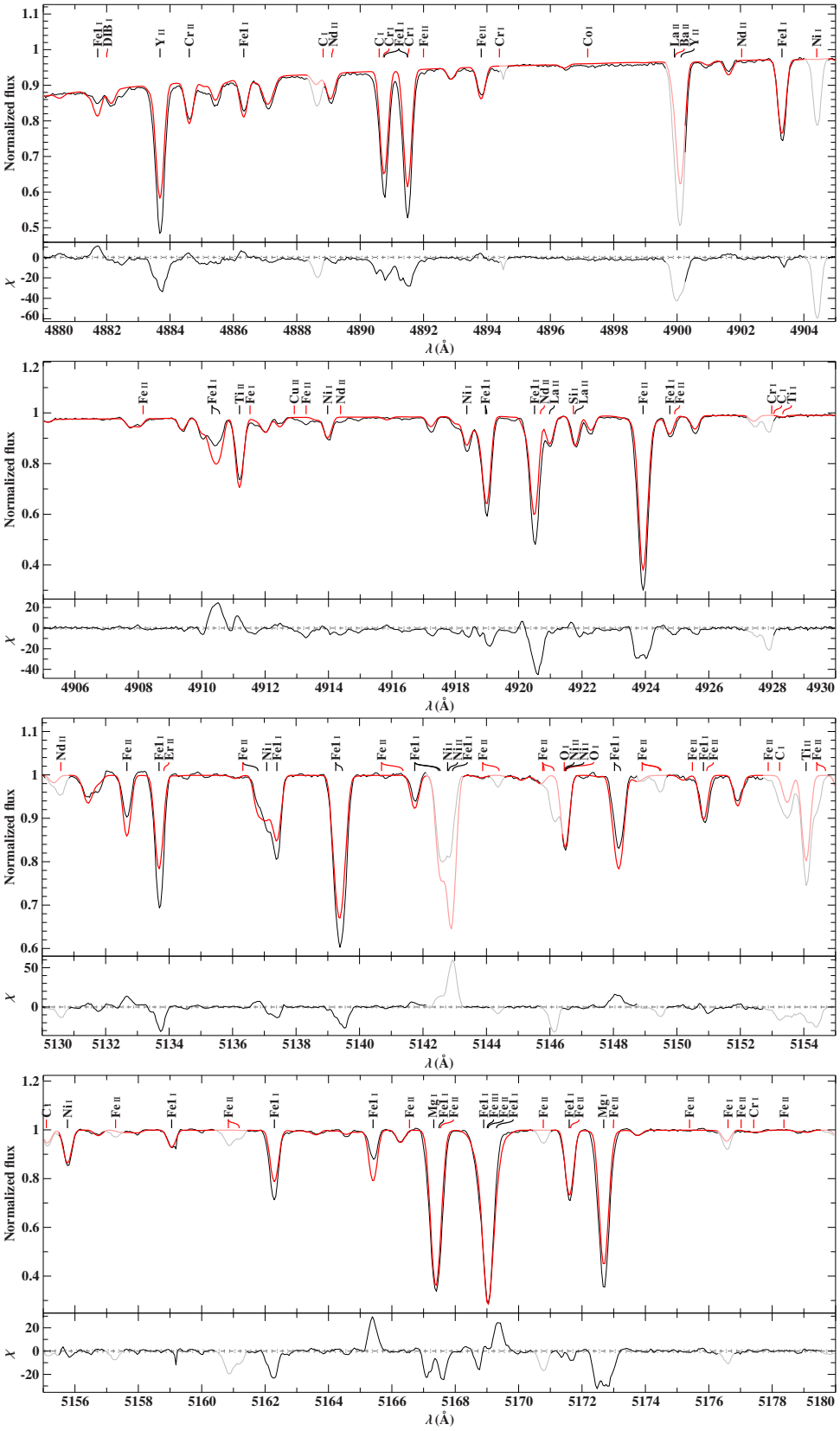

Figure D.8: Fit and residuals to the UVES spectrum of the chemically peculiar star HD189849. Only lines intrinsically stronger than 25% are labeled. The labels with red markers are observationally identified lines, which are not included in our models. Black is the data, red the best fit model. Grey areas are ignored for the fit.

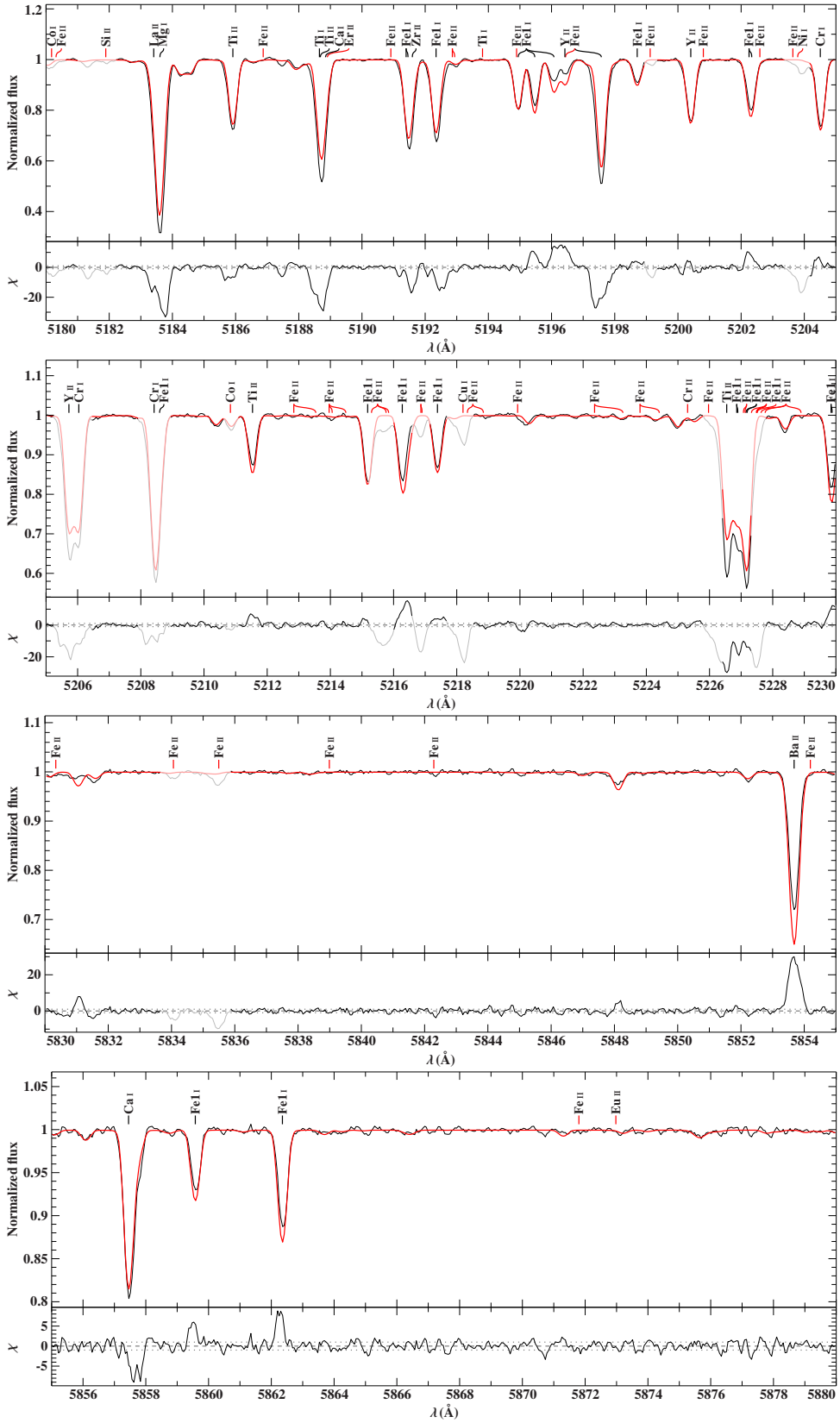

Figure D.9: Fit and residuals to the UVES spectrum of the chemically peculiar star HD189849. Only lines intrinsically stronger than 25% are labeled. The labels with red markers are observationally identified lines, which are not included in our models. Black is the data, red the best fit model. Grey areas are ignored for the fit.

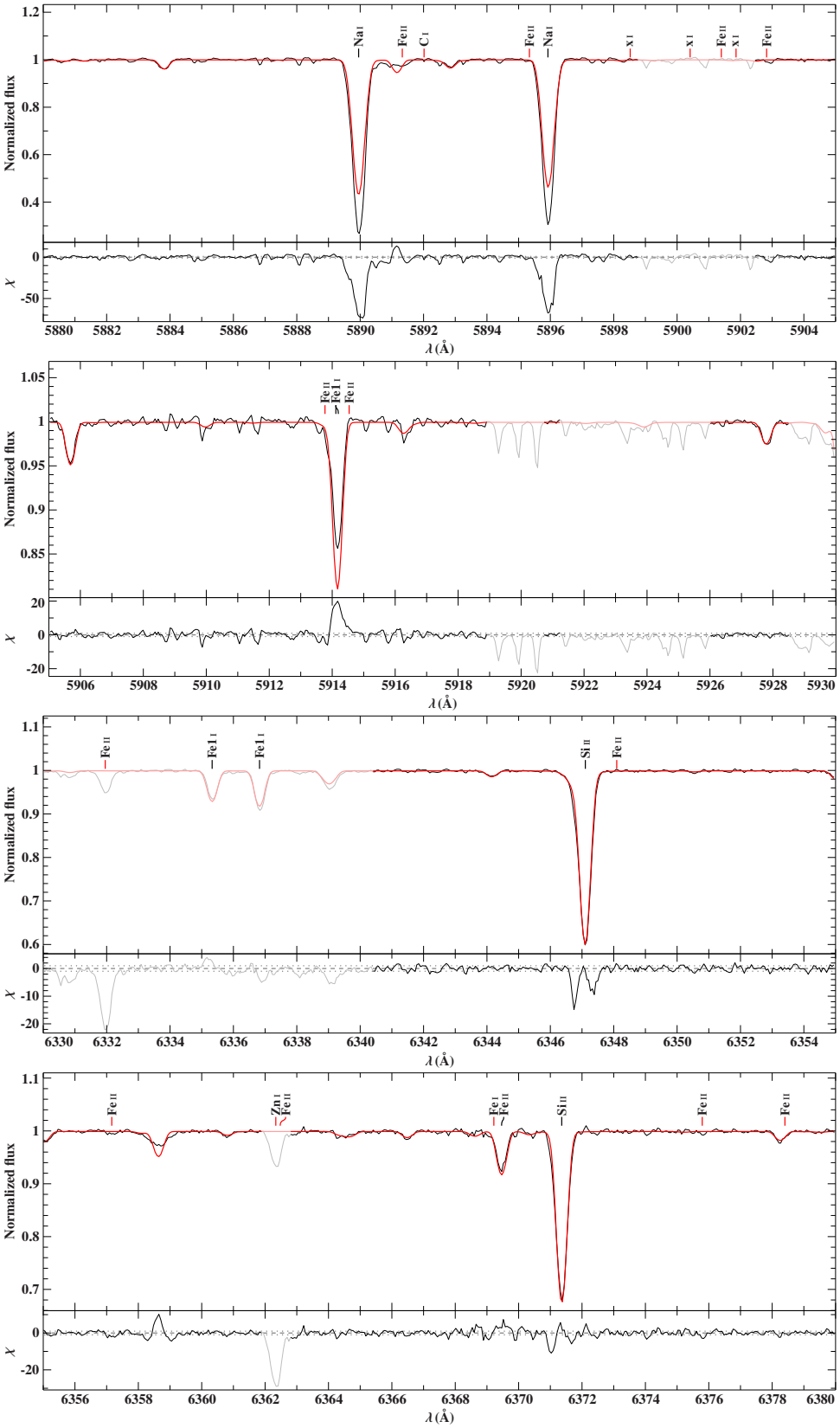

Figure D.10: Fit and residuals to the UVES spectrum of the chemically peculiar star HD189849. Only lines intrinsically stronger than 25% are labeled. The labels with red markers are observationally identified lines, which are not included in our models. Black is the data, red the best fit model. Grey areas are ignored for the fit.

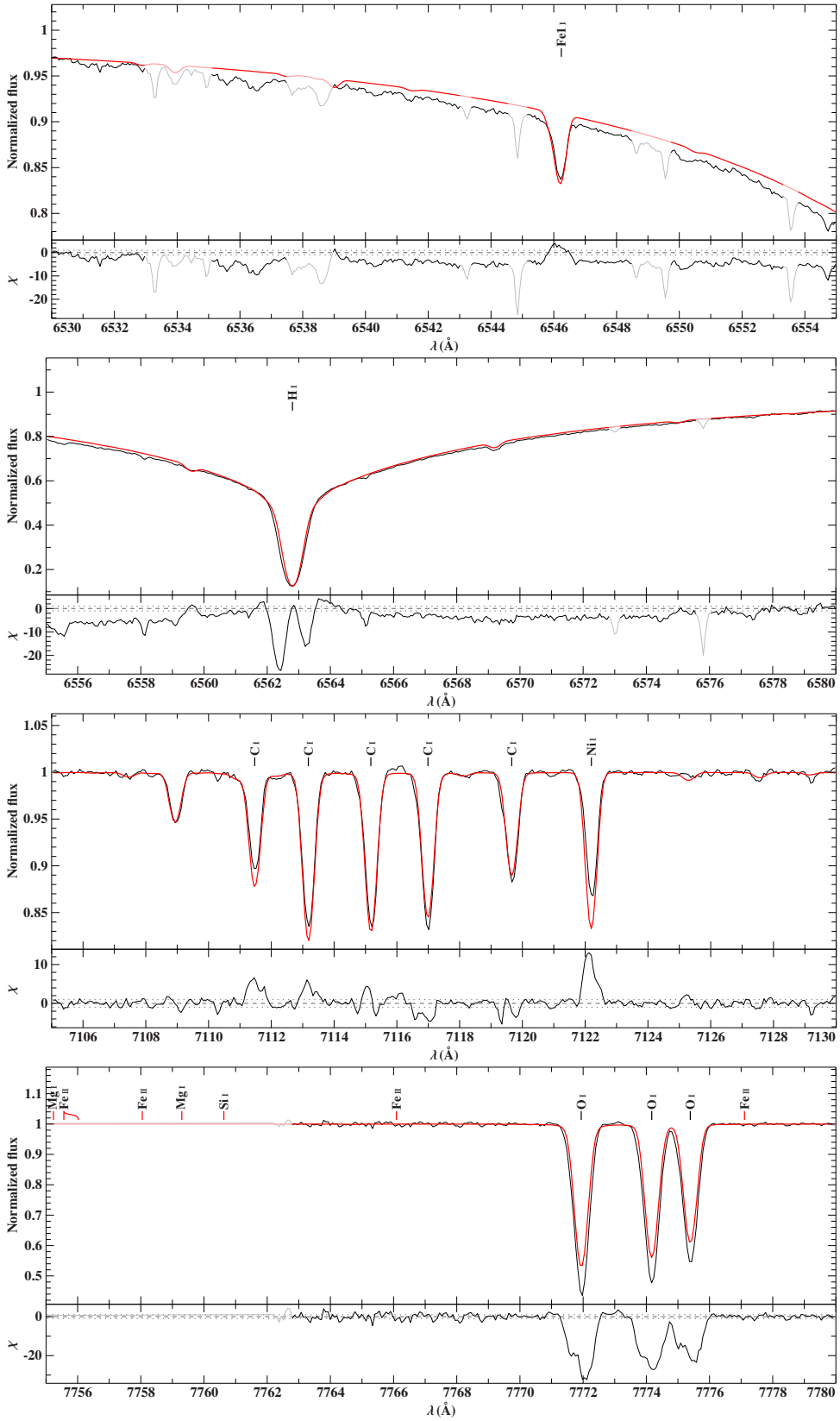

Figure D.11: Fit and residuals to the UVES spectrum of the chemically peculiar star HD189849. Only lines intrinsically stronger than 25% are labeled. The labels with red markers are observationally identified lines, which are not included in our models. Black is the data, red the best fit model. Grey areas are ignored for the fit.

Appendix E

Acknowledgements

EINE *Doktorarbeit ist in den seltensten Fällen das Werk einer einzelnen Person, sondern meistens das Ergebnis der Zusammenarbeit und der Beeinflussung durch viele Personen, denen ich hier Danken möchte.*
Als allererstes geht mein Dank an meinen Doktorvater Uli, der mich immer in allen Belangen unterstützt hat und mir sehr viel Freiraum in der Ausgestaltung meiner Arbeit gegeben hat. Die vielen Dienstreisen, sei es auf Konferenzen oder auf Beobachtungsruns an Großteleskopen der ganzen Welt wären ohne ihn nicht möglich gewesen und haben maßgeblich zum Spaß an der Arbeit beigetragen.
Dann möchte ich mich bei allen Remeisianern bedanken, die die Sternwarte zu einem besonderen Ort und den vielleicht schönsten Arbeitsplatz der Welt gemacht haben und machen. Viele der Kollegen sind auch privat gute Freunde geworden. Ein Dank auch an die Direktoren Uli, Horst, Jörn und Manami, die durch ihren Führungsstil diese Atmosphäre erst ermöglichen. Ebenso bedanke ich mich für die die Beantwortung vieler Fragen und Diskussionen, nicht nur durch meinen Betreuer Uli sondern auch einer ganzen Reihe von netten und kompetenten Kollegen: Andreas, Stephan, Eva, Matthias, Peter, Eike, Daniel, Simon, Marylin, Norbert, Sebastian, Horst, Veronika, Raoul, Ingo, Frau Bues, Eugenia, Heinz, Fernanda, Thomas und unzählige andere Personen, die mir bitte verzeihen mögen, sie hier nicht explizit erwähnt zu haben.
Ein besonderer Dank geht an meine zeitweisen Kniggezimmer-Kollegen Stephan, Sebastian, Patrick, Lew, Eugenia, Dominik, Minja, Macarena, Markus, Wiebke, Kurt und Helga. Ein besonders besonderer Dank geht hierbei an Matthias, mein einzig dauerhafter Kniggerianer, der mit mir neben Stephan, Sebastian und Eugenia einen großen Beitrag bei der Vorbereitung festlicher Anlässe beigetragen hat. Ausserdem hat er mir in programmier- und allgemeinen Denktechnischen Problemen immer zur Seite gestanden, egal wie sehr er gerade in einer Email-Flut zu ersticken drohte.
Stephan danke ich für die tolle Nacht im Texanischen Otto-Struve-Teleskop und für die vielen Gespräche über (un-)wissenschaftliche Themen und die Inspiration in vielen Belangen.
"Danke" an Sebastian für seine Wortwitze und für die Organisationen diverser Wanderungen.
Danke an Eva, die immer für einen Austausch von Erkenntnissen jeder Art stets zu haben war und für das Drachenspiel. Danke an die tolle Zeit in Schottland mit Marylin, Eva und Simon!
Danke an Eugenia, für ihre Merkfähigkeit und Kaffeestatistik und für Johannes #2.
Danke an alle Korrekturleser: Uli, Dominik, Michi, Arne, Robert und Jasmina!
Edith Day danke ich für den Überblick und die Geduld bei der Klärung von etlichen

Bürokratiefragen und für die teils sehr erheiternden Flüche über die Natur unseres Kopierers.
Besonders hervorzuheben ist auch Dr. Andreas #1, der mir durch seine unermüdliche Geduldigkeit seine Skripte auch zum xten mal erklärt hat und mit dem es sehr viel Spaß gemacht hat, die Studenten durch den Spektroskopieversuch im Praktikum zu führen. Ausserdem stammt er wie ich vom Planeten um den Stern Vega.
Dann möchte ich auch meinen Freunden danken, die mir privat immer zur Seite gestanden haben: Eva, Michi, Dominik, Ewie, Ferdi, Chrissy, Anna, Dustin sowie meinen Mitbewohnern, vor allem Jutta, Elli und Andi, meiner Band megaphon und meinen Vereinskollegen, allen voran Caro.
Mein letztgenanntes aber nicht letztgemeinter Dank geht an meine Eltern und meinen Bruder: Danke für Eure Unterstützung und das man sich immer auf Euch verlassen kann!
Diese Arbeit wurde finanziell unterstützt von der DFG im Rahmen des Projekts 203253810.
Danke!